Modelling the Impact of Heterogeneity in Tumour Composition on the Response to Fractionated Radiotherapy

Thomas Lewin
Pembroke College
University of Oxford

A thesis submitted for the degree of
Doctor of Philosophy
Trinity 2018

Abstract

Current protocols for delivering radiotherapy are based primarily on tumour stage and nodal and metastases (TNM) status, even though it is well known that tumours and their microenvironments are highly heterogeneous. Mathematical models have the potential to inform protocol selection on a more patient-specific basis. However such applications require early prediction of tumour response and, thus, calibration of the model parameters from pre-treatment data which is typically limited to two CT scans - one at diagnosis and one at the treatment planning stage. In this thesis we aim to determine whether pre-treatment tumour volume data may be used to accurately predict tumour response to radiotherapy. We further aim to provide a mechanistic description of the different qualitative responses to radiotherapy observed in clinical data and the influence of intratumoural heterogeneity on these dynamics.

Mathematical models for clinical applications typically contain few model parameters for ease of calibration with the sparse available data. Such models often take the form of single or multiple compartment ordinary differential equations (ODEs). We use parameter estimation and model selection techniques to perform both synthetic and clinical data studies and assess the predictive power of such models. We show that, while the models considered may be adequate in some cases, the range of qualitative dynamics exhibited by the clinical data extends beyond that which may be captured by these simple models.

To address this discrepancy, we develop a suite of increasingly complex models that account for spatial heterogeneity in tumours, and use a range of methods to assess their validity and predictive power. In particular, we use a combination of numerical simulation and asymptotic analysis to investigate the dynamics of each model and the impact of increasing spatial heterogeneity on tumour response to radiotherapy.

In vitro avascular tumour spheroids have a well-defined spatial structure, providing a simple geometry that is often exploited in tumour growth models. We extend one such model (Greenspan, 1972) to develop a new spatially-resolved model for tumour response to radiotherapy. Model simulations reveal a rapid transient increase in hypoxia upon regrowth of the tumour spheroid post-irradiation, a factor known to inhibit radiotherapy efficacy. We also investigate the response to different fractionation schedules and identify a tumour-specific relationship between inter-fraction time and dose per fraction to achieve cure.

We further use the framework of multiphase mixtures to develop new models of both tumour growth and radiotherapy response that allow for the greater degree of heterogeneity typically observed *in vivo*. The multiphase models describe a wider range of spatial tumour compositions and consider mechanical interactions between different constituents of the tumour microenvironment. They reproduce the qualitative radiotherapy response dynamics observed in clinical data, including behaviours not captured by simpler models. We characterise a range of dynamics exhibited by the model and demonstrate the important influence of the distribution of dead cellular material within the tumour on both the tumour growth dynamics and response to radiotherapy. In particular, we highlight that radiotherapy induces a significant change in the tumour composition and, as such, intratumoural heterogeneity is likely to be a significant factor in determining treatment response.

Acknowledgements

The list of people who I want to thank is a long one. First and foremost, I would like to thank my supervisors for their support and guidance throughout my DPhil. Helen and Philip, you have been engaging and enthusiastic at all times, which has made my life as a DPhil student so much more rewarding. I also want to thank you for your hard work and effort, always providing me with feedback faster than most people could even read it. I would like to say a big thank you to Heiko, who as well as helping me as a supervisor, also made me feel very welcome during my time spent out in Tampa, and showed me all the best spots for a mid-afternoon beer on a weekday. Thanks to everyone else at Moffitt who made my stay out there so enjoyable, and a special thanks to Shonagh who put up with me as a lodger for a few months.

Back in the UK, I guess I should probably acknowledge Josh who, despite his awful puns, has made the office an enjoyable place to be and always helped me find new ways to procrastinate. Thanks also to everyone else in the WCMB, of whom there are too many to mention.

I also want to thank all my friends at the tri club, which has been such a big part of my time in Oxford and has always provided a far too compelling distraction from work. Similar gratitude goes to all of my housemates over the last few years, who have always made everything fun and kept me well-fed with cake at all times.

Finally, I want to thank my family who have always offered me so much support in everything I do, for which I am immensely grateful.

Contents

Chapter 1

Introduction

1.1 Overview

Cancer continues to be one of the main causes of mortality worldwide, with 8.2 million deaths estimated to have occurred globally in 2012 as a result of cancer-related diseases [1]. Of the millions of people diagnosed with a form of cancer each year, almost half will receive radiotherapy as part of their treatment [2].

Typically, radiation is delivered to the tumour as a series of small doses, or fractions, administered over a period of several days or weeks in order to limit the toxic side effects to healthy cell populations. The conventional fractionation schedule, where a dose of approximately 2 Gy (Gray) is delivered once a day Monday to Friday for up to a total of 35 fractions, has remained unchanged as the standard of care for many years [3, 4]. Whilst altered schemes, such as hyperfractionation, accelerated fractionation and hypofractionation, have been suggested as better alternatives for certain indications, the selection of an optimal fractionation protocol for a particular tumour would clearly benefit from a more individualised approach. In particular, beyond tumour location and stage, patient-specific factors that may be important in determining response to a particular treatment are currently not considered [5]. It is in this regard that mathematical modelling has the potential to play an important role.

In this thesis we aim to investigate the potential applications of mathematical models, calibrated using pre-treatment tumour volume data, to accurately predict tumour response to radiotherapy. We further aim to provide a mechanistic description of the

different qualitative responses to radiotherapy observed in clinical data and the influence of intratumoural heterogeneity on these dynamics.

In this chapter we first provide an overview of the relevant literature. In Section 1.2 we discuss some of the key aspects of cancer biology that drive tumour growth and create complex *in vivo* microenvironments. In Section 1.3 we review the biological basis for radiotherapy, including some of the key radiobiological factors that are important for determining radiation response. We also present an explanation of the ubiquitous linear-quadratic (LQ) model for the dose-dependent survival fraction of cells post-irradiation. This model provides much of the rationale for the therapeutic radiotherapy protocols used in the clinic, which we discuss in Section 1.4.

Mathematical modelling of various aspects of cancer is an active area of research. We review some of the relevant models of tumour growth from the literature in Section 1.5. Mathematical models may be used to provide insight into a wide variety of topics within cancer research. Given the increased interest in personalised treatment planning, a growing number of models in the literature aim to model responses to different therapies. We review some of the relevant radiotherapy modelling literature in Section 1.6.

In order to use a mathematical model for making clinically relevant predictions, it should be first calibrated with respect to appropriate data and the model parameters estimated. We provide an overview of parameter inference techniques in Section 1.7, with a particular focus on the methods used throughout this thesis.

This introductory chapter ends in Section 1.8 where we outline the structure of the remainder of the thesis and the content presented in each chapter.

1.2 Cancer biology

Cancer is a complex family of diseases that typically result from successive genetic mutations that accumulate over time, transforming a cell from a 'normal' phenotype to a malignant cancerous cell. However, regardless of disease type, all cancers share common traits that have been termed the 'hallmarks of cancer' [6, 7]. These include sustaining proliferative signalling, evading growth suppressors, resisting cell death, enabling replicative immortality, inducing angiogenesis, activating invasion and metastasis, reprogramming

energy metabolism, and evading immune destruction. These eight traits combine to promote the formation of a complex tumour micro-environment.

Uncontrolled proliferation of tumour cells leads to expansive growth of cell populations that push the limits of the host tissue's capacity to sustain viable cell populations. To compensate for these limitations, as a tumour grows, it co-opts the existing vasculature, promoting angiogenesis and the formation of new blood vessels in order to increase its nutrient supply [8]. However, the neovasculature resulting from tumour angiogenesis is typically immature, tortuous and poorly perfused. Allied with increasing nutrient demand and high-interstitial pressure resulting in occlusion of existing blood vessels, this results in insufficient oxygen supply and the formation of regions of hypoxia within the growing tumour [9]. Extreme microenvironmental conditions, such as nutrient deprivation or high cellular stresses, may also induce regions of widespread cell death or necrosis [10, 11]. As such, *in vivo* tumours are highly heterogeneous entities [9].

The complexity of *in vivo* tumours makes them difficult study experimentally. As a result, *in vitro* multicellular tumour spheroids (MCTSs) are widely used as a simplified environment in which to study aspects of tumour growth and treatment effects [12, 13]. MCTSs are 3-dimensional cell aggregates which are cultured suspended in a serum providing nutrients to the tumour cells required for growth. The *in vitro* growth conditions promote inter-cellular adhesion and the cells aggregate to form approximately spherical structures [14]. As the MCTS grows, gradients in nutrient and oxygen concentrations form within the tumour since the sole supply to the tumour cells is at the boundary of the spheroid. As a result, the centre of the MCTSs become hypoxic, eventually developing into a central necrotic core upon sustained nutrient deprivation. *In vitro* MCTSs grown in this way typically develop the same reproducible structure; an outer proliferative rim of viable tumour cells, surrounds an annulus of quiescent or hypoxic tumour cells which in turn, surrounds a central, nutrient-deprived, necrotic core [15, 16]. A cross-section of a typical MCTS is shown in Figure 1.1a, with cells exhibiting mitotic activity labelled using [^{3}H]Thymidine, a marker for DNA synthesis [15]. MCTSs can reach 1-3mm in diameter, with the proliferative rim typically 5-7 cell widths thick.

The formation of fully-developed MCTSs, resulting in the well-defined structure shown in Figure 1.1a, encompasses three characteristic growth phases. The small, initial cellular

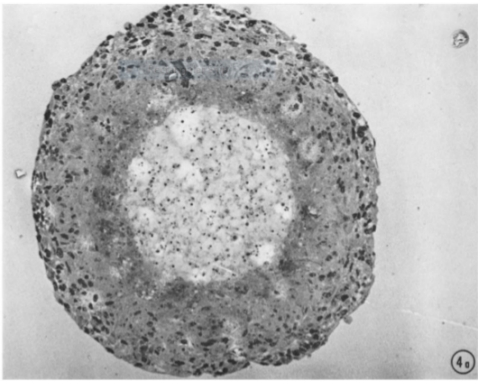

(a)

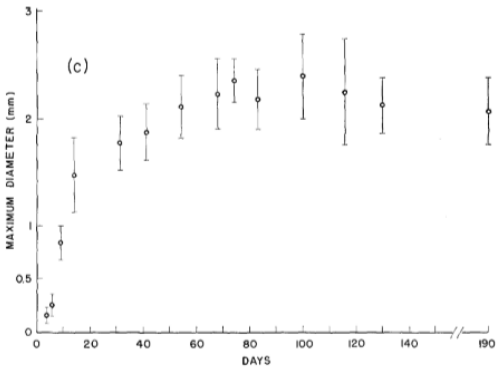

(b)

Figure 1.1: a) Cross-section of a tumour spheroid showing the distinct spatial structure. The outer layers of cells are labelled with [^{3}H]Thymidine. (from Folkman and Hochberg [15]) b) Tumour spheroid diameter measurements for the growth of 32 *in vitro* tumour spheroids. (from Folkman and Hochberg [15])

aggregates undergo rapid exponential growth, with the entire cell population well-supplied with nutrients and actively proliferating. As the spheroid grows larger and the centre becomes hypoxic, the fraction of mitotic cells decreases and growth decelerates. Eventually, the formation of a central necrotic core allows a balance to be achieved between the net rate of cell proliferation at the outer edge of the MCTS and the net rate of necrotic cell death occurring internally, and so the spheroid approaches a steady, equilibrium size. Growth saturation is typical for all MCTSs grown in this way and results in sigmoidal growth curves, as shown in Figure 1.1b [15]. Such nutrient-limited growth dynamics are not observed in 2D monolayer cell cultures.

MCTSs thus provide a controlled study environment of intermediate complexity between 2D culture media and *in vivo* models. While not encompassing the full complexity of a vascularised tumour *in vivo*, the well-defined, reproducible, heterogeneous structure of MCTSs can provide important insight into the biology of the tumour micro-environment [12, 14]. MCTSs have been used for many years for a wide range of applications, including studies of oxygen consumption [17, 18], nutrient deprivation [19], cell migration dynamics [20], amongst many others [13, 14]. Importantly, MCTSs also provide a useful *in vitro* paradigm in which to investigate the use of potential therapies, including radiotherapy [21].

1.3 Radiobiology

Radiotherapy involves the application of radiation to a tumour for therapeutic benefit. It is typically delivered in multiple doses or *fractions*. There are a range of different modes of irradiating *in vivo* tumours, including X-rays, light particles, such as protons, neutrons and α-particles, and heavy particles, such as fully-stripped carbon, neon, silicon or argon ions [22]. While the use of charged particles is being increasingly investigated [23], X-rays currently remain the most common method of delivering radiotherapy in the clinic.

Radiation acts on a cell by causing lesions in its DNA upon absorption, with ionisation events and free-radical reactions completed within $\sim$ 1ms of exposure [24]. Most damage is caused by the ionisation of molecules with which the radiation interacts. Ejected electrons proceed to cause further ionising collisions with other molecules, leading to clustered radiation tracks. The damage that occurs to a DNA fragment can be either a single- (SSB) or double-strand (DSB) break, with $\sim$ 1000 SSBs and $\sim$40 DSBs produced per Gy of radiation delivered [25–27]. DSBs arise when two SSBs occur in close proximity and may be caused either by one radiation track or two separate radiation tracks. A healthy normal cell has repair mechanisms designed to correct for DNA damage, with homologous recombination and non-homologous end-joining the two most important pathways for repairing DSBs [28]. However these can fail, with misrepair potentially leading to cell death. Whilst DSBs are rarer, they are more likely to result in cell death due to the increased difficulty in repairing the damaged DNA.

There are a variety of mechanisms by which a cell may die following irradiation. They are mediated via different signalling pathways and occur over different timescales [11, 28, 29]. These include apoptosis, necrosis, autophagy, senescence, and mitotic catastrophe.

- *Apoptosis* is a highly-regulated, programmed form of cell death which may be initiated as a result of intracellular conditions or extracellular signals. Apoptosis may be induced due to irradiation even though loss of sensitivity to apoptotic signals is recognised as a 'hallmark of cancer'.

- By contrast, *necrosis* is often thought of as catastrophic cell death, occurring under highly unfavourable conditions, such as chronic oxygen deprivation or high cellular

stress. Necrosis is characterised by cellular swelling, membrane blebbing, organelle breakdown and the release of lysosomal enzymes.

- *Autophagy* is a process by which a cell may digest parts of its own cytoplasm to generate small macromolecules of energy and is often activated in response to starvation.

- By contrast, *senescense* refers to the observed loss over time of certain cells' ability to divide.

- *Mitotic catastrophe* occurs when cells attempt to proceed through mitosis with unrepaired or misrepaired DNA. Failure to successfully complete mitosis, may serve as a trigger for other cell death mechanisms. As such, a cell may eventually die by one of the aforementioned pathways which was first initiated by the process of mitotic catastrophe.

The proportion of cells dying via each mechanism post-irradiation is unknown and likely to vary by tissue type, however it is thought that mitotic catastrophe is most prominent [30]. As such, while the programmed cell death process of apoptosis is usually complete within hours of irradiation, some cells may complete one or two cell cycles before dying and thus continue to occupy space within the tumour following irradiation.

1.3.1 The 4/5 Rs of radiobiology

There are many factors that are known to contribute to the overall radiotherapy response of the tumour. In 1975, Withers first characterised four important determinants of overall response known as the 4 'Rs' of radiobiology; namely *recovery* from sublethal damage, cell-cycle *redistribution*, *repopulation* of the tumour, and *reoxygenation* [31]. In 1989 Steel *et al.* proposed the addition of intrinsic *radiosensitivity* as a 5th 'R' [32].

The majority of DNA strand breaks induced by radiotherapy are successfully repaired within a few hours of radiotherapy. This recovery from sublethal damage results in the *split dose effect* whereby a dose of radiation split into two smaller fractions is less effective than a single fraction of the same total dosage. Most repair is typically complete within 6 hours of irradiation. Recovery from sublethal damage is thus largely responsible for the

sparing of tissue resulting from splitting the total radiation dose into fractions separated by more than 6 hours [33].

The radiosensitivity of cells varies markedly between different stages of the cell cycle. Cells in the late G2 phase or undergoing mitosis are the most sensitive to radiation, whilst those in S phase are the most resistant. As such, there is a degree of synchronisation in the cell cycles of the surviving cell population post-irradiation. Heterogeneity in cell cycle times results in redistribution of the cells across the cell cycle and a resensitising of the tumour cell population.

Cells that survive irradiation or successfully recover from sublethal damage are able to resume proliferation between fractions and repopulate the tumour cell population. As such, long time delays between succesive radiotherapy fractions may result in significant regrowth of the tumour.

As described previously, *in vivo* tumours are highly heterogeneous and often contain hypoxic regions not commonly found within normal tissues. The degree of intratumoural hypoxia has been shown to vary significantly between patients [34, 35] and correlates with outcome in head and neck cancers [36]. Indeed, hypoxic cellular environments, commonly defined to be for oxygen partial pressures $< 10\,\text{mmHg}$ [34], are known to be less radiosensitive than normoxic environments, with *in vitro* studies revealing up to a threefold decrease in radiation-induced cell kill [37]. The ratio of radiation doses required to achieve the same biological effect between hypoxic and normoxic microenviroments is known as the *oxygen enhancement ratio* (OER). The mechanism by which this phenomenon occurs is referred to as the *oxygen fixation hypothesis* [38].

When radiation interacts with molecules in a cell, it produces highly reactive free radicals which further interact with other molecules and may cause DNA damage not directly resulting from the initial irradiation. Most of the indirect damage occurring within a cell is due to free radicals resulting from the interaction of radiation with water molecules forming hydroxyl free radicals, $OH^{\bullet}$, which in turn interact with the target to produce free radicals, $R^{\bullet}$ say. In the presence of oxygen, these further react to form potent peroxyl free radicals, $RO_2^{\bullet}$, which in turn eventually react to form ROOH in the target molecule. This change in chemical composition is stable and thus the damage is said to be fixed. In the absence of oxygen, the $R^{\bullet}$ radicals last longer and may eventually react with

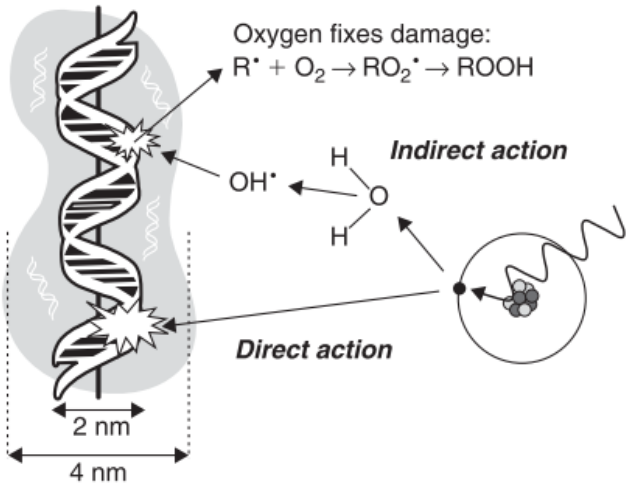

Figure 1.2: A schematic representation of the oxygen fixation hypothesis (from Horsman *et al.* [38]).

H^+ molecules to restore its original chemical form. Thus, oxygen acts as a radiosensitiser, whilst hypoxic conditions inhibit radiation efficacy. A schematic of this process is shown in Figure 1.2.

The extent of hypoxia within *in vivo* tumours may be imaged using newly-developed imaging techniques, such as FMISO PET, and is observed to be dynamic with reoxygenation of the tumour often occurring post-irradiation [39].

1.3.2 The linear-quadratic model and related concepts

As described above, irradiated cells may activate different cell death pathways at different times, with some cells attempting mitosis one or more times before dying. Clonogenic survival assays are used to assess the dose-dependent long-term survival fraction of irradiated cells *in vitro* [40]. Two tissue cultures from the same cell line are plated under identical conditions, with one culture irradiated and the other left as a control. In the irradiated tissue culture, a proportion of the cell population is assumed to have been fatally damaged, and so will eventually die along with any daughter cells. The number of cell colonies surviving after a period of incubation divided by the number of cells plated is termed the plating efficiency (PE). The ratio of the irradiated PE to the control PE then determines the surviving fraction of cells. Repeating this process for a range of radiation dosages allows one to determine how the tumour cell survival fraction depends on the

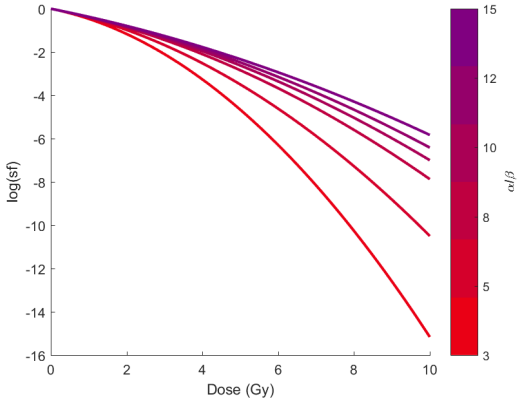

Figure 1.3: Simulated survival curves using the linear-quadratic model, Equation (1.1), for a range of α/β values with fixed $\alpha = 0.3$.

radiation dose.

The proposal of intrinsic radiosensitivity as a 5th 'R' of radiobiology arises from observations that the survival curves for different tissue types may differ significantly [40]. However, survival curves for all cell types are similar in shape, leading to the widely-adopted linear-quadratic (LQ) model for radiotherapy response. In the LQ model, the survival fraction, sf, of tumour cells after a dose, d Gy, of radiation is given by

$$sf = e^{-\alpha d - \beta d^2}, \tag{1.1}$$

where α (Gy^{-1}) and β (Gy^{-2}) are intrinsic radiosensitivity parameters specific to the tumour. We note that this model is empirical, although mechanistic models based upon repair and misrepair of DNA damage have been proposed to explain it [41–43].

The ratio of α/β (Gy) is often used to characterise the radiosensitivity of a particular tissue type and its sensitivity to fractionation [5]. This ratio corresponds to the dose at which the linear component of damage (αd) equals the quadratic component (βd^2). Values of α/β vary significantly, with typical values falling in the range of $3 - 10$ Gy. However, this can fall as low as 1 Gy for late-responding tissues such as prostate cancer, and reach as high as 20 Gy for early-responding, rapidly proliferating tissues such as in head and neck cancer [44]. Radiosensitivity α/β values for different tissue types and disease sites is given in Table 1.1. Example survival curves for a range of α/β ratios are shown in Figure 1.3.

α/β Gy	**Tissue or tumour site**
> 15	Squamous cell carcinoma of head and neck cancer, non-small cell lung cancer
~ 10	Non-melanoma skin cancer
~ 8	Colonic mucosa
~ 4	Lung, muscle, liver
< 2	prostate cancer, melanoma

Table 1.1: Table of α/β ratios for selected tissues and cancers (adapted from Withers [44]).

1.4 Radiotherapy in the clinic

It is estimated that almost half of all cancer patients will receive radiotherapy as part of their treatment, possibly concurrently with other therapies or surgery [2]. Computed tomography (CT) scans are widely used for imaging the tumour at diagnosis and assessing its severity [45–47]. Tumour severity is scored using the tumour, node and metastasis (TNM) staging system, with most common tumour sites having their own classification system. For head and neck cancers, the severity of the tumour is given a grade on a scale of 1-4, scores of 0-3 are used to assess progression of the tumour to lymph nodes, whilst scores of 0 or 1 denote any metastasis to other sites [48]. Combined with the location of the tumour, TNM staging is the main factor used to select a radiotherapy treatment protocol [5].

Radiotherapy is typically administered in a series of small doses, or *fractions*, delivered over a period of a few weeks. The basis of fractionated radiotherapy is closely linked to the radiobiological concepts described in the previous section, taking advantage of repair between fractions and limiting the overall toxicity to the surrounding normal tissue [49]. The *conventional fractionation* protocol consists of 1.8-2 Gy fractions delivered daily Monday-Friday with a break at the weekends, for 6-7 weeks up to total dose of 70 Gy [1]. This has remained unchanged as the standard-of-care for most cancers for many years [3].

Despite this, many altered fractionation protocols have been suggested and have undergone clinical trials. These include, but are not limited to, hyperfractionation, accelerated fractionation and hypofractionation [3]. The rationale behind each of these lies

[1] In the remainder of this thesis references to 'standard' or 'conventional' fractionation refer to a weekly schedule of 2 Gy fractions delivered on 5 consecutive days, with a subsequent weekend break.

in the LQ model and its characterisation of intrinsic radiosensitivity as presented in the previous section. A schematic comparison of each of these schedules is presented in Figure 1.4.

- *Hyperfractionation* refers to irradiation twice a day up to a higher total dose. This protocol is targeted towards early-responding cancers with high α/β ratios such as head and neck, cervix, skin and non-small cell lung cancers. For these tumours, the surrounding normal tissue is assumed to have a lower α/β ratio.

- *Accelerated fractionation* refers to protocols in which the total number of fractions is delivered over a shorter time span. This approach is designed to reduce repopulation between fractions. As such, accelerated fractionation is also targeted towards highly proliferative, early-responding cancers.

- *Hypofractionation*, where a larger dose is delivered per fraction, may be more efficacious for tumours with low α/β ratios. These tumours represent late-responding tissues and have a greater dependence on fraction size owing to the greater curvature of the survival curves. Tumours with low α/β values include breast and prostate cancers.

The development of new technologies for delivering radiotherapy has resulted in new innovative methods for delivering radiation more effectively to the tumour whilst reducing toxicity to the surrounding normal tissue and sparing organs-at-risk [5, 23, 50]. Reducing damage to normal tissue also provides motivation for considering dose de-escalation protocols. For example, human papillomavirus positive (HPV^+) head and neck cancers typically respond well to radiotherapy with good rates of locoregional control. As such, there is a growing interest in adaptive radiotherapy (ART) protocols for these tumours in which the dose is gradually reduced [51, 52].

Consequently, there are a number of clinically-approved protocols for most disease sites. We note that TNM staging does not explicitly incorporate patient-specific information such as pre-treatment growth dynamics or spatial composition. Development of predictive mathematical models may allow for prediction of outcome for each treatment plan and therefore aid selection of the best protocol on a patient-specific basis [5].

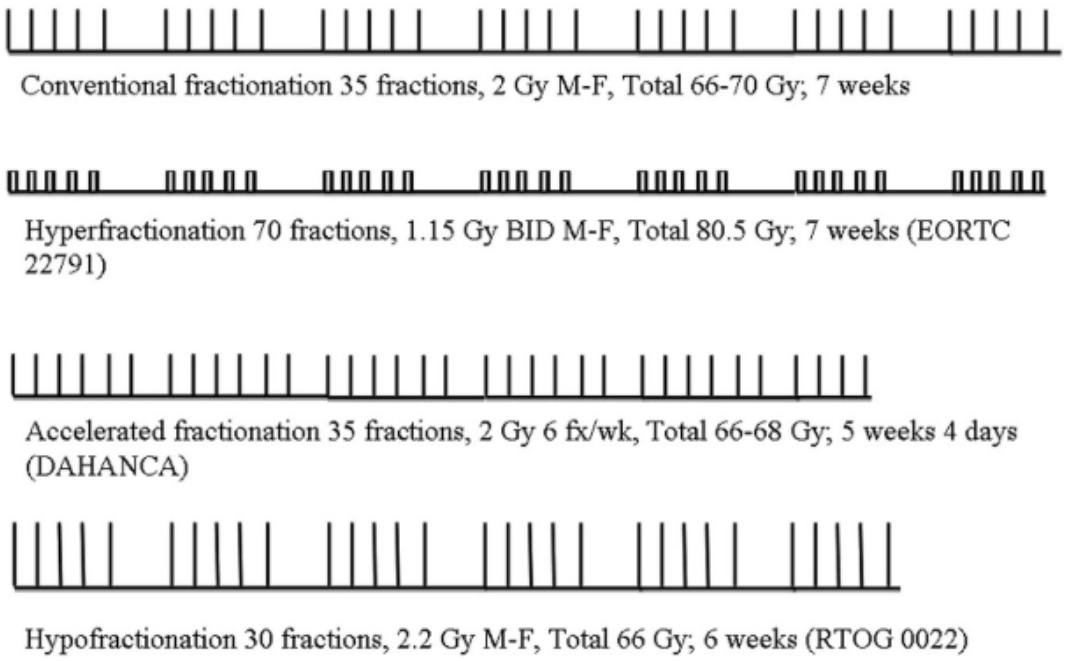

Figure 1.4: Schematic illustrating alternative fractionation protocols (from Ahmed *et al.* [3]).

1.5 Mathematical models of tumour growth

Many mathematical approaches are being used to model tumour growth, including, but not limited to, continuum models (phenomenological and mechanistic), agent-based computational models, and hybrid modelling approaches combining aspects of multiple different techniques. In this thesis our focus is on continuum models of tumour growth and radiotherapy response, which we review in more detail below. Reviews of other approaches to modelling tumour growth may be found in the literature [53, 54].

1.5.1 Phenomenological models of tumour growth

The simplest continuum models provide a phenomenological description for the evolution of the tumour volume over time. These models aim to capture the qualitative behaviour of the model system without incorporating much mechanistic detail. Many such models have been proposed, typically taking the form of ordinary differential equations (ODEs) [55]. Unrestricted proliferation may lead to exponential growth of tumour cell populations, mimicking the dynamics observed in *in vitro* 2D monolayers [56]. Simple, exponential dynamics for the tumour volume, $V(t)$, given by

$$\frac{dV}{dt} = \lambda V \tag{1.2}$$

may thus capture this behaviour well. However, while this may adequately describe the early stages of tumour growth, tumours growing in 3D typically saturate to an equilibrium size, as described in Section 1.2. Thus alternative phenomenological descriptions which generate sigmoidal growth curves have been proposed to match the full range of dynamics.

Perhaps the most widely used of these are the logistic and Gompertz models, given by Equations (1.3) and (1.4) respectively, which have long been used to investigate such dynamics [55, 57].

$$\frac{dV}{dt} = \lambda V \left(1 - \frac{V}{K}\right) \qquad \text{(logistic)} \tag{1.3}$$

$$\frac{dV}{dt} = -\lambda V \log\left(\frac{V}{K}\right) \qquad \text{(Gompertz)} \tag{1.4}$$

Both of these models approach an equilibrium tumour size, K, termed the *carrying capacity*.

There are a wide range of other similar models that have been proposed over many years, including the generalised logistic model (Equation (1.5)) and the Bertalanffy model (Equation (1.6)), among others [55, 56, 58–60].

$$\frac{dV}{dt} = \lambda V \left(1 - \left(\frac{V}{K}\right)^{\nu}\right) \qquad \text{(generalised logistic)} \tag{1.5}$$

$$\frac{dV}{dt} = \lambda V^{\frac{2}{3}} - \eta V \qquad \text{(Bertalanffy)} \tag{1.6}$$

Each of Equations (1.3)-(1.6) describe families of curves which exhibit growth-saturating behaviour.

It is not clear which of these models provides the best phenomenological description of tumour growth; each model generates a slightly different trajectory and these may not be distinguishable from biological heterogeneity and/or noise in tumour volume data [55, 58]. However, interest in such models continues due to their simplicity. Indeed, many

extensions to these basic models have been proposed to incorporate more biological detail, decomposing the tumour into two or more compartments, whose evolution may be described by coupled ODEs, which together describe the overall tumour volume dynamics [61, 62]. Such models have also been extended to simulate the effects of various treatments. Further discussion of some of these is provided in Section 1.6 in the context of radiotherapy.

1.5.2 Modelling *in vitro* tumour spheroids

While the models described in the previous section may describe qualitative tumour growth dynamics, the lack of biological detail means they afford little mechanistic insight. It is therefore desirable to develop more complex models which incorporate more aspects of the underlying tumour biology.

Cancer is a complex disease characterised by a large amount of intratumoural heterogeneity. As discussed in Section 1.2, tumour spheroids represent a useful *in vitro* tool for studying complex *in vivo* phenomena. In a similar manner, it is natural to develop mathematical models of avascular tumour spheroid growth as a first step to incorporating spatial heterogeneity and more biological detail. Their simplified geometry and reproducible structure make MCTSs ideal starting points for developing spatially-resolved, mechanistic models of solid tumour growth. Models of *in vitro* spheroids are typically unified in their assumptions of spherical symmetry and growth limited by the diffusion and consumption of available nutrients.

One of the first models for nutrient-limited tumour growth was presented by Greenspan [63]. Greenspan's model also assumes that adhesion and surface tension forces act between cells to maintain a compact tumour mass. Differential growth across the tumour drives cell movement from the outer tumour boundary towards the spheroid centre, while cellular debris resulting from central necrosis within the tumour spheroid is assumed to leak out across the tumour boundary. These assumptions combine so that the volume loss due to necrotic decay is balanced by inward movement of cells due to surface tension and proliferation at the spheroid boundary. The model equations can be reduced to an integro-differential equation for the evolution of the outer tumour radius and a reaction-diffusion equation for the nutrient concentration, commonly assumed to be oxygen. Greenspan's

model was one of the first mechanistic models to reproduce the sigmoidal growth curves observed *in vitro*. Internal radii may be tracked as contours of the nutrient profile to determine the evolution of the tumour composition throughout the growth dynamics. In Greenspan's original model, production of a mitotic inhibitor within the tumour was further assumed, although this assumption is not required to achieve growth saturation. This model is explored in further detail in Chapter 3 and Appendix A.

Other authors have extended Greenspan's original model to account for features that include symmetry breaking [64, 65], inclusion of apoptosis as a cell death mechanism [66, 67] and cell shedding from the tumour boundary [68]. Tumour spheroid models have further been used to investigate internal oxygen consumption and distribution dynamics [69, 70] and cell migration dynamics [71].

1.5.3 Multiphase modelling

Multiphase models may be used to describe the spatiotemporal evolution of a mixture of two or more constituent phases. Continuum partial differential equations (PDEs) may be formulated to describe the macroscopic dynamics of each phase. While conservation laws may be stated from the outset to form a system of model equations, they may also be more rigorously derived from consideration of microscale behaviour via *homogenisation* or *volume averaging*. These techniques exploit a separation of lengthscales within the model domain to filter out fluctuations on the microscale in the dependent variables.

A complete derivation of these equations is beyond the scope of this review. Excellent, comprehensive tutorials on the volume-averaging of multiphase flows can be found in a number of key papers in the literature [72–76].

Multiphase models have been applied to many modelling contexts and, more recently, extensively applied to biological tissue growth. Formal derivation of the macroscopic equations in this context was performed by O'Dea *et al.* [77], although development of the model equations may be performed without performing formal homogenisation analysis.

Most early multiphase tumour growth models considered the tumour as a two phase mixture. Ward and King proposed models describing the evolution of a tumour comprising continuum phases of alive and dead cells [78, 79]. Advection equations for the dynamics

of each phase were coupled to a reaction-diffusion equation for nutrient concentration within the tumour and an equation for the common velocity of the phases. Travelling wave profiles were reported in their original model [78]. The model is extended such that the dead cells within the tumour are assumed to comprise of 'cellular material' which may be taken up by proliferating cells and used for mitosis [79]. The extended model is shown to admit both travelling wave and steady state solutions, with passage of material across the tumour boundary required for achieving growth saturation.

Landman and Please developed an alternative two phase model comprising tumour cells and extracellular fluid in which a steady state profile was instead achieved via a surface tension applied on the tumour boundary [80]. The resulting steady state profile was shown to reproduce some of the characteristic structure of *in vitro* spheroids which contain a central necrotic core.

A variety of similar two phase models followed the model by Landman and Please, describing the tumour composition as a mixture of a viscous cell phase and inviscid extracellular fluid, with dynamics coupled to a diffusible nutrient. Byrne *et al.* proposed a model in which the two phases move with different phase velocities, resulting in additional interactions via interphase drag [81]. By taking appropriate limits, they show that their model may be reduced to recover earlier tumour growth models, including Greenspan's original model for *in vitro* tumour spheroid growth. These limits are equivalent to assuming a constant tumour cell volume fraction throughout the tumour and thus provide an alternative interpretation of Greenspan's model as an incompressible limiting case of this more general framework.

Breward *et al.* analyse the growth dynamics exhibited by a similar two phase model and use numerical simulation to show how the intratumoural volume fractions evolve over time [82]. Their analysis of the model equations revealed the importance of adhesion effects for achieving saturating tumour growth. Breward *et al.* further provided asymptotic analysis of transient waiting times for sparsely populated tumours, and the dynamics of the initial stages of tumour growth.

Breward *et al.* subsequently extended their model to describe vascular tumour growth by introducing a third phase for the blood vessel density [83]. Their model was one of the first three phase models of tumour growth. The model equations included terms for

angiogenesis and vessel occlusion. The model was shown to reproduce tumour structures similar to those observed *in vivo*, including the formation of a central necrotic core.

More recent multiphase models have extended the concepts incorporated in these early models in a number of different directions. Where early multiphase models were typically formulated in one spatial dimension, it is now possible to simulate such models in higher spatial dimensions [84–86]. Ease of computation also enables numerical investigation of models with more than two constituent phases [87, 88]. A number of authors have extended the constitutive models describing the mechanical behaviour of each phase, incorporating poroelastic [89, 90] or viscoelastic [91] behaviours, for example. Such extensions may be used to further determine the stresses and strains that may develop within a tumour and to investigate how mechanical interactions may influence its growth dynamics [81, 91, 92].

1.6 Radiotherapy response models

There is a large literature devoted to modelling tumour response to radiotherapy. A comprehensive review of this literature is beyond the scope of this thesis: we refer the interested reader to the excellent reviews by Hillen *et al.*, Rockne and Frankel, and Enderling *et al.* [93–95].

The LQ model, given by Equation (1.1), for the dose-dependent survival fraction after irradiation arises from empirical observations of survival curves obtained from *in vitro* survival assays. However, several authors have proposed more fundamental, mechanistic models to derive dose-response relations [41–43]. Such mechanistic interpretations provide a theoretical foundation for future model extensions which may incorporate more 'Rs' of radiobiology [96, 97]. While different methods of deriving such relationships may give slightly different dose-response formulae, Brenner *et al.* noted that the different formalisms yield the same approximate relationship [98]. These concepts are often extended further using probabilistic or stochastic methods to determine the *tumour control probability* (TCP) for a given fractionation schedule [99–103]. However, the original, empirical LQ formulation remains the most widely used model for combining tumour growth and radiotherapy response.

Pre-treatment data with which to calibrate predictive mathematical models in the clinic is often limited, with typically just 2 or 3 diagnostic and treatment planning scans prior to the start of radiotherapy which may be spaced over a month apart [45–47]. As such, simple phenomenological models with few parameters are commonly proposed to describe radiotherapy response [56, 104–106]. Wheldon *et al.* were among the first to incorporate tumour growth dynamics between fractions with the LQ model for radiotherapy response in this manner, assuming exponential growth of the tumour between fractions, as given in Equation (1.2) [104]. They derived optimal dosing protocols which were dependent on the LQ radiosensitivity parameters, α and β, and the tumour growth rate, λ, and subject to the radiation tolerance of normal tissue. McAneney and O'Rourke perform a systematic study of such models, incorporating the LQ model into a variety of different phenomenological tumour growth models [107]. They noted that while simulations of radiotherapy protocols for each model were broadly similar, they may predict different outcomes across a range of α/β values.

Prokopiou *et al.* proposed a variation on these models for making patient-specific predictions in the clinic [105]. They use the logistic growth model and assume that radiation-induced cell death is proportional to the logistic term. This is based on the assumption that the logistic term represents the proliferative activity of the tumour, which further implicitly assumes loss of radiosensitivity and thus quiescence of the entire tumour cell population at carrying capacity. Prokopiou *et al.* further assume that inter-patient variation in growth rates, λ, and radiation-induced death rates, γ, is significantly smaller than the variation in carrying capacity, K. Consequently, the parameters λ and γ may be fixed as global population-level parameters. The ratio of pre-treatment tumour volume to the carrying capacity, V/K, is assumed to be a patient-specific determinant of radiotherapy response, which they term the 'proliferation saturation index', or PSI. The full model can be written as

$$\frac{dV}{dt} = \lambda V\left(1 - \frac{V}{K}\right) - \sum_{i=1}^{N} \gamma V\left(1 - \frac{V}{K}\right)\delta(t - t_i), \tag{1.7}$$

where $\delta(\cdot)$ is the Dirac delta function and t_i denotes the delivery time of fraction $i = 1, ..., N$. Reducing the model to one patient-specific parameter facilitates easier parametri-

sation given the limited data typically available. Poleszczuk *et al.* consider alternatives to this model in which the logistic growth term is replaced by the generalised logistic term, as in Equation (1.5) [106]. They note that the model may fit equally well to their non-small cell lung cancer (NSCLC) dataset across a range of values for the exponent ν, although patient-specific predictions varied. We note though that both studies used a very small dataset [105, 106], and thus the applicability of the model in Equation (1.7) warrants further study.

In all of the aforementioned models radiotherapy effects an instantaneous loss of volume. This is clearly an over-simplification of the true underlying dynamics. The LQ model is based on observations from long-term clonogenic survival assays. As such, its relevance for predicting short-term responses to radiotherapy is unclear. The variation in biological cell death mechanisms post-irradiation means that dead or dying cells may continue to occupy volume for some time after irradiation. The presence of such dead material may confound the observed response to subsequent radiotherapy fractions as well as the measured tumour volume post-irradiation. Using mathematical models to understand the possible impact of these effects will be a recurring theme throughout this thesis.

In a similar manner to phenomenological modelling of tumour growth, compartmental models have been proposed to incorporate additional biological detail within such models whilst maintaining simplicity [108–110]. The most common extensions consider two compartment models for tumours comprised of viable tumour cells and dead or lethally-damaged cells. Further decomposition of the tumour to include hypoxic compartments, for example, have also been considered [111, 112]. While such models may exhibit more biologically realistic dynamics, even these simple extensions may prove too complex to reliably calibrate with pre-treatment clinical data [113]. Furthermore, model calibration using insufficient data to determine the model parameters may result in unrealistic parameter regimes, despite a good overall fit to the data. Examples of this may be seen in the literature. Tariq *et al.* consider a two compartment model which is shown to fit well to their dataset of NSCLC tumour volume measurements, but which exhibits unrealistic dynamics for the underlying composition, whereby the proliferative compartment is killed just a few days into the fractionation protocol [110]. Similarly, Leder *et al.* parametrise

their model containing a large number of parameters to *in vivo* mouse data, and obtain unfeasibly large α/β ratios [114]. Such issues become important when considering the use of calibrated mathematical models for making subsequent clinical predictions. As such, predictive mathematical models should balance the need for biological detail with availability of sufficient data for parametrisation [115]. These parameter inference issues motivate the investigation in this thesis of more complex mechanistic models for radiotherapy response, which may subsequently be used to guide the development of simpler models which capture sufficient detail.

A variety of spatially-resolved models have also been proposed for clinical application which are designed to be calibrated directly to the imaging data, rather than to summary tumour volume statistics. These include numerous papers by Swanson's group modelling glioma growth and radiotherapy response [116–118]. They propose the use of contrast-enhanced MRI images for calibration of their models. We note that the imaging data routinely available for most other disease sites is likely insufficient for such purposes, comprising just 2 or 3 pre-treatment CT scans which may be taken months apart on different machines of possibly different resolutions [45–47].

Mathematical models have also been proposed for investigating questions other than the prediction of response for clinically approved protocols. These include radiation bystander effects [2] [119], simulation of dose painting protocols [120], modelling the abscopal effect [3] [121], and optimisation of treatment protocols [122, 123].

1.7 Parameter inference techniques

Mathematical models proposed for clinical application should be sufficiently calibrated and validated against appropriate data [115, 124, 125]. This requires precise estimation of model parameters in order to subsequently make accurate model-based predictions. There are many techniques for investigating parameter identifiability and estimating parameter values.

Structural identifiability analysis methods aim to determine analytically whether it

[2] The bystander effect is a term commonly used to refer to the observation that irradiated cells can influence the behaviour of nearby non-irradiated cells.

[3] The abscopal effect refers to possible systemic effects due to localised radiotherapy.

is theoretically possible to precisely identify model parameters given the form of the model equations and the type of data used for calibration. Many methods have been developed to determine the structural identifiability of a given model. For linear ODE systems the problem is well understood, for non-linear or rational ODE systems state-of-the-art techniques may fail in practice, while for PDEs few successful methods have been developed. While many approaches have been proposed that theoretically address this problem, all of the aforementioned methods may fail to be tractable computationally depending on the particular model's complexity. Comprehensive reviews of the many different approaches to the problem of structural identifiability analysis can be found in [126–128].

In practice, tumour volume measurements obtained from computed tomography (CT) scans used for model calibration are typically limited in number and may be noisy. In such cases, the practical estimation of model parameters and quantifying the uncertainty of subsequent model predictions is of importance.

In the following sections we briefly review two different types of approach to practical parameter inference, with a more detailed focus on methods used throughout the remainder of this thesis.

1.7.1 Optimisation methods

Optimisation methods, intuitively, aim to optimise the fit of a mathematical model to data, thus identifying the single best fitting parameter set. These methods may often involve fewer model evaluations than the approaches discussed in Section 1.7.3, thus reducing computation time and allowing for faster identification of parameter estimates. A review of such methods is presented by Andradottir [129]. For the remainder of this section we proceed to describe a genetic algorithm which we use for parameter fitting throughout this thesis.

The 'evolution-based optimisation' (EBO) algorithm uses principles from genetic replication and mutation to iterate towards an optimal parameter set [130]. This algorithm optimises the fit of the model to the data by minimising the 'sum of squares' error. For a model, f, with parameters, $\boldsymbol{p}$, and a dataset of tumour volume measurements, v_i, taken at times, t_i, for $i \in 1, ..., n$, the sum of squares error is defined to be

$$\Sigma(\boldsymbol{p}) = \sum_{i=1}^{n} \frac{(v_i - f(t_i; \boldsymbol{p}))^2}{w_i^2}, \tag{1.8}$$

where the w_i may be used to weight each data point.

In the first 'generation' of the genetic algorithm, an initial 'population' of parameter sets is randomly generated. The fitness of each parameter set is evaluated using Equation (1.8). The population is sorted by fitness value, with the top 50% of parameter sets being carried forward to the next generation. The rest of the population for the next generation is generated by 'crossover' (25%) and 'mutation' (25%) of the surviving parameter sets. Crossover involves randomly selecting two surviving parameter sets from the previous generation and creating a new parameter set by randomly selecting each parameter from one of the 'parent' sets. Parameter sets occurring via mutation are the result of a surviving parameter set with one parameter randomly altered by up to $\pm 10\%$. Subsequent generations then proceed in the same manner, each time carrying forward the top 50% of the population.

After m generations, where m is an integer deemed sufficiently large enough for the genetic algorithm to converge, the parameter set with smallest sum of squares value is taken to be near to the optimum set of parameters for that particular model and data. In our implementation of the EBO algorithm, this parameter set is then refined using MATLAB's *lsqnonlin* function to return the local minimum in a neighbourhood around this point in parameter space. The resulting parameters are taken to be those that best fit the model to the data.

The *Akaike information criterion* (AIC) may be used to compare performance between competing calibrated models [131]. When the data sample size is small the corrected AIC value, or AICc, is preferred and is given by

$$AICc = 2k + n \log\left(\frac{\Sigma(\boldsymbol{p})}{n}\right) + \frac{2k(k+1)}{n-k-1}, \tag{1.9}$$

where n is the sample size, k is the number of model parameters, and $\Sigma(\boldsymbol{p})$ is the residual sum of squares defined in Equation (1.8). The last term in this formula is the correction factor in the case of small n. Comparing values for the AICc across different models allows for quantitative model comparison, with lower values of AICc signifying better per-

formance of that model. We note that the magnitude of the AICc value is not important since it is affected by the choice of objective function, here $\Sigma(\boldsymbol{p})$.

1.7.2 Bayesian methods for parameter inference and model selection

Bayesian techniques for parameter inference allow us to generate probability distributions rather than point estimates. For any given model, the highly heterogeneous nature of the tumour micro-environment that leads to variations in the measured variable of interest (including inter-patient variability), uncertainty inherent in the data, and even uncertainty in the model itself means that it is natural to consider each parameter as a random variable rather than a fixed point estimate of some 'true' value. While computationally more expensive, the extra information gained about the underlying distributions of each parameter make Bayesian methods useful in assessing a model with respect to data. For example, we may more readily quantify the uncertainty of any model predictions.

At the centre of all Bayesian analysis and techniques is Bayes' rule (Equation (1.10)) [124]. Bayes' rule allows us to formulate the *posterior density* (up to normalisation) for a set of parameters, θ, conditioned on some data, y, by updating the *prior density* using the *likelihood*. The prior density captures our belief about the probability distribution of θ before observing the data, whilst the likelihood, for fixed y, tells us about the probability of generating those data for any given θ.

$$p(\theta \mid y) \propto p(y \mid \theta)p(\theta) \tag{1.10}$$
$$posterior \propto likelihood \ \times \ prior$$

In general, Monte Carlo methods enable sampling from complex, often high-dimensional, probability distributions, say π on a space X [132]. In many situations, it is desirable to calculate integrals of the form

$$I = \int_X f(x)\pi(x)dx, \tag{1.11}$$

which are often analytically untractable for the distribution required. Given a sample

$\{X_i\}$, $i = 1, ..., N$, from the distribution π generated from some suitable Monte Carlo algorithm, this integral can be approximated by

$$\hat{I} = \frac{1}{N} \sum_i f(X_i). \tag{1.12}$$

Using Equations (1.10) and (1.12) as starting points, given some data, y, we are able to approximate the underlying distribution of the model parameters, θ, for a given model.

There are a multitude of Bayesian techniques in the literature [124, 133, 134]. In the following section, we explain in detail the ABC SMC algorithm proposed by Toni *et al.* [135, 136], which we use for parameter inference throughout this thesis.

1.7.3 The Approximate Bayesian Computation Sequential Monte Carlo (ABC SMC) algorithm

Approximate Bayesian Computation

Approximate Bayesian Computation (ABC) algorithms are a class of Monte Carlo methods that are 'likelihood-free'; they do not require explicit calculation of the likelihood. This can be useful if the likelihood is difficult (or impossible) to calculate or, for example, if there are errors in the data that can not be easily estimated.

The simplest ABC algorithm is the rejection sampler. It relies on a pre-determined threshold value, ϵ, and a distance function to the data, $d(\cdot, y)$. Sample parameter sets are drawn from the prior distribution, $\pi(\theta)$, and the model is used with these parameters to generate a simulated dataset, y^*. If $d(y^*, y) < \epsilon$, then the parameter set is accepted. The result of this algorithm, as with all ABC approaches, is a sample from $\pi(\theta \mid d(y^*, y) < \epsilon)$, which for sufficiently small ϵ will be a good approximation for the true posterior, $\pi(\theta \mid y)$.

Importance sampling

Importance sampling is a technique that enables the generation of a sample from a known probability distribution from which we can not easily draw samples directly. If we are unable to sample from a distribution, π say, but are instead able to sample from another similar proposal distribution, η, such that $\pi(x) > 0 \implies \eta(x) > 0$, then we may instead

sample from η and obtain a sample indirectly from π using importance weights [133]. Put simply, we note that the integral in Equation (1.11) may be rewritten as

$$I = \int_X f(x)\frac{\pi(x)}{\eta(x)}\eta(x)dx. \tag{1.13}$$

So given a sample, $\{X_i\}$, from η, the target distribution π can be approximated by

$$\hat{\pi}(x) = \frac{1}{N}\sum_i w(X_i)\delta(x - X_i), \tag{1.14}$$

where $\delta(\cdot)$ is the Dirac delta function, and with weights given by

$$w(x) = \frac{\pi(x)}{\eta(x)}. \tag{1.15}$$

ABC SMC

The Approximate Bayesian Computation Sequential Monte Carlo (ABC SMC) algorithm as presented by Toni *et al.* [135, 136] combines the approaches of ABC with a sequential version of importance sampling.

A set of parameter values called *particles*, $\{\theta_i\}$, sampled from the prior distribution, $\pi(\theta)$, are propagated through a sequence of intermediate distributions, $\pi(\theta \mid d(y^*, y) < \epsilon_t)$ for $t = 1, ..., T$, until it represents a sample from the target distribution at the desired tolerance level ϵ_T. The threshold sequence is chosen such that $\epsilon_1 > ... > \epsilon_T > 0$ and therefore the distribution of the particles gradually evolves towards the posterior. At each stage, importance sampling is used to generate the subsequent sample with the importance sampling proposal distribution, η_t, being the previous distribution, $\pi(\theta \mid d(y^*, y) < \epsilon_{t-1})$, perturbed by the perturbation kernel, K_t. The full algorithm is shown in Algorithm 1.

Algorithm 1: ABC SMC algorithm [136].

S1 Initialise $\epsilon_1, ..., \epsilon_T$.
Set the population indicator $t = 0$.
S2.0 Set the particle indicator $i = 1$.
S2.1 **if** $t = 0$ **then**
  Sample θ^{**} independently from $\pi(\theta)$
else
  Sample θ^* from the previous population $\{\theta_{t-1}^{(i)}\}$ with weights w_{t-1} and perturb the particle to obtain $\theta^{*}* \sim K_t(\theta|\theta^*)$, where K_t is a perturbation kernel.
end
if $\pi(\theta^{**}) = 0$ **then**
  Return to **S2.1**.
end
Simulate a candidate dataset $x^* \sim f(x|\theta^{**})$.
if $d(x^*, x_0) \geq \epsilon_t$ **then**
  Return to **S2.1**.
end
S2.2 Set $\theta_t^{(i)} = \theta^{**}$ and calculate the weight for the particle $\theta_t^{(i)}$,

$$w_t^{(i)} = \begin{cases} 1 & \text{if } t = 0, \\ \frac{\pi(\theta_t^{(i)})}{\sum_{j=1}^{N} w_{t-1}^{(j)} K_t(\theta_{t-1}^{(j)}, \theta_t^{(i)})} & \text{if } t > 0. \end{cases}$$

if $i < N$ **then**
  Set $i = i + 1$.
  Go to **S2.1**.
end
S3 Normalize the weights.
if $t < T$ **then**
  Set $t = t + 1$.
  Go to **S2.0**.
end

ABC SMC model selection

As mentioned previously, inherent to the mathematical modelling process is uncertainty in the model itself. As such, given multiple candidate models, it may be desirable to test each model against a given dataset. A model selection framework may be simultaneously incorporated alongside parameter estimation in the ABC SMC algorithm. The extension to the algorithm requires a separate model prior, $\widetilde{\pi}(m)$, and model perturbation kernel, $\widetilde{K}_t$. At each stage, a model is first chosen using the previous marginal posterior distribution for the models, $\widetilde{\pi}_{t-1}(m \mid y)$, and perturbed using $\widetilde{K}_t$. The chosen model then generates a candidate parameter set from the previous intermediate distribution, $\pi(\theta \mid d(y^*, y) < \epsilon_{t-1}, m)$, using importance sampling as before. The full ABC SMC algo-

rithm incorporating model selection is shown in Algorithm 2.

Algorithm 2: ABC SMC algorithm with model selection [136].

MS1 Initialise $\epsilon_1, ..., \epsilon_T$.
Set the population indicator $t = 0$.
MS2.0 Set the particle indicator $i = 1$.
MS2.1 Sample m^* from $\pi(m)$.
if $t = 0$ **then**
  Sample θ^{**} from $\pi(\theta(m^*))$.
end
if $t > 0$ **then**
  Sample θ^* from the previous population $\{\theta(m^*)_{t-1}\}$ with weights $w(m^*)_{t-1}$.
  Perturb the particle θ^* to obtain $\theta^{**} \sim K_t(\theta|\theta^*)$.
end
if $\pi(\theta^{**}) = 0$ **then**
  Return to **MS2.1**.
end
Simulate a candidate dataset $x^* \sim f(x|\theta^{**}, m^*)$.
if $d(x^*, x_0) \geq \epsilon_t$ **then**
  Return to **MS2.1**.
end
MS2.2 Set $m_t^{(i)} = m^*$ and add θ^{**} to the population of particles $\{\theta(m^*)_t\}$, and calculate its weight as,

$$w_t^{(i)} = \begin{cases} 1 & \text{if } t = 0, \\ \frac{\pi(\theta^{**})}{\sum_{j=1}^{N} w_{t-1}^{(j)} K_t(\theta_{t-1}^{(j)}, \theta^{**})} & \text{if } t > 0. \end{cases}$$

if $i < N$ **then**
  Set $i = i + 1$.
  Go to **MS2.1**.
end
MS3 **for** *every* m **do**
  Normalize the weights.
end
if $t < T$ **then**
  Set $t = t + 1$.
  Go to **MS2.0**.
end

The outputs of the ABC SMC model selection algorithm are the posterior marginal distributions for the models, $\widetilde{\pi}(m \mid y)$ and the posterior distributions of parameters, $\pi(\theta \mid y, m)$, for m=1,...,M, where M is the number of models. Bayes factors summarise the evidence for one model over another and can be calculated according to Equation (1.16) in the case of a uniform prior on models. If the result of the model selection is not conclusively in favour of one model in particular, then the marginal probabilities for each

model may be used to inform model-averaging predictions.

$$B_{1,2} = \frac{p(m_1 \mid y)}{p(m_2 \mid y)} \tag{1.16}$$

Table 1.2 provides an interpretation of different values of Bayes Factors.

$\mathbf{B_{10}}$	**Evidence against $\mathbf{H_0}$**
1 to 3	Not worth more than a bare mention
3 to 20	Positive
20 to 150	Strong
> 150	Very strong

Table 1.2: Interpretation of Bayes factors, expressed here as B_{10} (reproduced from [137]).

While more efficient than the standard rejection sampler and many other Monte Carlo Markov chain (MCMC) algorithms, for models with many parameters or those that can not be simulated quickly, the algorithm may be slow and it may be necessary to seek further optimisation. Typical targets for optimisation include the choice of perturbation kernels and the determination of the threshold schedule.

Choice of perturbation kernels

A good perturbation kernel will allow sufficient exploration of the parameter space whilst also achieving a high acceptance rate. More specifically, the joint proposal distribution, in which a particle is first sampled from the previous population, $\{\theta_i\}_{(t-1)}$, and then perturbed, should resemble the target joint distribution of sampling one particle each from $\pi(\theta \mid d(y^*, y) < \epsilon_{t-1})$ and $\pi(\theta \mid d(y^*, y) < \epsilon_t)$. As a measure of the difference between two probability distributions, P and Q say, the Kullback-Leibler divergence, D_{KL}, (given by Equation (1.17)) provides a quantity with respect to which we can optimise our choice of kernel.

$$D_{KL}(P \mid\mid Q) = \int p(\boldsymbol{x}) log \frac{p(\boldsymbol{x})}{q(\boldsymbol{x})} d\boldsymbol{x} \tag{1.17}$$

As the population of particles is propagated through the tolerance thresholds, it is

likely that the 'optimal' choice of kernel changes. As such adaptive schemes have been developed to succesively generate a kernel for the upcoming iteration [138]. In each case, the class of kernel is initially chosen and then the 'optimal' kernel from that class is selected at each stage. Filippi *et al.* [138] present methods for adaptively generating kernels from families of uniform distributions, multivariate normal distributions, and multivariate normal distributions with local covariance matrices, among others.

A commonly used perturbation kernel is the uniform kernel applied component-wise to each parameter independently in θ_i. In this case, each parameter, $\theta_{i,j}$, has a specific interval of width $2\sigma_j$ and centred on $\theta_{i,j}$ such that the density within this range is $1/2\sigma_j$. In order to optimise the component-wise uniform kernel, a natural choice at each time step is to scale σ_j by the width of the previous population so that

$$\sigma_j = \frac{1}{2}\left(\max_{1\leq i\leq N}\{\theta_{i,j}\}_{(t-1)} - \min_{1\leq i\leq N}\{\theta_{i,j}\}_{(t-1)}\right). \tag{1.18}$$

Among kernels that treat θ component-wise, particles are also often perturbed using independent Gaussian distributions for each parameter centred on θ with variances (σ_j). Using the Kullback-Leibler divergence as previously described, Filippi *et al.* present an optimal choice of (σ_j) for population t to be

$$\sigma_j = \left(\int\int p_{\epsilon_{t-1}}(\theta_j^{t-1} \mid y)p_{\epsilon_t}(\theta_j^t \mid y)(\theta_j^t - \theta_j^{t-1})^2 d\theta_j^t d\theta_j^{t-1}\right)^{\frac{1}{2}}, \tag{1.19}$$

where $p_{\epsilon_t}(\theta_j^t \mid y)$ is the probability density function of the distribution $\pi(\theta \mid d(y^*, y) < \epsilon_t)$. This may be approximated from the previous population, $\{\theta_i, w_i\}$, by

$$\sigma_j \approx \left(\sum_{i=1}^{N}\sum_{k=1}^{N_0} w_i\widetilde{w}_k(\widetilde{\theta}_{k,j} - \theta_{i,j})^2\right)^{\frac{1}{2}}, \tag{1.20}$$

where

$$\{\widetilde{\theta}_k, \widetilde{w}_k\}_{1\leq k\leq N_0} = \left\{\left(\theta_i, \frac{w_i}{\bar{w}}\right) \quad s.t. \quad d(y^*, y) < \epsilon_t\right\} \tag{1.21}$$

and $\bar{w}$ is a normalising constant such that $\sum_{k=1}^{N_0}\widetilde{w}_k = 1$.

As is often the case for many models, parameter values may not influence the model

independently and are instead correlated. In this case, a more optimal family of perturbation kernels may be multivariate normal kernels which take into account the covariance between different parameters via the matrix Σ. An optimal choice of Σ is then given by

$$\Sigma = \int\int p_{\epsilon_{t-1}}(\theta^{t-1} \mid y) p_{\epsilon_t}(\theta^t \mid y)(\theta^t - \theta^{t-1})(\theta^t - \theta^{t-1})^T d\theta^t d\theta^{t-1}, \tag{1.22}$$

where v^T denotes the transpose of a vector v [138]. In a manner similar to the component-wise normal kernel, this can be approximated by

$$\Sigma \approx \sum_{i=1}^{N} \sum_{k=1}^{N_0} w_i \widetilde{w}_k (\widetilde{\theta}_k - \theta_i)(\widetilde{\theta}_k - \theta_i)^T, \tag{1.23}$$

where the set $\{\widetilde{\theta}_k, \widetilde{w}_k\}_{1 \leq k \leq N_0}$ is defined as before in Equation (1.21).

Filippi *et al.* go one stage further and consider multivariate normal perturbation kernels local to the particle that is being perturbed. In this case, the covariance matrix Σ is defined uniquely for each particle in the preceding population. The optimal local covariance matrix for the particle θ_i^{t-1} is then given by

$$\Sigma_{\theta_i^{t-1}} = \int p_{\epsilon_t}(\theta^t \mid y)(\theta^t - \theta_i^{t-1})(\theta^t - \theta_i^{t-1})^T d\theta^t d\theta^{t-1}, \tag{1.24}$$

which can be similarly approximated by

$$\Sigma_{\theta_i^{t-1}} \approx \sum_{k=1}^{N_0} \widetilde{w}_k (\widetilde{\theta}_k - \theta_i^{t-1})(\widetilde{\theta}_k - \theta_i^{t-1})^T. \tag{1.25}$$

Filippi *et al.* argue that the computational cost of calculating a covariance matrix for each particle individually is outweighed by the improved acceptance rate for particles generated using multivariate normal perturbation kernel with this optimal local covariance matrix.

Determining the threshold schedule

In addition to the choice of perturbation kernel, determining the threshold schedule is another area which can affect the performance of the ABC SMC algorithm. Too gradual a decrease in ϵ may lead to too many particles being accepted from a large local minimum in which the algorithm may eventually get stuck, while a decrease in ϵ that is too rapid

may result in loss of computational efficiency. Adaptive schedules, as opposed to fixing the threshold levels of each population at the start, attempt to improve the performance of the algorithm with respect to some of these problems.

A simple adaptive method for determining thresholds that is most commonly used is the quantile method. Before the start of each iteration, the new value of ϵ is chosen based upon the pre-determined quantile of the distances between the empirical dataset and the simulated data from the previous population. That is, for a pre-determined α, the new threshold ϵ_t is chosen such that $\alpha\%$ of the previous population gives rise to simulated data, y^*, that satisfies $d(y^*, y) < \epsilon_t$.

An alternative method, proposed by Silk *et al.* [139], attempts to address the issue of the algorithm potentially getting stuck in local optima. This method relies on estimating the acceptance rate curve across a range of values for ϵ. A steep incline in this curve is interpreted to be a potential sign of the existence of a local minimum and in such cases the value of ϵ_t is chosen to be at the foot of this incline. The full proposed method for selecting ϵ on this basis is shown in Algorithm 3, where $\aleph_t(\epsilon^*)$ is the approximated acceptance rate curve.

Algorithm 3: Method of determining ϵ in order to avoid local minima [139].

if $t > 0$ **then**
  Define d_{min} to be the minimum distance produced by past simulations.
end
Define $\epsilon^* = \text{argmax}_\epsilon \frac{\partial^2 \aleph_t(\epsilon)}{\partial \epsilon^2}$.
if $\aleph_t(\epsilon^*) > \delta$ *or* $\epsilon^* > d_{min}$ *(for the case* $t > 0$*)* **then**
  Set $\epsilon_t = \epsilon^*$. (*Detection of a possible local minimum*)
end
if $\aleph_t(\epsilon^*) \leq \delta$ *and* $\epsilon^* \leq d_{min}$ **then**
  Choose $\epsilon_t = \text{argmin}_\epsilon \Delta\left(\left(\frac{\epsilon}{\epsilon_t - 1}, \frac{\aleph_t(\epsilon)}{\aleph_t(\epsilon_t - 1)}\right), (0, 1)\right)$. (*Reduction of threshold vs. Computational expense*)
end

We note that, under this method, it is possible for $\epsilon_t < d_{min}$, where d_{min} is the smallest distance to the data from simulations of the previous population. In this case, if we were to use multivariate normal kernels as described previously, then we may run into problems since the set defined in Equation (1.21) would be empty.

1.8 Thesis structure

The main content of this thesis comprises 4 chapters in which we develop and analyse a range of different models of increasing complexity for tumour growth and radiotherapy response.

In Chapter 2 we consider the use of a variety of phenomenological ODE models for predicting *in vivo* radiotherapy response. Due to the limited nature of clinically available data, this type of approach is the current state-of-the-art with respect to patient-specific modelling of radiotherapy response. We use synthetic data studies to illustrate some of the key issues regarding uncertainty quantification, predictive power and model selection in the face of limited and potentially noisy data obtained from clinical CT scans. We further study the performance of the PSI model proposed as a potential prognostic indicator for clinical applications by Prokopiou *et al.*. We use the techniques described in Section 1.7 to fit the model to clinical datasets of oropharyngeal cancer patients and assess the quality of fit and the ability of the model to capture the observed *in vivo* dynamics. The model is shown to describe the response dynamics for some patients adequately but is not able to capture the full range of dynamics exhibited by the entire patient cohort.

The tumour microenvironment is well-known to be highly heterogeneous and so, while attractive for their low numbers of parameters and the ease with which they may be estimated in practice, it perhaps unsurprising that the simple, phenomenological models considered in Chapter 2 may not fully capture the full range of dynamics observed *in vivo*. As such, in Chapter 3 we develop a simple, spatially-resolved model describing tumour response to radiotherapy. We extend an existing model of avascular tumour spheroid growth first proposed by Greenspan [63] to account for radiotherapy. We use the additional spatial heterogeneity afforded by the new model to take into account the effect of local oxygen tension on radiation-induced cell death. We use numerical simulation to identify the influence of the internal tumour composition on the resulting response to treatment. Transient response dynamics arising due to spatial heterogeneity are observed within the tumour and characterised analytically. The long-term response dynamics are also considered and a relationship identified for which treatment protocols result in periodic behaviour.

Whilst the model in Chapter 3 represents a step towards a more mechanistic, spatially-resolved model, it remains relatively simple with some restrictive assumptions. In Chapter 4 we further increase model complexity and develop a model of tumour growth using the framework of multiphase mixtures in which we relax some of these assumptions. We develop a new three phase model in which the tumour is assumed to be comprised of tumour cells, dead material and extracellular fluid. We incorporate the differential mechanical properties of the dead material in a novel manner. We develop a numerical scheme for simulating the solutions of the model equations and characterise the dynamics exhibited for different parameter regimes. We further investigate the effects of varying the physical properties of the dead material within the tumour on the qualitative growth dynamics.

In Chapter 5 we extend the multiphase model to include the effects of radiotherapy. We model radiation-induced cell death as an instantaneous mass transfer between the tumour cell and dead material phases, avoiding the unrealistic instantaneous volume loss associated with many simpler models for radiotherapy response. Numerical simulations reveal that the model can capture the range of qualitative response dynamics characterised within our clinical datasets. We further characterise interesting qualitative regrowth dynamics and again investigate the influence of the dead material in the context of radiotherapy response.

In Chapters 2-5 we develop a range of models for tumour growth and radiotherapy response of increasing complexity. Whilst incorporating more biological detail, the limited data typically makes the more sophisticated models less applicable for making patient-specific clinical predictions. In Chapter 6 we present an extended discussion of future work perspectives. We use preliminary results to illustrate the way in which complex, mechanistic models may be used to guide the development of simpler, predictive models. More general conclusions are presented in Chapter 7.

Chapter 2

Phenomenological ODE models

2.1 Introduction

For most cancers the standard radiotherapy fractionation protocol has remained unchanged as the standard-of-care for many years, although altered schemes, such as hyperfractionation, accelerated fractionation and hypofractionation, have been proposed as improved alternatives for certain indications [3]. However, selection of the most appropriate protocol could benefit from a more individualised approach and incorporate more patient-specific information beyond tumour location and stage. As such, there is a growing literature of mathematical models that aim to predict radiotherapy response and guide selection of an optimal treatment protocol [105, 106, 118, 140].

Models proposed for clinical applications should simulate tumour response at a level that is compatible with the data available for model calibration. CT scans are routinely used to image the tumour at diagnosis and treatment planning stages [45–47]. Further scans are taken upon delivery of each fraction of radiation but are simply utilised for alignment purposes. Since mathematical models are not in widespread use for predicting radiotherapy response, the imaging modalities used are not necessarily of high-resolution and do not differentiate the heterogeneity in composition between different tumour regions. As such *in vivo* tumour data is typically limited and measurements may contain sources of error that are difficult to quantify. Therefore, whilst not incorporating as much biological detail, phenomenological models containing few parameters, but which may be more easily identified, are attractive prospects for predicting radiotherapy response in the

clinic at a patient-specific level [105]. However, any predictive model should primarily be fit for purpose, capturing sufficient detail in order to determine radiotherapy response and accurately predict outcome.

In this chapter we consider the applicability of some current simple models from the literature. In Section 2.3 we use synthetic data to showcase some of the methods used to calibrate these models and assess their predictive power. We also use these studies to show how noise and lack of data points affect the performance of these models. In Section 2.4 we focus on one such model, first proposed by Prokopiou *et al.* [105], with respect to clinical datasets and analyse its potential for clinical application.

2.2 Connecting mathematical models and clinical data

When integrating mathematical models and clinical data there are numerous modelling choices to be made. In many cases, these choices depend on the desired output from the modelling and the quantities of interest. However, irrespective of the many possible methodologies and modelling scenarios, the approach taken follows the schematic outlined in Figure 2.1.

Mathematical models and clinical datasets are brought together via parameter estimation methods, which enable us to calibrate our models. After parameter fitting we may perform further analysis on the resulting model parameters, model predictions and any quantities of interest (QOIs) that are the target of our modelling efforts. The desired outputs in any given case may affect the choices made regarding the parameter fitting methods, data subsets and model(s) used. Given the numerous possible combinations involved, we first summarise the options available in Sections 2.2.1-2.2.3.

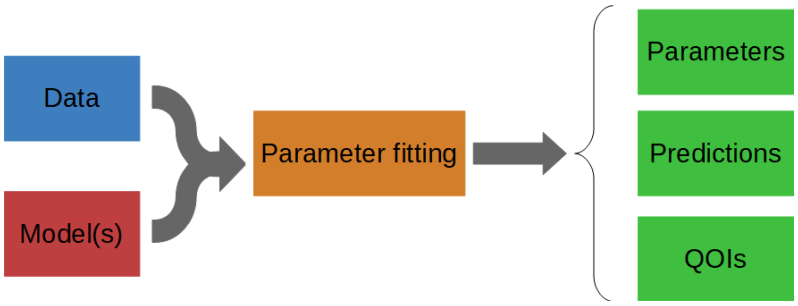

Figure 2.1: Pipeline for integrating mathematical models and data.

2.2.1 Data

Current best practice in the clinic involves two CT (computed tomography) scans for each patient - one at diagnosis and one at the treatment planning stage. These scans can then be used to estimate tumour volume measurements [45–47]. It is feasible to obtain further scans at the time of delivery of each fraction, as is the case for several past and ongoing clinical trials, although this is not routinely done.

An example of such data for an oropharyngeal cancer patient across multiple time points is shown in Figure 2.2 (tumour contoured in blue). The contouring of the tumour, and therefore volume measurement, is performed using an image segmentation algorithm guided by a radiation oncologist. It is important to note that such image analysis programs detect abnormal tissue from CT scans and not directly tumour volume. Therefore, for certain tumours our measured volume may incorporate additional effects such as oedema or swelling. We note that there will be errors associated with calculating the overall volume in this way, although is not obvious how to quantify them. In addition, such CT scans are commonly performed on different machines, often at different resolutions. As a result, for a patient dataset showing large variation in pre-treatment behaviours, for just three time points, it is not straightforward to distinguish biological heterogeneity from noise.

More sophisticated imaging modalities are being developed for which it is possible to image certain features within the tumour microenvironment, which is well known to be heterogeneous [5, 39, 50, 141]. This could enable identification of regions of hypoxia or necrosis, for example. As a result, there is potential for more data to be routinely collected in the clinic (including spatial data) if modelling efforts demonstrate that the extra data can result in the accurate calibration of more detailed models which have the potential to improve treatment outcomes for patients and, as such, improve upon the current standard of care.

Throughout this chapter we discuss a number of different datasets. We summarise these in Table 2.1 for ease of reference. Where possible, any missing data were interpolated in a logical and consistent manner, assuming regular, weekly scans, for example.

The dataset used in Prokopiou *et al.* [105], where the PSI model was first proposed

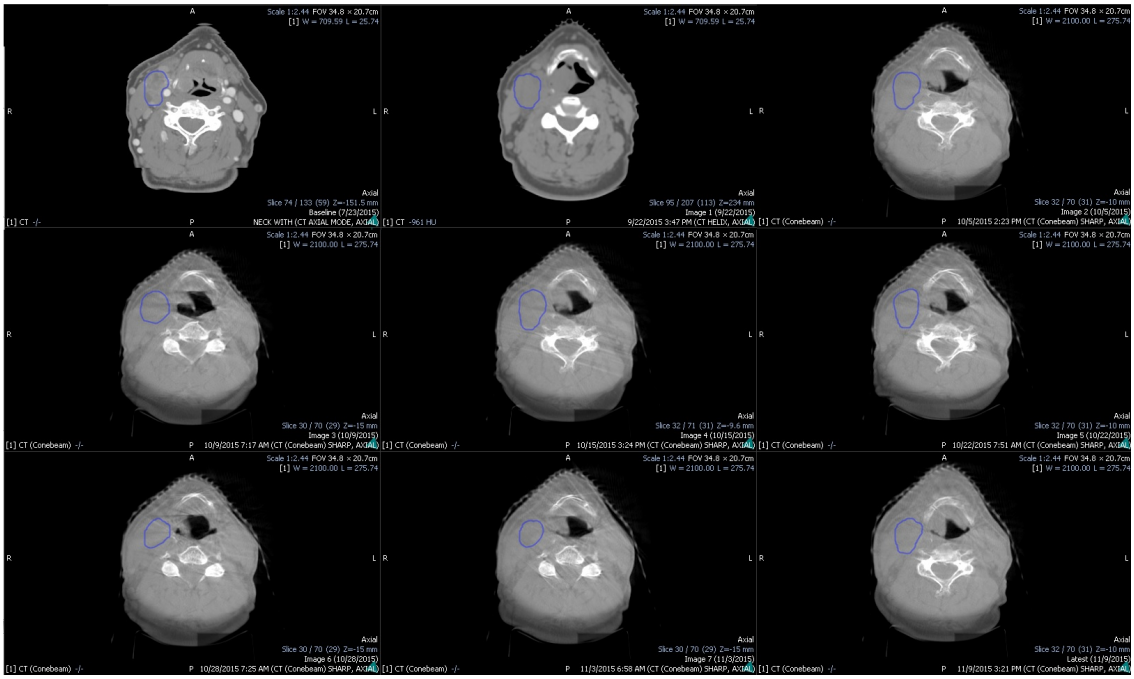

Figure 2.2: Example of a CT scan of a single oropharyngeal cancer patient across multiple time points; tumour contoured in blue. (data courtesy of CD Fuller and MD Anderson)

(see Section 2.2.2), consists of tumour volumes from 4 non-small cell lung cancer patients undergoing standard fractionated radiotherapy. The tumour volume measurements per patient in this dataset are fairly sparse, with an initial tumour volume measurement before the start of treatment and either 2 or 3 subsequent measurements. The dataset as originally used in [105] was obtained from Wang and Feng [112].

The second dataset contains tumour volume measurements segmented from CT images of 9 oropharyngeal cancer patients who received treatment at MD Anderson, Texas, USA, courtesy of CD Fuller. Work on this dataset focussed on the data points after the start of radiotherapy only, with weekly volume measurements available for each patient throughout a 7-week treatment period.

The most comprehensive dataset that we analyse is from a cohort of 51 patients comprised of 32 who were treated at Moffitt Cancer Center, Florida and 19 at MD Anderson, Texas. The dataset is from a mixture of head and neck cancer sites including the oropharynx, tonsil and base of tongue. Each CT scan was segmented by the same person, giving weekly tumour volumes throughout treatment, a volume measurement at the treatment planning stage for all patients and an additional measurement at diagnosis for the 32 Moffitt patients.

Dataset	Source	Disease type	# patients	# data points
DS1	Original PSI paper/literature	Non-small cell lung cancer	4	2/3 RT only
DS2	MD Anderson	Oropharyngeal cancer	9	6 (weekly) RT only
DS3	Moffitt & MD Anderson	Head & neck cancer*	51 (32 & 19 resp.)	1/2 pre-RT & weekly during RT

*mixture of sites - orophraynx/tonsil/base of tongue

Table 2.1: Summary of the different datasets used in this chapter.

Broadly speaking, we observe several different classes of qualitative response within the clinical data. From a modelling point of view, these are response dynamics which we may hope to reproduce accurately from our model and even predict from pre-treatment/initial data. We highlight and characterise some of these response types in Figure 2.3.

In Figure 2.3a the patient responds well to radiotherapy with the tumour decreasing markedly in volume throughout the treatment. We refer to this type of behaviour hereafter as a 'fast responder'. By contrast, in a number of cases, the initial response of the tumour to radiotherapy appears to be favourable, but the response plateaus in the latter stages of treatment resulting in a non-negligible final tumour volume (Figure 2.3b). However, this radiographic volume may subsequently recede in the weeks after radiotherapy. Occasionally, as in Figure 2.3c, a patient may appear to exhibit continued tumour progression throughout the first few weeks of radiotherapy before showing a delayed response characterised by a decrease in tumour volume towards the end of treatment. We characterise this type of response as 'pseudo-progression'. Finally, there are those patients for whom the effects of radiotherapy appear to be marginal when viewed as tumour volume over time alone, as is the case in Figure 2.3d. We classify these patients as 'poor responders'.

2.2.2 Models

If a particular mathematical model is to provide clinically relevant insight then it should be compatible with the data that are available. Phenomenological ODE models provide a high-level description of the tumour dynamics which model the shape of the observed behaviour without accounting for much of the complex underlying biology. As such, these models tend to have relatively few parameters which may be more easily estimated from the potentially limited available data.

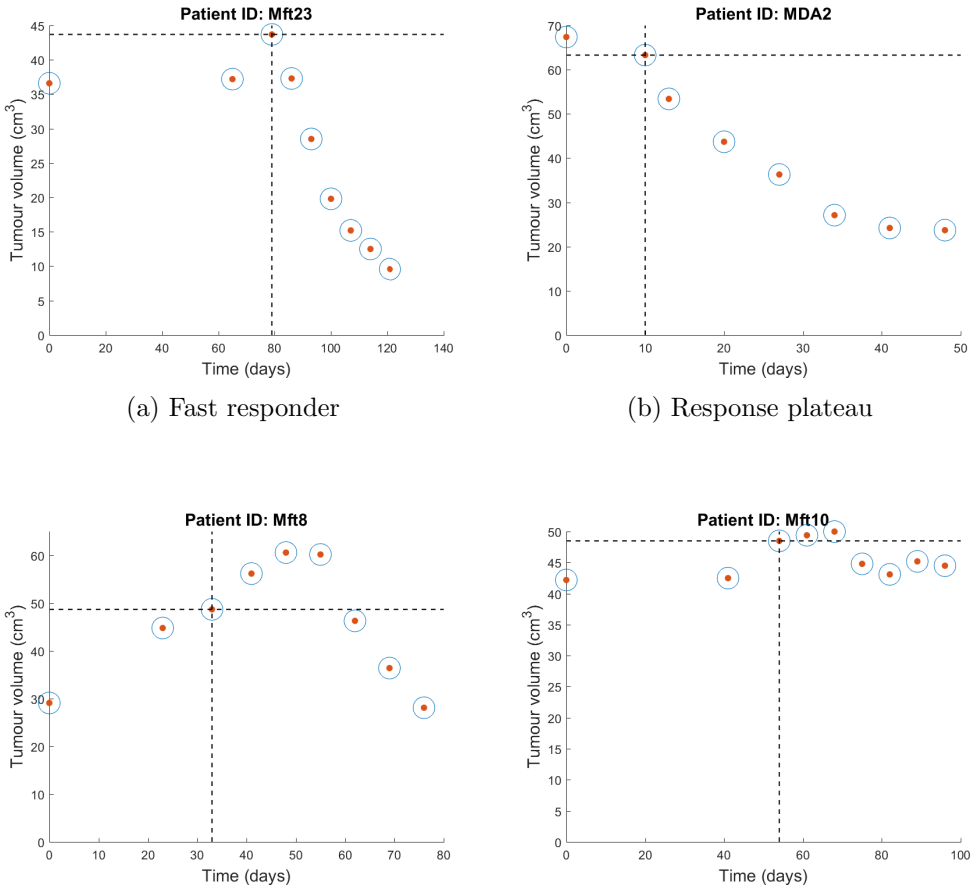

(a) Fast responder (b) Response plateau

(c) Pseudo-progression (d) Poor responder

Figure 2.3: Examples of four different categories of qualitative radiotherapy response observed in the data. Dashed black lines represent tumour volume and time at the start of treatment. **(a)** Fast response to radiotherapy with small resultant tumour volume. **(b)** Initial response to radiotherapy followed by a plateau and non-negligible tumour volume at the end of treatment. **(c)** Initial increase in apparent tumour volume before positive treatment response observed. **(d)** No significant response to radiotherapy throughout the duration of treatment.

As described in Chapter 1, the simplest tumour growth models comprise a single ODE to describe the tumour volume dynamics. There are a number of phenomenological growth laws which consider a spatially-averaged description for the change in tumour volume, V. These include the exponential, logistic, Gompertz and generalised logistic models, given by Equations (2.1), (2.2), (2.3) and (2.4), respectively [56, 107].

$$\frac{dV}{dt} = \lambda V \tag{2.1}$$

$$\frac{dV}{dt} = \lambda V \left(1 - \frac{V}{K}\right) \tag{2.2}$$

$$\frac{dV}{dt} = -\lambda \log\left(\frac{V}{K}\right) V \tag{2.3}$$

$$\frac{dV}{dt} = \lambda V \left(1 - \left(\frac{V}{K}\right)^{\nu}\right) \tag{2.4}$$

While not encompassing all phenomenological models in the literature, these are some of the more widely-considered descriptions of tumour growth.

Each of the models may be extended to account for the effects of radiotherapy. The simplest manner for achieving this would be to assume instantaneous cell death at the time of each fraction of radiotherapy proportional to the tumour volume, V.

Prokopiou *et al.* [105] consider a different form for the radiation-induced cell death, assuming that the stage of growth is representative of the proliferative capacity of the tumour. In this chapter we focus much of our attention on this model, also termed the *proliferation saturation index* or PSI model, which was first proposed by our collaborators at Moffitt Cancer Center [105], and so we explain it in further detail here.

The PSI model, given by Equation (2.5), has been proposed for patient-specific prediction of tumour response to radiotherapy. Tumour growth is governed by the logistic growth law, while response to radiotherapy is incorporated as an instantaneous effect which also takes the logistic functional form. This model further assumes that the tumour growth rate, λ, and radiation-induced death rate, γ, are global, population-level parameters. The carrying capacity, K, is assumed to be a patient-specific parameter which may be estimated from data, with the tumour volume to carrying capacity ratio at the start of treatment being proposed as a prognostic indicator of radiotherapy response. In Prokopiou *et al.* [105], this ratio is termed the *proliferation saturation index* (PSI).

$$\frac{dV}{dt} = \lambda V \left(1 - \frac{V}{K}\right) - \sum_{i=1}^{n} \gamma V \left(1 - \frac{V}{K}\right) \delta(t - t_i) \tag{2.5}$$

It is natural to consider common alternative models within this setup for comparison

with the logistic PSI model. The other growth laws presented in Equations (2.1)-(2.4) may be similarly extended to incorporate radiotherapy following the rationale of Prokopiou *et al.*, with instantaneous cell death due to irradiation thus assumed to be proportional to the growth term. In the case of the Gompertz and generalised logistic models we may therefore define a similar notion of $PSI = V/K$ within these models. Note that although the exponential model (Equation (2.1)) does not exhibit growth-saturation, it is often considered a reasonable description of the early stages of tumour growth and thus, when considering the data available to us, could plausibly be an adequate model.

The above ODE models provide a phenomenological description of tumour growth and treatment response while not explicitly accounting for the complexity and heterogeneity of the underlying biology. These models may be extended to instead treat the tumour mass as being composed of two (or more) well-mixed compartments. By specifying the dynamics of each compartment such models aim to account for more of the heterogeneity in tumour composition observed within both *in vitro* spheroids and *in vivo* tumours, whilst maintaining the relative simplicity afforded by such a framework. In this chapter we focus on single ODE models for tumour growth and radiotherapy response. We acknowledge that there are a number of other types of phenomenological models in the literature, including multi-compartment ODE models, that have also been proposed for this purpose [61, 111, 142]. We revisit these types of model in Chapter 6.

2.2.3 Parameter fitting techniques

If a model is to be useful in a clinical setting it must be calibrated and validated against experimental or clinical data [125]. To calibrate (and validate) a proposed mathematical model with data we require techniques to fit and estimate the model parameters. There are many methodologies that have been developed for this purpose, with the choice of approach being largely a combination of desired output or analysis, and personal preference.

In this chapter we use a combination of two different parameter fitting techniques in order to integrate the models outlined in Section 2.2.2 with the datasets described in Section 2.2.1. In the remainder of this section we briefly mention two such techniques; namely a genetic or evolution-based optimisation (EBO) algorithm and a Bayesian ap-

proach known as the Approximate Bayesian Computation Sequential Monte Carlo (ABC SMC) algorithm. These methods were explained in more detail in Chapter 1. Here we focus on the outputs of these inference techniques and how they may be used to analyse the fit of a model to data.

Genetic algorithm (EBO)

In order to assess how well these models capture the observed response of *in vivo* tumours to radiotherapy we may fit them to clinical data using an 'evolution-based optimisation' (EBO) algorithm, as outlined in Section 1.7.1 and [105]. This algorithm optimises the fit of the model to the data by minimising the 'sum of squares' error. The result of the EBO algorithm is a single, best-fit parameter set for which the model solutions pass closest to the data points. We may visualise the solution for the resulting parameter set alongside the data as in Figure 2.11. The coefficient of determination, or R^2, may be evaluated to quantify how much of the data may be explained by the calibrated model. The R^2 value is given by

$$R^2 = 1 - \frac{\sum_i (y_i - f_i)^2}{\sum_i (y_i - \bar{y})^2}, \tag{2.6}$$

where y_i are the data, f_i the corresponding values taken by the model and $\bar{y}$ the mean of the data. An R^2 value equal to 1 corresponds to a perfect model fit.

If we continue this solution trajectory to project forward in time, we may use the calibrated model to predict future data points (see Figure 2.13). In particular, we may also use this forecasting to classify radiotherapy response. There are numerous statistics that may be used to assess the performance of binary classifiers. These include

$$\text{Accuracy} = \frac{TP + TN}{TP + TN + FP + FN} \tag{2.7}$$

$$\text{Recall} = \frac{TP}{TP + FN} \tag{2.8}$$

$$\text{Dice coefficient} = \frac{2TP}{2TP + FP + FN}, \tag{2.9}$$

where the classified patients have been categorised as true positives (TP), true negatives

(TN), false positives (FP) or false negatives (FN). Classification accuracy measures the proportion of all patients correctly classified, recall measures the proportion of positives correctly identified, whilst the Dice coefficient has been proposed for use as an overall statistic for comparing the similarity between the observed and predicted data.

The residual sum of squares, as defined by Equation (1.8), provides a metric for determining the distance between the model and data. However, for different models with different numbers of model parameters the quality of fit may not be compared simply using this statistic. In this case we may compare the *Akaike information criterion*, or AIC, for each candidate model. When the data sample size is small, we may instead calculate a corrected AIC value, or AICc, given by Equation (1.9). Comparing values for the AICc across different models allows us to compare the models quantitatively.

ABC SMC

Bayesian techniques for parameter inference allow us to generate probability distributions rather than point estimates. As a result of the ABC SMC algorithm, we obtain a weighted sample of parameter sets which approximate the true posterior distribution. We may visualise the marginal densities for each parameter as histograms in order to analyse the distribution as a whole. We may also compare the posteriors for parameters in a pairwise manner in order to consider any correlations between model parameters (see Figure 2.4). In this manner, the ABC SMC algorithm may be used to investigate the practical identifiability of the model with respect to potentially noisy data.

The resulting population of parameter sets representing the posterior distribution may also be used to get a handle on the uncertainty of our calibrated model, and any model predictions. As more data is obtained, we update our posterior distribution and model predictions. In this way, we are able to calibrate the model and use it to forecast future behaviour on a rolling basis (c.f. Figure 2.6).

The posterior predictive distribution for new data, y^*, is defined as

$$p(y^* \mid y) = \int p(y^* \mid \theta, y) p(\theta \mid y) d\theta, \tag{2.10}$$

and can be obtained for any y^* from the posterior distribution for θ. The posterior

predictive distribution allows us to assess the uncertainty in our model predictions given a set of data and a particular quantity of interest.

The ABC SMC algorithm is easily extended to simultaneously perform model selection for multiple candidate models, as described in Section 1.7.3. The outputs of the ABC SMC model selection algorithm are the posterior marginal distributions for the models, $\widetilde{\pi}(m \mid y)$ and the posterior distributions of parameters, $\pi(\theta \mid y, m)$, for m=1,...,M, where M is the number of models. Bayes factors summarise the evidence for one model over another and can be calculated according to Equation (1.16) in the case of a uniform prior on models. If the result of the model selection is not conclusively in favour of one model in particular, then the marginal probabilities for each model may be used to inform model-averaging predictions.

2.3 Synthetic data studies

In this section we use synthetic data studies to showcase some of the methods available for analysing the calibration and predictive power of a mathematical model, whilst also highlighting some of the issues relating to the quality of the data used for calibration and subsequent parameter inference. We emphasise that the results presented in this section are not comprehensive studies but are intended as illustrative examples of the techniques.

For each study in this section we generate synthetic data using a logistic model of the form given by Equation (2.5). However, for simplicity, we consider individual *in silico* patients such that the model parameters for the synthetic data is generated using randomly generated patient-specific values for all model parameters, that is, we make no distinction between global and patient-specific values as in the PSI model proposed by Prokopiou *et al.*.

We use the ABC SMC algorithms presented in Chapter 1 and discussed in Section 2.2.3 for parameter inference. The setup options used for the ABC SMC algorithm are summarised in Table 2.2. We use the residual sum of squares as a metric for the distance between the model and the data, weighting each residual by the magnitude of the data point.

Algorithm option	**Setup used**
Threshold schedule method, ϵ_t	Adaptive - 10% quantile
Growth rate prior, λ	$U(0,1)$
Death rate prior, γ	$U(0,1)$
PSI prior	$U(0,1)$
Parameter perturbation kernel type	Multivariate normal optimal local covariance matrix
Model pertubation kernel	$P(\text{switch models}) = 0.7$

Table 2.2: Options used for setting up the ABC SMC algorithms. Further explanation of these options can be found in Chapter 1.

2.3.1 Calibrating tumour growth models

In this section we demonstrate the use of parameter inference techniques to recover the underlying parameters used for generating the synthetic data. We also illustrate the effects of noise on the precision of the resulting parameter estimates. We generate synthetic data for an *in silico* cohort of 100 patients. The patient-specific tumour growth rates, λ_i, are randomly chosen from a $U(0, 0.1)$ distribution with PSI_i values at $t = 0$ chosen uniformly from $[0, 1]$. Tumour growth trajectories, in the absence of radiotherapy, are then simulated for each parameter set with normalized tumour volumes such that $V(0) = 1$. We generate datasets from the resulting simulations for each patient taking 10 time points equally-spaced 4 days apart. We perform a sequence of parameter fits adding uniform random noise to each data point with noise levels taken from $\{0\%, 1\%, 3\%, 5\%\}$.

We use the ABC SMC algorithm with 2000 particles to approximate the posterior distributions for the parameter set for patient. We specify the tolerance for convergence of the algorithm (ϵ_T) as being equivalent to the level of noise ($x\%$) added to each data point (n time points) in each case such that $\epsilon_T = \frac{nx}{100}$ [1]. We justify this choice since it would not make sense to impose a convergence tolerance that is more stringent than our belief about the error in the measured data. As such the posterior distributions reflect some of the underlying noise in the data.

We visualise the posterior parameter distributions for a representative patient from the cohort in Figures 2.4a-b. Figure 2.4a shows the inference results using perfect data, while Figure 2.4b corresponds to up to 5% noise added to each data point. The marginal

[1] For data sets with no noise added we choose the same tolerance as for 1% noise.

density histograms show that for each parameter that, while both distributions contain the true generating parameters, the addition of noise to the data affects the precision of our inference. The spread of the resulting trajectories from simulating tumour growth using parameter sets from the posterior distribution reflect this uncertainty. We visualise sample trajectories for from the two posteriors in Figures 2.4c-d.

We further visualise the precision of our inference for the entire patient cohort with increasing noise levels in Figure 2.5. We collate the posterior parameter distributions relative to the generating parameters for all patients in order to compare the effect of noise in the data on the inferred distributions. We see that for both model parameters, λ and K, the effect of increasing noise is to increase the spread of the resulting parameter estimates.

From this study we see that even when we know the model used to generate the underlying data, noise in the measured data may affect the precision of our parameter inference. More pertinently, we also observe a wider range of model predictions from the resulting simulations. In light of some of the issues discussed in section 2.2.1, conservative error estimates in clinical data could lead to imprecise model predictions.

2.3.2 Assessing predictive power

In addition to potential noise in tumour volume measurements, the limited number of data points typically available in the clinic also presents an issue for accurately calibrating models and producing accurate model predictions. In this section we investigate how the number of data points available has an impact on the resulting model predictions. For this study we fit the logistic model to synthetic data throughout radiotherapy for a 6 week standard fractionation protocol. We generate the growth rate, λ, and pre-treatment PSI, parameter values from the same distributions as for the study in the previous section, while the death rate, γ, is chosen from a $U(0, 0.3)$ distribution.

For a given parameter set, we use the ABC SMC algorithm with 2000 particles to fit the model to the synthetic data using an increasing number of data points taken weekly throughout the treatment protocol. We specify a convergence tolerance to be equivalent to 5% noise for the number of data points used for the model calibration. The trajectories resulting from inference using the extremes of just 2 data points and the entire dataset, 6

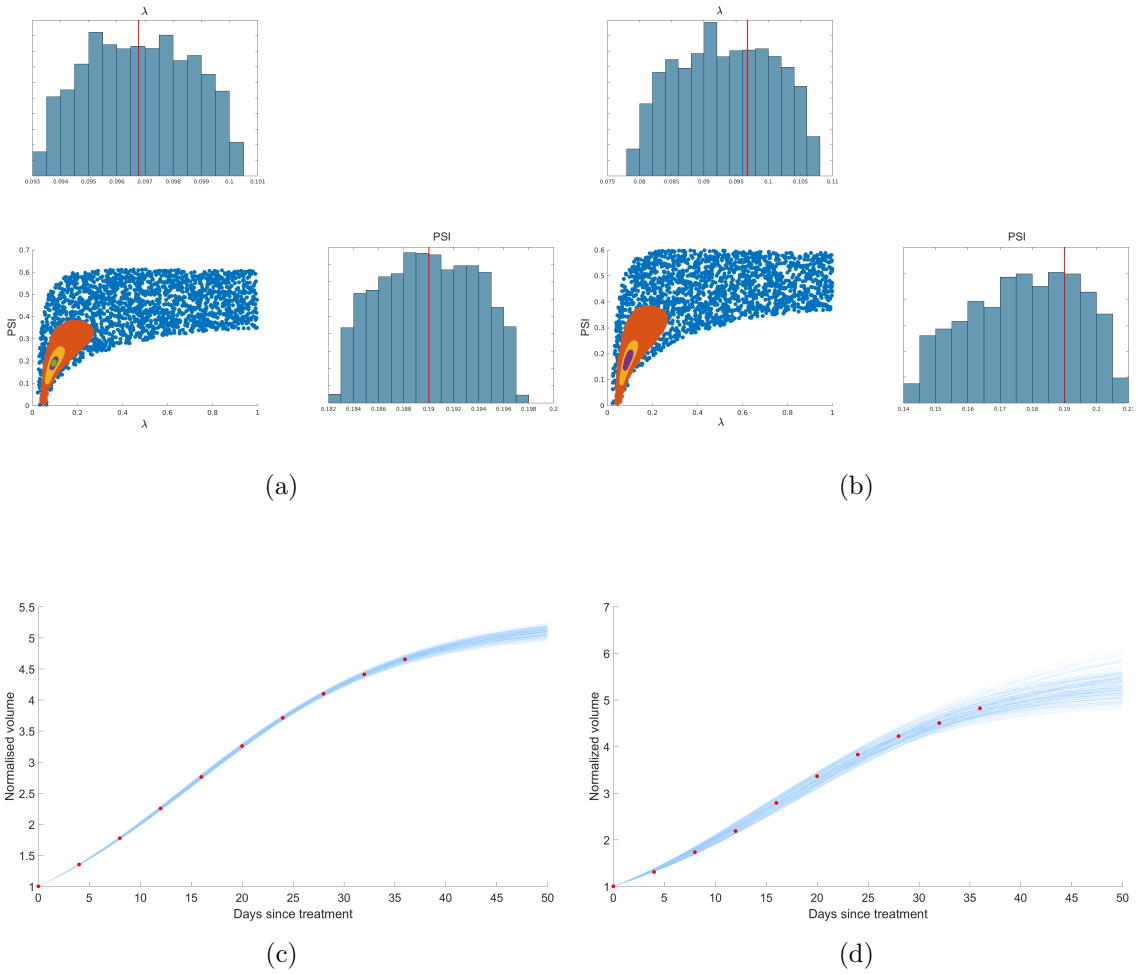

Figure 2.4: A representative example of parameter inference and model calibration of the logistic tumour growth model (Equation (2.5) considered in the absence of radiotherapy) for a single *in silico* patient. Figures a) and c) correspond to calibrating the model with no noise added to the synthetic data, whilst b) and d) incorporate up to 5% random noise in each data point. **a), b)** Visualisation of the posterior distributions resulting from the ABC SMC algorithm. The successive populations of particles from each iteration of the ABC SMC algorithm appear as contours in the posterior parameter space. The histograms represent the marginal posterior distributions for each model parameter, with the true generating parameter given by the solid red line. **c), d)** Trajectories obtained from simulating the model using a sample of 120 parameter sets from the posterior distribution (blue curves). The data points used for calibrating the model are marked by the red points.

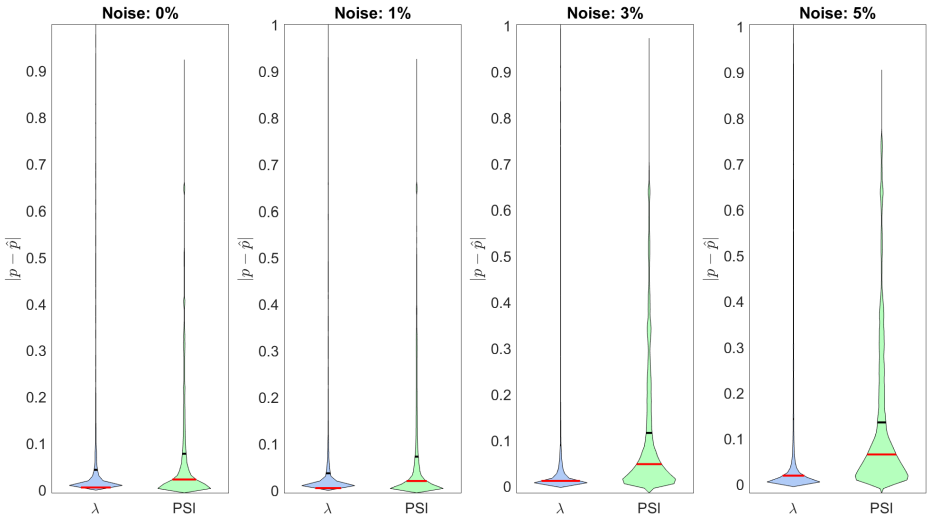

Figure 2.5: Violin plots showing the collated distribution of parameter values, λ (blue) and PSI (green), in the posteriors for all 100 patients in the *in silico* cohort relative to the generating parameters, $\hat{\lambda}$ and $\hat{PSI}$. The distributions are shown for increasing levels of noise in the data. The mean and median of each distribution are respresented by the black and red lines respectively.

volume measurements, are shown for a representative example from the *in silico* patient cohort in Figure 2.6. We note that in the extreme case of just using 2 data points the data is insufficient to determine the 3 model parameters.

We see that the trajectories exhibit a much greater spread in the model predictions when limited data is available for model calibration. In particular, we observe that the majority of the trajectories in the sample from the posterior for 2 data points do not accurately predict the final data point from the last week of the radiotherapy treatment protocol. Using the definition in Equation (2.10), we may use the inferred parameter distributions to approximate the posterior predictive distribution for the final data point. We visualise these distributions as histograms for increasing dataset size in Figure 2.7. We observe that increasing the number of data points results in increased predictive power of the model, as indicated by a narrower range of values around the final data point in the posterior predictive distribution.

2.3.3 Model selection

In Sections 2.3.1 and 2.3.2 we used synthetic data studies to illustrate the effects of noise and dataset size on model calibration. In both cases we used the same model for both

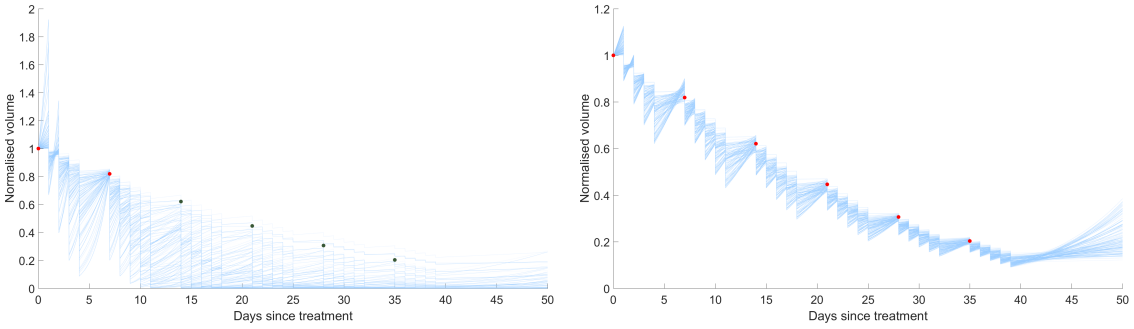

(a) (b)

Figure 2.6: Tumour response trajectories (blue curves) obtained from simulating the model (Equation (2.5)) for the standard 6-week fractionation protocol using a sample of 120 parameter sets from the posterior distributions resulting from the ABC SMC algorithm. The data points used for calibrating the model are marked by the red points, while remaining data not used for calibration are shown in dark green. The opacity of each line is determined by its quality of fit to the final data point. **a)** The results of calibrating the model using just the first two data points at the start of radiotherapy. **b)** Trajectories obtained from fitting the model to the entire dataset.

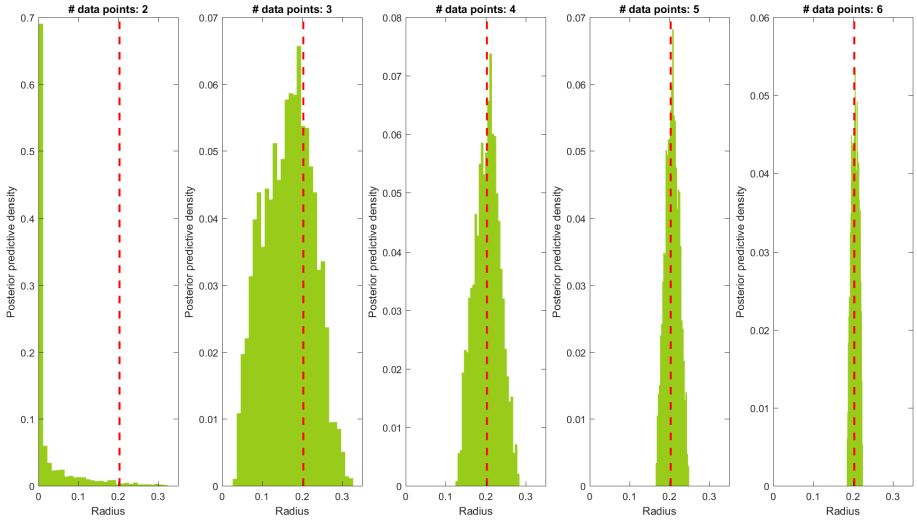

Figure 2.7: The posterior predictive distributions for the final data point of the dataset shown in Figure 2.6 as the number of data points used for model calibration varies. The true value of the final data point is marked by the dashed red line.

generating the data and parameter inference. However, in practice the underlying tumour dynamics are far more complex than the simplified models with which we hope to predict radiotherapy response. As such, there is an inherent uncertainty in the most appropriate model to use for making predictions, as well as the parameter values for each candidate model. In this section we generate synthetic datasets using the logistic model of the form of Equation (2.5) but use the extension to the ABC SMC algorithm for model selection with 5000 particles to infer the quality of fit for both the logistic model and the Gompertz model (Equation (2.3)).

We simulate a cohort of 30 patients incorporating both pre-treatment growth and radiotherapy response to a standard 6 week protocol. Model parameters are picked at random from the distributions used in Sections 2.3.1 and 2.3.2. The length of the pre-treatment growth period simulated before the start of radiotherapy is also randomly chosen between 30-60 days. We take 3 pre-treatment data points (representative of the diagnosis, treatment-planning and start of treatment scans taken in the clinic) and a further 2 data points at the start of treatment as a dataset for model calibration. We add incremental amounts of noise to the data, $x \in \{0\%, 1\%, 3\%, 5\%\}$, and correspondingly choose appropriate convergence tolerances, ϵ_T, for parameter inference as described in Section 2.3.1. The priors for the Gompertz model parameters are taken to be the same as for the logistic model, and we assume equal prior probabilities for each model.

We compare the results for no noise and 5% noise for a representative dataset in Figure 2.8. In Figures 2.8a-b we visualise the tumour response trajectories from simulating a sample of parameter combinations from the posterior distributions. The marginal probabilities for each model are shown inset. As with the results in the previous studies, increasing the level of noise in the data results in a greater spread of trajectories. Here, we additionally observe uncertainty in the best fitting model for greater amounts of noise. For perfect data, the logistic model is preferred over the Gompertz model, with a Bayes factor of 9.33. However, for a 5% noise level in the data measurements, we find that the marginal probabilities for each model are much closer. The larger errors in the underlying data allows for a greater variety of simulation trajectories to equally fit the data. This again corresponds to a lack of precision in the posterior predictive distribution for the final data point (Figures 2.8c-d). We observed that, for no noise, the bulk of the density

is concentrated around the true value for the tumour volume at the end of treatment. However, the parameter sets for which the Gompertz model provides a good fit to the calibration data result in a small contribution to the posterior predictive distribution of the final data point which underestimates the tumour volume. As the noise level in the data increases to 5% we see that the posterior predictive distribution spreads out. Correspondingly, the contributions to this distribution from each model also spread out and overlap with each other.

We average the marginal probabilities across the entire patient cohort for each of the noise levels in Figure 2.9. We observe that it is more difficult to discriminate between the two models as the noise levels in the underlying data increases. We note that the average marginals for no noise in the data are not as conclusively in favour of the logistic model as for the example presented in Figure 2.8. Since we have used synthetic datasets similar to those which may be obtained in the clinic, we suffer from a lack of time points. As such the effects discussed in the previous study mean that, for some cases, the Gompertz model may provide an adequate description of the data, even in the absence of noise.

However, *in vivo* there is no 'correct' underlying model generating the data and, in practice, multiple mathematical models in the clinic may be used to generate a range of predictions for response in the manner presented here. Such an approach using a population of predictive models has proved successful in other fields [143].

2.4 PSI as a prognostic indicator

With the conclusions of Section 2.3 in mind, we proceed to analyse the performance these types of model with respect to clinical data. As described in Chapter 1 and Section 2.2.2 there is a growing literature of proposed models of this type. In this section we focus on one such model, the PSI model, as given by Equation (2.5), with respect to clinical data and its applicability as a prognostic indicator for radiotherapy response.

The initial work by Prokopiou *et al.* [105] involved only a very small initial dataset (DS1 in Table 2.1). For the proposed model to be of interest for clinical application it is necessary to validate its effectiveness for a much larger dataset. More specifically, the model should be capable of reproducing the dynamics observed in the data with

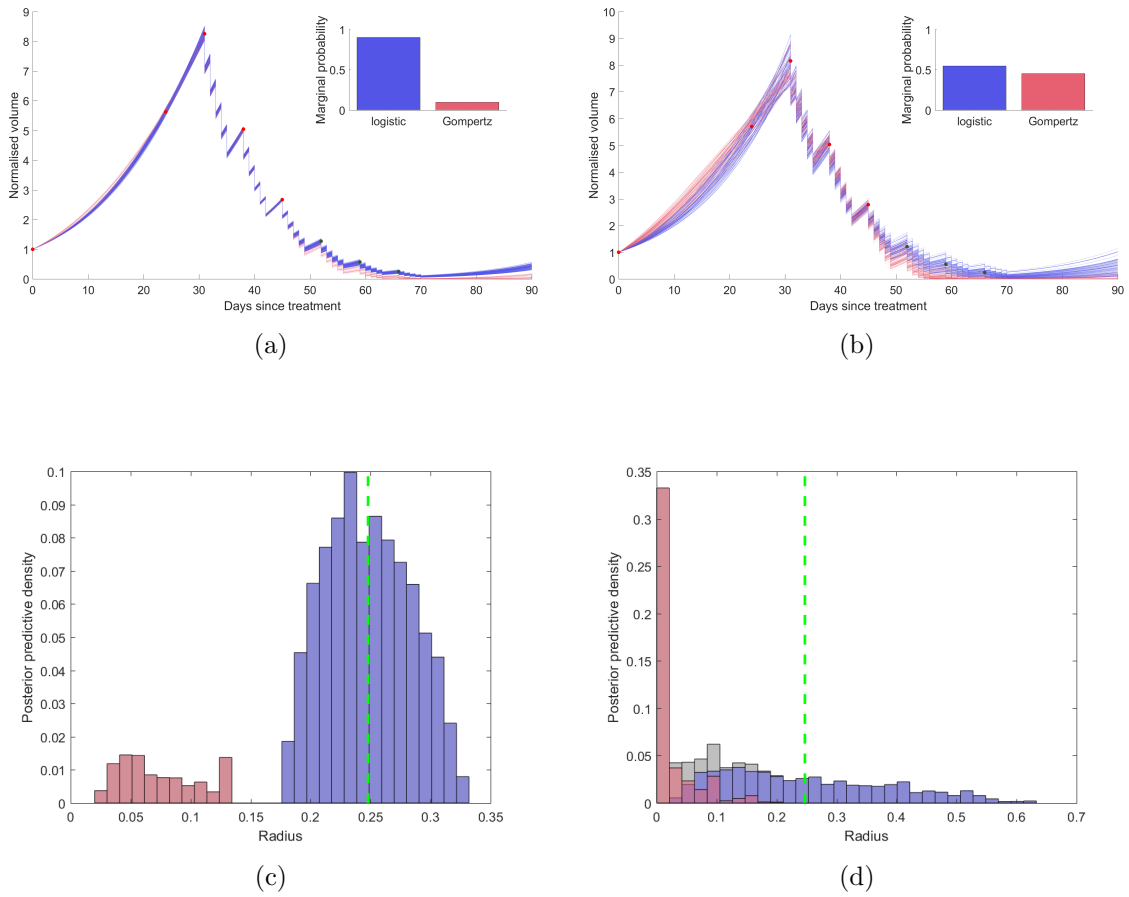

Figure 2.8: A representative example of results from using the ABC SMC model selection algorithm to fit both the logistic (Equation (2.5)) and Gompertz (Equation (2.3)) models to a dataset synthetically generated using the logistic model with varying noise levels; panels a) and c) correspond to no noise, while b) and d) contain up to 5% in each data point. The pre-treatment data points and those from the first 3 weeks of the radiotherapy protocol are used for model calibration. **a), b)** Tumour volume trajectories from simulating a sample of 120 parameter sets from the posterior distribution. Simulations using the logistic model are shown in blue, whilst the red curves correspond to simulations of the Gompertz models. The opacity of the lines is given by the distance of the simulation to the final data point at the end of treatment. The data points used for model calibration are shown in red, with the remainder of the dataset marked by the dark green points. The posterior marginal probabilities for each model are shown inset top right. **c), d)** The posterior predictive distributions for the final data point. The contribution of each model to the density are shown by the blue and red bars, whilst the total height of the bars shows the total posterior density (shown in grey where the models overlap). The true value of the final data point is marked by the dashed green line.

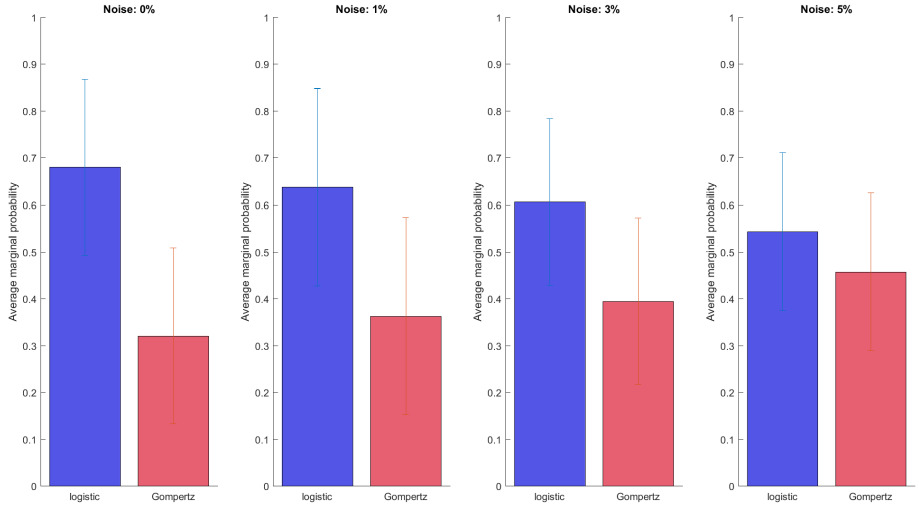

Figure 2.9: The posterior marginal probabilities for each model as the amount of noise added to the synthetic data points increases. In each case the probabilities have been averaged over the entire *in silico* cohort of 30 patients.

reasonable precision. Following this, we may test whether the properly calibrated model can accurately forecast the response to radiotherapy for an individual patient.

2.4.1 Fitting to clinical data

We test the ability of the PSI model to fit clinically observed response dynamics using a dataset of 9 squamous cell oropharyngeal cancer (OPX) patients (DS2 in Table 2.1). For the 9 patients we require 11 model parameters; a global growth rate λ, a global death rate γ, and 9 patient-specific carrying capacities K_i, with corresponding values for the PSI_i at the start of treatment.

We first use the ABC SMC algorithm to investigate the parameter space for the calibrated model and gain insight into the variation in the model simulations resulting from uncertainty in the model parameters. We find that the best fitting parameter sets result in very similar trajectories for all patients, showing little variation in predictions for the final tumour volume. In Figure 2.10 we visualise the trajectories corresponding to the 95% equal-tailed credible interval from the posterior predictive distribution for the final data point for a representative patient in the dataset. The data points are well-represented by the model and the spread of the trajectories is very narrow.

Given the lack of variability in the model simulations shown in Figure 2.10, we pro-

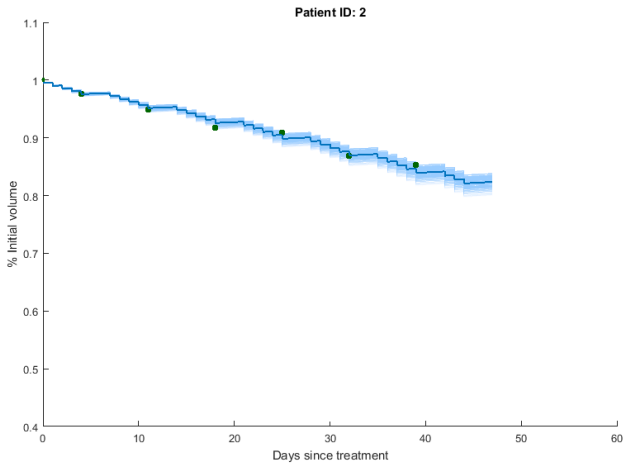

Figure 2.10: Trajectories (blue curves) obtained from simulation the PSI model (Equation (2.5)) from a sample of 120 parameter sets from the posterior distribution using the ABC SMC algorithm with dataset DS2 (Table 2.1). The simulation pertaining to the best-fitting parameter set is shown as the dark blue line. The data shown is for a single representative patient and is marked by the dark green points.

ceed to consider the single best-fitting parameter set for further analysis of the model's performance, as identified using the EBO algorithm. We implement the EBO algorithm with a population of 500 parameter sets iterated for 150 generations. Simulation results for all patients pertaining to the best-fit parameter set are shown in Figure 2.11. Here, the data points do not include pre-treatment growth data, with attention instead focussed on the ability to reproduce the observed response dynamics.

With the dataset taken as a whole, the model can qualitatively match the data with good accuracy. In Figure 2.12a, we compare the model predicted data points, V_p, with those measured in the data, V_m. The calculated R^2 value of 0.870 confirms the reasonably good fit of the calibrated model. The variation in the PSI values obtained from the model fitting is shown in Figure 2.12b. We note that despite the reasonable accuracy of fit to the data, for those patients which exhibit a plateau in response towards the end of treatment, the model appears to be unable to capture the qualitative shape of response (see patient ID 35 in Figure 2.11, for example).

2.4.2 Predicting treatment outcome from early-stage response

Figures 2.11 and 2.12 demonstrate that the PSI model may retrospectively fit to *in vivo* tumour volume data throughout radiotherapy. However, to provide clinically-relevant insight, the model should have sufficient predictive power. To assess the potential use of

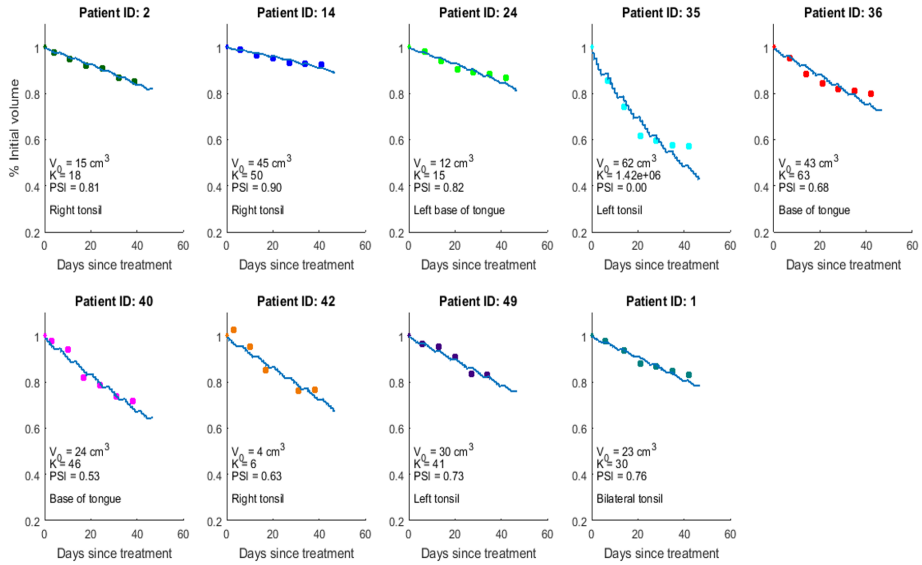

Figure 2.11: Simulated tumour volume trajectories (blue curves) obtained from fitting the PSI model (Equation 2.5) to dataset DS2 (see Table 2.1) using the EBO algorithm. The data points are marked by the coloured circles. The results shown correspond to a global growth rate $\lambda = 0.0033$ and death rate $\gamma = 0.0281$, with carrying capacities, K, and hence pre-treatment PSI values, as shown.

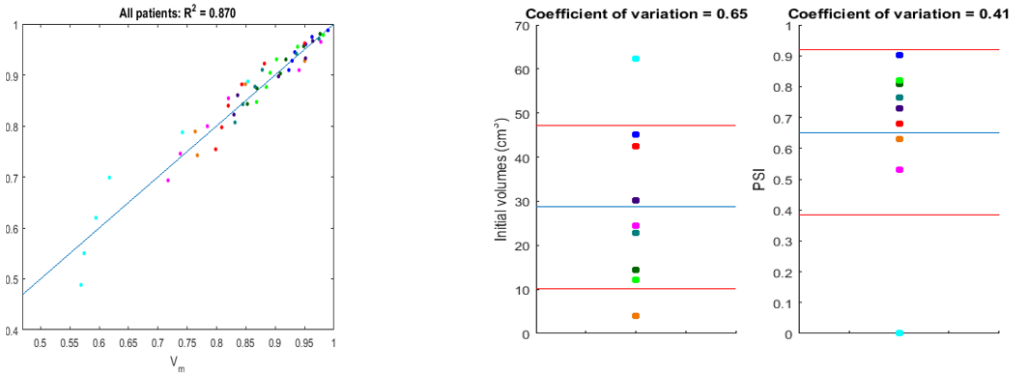

(a) (b)

Figure 2.12: **a)** Comparison between the measured tumour volumes in the data, V_m, and the model predicted values, V_p, for logistic fits to dataset DS2. We calculate the coefficient of determination, R^2, as defined by Equation (2.6). **b)** Variation in initial tumour volumes and fitted PSI values for each patient.

PSI as a prognostic indicator, we perform a leave-one-out study on the same dataset of 9 OPX patients (DS2).

Taking each patient in turn, we use the EBO algorithm to first fit the model to a training dataset comprising the remaining 8 patients, thus estimating the global model parameters, λ and γ. We then estimate a patient-specific PSI_i value for that patient using just the first two data points at the start of treatment whilst holding the global model parameters fixed. We use the estimated parameters to simulate the subsequent response for the remainder of the fractionation schedule and classify the predicted response. The results of this study are shown in Figure 2.13.

Radiotherapy for HPV positive oropharyngeal squamous cell cancer (OPX) provides three-year locoregional control rates of 75-95%. Given the excellent cancer control outcomes for OPX following radiotherapy, there is significant interest in reducing therapy intensity, such as adaptive radiotherapy (ART) for rapidly shrinking tumour volumes to improve organs-at-risk sparing [51, 52].

For these purposes we consider patients as potential candidates for ART if greater than a 15% reduction in gross tumour volume (GTV) is predicted after 3 weeks of treatment, which we take as our quantity of interest in this case. Of the 9 patients in our cohort, 4 exhibit a greater than 15% GTV reduction after 3 weeks of treatment. We use the binary classification measures defined in Equations (2.7)-(2.9) to determine the performance of the model for this purpose. We see that the PSI model is able to classify patients as either candidates for ART or not with good accuracy (0.78) in this case, although recall is low (0.5). We note the lack of false positives which would have erroneously suggested dose de-escalation.

However, interpretation of these results should be considered in light of the results of the synthetic data study presented in Section 2.3.2. Even when the data originates from the same model, a lack of data points for parameter estimation may result in large variation in the posterior predictions. As such, this study would require a much larger dataset for further investigation.

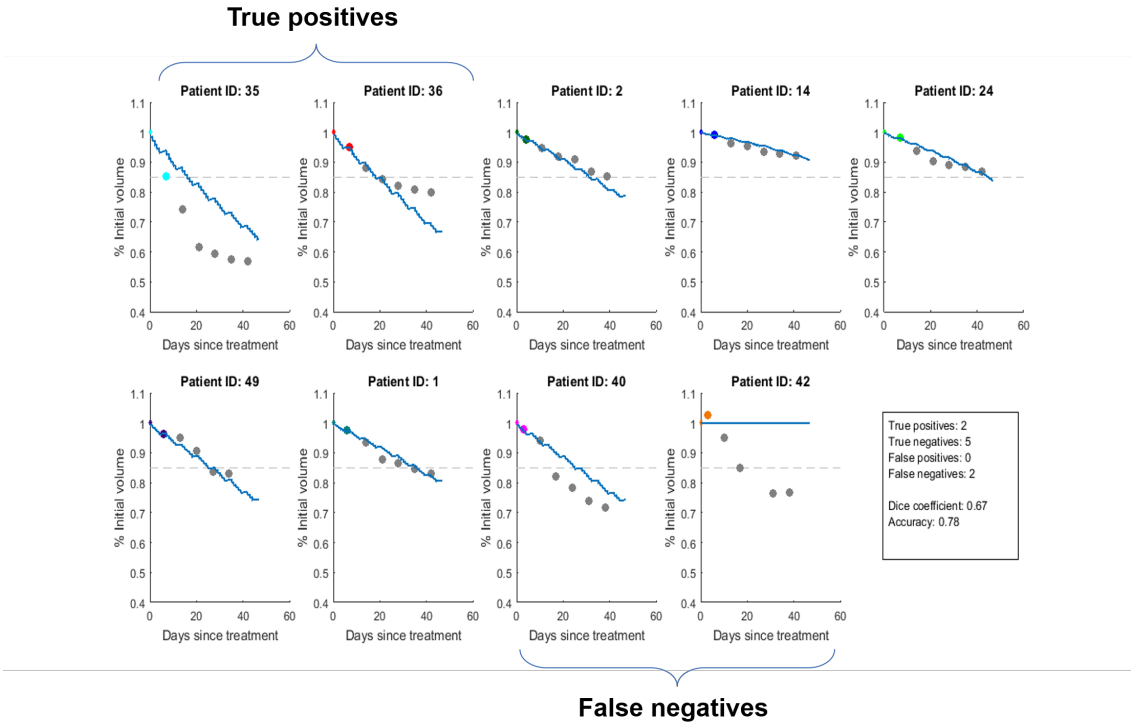

Figure 2.13: Results of a leave-one-out study. Global growth and death rates, λ and γ respectively, are fitted using 8 of the 9 patients, with the patient-specific PSI estimated based upon fitting to the first two data points (shown in colour) of the remaining patient. We use the model to determine whether the remaining patient in each case is a prospective candidate for ART ($>$ 15% GTV reduction after 3 weeks).

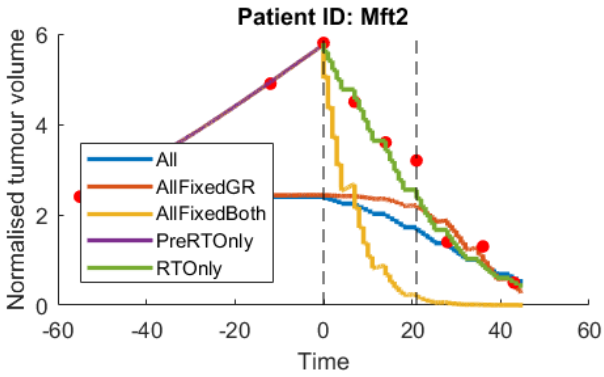

Figure 2.14: Example of a single patient and the best fits of the PSI model to a selection of patients using various parts of the dataset DS3 for fitting. Each line colour pertains to a different parameter fitting procedure with respect to the data (described in detail in the main text and summarised in Table 2.3). Vertical dashed lines correspond to the start of radiotherapy ($t = 0$) and after 3 weeks of treatment.

2.4.3 Fitting to an entire patient cohort

Ideally, a proper calibrated and validated model will be able to predict patient-specific radiotherapy response from pre-treatment measurements and/or data points from the early stages of treatment. Indeed, the PSI model has been proposed as a prognostic indicator of response from pre-treatment data [105]. It is therefore instructive to consider the ability of the model to fit to a larger dataset (DS3 in Table 2.1) for which we consider all data points. The larger dataset is more representative of the range and variability of qualitative responses observed *in vivo*. We again use the EBO algorithm to consider a variety of permutations for calibrating both the population-level parameters and those that are patient-specific. An example of the resulting model simulations for the best fit parameter sets in each case is shown in Figure 2.14, with a larger selection shown in Figure 2.15. While the data used for calibrating the model differ, in each case the growth and death rates, λ and γ, are global, while the carrying capacities are patient-specific, resulting in a patient-specific value for the PSI_i at the start of treatment for patient i. A summary of the different methods for fitting the model to the data is listed in Table 2.3.

Separating the pre-treatment and treatment data points (purple and green curves respectively) we see that the model is able to accurately fit each of these stages of the tumour dynamics for most patients. Although we note that the PSI model is unable to capture the 'pseudo-progession' exhibited in the data from patient ID Mft8.

However, when we require a single set of parameters to capture both pre-treatment

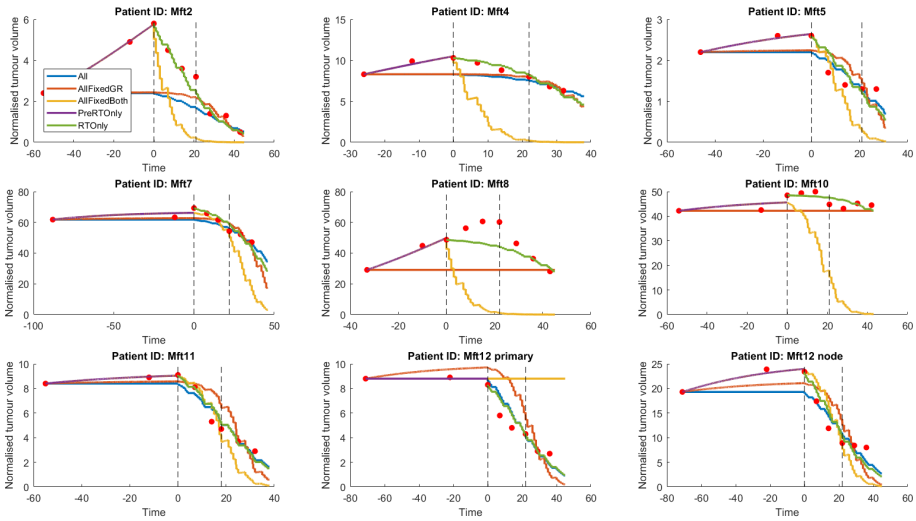

Figure 2.15: Best fits of the PSI model to a selection of patients using various parts of the dataset DS3 for fitting. Each line colour pertains to a different parameter fitting procedure with respect to the data (described in detail in the main text and summarised in Table 2.3). Vertical dashed lines correspond to the start of radiotherapy ($t = 0$) and after 3 weeks of treatment.

Colour	**Calibration method**
Blue	Model parameters fit to all data points
Purple	Model parameters fit to pre-treatment data points only
Green	Model parameters fit to radiotherapy data points only
Yellow	λ and K_i estimated from pre-treatment fit and subsequently held fixed for fit to the whole data set
Red	λ estimated from pre-treatment fit and subsequently held fixed for fit to the whole data set

Table 2.3: Summary of the methods used to calibrate the PSI model to dataset DS3. The colours for each method pertain to the colour of the best fit trajectories shown in Figure 2.15.

growth dynamics and radiotherapy response we see that the model is unable to accurately fit all data points. We may hope that the growth dynamics, and correspondingly the inferred pre-treatment patient-specific PSI, are a prognostic indicator for the following treatment response. As such, we consider using the pre-treatment data points to estimate the growth rate, λ, and PSI_i values. We then fix these values and re-iterate the EBO algorithm on the radiotherapy data points in order to estimate the global death rate parameter, γ. The results of this method of fitting the data are shown by the yellow curves in Figure 2.15. We see that, as expected, we may fit the pre-treatment data well, however the single degree of freedom from fitting the radiation-induced death rate to the radiotherapy data is insufficient to accurately reproduce the treatment responses for each patient.

If we instead relax this methodology slightly and only fix the growth rate, λ, from the pre-treatment data (shown by the red curves in Figure 2.15), we instead observe a poor resulting fit to the pre-treatment growth behaviour. Indeed, when the EBO parameter fitting forces the model to compromise, it favours attempting to fit the greater number of data points from the response data in order to optimise overall fit, as seen from the blue trajectories for which we fit the parameters to the entire dataset from the outset. If the sizes of the pre-treatment and treatment datasets were similar, then we might expect the posterior parameter distributions from fitting to the entire dataset to be bimodal, fitting adequately to each portion of the data but not both simultaneously.

The resulting distributions for the PSI values estimated from each of these data fitting exercises are shown in Figure 2.16. It is evident that the distributions of the estimated PSI values in each case does not remain broadly similar in each case. This suggests that our inference is not robust to the selection of data that we use for parameter fitting, and consequently, that this method may not be an accurate prognostic indicator for radiotherapy response from pre-treatment data. Furthermore, inspection of the individual changes to parameter values in each case does not reveal any correlations between the different estimated values (results not shown). Note that in the cases where the entire dataset is used for parameter fitting we may observe PSI values greater than 1, which would indicate a pre-treatment tumour volume larger than its assumed carrying capacity. This is a result of inadequate fitting of the pre-treatment data for which the simulation

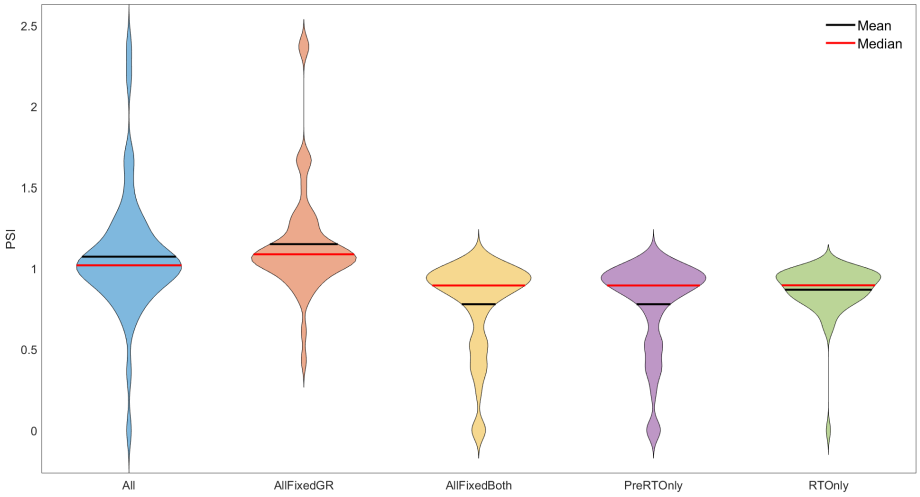

Figure 2.16: Violin plots corresponding to Figure 2.15 showing the distribution of PSI values obtained when using each of the different methods to calibrate the PSI model to dataset DS3.

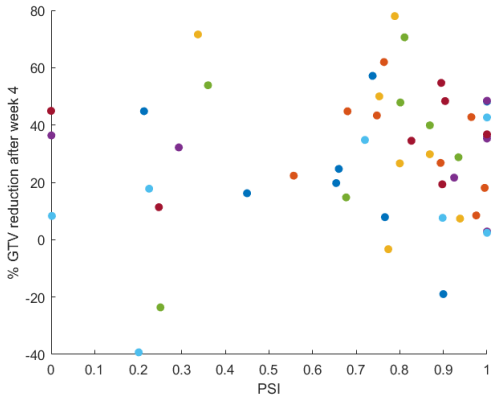

Figure 2.17: Scatter plot showing the lack of discernible correlation between inferred PSI values and the percentage GTV reduction observed in dataset DS3 after 4 weeks of treatment. Each point corresponds to a single patient in the dataset.

pertaining to the 'optimal' parameter set significantly underestimates the pre-treatment growth. Indeed, if we plot a scatter graph of the estimated PSI values from the pre-treatment data alone, we see that this does not obviously correlate with radiotherapy response as defined by gross tumour volume (GTV) reduction after 4 weeks of treatment as we may hope (Figure 2.17).

The inability of the model to simultaneously fit both pre-treatment growth and radiotherapy response suggests that the proposed model incorporates insufficient detail to accurately capture all response dynamics observed *in vivo*. However, while the model does not appear to be a good representation for the entire patient population (DS3), there are

those for whom the model appears to match the data points reasonably well (see Figure 2.15 patients Mft7 and Mft11, for example). If it were possible to stratify patients a priori, then it may be the case that there are subpopulations for which the PSI model provides an adequate description. Future work on this model may consider methods to identify such cohorts.

2.5 Discussion

For a mathematical model to have clinical relevance it should be suitably calibrated and validated with appropriate data and demonstrate sufficient predictive power [125]. Such considerations in the context of predicting patient-specific *in vivo* tumour response to radiotherapy raise a number of questions regarding parameter estimation and the limited data typically available in the clinic. In Section 2.3 we highlighted some of these issues by way of synthetic data studies. In particular we considered the influence of both noise and lack of temporal resolution in clinical datasets on the predictive power of the proposed models, and demonstrate that both issues may have a significant impact on the accuracy of model predictions. The results presented used the same model to generate the synthetic data as being used to fit to the data. In practice, the biological system *in vivo* is significantly more complex than the models proposed for predicting the dynamics. As such, the synthetic studies in Section 2.3 studies presented represent a simplified version of the issues with respect to clinical data.

The issues highlighted in our synthetic data studies motivate the development of simple phenomenological models with few parameters for prognostic use in the clinic. However, any models considered for such purposes should be minimally complex whilst still adequately describing the range of dynamics observed *in vivo*. The investigation of the PSI model [105] using clinical datasets in Section 2.4 showed that the level of detail within the model is insufficient to describe the range of radiotherapy response dynamics observed across the entire patient cohort. We may highlight a few cases of note to further emphasise this. In Figure 2.11, we observed that, while the PSI model may fit to the data reasonably well as given by the R^2 statistic, it may not necessarily represent all of the data well qualitatively. In particular, we see that the plateau in treatment response exhibited

by patient ID 35 is not well described by the model. Similarly, those patients for which the tumour volume initially increases at the start of the radiotherapy protocol, such as patient ID 42 in Figure 2.13 or patient ID Mft8 in Figure 2.15, are also not captured accurately by this model.

Additionally, in considering pre-treatment growth and radiotherapy response data separately, we observe different dynamical behaviour between the two stages and an inability to calibrate to both datasets simultaneously with a single parameter set. The lack of correlation between the parameter sets in each case is suggestive of additional underlying biological processes which influence radiotherapy response and which are not captured by the spatially-averaged descriptions of proliferative activity in current single ODE models. While in this chapter we have considered the performance of just one such model, we anticipate that other ODE models of similar complexity would perform similarly [106].

It is well-known that *in vivo* tumours are highly heterogeneous entities. In particular, the unregulated proliferation common to all cancers typically results in a tumour outgrowing its nutrient supply, resulting in regions of hypoxia and necrosis within the tumour. Furthermore, irradiation causes widespread cell death throughout the tumour and is likely to be a significant change to tumour composition. We hypothesise that the tumour composition affects the growth dynamics and thus the response dynamics and subsequent regrowth of the tumour are also likely to be affected by intratumoural heterogeneity. As such, we might anticipate that tumour regrowth dynamics may differ from those prior to irradiation and that the effects of radiation-induced cell death may not be confined to just the instantaneous volume loss commonly modelled using the linear-quadratic model. We are thus motivated to consider models which incorporate descriptions of heterogeneity in tumour composition. In Chapters 3-5 we develop spatial models of tumour growth and radiotherapy response of increasing complexity in order to gain mechanistic insight into the influences of heterogeneity in tumour composition on the observed response dynamics. Such insight may then be used to guide the development of simpler compartmental models that may more adequately describe the clinical data.

Chapter 3

A simple spatial model for *in vitro* tumour spheroids

3.1 Introduction

In vivo tumours are well-known to be highly heterogeneous in spatial composition. In particular, as a tumour grows, inadequate oxygen supply due to insufficent vascularisation can often result in regions of hypoxia and necrosis within the tumour. Moreover, it is well established that the local oxygen tension plays an important role in radiation-induced cell death, with hypoxic tumour regions responding poorly to irradiation [26, 37, 144]. Such heterogeneity is likely to influence radiation response and result in dynamics which may not be adequately captured by the simple, spatially-averaged models considered in Chapter 2.

Due to the difficulties of studying tumours *in vivo*, such effects are often investigated experimentally using *in vitro* multicellular tumour spheroids. Tumour spheroids represent a controlled environment of intermediate complexity between 2D culture media and *in vivo* models in which important insight can be gained about the tumour micro-environment and the effect of therapies on a growing tumour [13, 15, 16, 97, 145]. In a similar manner, it is natural to develop mathematical models for avascular tumour spheroids before considering the more complex case of *in vivo* tumour growth. Tumour spheroids have a well-defined structure, providing a simple geometry which may be exploited to develop spatially-

resolved mathematical models.

One of the simplest spatially-resolved models of avascular tumour growth was proposed by Greenspan [63]. In this model, under the assumption of spherical symmetry, the outer tumour radius evolves in response to a single diffusible, growth-rate limiting nutrient, commonly taken to be oxygen. Internal free boundaries, decomposing the tumour spheroid into a central necrotic core, an outer proliferating rim and an intermediate hypoxic annulus, are identified as contours of the oxygen profile across the tumour, reproducing the structure typically observed *in vitro*.

In this chapter we present a simple spatially-resolved model for tumour spheroid growth and response to radiotherapy in order to investigate the effects of spatial heterogeneity. We develop the new model in Section 3.2, extending Greenspan's original spatial model for tumour spheroid growth to include radiation effects. In Section 3.3 we numerically solve the model equations and discuss key features of the resulting dynamics. We present further numerical simulations and model analysis in order to understand the tumour dynamics exhibited by the model. We analyse some key tumour regrowth dynamics post-irradiation in Section 3.4.2. In Section 3.5 we consider the long-term behaviour of tumour spheroids for different fractionation schedules, identifying a tumour-specific relationship between inter-fraction time and dose per fraction to achieve cure. Finally, in Section 3.6 we isolate the influence of tumour composition on the tumour response dynamics.

The work presented in Sections 3.2, 3.3, 3.4.1 and 3.5 has been published in:

Lewin, Thomas D., Philip K. Maini, Eduardo G. Moros, Heiko Enderling, and Helen M. Byrne. 'The evolution of tumour composition during fractionated radiotherapy: implications for outcome.' *Bulletin of Mathematical Biology* 80, no. 5 (2018): 1207-1235.

3.2 Model development

In this section, we introduce a spatial model of avascular tumour growth originally presented in [63]. Although many spatially-resolved models that account for tumour growth and hypoxia have been proposed, a significant portion of these are based upon Greenspan's

original work, and it remains a simple, yet useful starting point for investigating the effect of hypoxia on tumour responses to radiotherapy. Accordingly, in this chapter we extend Greenspan's model to account for the effects of radiation and arrive at a new model for tumour response to radiotherapy.

3.2.1 Summary of Greenspan's original model

We consider the growth of a radially-symmetric, avascular tumour spheroid in response to a single, growth-rate limiting, diffusible nutrient, here oxygen. Following [63], we assume that growth inhibition is caused by nutrient deficiency rather than a tumour-derived inhibitory factor. We denote the outer tumour radius by $R(t)$ and the oxygen concentration at a distance $0 \leq r \leq R(t)$ from the tumour centre by $c(r,t)$. We suppose that the oxygen concentration is maintained at a constant level, c_∞, on $r = R(t)$. Oxygen diffuses on a much shorter timescale than tumour growth, taking ~ 10 seconds to diffuse 100 μm by comparison with a tumour growth period measured in days [63]. As such we assume that the oxygen concentration is in a quasi-steady state. Internal free boundaries at $r = R_H(t)$ and $r = R_N(t)$ are defined implicitly and denote contours on which the oxygen concentration attains the threshold values c_H and c_N, respectively. These interfaces decompose a well-developed tumour into a central necrotic core ($0 < r < R_N$) where $c \leq c_N$, and an outer, oxygen-rich region ($R_H < r < R$) in which $c_H < c$, these regions being separated by a hypoxic annulus ($R_N < r < R_H$) in which $c_N < c < c_H$ (see Figure 3.1 for a schematic).

Greenspan's original model [63] describes how the dependent variables $c(r,t)$, $R(t)$, $R_H(t)$ and $R_N(t)$ evolve over time and can be written in dimensionless form as follows:

$$0 = \underbrace{\frac{1}{r^2}\frac{\partial}{\partial r}\left(r^2\frac{\partial c}{\partial r}\right)}_{\text{diffusion term}} - \underbrace{\Gamma H(c - c_N)}_{\text{oxygen consumption}}, \tag{3.1}$$

$$\underbrace{\frac{1}{4\pi}\frac{d}{dt}\left(\frac{4\pi R^3}{3}\right)}_{\text{rate of change of tumour volume}} = \int_0^R [\underbrace{cH(c - c_H)}_{\text{cell proliferation term}} - \underbrace{\lambda_A - \lambda_N H(c_N - c)}_{\text{cell death term}}]r^2 dr, \tag{3.2}$$

$$R_H = 0 \quad \text{if} \quad c > c_H \, \forall r \quad \text{and otherwise} \quad c(R_H, t) = c_H, \tag{3.3}$$

$$R_N = 0 \quad \text{if} \quad c > c_N \, \forall r \quad \text{and otherwise} \quad c(R_N, t) = c_N, \tag{3.4}$$

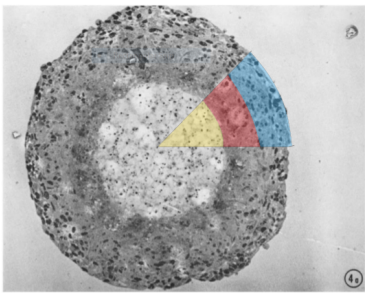

(a) Image of an *in vitro* tumour spheroid highlighting the distinct micro-environments. (adapted from ©1973 Folkman and Hochberg. Journal of Experimental Medicine. 138:745-753; DOI: 10.1084/jem.138.4.745)

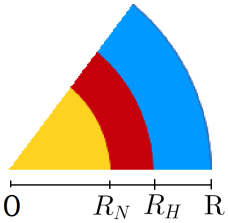

(b) Schematic of the corresponding model tumour spheroid geometry.

Figure 3.1: Diagrams highlighting the distinct regions within a tumour spheroid and how they are influenced by the oxygen profile. A central necrotic core ($0 < r < R_N$) is surrounded by a hypoxic annulus ($R_N < r < R_H$) and an outer proliferating rim ($R_H < r < R$). The moving boundaries $r = R_N(t)$, $R_H(t)$ and $R(t)$ delineate these regions.

$$\frac{\partial c}{\partial r} = 0 \quad \text{at } r = 0, \tag{3.5}$$

$$c = c_\infty \quad \text{at } r = R, \tag{3.6}$$

$$R(0) = R_0, \tag{3.7}$$

where $H(.)$ is the Heaviside function ($H(x) = 1$ for $x > 0$, and $H(x) = 0$ otherwise), and Γ, λ_A, λ_N, c_∞, c_H & c_N are positive constants, with Γ, λ_A & λ_N corresponding to rates of oxygen consumption, apoptosis and necrosis, respectively. Equations (3.1)-(3.7) may be reduced to a system involving a single ODE for $R(t)$ and algebraic equations for $R_H(t)$ and $R_N(t)$. Analysis of the resulting equations and details of the non-dimensionalisation may be found in [63, 146], and for further explanation of the underlying model assumptions see Appendix A.1. Figure 3.2 shows how the size and composition of the tumour spheroid evolve for a typical simulation of the Greenspan model using the dimensionless parameter values in Table 3.1. A table of dimensional parameter values is given in Appendix A.1. Where possible, parameter estimates are taken from the literature, however we note that some values pertain to estimates used in other modelling scenarios. In this chapter, specific parameter combinations serve only to highlight the dynamics of the model and, in particular, the resulting model analysis is independent of the choice of parameter values. The influence of some of the parameters on the growth dynamics and steady state tumour

Parameter	Symbol	Value	Source
Oxygen consumption rate	Γ	1.1051	[70]
Oxygen concentration at tumour boundary	c_∞	1	[70]
Hypoxic oxygen threshold	c_H	0.1	[70]
Anoxic oxygen threshold	c_N	0.008	[70]
Apoptosis constant	λ_A	0.32	[147]
Necrosis constant	λ_N	0.0061	[148]

Table 3.1: Dimensionless parameter values for tumour spheroid growth model.

composition are explored in Appendix A.2.

3.2.2 Incorporating radiotherapy into the Greenspan model

We adapt Greenspan's model to account for radiotherapy by assuming that when a dose of radiotherapy is applied it causes an instantaneous dose-dependent death of viable cancer cells and, thus, a change in the size and composition of the tumour. The efficacy of the radiation and subsequent cell death depends on the local oxygen concentration. As such, we determine the radiation-induced cell death in each tumour region separately. We denote by $R^{\pm}$, $R_H^{\pm}$ and $R_N^{\pm}$ the radii immediately before (-) and after (+) radiotherapy in the proliferating, hypoxic and necrotic tumour compartments.

Radiation-induced cell death and the Linear-Quadratic model

We use the linear-quadratic model [2, 95, 144] to account for cell kill due to radiotherapy in the well-oxygenated outer rim, $R_H < r < R$, so that the volume survival fraction, $sf(d)$, immediately after a dose d of radiation is given by

$$\begin{aligned} sf_{normoxic} &= \frac{\text{[volume of normoxic region after radiotherapy]}}{\text{[volume of normoxic region before radiotherapy]}} \\ &= exp(-\alpha d - \beta d^2), \end{aligned} \tag{3.8}$$

for radiosensitivity parameters α and β. Values of α/β vary markedly, with typical values falling in the range of 3-10 Gy. However extremal values of 1 Gy and 20 Gy have been reported for late-responding tissues such as prostate cancer and early-responding,

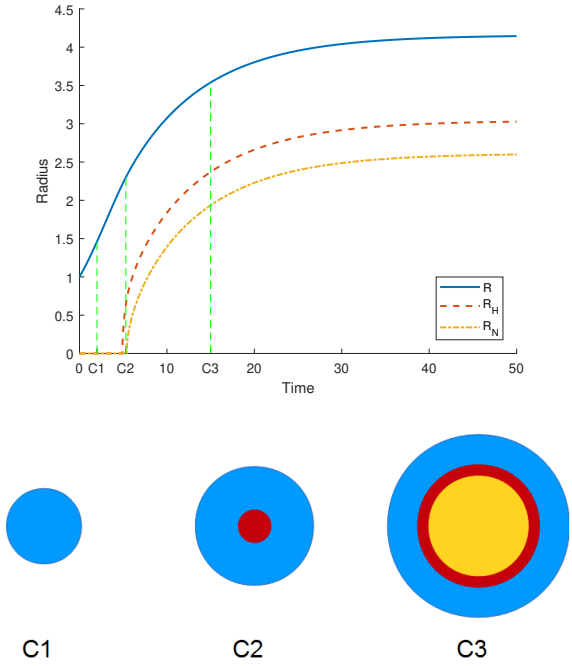

Figure 3.2: Results from a typical simulation of Equations (3.1)-(3.7) showing how the size and composition of the tumour spheroid change over time (parameter values in Table 3.1). Key: blue solid line - proliferating cells, red dashed line - hypoxic region, yellow dot/dashed line - necrotic core. The schematics represent the tumour compositions C1-C3 as the spheroid progresses through different stages of growth.

Parameter	**Value**	**Source**
α (Gy^{-1})	0.35	[2, 27, 56]
α/β (Gy)	10	[44]
OER (dimensionless)	3	[97]

Table 3.2: Typical radiosensitivity parameters

rapidly proliferating tissues such as head and neck cancer, respectively [44]. Typical radiosensitivity parameters for rapidly-proliferating, early-responding tumours are shown in Table 3.2.

When exposed to ionising radiation, the potent oxygen free radicals that form in well-oxygenated regions increase the amount of DNA damage by up to a factor of 3 when compared with hypoxic tumour regions [37]. Following Carlson *et al.* [97], we incorporate the oxygen enhancement ratio, OER, to account for this effect. Radiosensitivity parameters are typically quoted for normoxic conditions. As such we take the common approach and use the OER as a constant factor (taken to be equal to 3 in the presented simulations) that reduces the intrinsic radiosensitivity parameters of tumour cells, α and β, in hypoxic

regions. This creates a discontinuity in the response to radiotherapy at $r = R_H$. The volume survival fraction immediately after a dose of radiation is delivered to a population of hypoxic cells is given by

$$\begin{aligned} sf_{hypoxic} &= \frac{[\text{volume of hypoxic region after radiotherapy}]}{[\text{volume of hypoxic region before radiotherapy}]} \\ &= exp\left(-\frac{\alpha}{OER}d - \frac{\beta}{OER^2}d^2\right). \end{aligned} \tag{3.9}$$

There is no consensus in the literature about how to modify the 'quadratic' component of cell death, however the form used in Equation (3.9) affords the interpretation of the OER as the multiplying factor for the dose escalation required under hypoxia in order to achieve the same cell kill as under normoxic conditions. We note that, in practice, this effect is likely to depend continuously on the local oxygen concentration. A continuous functional form for the OER ($OER = OER(c)$) was proposed in [37]. For realistic parameter regimes, simulations using the continuous OER presented in [37] and the discrete OER presented here did not significantly vary. For these reasons we restrict attention to the discrete OER stated above. A more detailed comparison is presented in Appendix B.1.

We assume further that dead material within the necrotic core is unaffected by radiation and so we impose that $R_N^+ = R_N^-$.

Combining these assumptions we deduce that, for a well-developed tumour spheroid (Figure 3.2, case C3) with $0 < R_N^- < R_H^- < R^-$, a dose d of radiation gives a total volume change of

$$\begin{aligned} [V]_-^+ &= \underbrace{\frac{4\pi}{3}(R^{+^3} - R_N^{+^3})}_{\text{viable volume after radiotherapy}} - \underbrace{\frac{4\pi}{3}(R^{-^3} - R_N^{-^3})}_{\text{viable volume before radiotherapy}} \\ &= \underbrace{-\frac{4\pi}{3}(R^{-^3} - R_H^{-^3})(1 - sf_{normoxic})}_{\text{loss from proliferating rim}} \underbrace{-\frac{4\pi}{3}(R_H^{-^3} - R_N^{-^3})(1 - sf_{hypoxic})}_{\text{loss from hypoxic region}}, \end{aligned}$$

which, on rearrangement, yields the following expression for R^+ in terms of R^-, R_H^-, and $R_N^- = R_N^+ = R_N$:

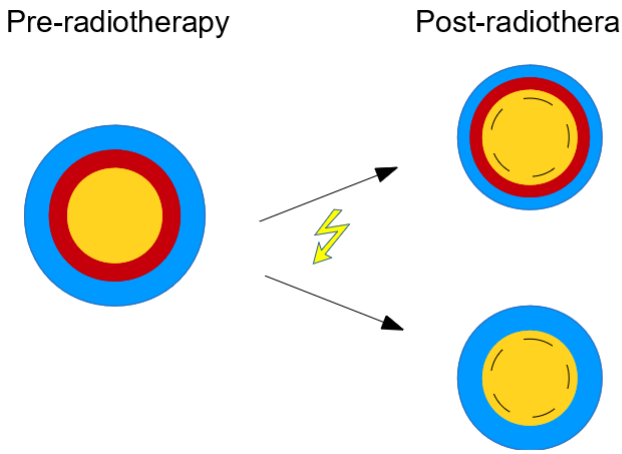

Figure 3.3: Schematic of the model tumour spheroid post-radiotherapy. Dashed line represents new position of the internal contour $c = c_N$ and shows the resulting mismatch between this contour and R_N.

$$R^{+^3} = \left(R^{-^3} - R_H^{-^3}\right) sf_{normoxic} + \left(R_H^{-^3} - R_N^3\right) sf_{hypoxic} + R_N^3. \tag{3.10}$$

The oxygen concentration profile associated with the new tumour structure can be determined (Equation (3.1)) and R_H defined implicitly as before (see Equation (3.3)). We note that while not all hypoxic tumour cells will be killed from a single radiotherapy fraction ($sf_{hypoxic} > 0$), the instantaneous volume loss due to irradiation and the subsequent reoxygenation of the tumour spheroid may result in a post-radiotherapy tumour composition without a hypoxic region.

Two cases can arise when a well-developed, 3-layer tumour is irradiated (see Figure 3.3):

(i) $c_N < c(R_N^+) < c_H$ - irradiated tumour is a fully-developed tumour spheroid with 3 layers;

(ii) $c_N < c_H < c(R_N^+)$ - irradiated tumour has a necrotic core, but no hypoxic annulus.

Since the necrotic core is assumed to be unaffected by radiotherapy, these are the only possible options. We have already described how a tumour spheroid of case (i) responds to radiation (Equation (3.10)). If a tumour with a pre-radiotherapy composition as in case (ii) is irradiated then the corresponding volume change is given by

$$[V]_{-}^{+} = -\frac{4\pi}{3}(R^{-^3} - R_N^3)(1 - sf_{normoxic}),$$

which, on rearrangement, supplies the following expression for R^+ in terms of R^- and R_N

$$R^{+^3} = \left(R^{-^3} - R_N^3\right) sf_{normoxic} + R_N^3. \tag{3.11}$$

Reconciling pre- and post-radiation tumour growth

In the normal growth regime without radiotherapy, R_N is defined implicitly by the oxygen concentration (see Equation (3.4)). When the tumour volume is reduced due to radiation, the oxygen concentration at the centre of the tumour increases and the location of the interface on which $c = c_N$ will shift towards the tumour centre or disappear. As the necrotic core is unaffected by radiation, $c(R_N^+) > c_N$ and the growth of the tumour spheroid immediately post-radiotherapy does not follow the original dynamics in the absence of treatment.

Between fractions of radiotherapy, repopulation of the tumour occurs. The tumour cells proliferate and die as before, however, whilst $c(R_N) > c_N$ no new material is added to the necrotic core, and so the existing necrotic material simply decays at the rate $\lambda_A + \lambda_N$, since apoptotic cell death is assumed to occur throughout the spheroid with additional necrotic cell death localised to the necrotic core. In this case R_N evolves according to

$$R_N = R_N(t_{fraction}) exp\left(-\frac{1}{3}(\lambda_A + \lambda_N)(t - t_{fraction})\right), \tag{3.12}$$

where $t_{fraction}$ is the time of the last fraction delivered for which $c(R_N) = c_N$, and $R_N(t_{fraction})$ is the radius of the necrotic core upon irradiation. As such, prior to treatment with radiotherapy at $t = t_{fraction}$ the tumour composition is consistent with the Greenspan growth dynamics, while Equation (3.12) governs the evolution of R_N post-irradiation.

Equations (3.1)-(3.3), (3.5)-(3.7) and (3.12) drive growth while $c(R_N) > c_N$, until the necrotic radius is such that $c(R_N) = c_N$, at which time the standard Greenspan model holds and growth is driven by Equations (3.1)-(3.7).

3.2.3 Summary: statement of full model (dimensionless)

The tumour growth model combined with fractionated radiotherapy (dose d_i Gy delivered at times $t = t_i$, $i = 1, 2, ...$) can be summarised as follows:

$$0 = \frac{1}{r^2}\frac{\partial}{\partial r}\left(r^2\frac{\partial c}{\partial r}\right) - \Gamma H(c - c_N), \tag{3.13}$$

$$\frac{1}{4\pi}\frac{d}{dt}\left(\frac{4\pi R^3}{3}\right) = \int_0^R [cH(r - R_H) - \lambda_A - \lambda_N H(R_N - r)]r^2 dr, \tag{3.14}$$

$$R_H = R_N \quad \text{if} \quad c > c_H \,\forall r \quad \text{and otherwise} \quad c(R_H, t) = c_H, \tag{3.15}$$

$$\begin{aligned} R_N = R_N(t_i) exp\left(-\frac{1}{3}(\lambda_A + \lambda_N)(t - t_i)\right) \quad \text{if } c(R_N) > c_N \text{ and } t_i < t < t_{i+1}, \\ R_N = 0 \quad \text{if} \quad c > c_N \,\forall r \text{ and } t < t_i \,\forall i, \quad c(R_N, t) = c_N \quad \text{otherwise} \end{aligned} \tag{3.16}$$

$$\frac{\partial c}{\partial r} = 0 \quad \text{at } r = 0, \tag{3.17}$$

$$c = c_\infty \quad \text{at } r = R, \tag{3.18}$$

$$R(0) = R_0. \tag{3.19}$$

Continuity conditions for c and $\frac{\partial c}{\partial r}$ continuous across $r = R_H, R_N$ are imposed.

Radiotherapy, of dose d_i applied at times $t = t_i$, effects an instantaneous volume change [1]. The survival fraction of the normoxic tumour cell population is given by

$$sf_{normoxic} = exp(-\alpha d_i - \beta d_i^2), \tag{3.20}$$

whilst the survival fraction in hypoxic regions is given by

$$sf_{hypoxic} = exp\left(-\frac{\alpha}{OER}d_i - \frac{\beta}{OER^2}d_i^2\right). \tag{3.21}$$

The necrotic core of the tumour spheroid is unaffected by radiotherapy. Immediately after a dose of radiation, the outer tumour radius is given by

[1] We note that while the model equations presented here are dimensionless, the timescale we use is days and as such we interchangeably refer to time t and days/weeks of a fractionation protocol for ease of description and without loss of generality.

$$R^{+^3} = \left(R^{-^3} - R_H^{-^3}\right) sf_{normoxic} + \left(R_H^{-^3} - R_N^3\right) sf_{hypoxic} + R_N^3. \tag{3.22}$$

NB: We subtly alter the equation for R_H from the original Greenspan model so that $R_H = R_N$ if the threshold for hypoxia, c_H, is not reached. This does not change the dynamics in the case of untreated tumour growth, but ensures that the ordering of the tumour boundaries is conserved in the post-radiotherapy regime ($0 \leq R_N \leq R_H \leq R$).

3.3 Investigation of model behaviour

In this section we solve the model numerically and highlight key features of the simulations for different parameter combinations. We explore these features in more detail in the following sections.

For each tumour growth regime, the oxygen profile $c(r, t)$ may be solved analytically. Equations (3.13)-(3.22) may then be reduced to an ODE for R and two algebraic equations for R_H and R_N, as described in Appendix A.1. We solve the resulting system of equations numerically using a finite difference scheme implemented in MATLAB.

In Figure 3.4a we present results showing a typical tumour response to a conventional fractionation schedule (2 Gy, 5 days / week) simulated for 6 weeks using the parameter values in Tables 3.1 and 3.2. Cell death induced by the first fraction of radiation delivered at $t = 1$ results in the loss of the hypoxic annulus. While $c(R_N) > c_N$, the necrotic core decays exponentially, as defined by Equation (3.12). Figure 3.5a shows how the oxygen concentration in the necrotic core evolves throughout the first week of the radiotherapy protocol. We see the mismatch between $c(R_N)$ and c_N following delivery of the first fraction (at $t = 1$). As the tumour grows between fractions, oxygen concentration in the necrotic core decreases, while each fraction of radiation and the corresponding volume loss results in reoxygenation.

For this parameter combination, radiotherapy results in a tumour volume at the end of treatment that is sufficiently small such that the spheroid is almost entirely composed of proliferative cells. In particular, the necrotic core has decayed so that $R_N \ll R$.

Figure 3.4b shows how the system dynamics change when a tumour with a much lower apoptotic rate (λ_A) is exposed to the standard fractionation protocol. The slower rate of

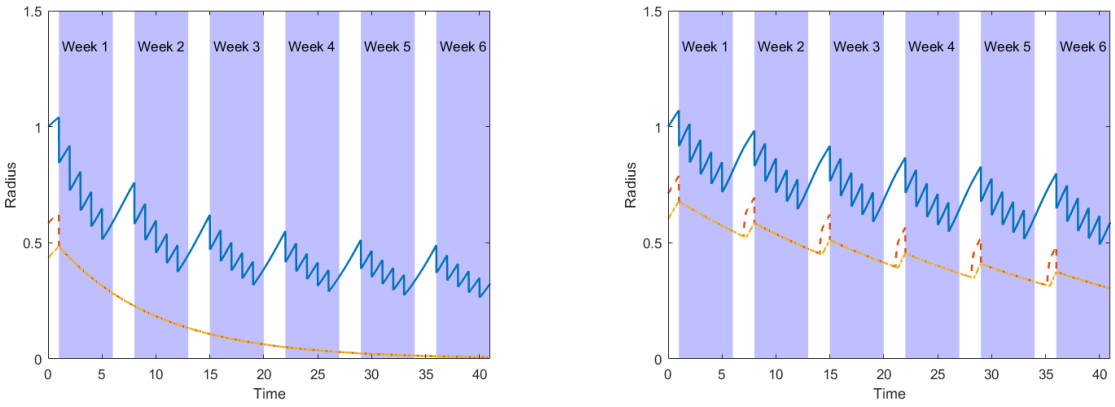

(a) (b)

Figure 3.4: Two solution of Equations (3.13)-(3.22) in response to a standard fractionation protocol (2 Gy fractions delivered daily Monday-Friday) simulated for 6 weeks. Overall tumour radius, R - blue solid line; hypoxic radius, R_H - red dashed line; radius of the necrotic core, R_N - yellow dot/dashed line. In (a) we use the parameter values given in Tables 3.1 & 3.2 with an initial tumour radius of 3. In (b) we simulate irradiating a tumour spheroid with lower rates of apoptosis ($\lambda_A = 0.1213$) and oxygen consumption ($\Gamma = 0.3032$). The evolution of the tumour contours R, R_H and R_N is shown by the blue, red and yellow lines, respectively.

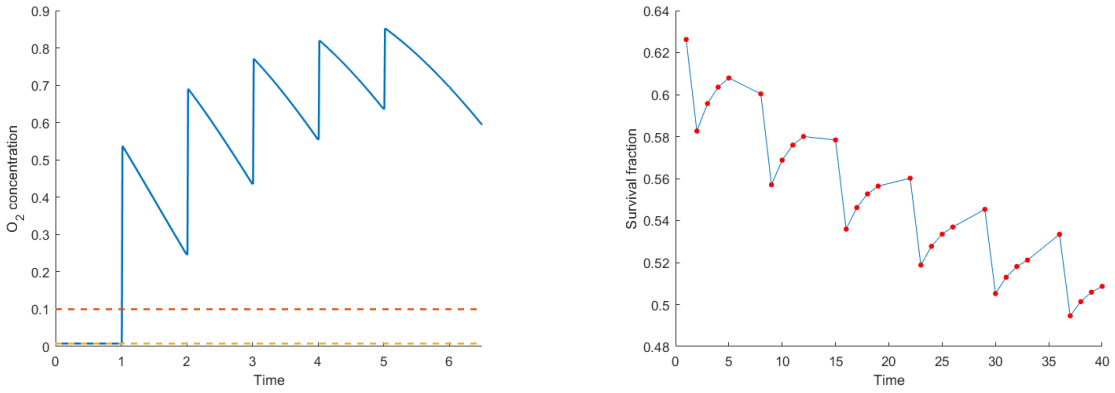

(a) (b)

Figure 3.5: Two plots highlighting key behaviours in the simulations shown in Figure 3.4. (a) Blue line shows oxygen concentration within the necrotic core during the first week of treatment for the simulation in Figure 3.4a. The oxygen thresholds for hypoxia, c_H, and necrosis, c_N, are shown by dashed red and yellow lines, respectively. (b) Change in average tumour survival fraction following successive doses of radiotherapy corresponding to the simulation presented in Figure 3.4b. Red points correspond to the survival fraction for each fraction of radiotherapy delivered, blue line added for ease of visualisation. (NB. y-axis not [0,1])

apoptosis results in a larger steady state tumour in the absence of radiotherapy. Similarly, a larger tumour volume is supported throughout treatment and a more gradual volume reduction is observed. In this case the hypoxic annulus reappears during treatment (as observed during the weekend breaks in the protocol) since the necrotic core decays such that $c(R_N) = c_H$ before the end of the fractionation protocol. A rapid transient increase in R_H is observed when the hypoxic annulus reappears. We characterize this behaviour in Section 3.4.1 where we show that R_H increases like $\sqrt{t}$ on this short timescale.

For the simulation in Figure 3.4b, a tumour spheroid comprising a necrotic core and transient hypoxia persists at the end of treatment. The tumour volume appears to be evolving towards a periodic orbit and, as such, the model predicts that continuing the same fractionation schedule indefinitely will not yield significant further volume reduction.

Since the tumour composition changes dynamically throughout treatment, the efficacy of each radiation fraction also varies. The survival fraction changes by about 10% from the start to the end of treatment due to the shrinkage of the necrotic core (Figure 3.4b). In this case a characteristic shape within the curve in Figure 3.5b repeated weekly due to the weekly oscillations in tumour composition, with the spike associated with the rapid reappearance of hypoxia. Such dynamic behaviour clearly depends on tumour-specific parameters and highlights the additional details that can be observed when spatial effects are included in a mathematical model (c.f. difference in tumour composition between Figures 3.4a & 3.4b).

3.4 Post-irradiation tumour dynamics

Our simulation results reveal interesting post-radiotherapy dynamics which we characterise in this section. In particular we notice a fast, transient increase in R_H on the re-emergence of hypoxia following radiotherapy. Since hypoxic cells are less radiosensitive, such a rapid increase in the hypoxic volume could have implications for the efficacy of further fractions of radiation. We characterise this behaviour in Section 3.4.1. In Section 3.4.2 we identify scenarios in which the tumour volume may continue to decrease after irradiation.

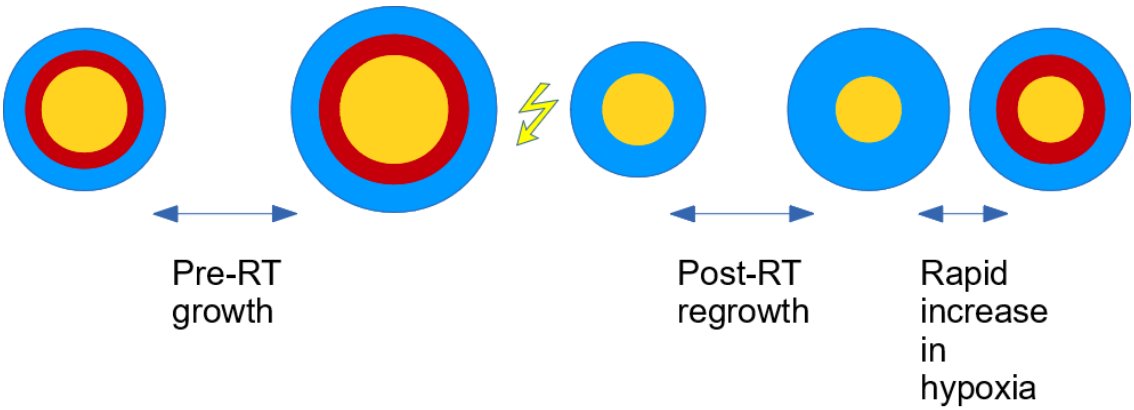

Figure 3.6: Schematic contextualising the scenario in which the rapid transient increase in hypoxia is observed, corresponding to the different growth phases observed in Figure 3.7.

3.4.1 Rapid transient increase in R_H upon regrowth

When a fully-developed tumour spheroid including a hypoxic annulus and necrotic core is exposed to fractionated radiation, the composition of the spheroid immediately after irradiation depends on the dose d, as described in Section 3.2.2. If the dose is sufficiently large, then the post-radiotherapy composition comprises a proliferating rim and a necrotic core, but with the absence of a region of hypoxia. In this scenario, the oxygen concentration in the necrotic core is greater than the threshold for hypoxia (i.e. $c(R_N) > c_H$). Upon regrowth, the outer tumour radius, R, will increase, while R_N will decrease as the necrotic core undergoes decay. Since this parameter regime yields tumour spheroids with proliferating, hypoxic and necrotic compartments prior to radiotherapy, left untreated the tumour will eventually evolve so that the hypoxic annulus will start to re-develop (when $c(R_N) = c_H$). This sequence of events is summarised in Figure 3.6. Simulation results reveal the re-emergence of hypoxia following radiotherapy via a fast, transient increase in R_H (see Figure 3.4b). Since hypoxic cells are less radio-sensitive, such a rapid increase in the hypoxic volume could have implications for the response to further doses of radiation. We now characterise this behaviour.

The fast initial increase in R_H upon regrowth of the tumour spheroid in the Greenspan model after a radiation fraction (see Figure 3.7) occurs when the necrotic core is undergoing exponential decay and a region of hypoxia is about to develop outside the necrotic core. We analyse this situation by supposing that (without loss of generality at $t = 0$) $c(R_N) = c_H$. Then solution of Equations (3.13), (3.17) and (3.18) yields

$$c = \begin{cases} c_\infty + \frac{\Gamma}{6}(R_N^2 - R^2) + \frac{\Gamma}{3}R_N^3(\frac{1}{R_N} - \frac{1}{R}), & \text{for} \quad 0 < r < R_N, \\ c_\infty + \frac{\Gamma}{6}(r^2 - R^2) + \frac{\Gamma}{3}R_N^3(\frac{1}{r} - \frac{1}{R}), & \text{for} \quad R_N < r < R, \end{cases} \tag{3.23}$$

while Equation (3.14) reduces to give

$$\frac{dR}{dt} = \frac{R}{3}\left[c_\infty(1 - \frac{R_H^3}{R^3}) - (\lambda_A + \lambda_N\frac{R_N^3}{R^3})\right] + \frac{\Gamma}{6}R^3\left[\frac{1}{5}(1 - \frac{R_H^5}{R^5}) - \frac{1}{3}(1 - \frac{R_H^3}{R^3}) + 2\frac{R_N^3}{R^3}(\frac{1}{6} - \frac{1}{2}\frac{R_H^2}{R^2} + \frac{1}{3}\frac{R_H^3}{R^3})\right], \tag{3.24}$$

and the internal free boundaries $R_H(t)$ and $R_N(t)$ satisfy

$$\left(1 - \frac{R_H}{R}\right)\left(\frac{R^2}{R_H^2} + \frac{R}{R_H} - 2\frac{R_N^3}{R_H^3}\right) = \frac{6}{\Gamma R_H^2}(c_\infty - c_H), \tag{3.25}$$

$$R_N = R_N(0)e^{-\frac{1}{3}(\lambda_A + \lambda_N)t}, \tag{3.26}$$

with $R_H(0) = R_N(0)$, and $R(0)$ defined by Equation (3.25).

With $R_N(t)$ defined by Equation (3.26), we seek approximate solutions for R and R_H. Differentiating Equation (3.25) with respect to t we obtain an ODE for $R_H(t)$, which is singular in the limit as $R_H \to R_N$:

$$\frac{2}{R_H^2}(R_H^3 - R_N^3)\frac{dR_H}{dt} = (\frac{R_H^2}{R^2} - 2\frac{R_N^3}{R^3} + 2)R\frac{dR}{dt} + 2(\lambda_A + \lambda_N)(R - R_H)\frac{R_N^3}{RR_H}. \tag{3.27}$$

We investigate the behaviour in this limit by making the change of variables $S = \frac{R_H}{R_N}$ with $S = 1$ at $t = 0$. Then Equations (3.24) and (3.27) become

$$\frac{dR}{dt} = \frac{R}{3}\left[c_\infty(1 - S^3\frac{R_N^3}{R^3}) - (\lambda_A + \lambda_N\frac{R_N^3}{R^3})\right] + \frac{\Gamma R^3}{6}\left[\frac{1}{5}(1 - S^5\frac{R_N^5}{R^5}) - \frac{1}{3}(1 - S^3\frac{R_N^3}{R^3}) + 2\frac{R_N^3}{R^3}(\frac{1}{6} - \frac{1}{2}S^2\frac{R_N^2}{R^2} + \frac{1}{3}S^3\frac{R_N^3}{R^3})\right], \tag{3.28}$$

$$\left(S^2\frac{R_N^2}{R^2}-2\frac{R_N^3}{R^3}+2\right)R\frac{dR}{dt}-2\frac{R_N^2}{S^2}(S^3-1)\left[\frac{dS}{dt}-\frac{1}{3}(\lambda_A+\lambda_N)S\right] + 2(\lambda_A+\lambda_N)\left(1-S\frac{R_N}{R}\right)\frac{R_N^2}{S}=0. \quad (3.29)$$

We construct approximate solutions to Equations (3.28) and (3.29) in the limit when S is close to 1. Introducing the small parameter ϵ ($0<\epsilon\ll 1$), we consider the short timescale $t=\epsilon^2\tau$ and propose expansions for S and R in this boundary layer of the form

$$S(\tau)\sim 1+\epsilon S_1(\tau)+\epsilon^2 S_2(\tau)+\mathcal{O}(\epsilon^3), \quad (3.30)$$

and

$$R(\tau)\sim R_0(\tau)+\epsilon R_1(\tau)+\epsilon^2 R_2(\tau)+\mathcal{O}(\epsilon^3). \quad (3.31)$$

The choice of timescale can be justified by a dominant balance argument, allowing us to regularise the ODE for S at leading order. Note that $\frac{dR}{d\tau}=\mathcal{O}(\epsilon^2)$, so we deduce that

$$\frac{dR_0}{d\tau}=0=\frac{dR_1}{d\tau}, \quad (3.32)$$

$$\frac{dR_2}{d\tau}=\frac{R_0}{3}\left[c_\infty(1-\frac{R_{N0}^3}{R_0^3})-(\lambda_A+\lambda_N\frac{R_{N0}^3}{R_0^3})\right] + \frac{\Gamma R_0^3}{6}\left[\frac{1}{5}(1-\frac{R_{N0}^5}{R_0^5})-\frac{1}{3}(1-\frac{R_{N0}^3}{R_0^3})+2\frac{R_{N0}^3}{R_0^3}(\frac{1}{6}-\frac{1}{2}\frac{R_{N0}^2}{R_0^2}+\frac{1}{3}\frac{R_{N0}^3}{R_0^3})\right] \quad (3.33)$$

$$=f(R_0,R_{N0}), \quad \text{say.} \quad (3.34)$$

Hence, $R\sim R_0+\epsilon^2R_2(\tau)+\mathcal{O}(\epsilon^3)$, where $R_0=const=R(0)$. We also find that R_N has no $\mathcal{O}(\epsilon)$ term, since expanding Equation (3.26) gives $R_N\sim R_{N0}(1-\frac{1}{3}(\lambda_A+\lambda_N)\epsilon^2\tau+\mathcal{O}(\epsilon^4))$, where $R_{N0}=R_N(0)$.

Turning our attention back to Equation (3.29), we find at leading order

$$3R_{N0}^2 S_1 \frac{dS_1}{d\tau} = \left(1 - \frac{R_{N0}^3}{R_0^3} + \frac{1}{2}\frac{R_{N0}^2}{R_0^2}\right) R_0 f(R_0, R_{N0}) + (\lambda_A + \lambda_N)\left(1 - \frac{R_{N0}}{R_0}\right) R_{N0}^2 \quad (3.35)$$

where $f(R_0, R_{N0})$ is defined via Equation (3.34). Integrating Equation (3.35) gives

$$S_1 = \left[\frac{1}{3}\left((\frac{1}{R_0} - 2\frac{R_{N0}}{R_0^2} + 2\frac{R_0}{R_{N0}^2})f(R_0, R_{N0}) + 2(\lambda_A + \lambda_N)(1 - \frac{R_{N0}}{R_0})\right)\right]^{\frac{1}{2}} \tau^{\frac{1}{2}}. \quad (3.36)$$

So for $t \ll 1$,

$$R_H(t) \sim R_{N0} + R_{N0}\left[\frac{1}{3}\left((\frac{1}{R_0} - 2\frac{R_{N0}}{R_0^2} + 2\frac{R_0}{R_{N0}^2})f(R_0, R_{N0}) + 2(\lambda_A + \lambda_N)(1 - \frac{R_{N0}}{R_0})\right)\right]^{\frac{1}{2}} t^{\frac{1}{2}}. \quad (3.37)$$

This approximate solution for $R_H(t)$ and the numerical solution obtained by solving the full problem are in good agreement (Figure 3.7).

As a result of this analysis we conclude that whenever a hypoxic region re-emerges within a tumour post-radiotherapy, it does so rapidly over a short timescale on which both the outer tumour radius and the radius of the necrotic core do not change dramatically. This phenomenon arises naturally from the model. We note that similar analysis was performed on the original, untreated growth equations by Byrne *et al.* [67].

3.4.2 Post-radiotherapy decrease in tumour volume

Under certain conditions our model predicts a continued decrease in overall tumour volume in the period following the instantaneous radiation-induced death (see Figure 3.8). Such a scenario occurs when either a single, large fraction of radiation is applied to the tumour, or multiple doses are delivered in quick succession, resulting in a tumour composition such that the width of the viable rim is very small.

More precisely, if immediately after the final radiotherapy fraction, the tumour composition is such that $R - R_N = \mathcal{O}(\epsilon)$, then it is straightforward to show that the evolution

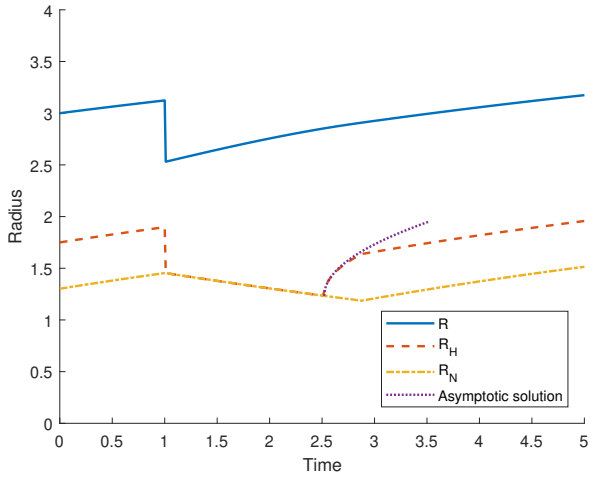

Figure 3.7: Asymptotic solution given by Equation (3.37) (dotted line) plotted alongside the numerical solution to Equations (3.13)-(3.22) showing the regrowth of the tumour spheroid after radiotherapy and the fast initial increase in R_H. We note that during regrowth the mismatch in the oxygen tension on the necrotic core boundary is eventually resolved and the tumour resumes standard Greenspan growth dynamics.

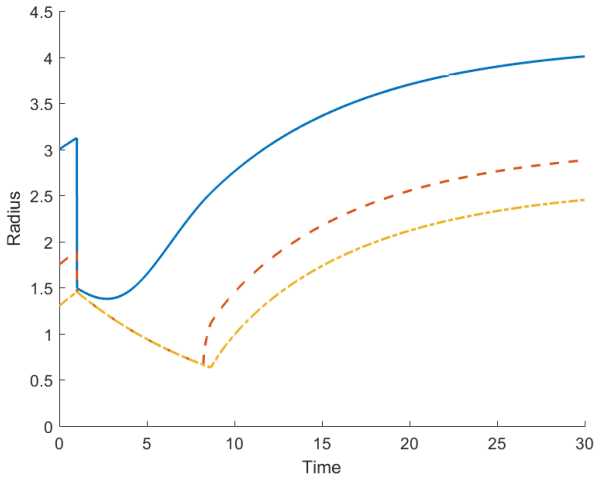

Figure 3.8: Simulation results showing a sustained decline in tumour volume in the period following exposure to a single, large fraction of radiotherapy, $d = 15$Gy, delivered at time $t_1 = 1$ given by numerical solution of Equations (3.13)-(3.22) with parameter values from Tables 3.1 & 3.2.

of the outer tumour radius is of the form

$$R \sim R_{N0}(1 - \frac{1}{3}(\lambda_A + \lambda_N)t). \tag{3.38}$$

In this case, the radiotherapy results in a tumour composition for which the necrotic core constitutes a large proportion of the tumour volume. As such the resulting tumour dynamics for short times after irradiation are dominated by decay of the necrotic material, as opposed to proliferation of the viable tumour cells.

Such a result is again of interest for deciding when next to irradiate the tumour. If we expect to observe a continued decrease in tumour volume post-radiotherapy then the next fraction could be delayed while the overall tumour volume decreases further and the volume of viable cells which are targeted by radiotherapy increases.

3.5 Characterising the tumour response to different fractionation protocols

We now consider the effects of various treatment protocols on a given tumour under this model. In Section 3.5.1 we study tumour regrowth following a single dose of radiation, and in Section 3.5.2 we consider the long-term behaviour of a tumour for different fractionation schedules.

3.5.1 Single hit regrowth

We now consider the effect of irradiating a small tumour spheroid composed entirely of proliferating cells and its subsequent regrowth. This situation is relevant for tumours of radius R such that $0 < R^2 < \frac{6}{\Gamma}(c_\infty - c_H)$ and $R_H = R_N = 0$, since when $R = \sqrt{\frac{6}{\Gamma}(c_\infty - c_H)}$, $c(0) = c_H$ and therefore larger tumours will contain a hypoxic region and/or necrotic core. Solving Equation (3.13) subject to boundary conditions (3.17)-(3.18) we deduce that the oxygen profile for this tumour composition is given by

$$c(r,t) = c_\infty - \frac{\Gamma}{6}(R^2 - r^2). \tag{3.39}$$

Substituting from Equation (3.39) into Equation (3.14), with $R_H = R_N = 0$, we arrive at

the following ODE for $R(t)$:

$$\frac{dR}{dt} = \frac{R}{3}\left(c_\infty - \frac{\Gamma R^2}{15} - \lambda_A\right), \tag{3.40}$$

with solution

$$\frac{R}{R_0} = \sqrt{\frac{c_\infty - \lambda_A}{\frac{\Gamma R_0^2}{15} + A_0 e^{-\frac{2}{3}(c_\infty - \lambda_A)t}}} \tag{3.41}$$

where $A_0 = c_\infty - \lambda_A - \frac{\Gamma R_0^2}{15}$.

We can use Equation (3.41) to calculate the time taken for a tumour spheroid of radius $0 < \tilde{R}^2 < \frac{6}{\Gamma}(c_\infty - c_H)$ following a single fraction of radiation of dose d to regrow to its initial (i.e. pre-radiotherapy) size. The tumour radius immediately after irradiation is given by $\gamma(d)\tilde{R}$, where $\gamma(d) = exp(-\frac{1}{3}(\alpha d + \beta d^2))$ is the survival fraction given by the linear quadratic formula. It is straightforward to show that the time, Δt, until the tumour regrows to its original size is given by

$$\Delta t = \frac{3}{2(c_\infty - \lambda_A)} \ln\left[\frac{c_\infty - \lambda_A - \frac{\gamma^2 \Gamma \tilde{R}^2}{15}}{\gamma^2(c_\infty - \lambda_A - \frac{\Gamma \tilde{R}^2}{15})}\right], \tag{3.42}$$

where $\gamma = \gamma(d)$. We assume that the parameters are such that the tumour spheroid was growing pre-irradiation and therefore $R^2 < \frac{15}{\Gamma}(c_\infty - \lambda_A)$ (from (3.40)). In this parameter regime, the logarithm in Equation (3.42) is defined and $\Delta t > 0$. By extension, we require that $c_\infty > \lambda_A$ since otherwise the tumour spheroid shrinks for all values of $\tilde{R}$ and a viable tumour of any size cannot be supported. We note for future reference that

$$\Delta t \to \frac{\alpha d + \beta d^2}{c_\infty - \lambda_A} \quad \text{as} \quad \tilde{R} \to 0. \tag{3.43}$$

Differentiating Equation (3.42) with respect to $\tilde{R}$, we obtain

$$\frac{d}{d\tilde{R}}(\Delta t) = \frac{\Gamma \tilde{R}}{5} \frac{(1 - \gamma^2)}{(c_\infty - \lambda_A - \frac{\Gamma \tilde{R}^2}{15})(c_\infty - \lambda_A - \gamma^2 \frac{\Gamma \tilde{R}^2}{15})}. \tag{3.44}$$

Therefore, at least for small $\tilde{R}$, $\frac{d\Delta t}{d\tilde{R}}\Big|_{\gamma(d)} > 0$, and so the regrowth time, Δt, is an increasing function of $\tilde{R}$ for fixed dose d. This holds for all $0 < \tilde{R}^2 < \frac{6}{\Gamma}(c_\infty - c_H)$ if the inequality $3c_\infty - 5\lambda_A + 2c_H > 0$ is satisfied. Then Equation (3.42) represents an increasing family

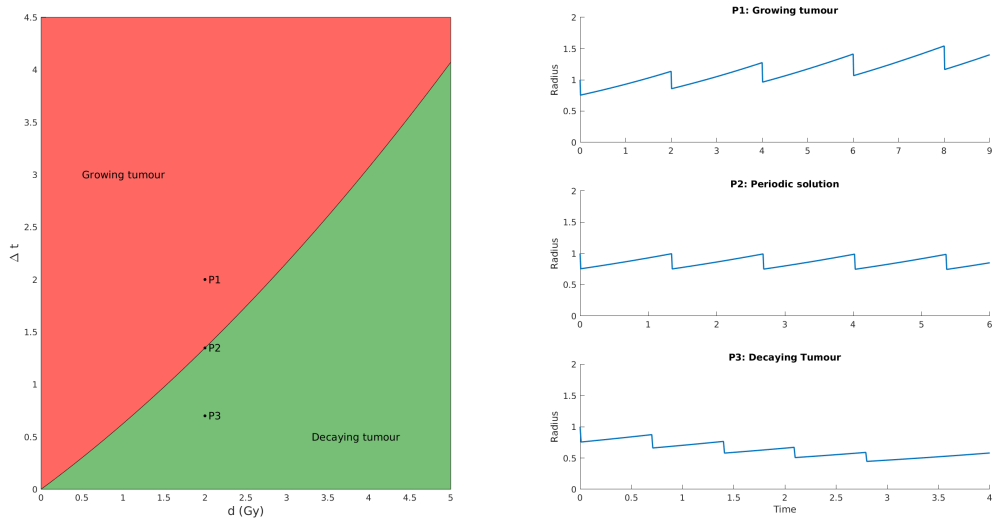

Figure 3.9: Radiation dose and fractionation-dependent behaviour for a tumour spheroid composed of proliferating cells. Line for periodic behaviour given by Equation (3.42). Plots on the right show response to 5 fractions of radiotherapy given by the protocols corresponding to points P1, P2 & P3.

of curves where the minimum bounding curve is given by Equation (3.43). That is, for $0 < \tilde{R}_1 < \tilde{R}_2 < \sqrt{\frac{6}{\Gamma}(c_\infty - c_H)}$ and fixed dose d, $\Delta t(d; R_1) < \Delta t(d; R_2)$.

Returning to Equation (3.42), we see that for an initial radius $\tilde{R}$, a strategy that combines a dose d with an inter-fraction time less than Δt will result initially in a net shrinkage of the tumour throughout treatment (i.e. the tumour volume is smaller at the delivery of each radiation fraction). Conversely, if we wait longer than Δt to re-irradiate then the tumour will have grown larger than its original size. Thus, Equation (3.42) defines a curve in the $(d, \Delta t)$-plane for treatment protocols which give rise to periodic behaviour for a given initial tumour radius $\tilde{R}$, since the cell kill induced by radiotherapy is exactly balanced by the regrowth between fractions. This curve is indicated in Figure 3.9. We note that the curve describing protocols that yield periodic behaviour becomes concave for large R, and in particular, as R tends to its steady state value, R^* say, then for a given dose, $d > 0$, $\Delta t(d) \to \infty$.

3.5.2 Periodic surface in 'treatment space'

In the previous section we investigated the response of tumours of fixed initial radius $\tilde{R}$ to different fractionation protocols as specified by a dose, d, and inter-fraction time, Δt. The $(d, \Delta t)$-plane can be partitioned into regions in which the tumour volume increases or

decreases during treatment. However, we note that the location of these regions depends on the tumour radius at the time of irradiation, $\tilde{R}$. As such, when considering the behaviour of a tumour throughout an entire course of radiotherapy, it is not a line in the $(d, \Delta t)$-plane that we are interested in, but a surface in 'treatment space', $\mathbb{T} \subset \mathbb{R}^3$, with components $(R, d, \Delta t)$.

For a protocol delivering n fractions of radiation, we can identify the response of a given tumour with a discrete trajectory, $(R(t_i), d_i, \Delta t_i) \in \mathbb{T}$, through treatment space. Note, we consider the trajectory as discrete points pre-irradiation so that $R(t_i) = R(t_i)^-$ in our previous notation. Here t_i, d_i and Δt_i are the time, dose and inter-fraction time, respectively, of the ith fraction, for $i = 1, ..., n$. The union of the curves in the $(d, \Delta t)$-plane determining periodicity define a surface, S, in $\mathbb{T}$ (see Figure 3.10a). Correspondingly, as a tumour progresses through the course of radiotherapy, points on its trajectory that lie above this surface indicate net growth of the tumour by the time of delivery of the next radiation dose, whilst points below the surface result in a more desirable decrease in tumour volume. Therefore, for a given tumour spheroid, S defines a surface that partitions $\mathbb{T}$ into treatment protocols that cannot halt tumour progression and those that lead to tumour decay.

With this understanding more general statements about the outcome of different fractionation protocols can be made. We first consider dosing schedules in which the same dose d is administered at constant intervals Δt. In this case, if a point in $\mathbb{T}$ lies above S, then the tumour spheroid will grow until it converges to a point on S, at which time it becomes periodic (Figure 3.10b).

Below S, then the outcome of radiotherapy depends on the boundary curve of S as $R \to 0$ (see Equation (3.43)). If the fractionation schedule lies above this curve in the $(d, \Delta t)$-plane then the system will eventually converge to the corresponding point on S. However, d and Δt below this can be chosen such that the tumour decays to arbitrarily small volumes (Figure 3.10b). We note that Equation (3.43) still holds for this analysis even though its derivation requires an initial tumour composed entirely of viable cells. This is the case since, in the model, necrotic material is only created via nutrient starvation and not as a result of irradiation. As such, for ongoing treatment protocols that result in a decreasing tumour volume, as $t \to \infty, R \gg R_N$.

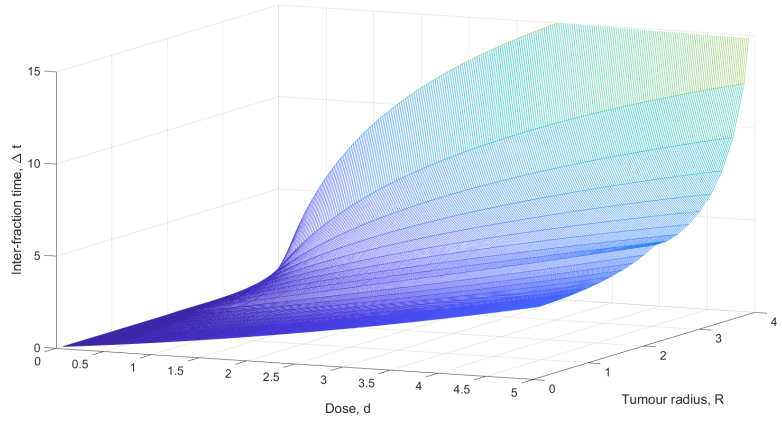

(a)

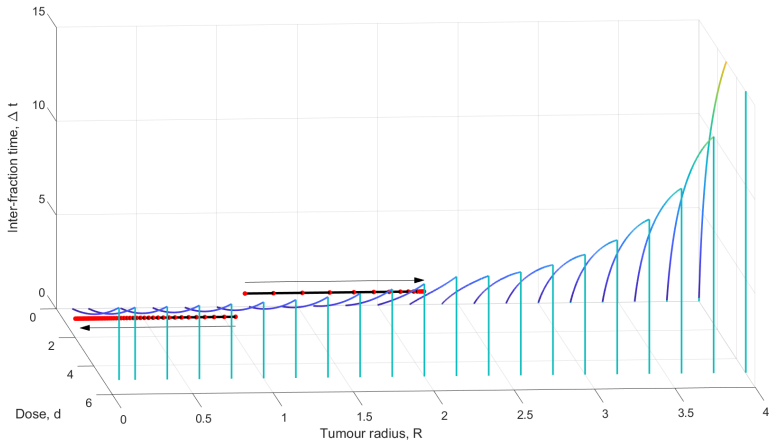

(b)

Figure 3.10: (a) Surface, S, corresponding to protocols giving rise to periodic treatment responses. (b) Simulated trajectories (black lines) in 'treatment space', $\mathbb{T} \subset \mathbb{R}^3$ with components $(R, d, \Delta t)$, for two different constant dosing schedules (fractions plotted as red points) applied to the same tumour spheroid (i.e. same model parameters). A dose of 3 Gy every 3 days (top trajectory) results in a tumour that grows until it reaches a periodic state, while a dose of 2 Gy delivered daily (bottom trajectory) is sufficient to drive the tumour volume arbitrarily close to zero. The surface describes treatment protocols which give rise to periodic behaviour.

We can extend this concept to more general treatment schedules. If there exists $m \in \mathbb{N}$ such that for all $i > m$ the point $(d_i, \Delta t_i)$ of the ith fraction lies below the curve given by Equation (3.43), then treatment is sufficient to drive the tumour volume arbitrarily close to 0. However, using Figure 3.4b as an illustrative example, we observe a simulation in which the weekend break of the standard fractionation protocol corresponding to $\Delta t = 3$ days gives rise to the periodic orbit.

When predicting how a tumour may respond to radiotherapy, two quantities of interest are the *potential volume doubling time*, T_{pot}, and the *survival fraction after 2 Gy of*

radiation, S_{2Gy}, of the tumour. We translate these definitions into the model and identify tumour characteristics for which this model would eventually predict regrowth over the weekend.

The survival fraction at 2 Gy, S_{2Gy}, for normoxic tumour cells is given by the linear-quadratic formulation. In order to find an expression for T_{pot}, we consider the tumour dynamics for small tumour volumes that are in an 'exponential growth' phase. Linearising the model equations for small R we obtain

$$\frac{dR}{dt} \sim (c_\infty - \lambda_A)\frac{R}{3},$$

which yields a volume doubling time of

$$T_{pot} = \frac{\ln 2}{c_\infty - \lambda_A},$$

where the factor of $\frac{1}{3}$ disappears when we convert from tumour radius to tumour volume. Substituting these expressions into Equation (3.43) for a standard 2 Gy dose we obtain

$$\Delta t = -\ln(S_{2Gy})\frac{T_{pot}}{\ln 2}. \tag{3.45}$$

We note that this expression holds for tumour growth models in which the growth of small tumours is exponential and radiation-induced cell death is modelled as an instantaneous volume loss. Similar analysis for one compartment phenomenological models was performed by McAneney *et al.* [107]. We also note that this is similar in form to the optimal protocols found for an exponential model by Wheldon *et al.* [104].

If we now consider Equation (3.45) in the context of the weekend break ($\Delta t = 3$) within the standard fractionation protocol, then we see that $-T_{pot}\ln(S_{2Gy}) < 3\ln 2$ defines a class of tumour characteristics for which regrowth of the tumour over the weekends impedes tumour decay (Figure 3.11).

3.6 Influence of tumour composition on response dynamics

Patient-specific pre-treatment data in the clinic is often limited, with CT scans and subsequent measurements of tumour volume at diagnosis and the treatment planning stage

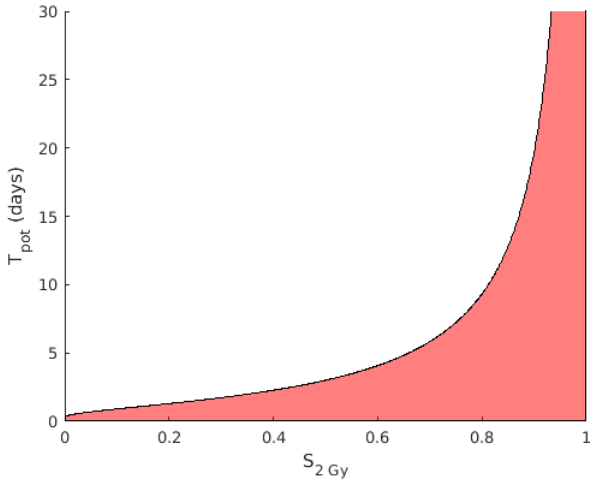

Figure 3.11: Region for which tumours will eventually exhibit net growth over the weekend (shown in red).

typically being the only data available. The simulations and analysis in the previous section reveal rich dynamics with regards to tumour composition throughout radiotherapy. As such, it is natural to question the predictive power of our model in the absence of relevant spatial data summarising the tumour structure. Specifically, for tumours of similar total size, how does the underlying composition influence the response dynamics? In this section we identify parameter regimes that give rise to equilibrium tumours of the same overall size but different spatial structures and consider the responses of these different tumours to radiotherapy.

For a fully-developed 3-layer tumour spheroid with $0 < R_N < R_H < R$, the oxygen profile within the tumour may be found by solving Equations (3.13), (3.17) and (3.18) to give

$$c = \begin{cases} c_N + \frac{\Gamma}{6r}(r - R_N)^2(r + 2R_N) & R_N(t) < r < R(t) \\ c_N & 0 < r < R_N(t). \end{cases} \tag{3.46}$$

This also satisfies the relations

$$c_\infty - c_N = \frac{\Gamma}{6R}(R - R_N)^2(R + 2R_N), \tag{3.47}$$

$$c_H - c_N = \frac{\Gamma}{6R_H}(R_H - R_N)^2(R_H + 2R_N), \tag{3.48}$$

such that $c = c_\infty$ on $r = R(t)$, and $c = c_H$ on $r = R_H(t)$.

The evolution of the outer radius during tumour growth is governed by Equation (3.14). Evaluating the integral on the right hand side we find that at steady state the tumour radii, R, R_H and R_N, satisfy

$$c_N\left(1-\frac{R_H^3}{R^3}\right)-\lambda_A-\lambda_N\frac{R_N^3}{R^3} + \frac{\Gamma R^2}{2}\left[\frac{1}{5}\left(1-\frac{R_H^5}{R^5}\right)-\frac{R_N^2}{R^2}\left(1-\frac{R_H^3}{R^3}\right)+\frac{R_N^3}{R^3}\left(1-\frac{R_H^2}{R^2}\right)\right]=0. \quad (3.49)$$

For fixed steady state radius, R, we may view Equations (3.47) and (3.48) as specifying the positions of the internal contours R_N and R_H, respectively. Equation (3.49) thus provides a constraint on the remaining model parameters, which we may view as specifying the value of λ_A given free choice of the other parameters. Using Equations (3.47)-(3.49), we may generate tumour spheroids which evolve to the same steady state radius, R, but have different underlying compositions. In particular, we may use the oxygen consumption rate, Γ, and hypoxia threshold, c_H, parameters to vary the positions of R_N and R_H at steady state. In Figure 3.12a we visualise the surfaces governing the positions of R_H (red) and R_N (yellow) at steady state for fixed $R = 3.5$ as we vary Γ and c_H. Figures 3.12b-d visualise R_H, R_N and λ_A as contours in (Γ, c_H) parameter space.

By choosing parameters in this way, we may simulate radiotherapy protocols for different tumours near steady state and investigate the influence of tumour composition on treatment response. In Figure 3.13 we traverse the diagonals between the corners of the region of (Γ, c_H) parameter space shown in Figure 3.12 to generate different steady state tumour compositions. We visualise the resulting trajectories throughout radiotherapy as we move through parameter space. It is evident from the trajectories in Figures 3.13e and f that tumours of the same size prior to the start of treatment may respond significantly differently to radiotherapy, with some trajectories approaching a plateau in response towards the end of the fractionation protocol. Furthermore, by comparing the simulations with the steady state compositions (Figures 3.13c and d), we see that the size of the necrotic core is a dominant factor in determining radiotherapy response, with larger val-

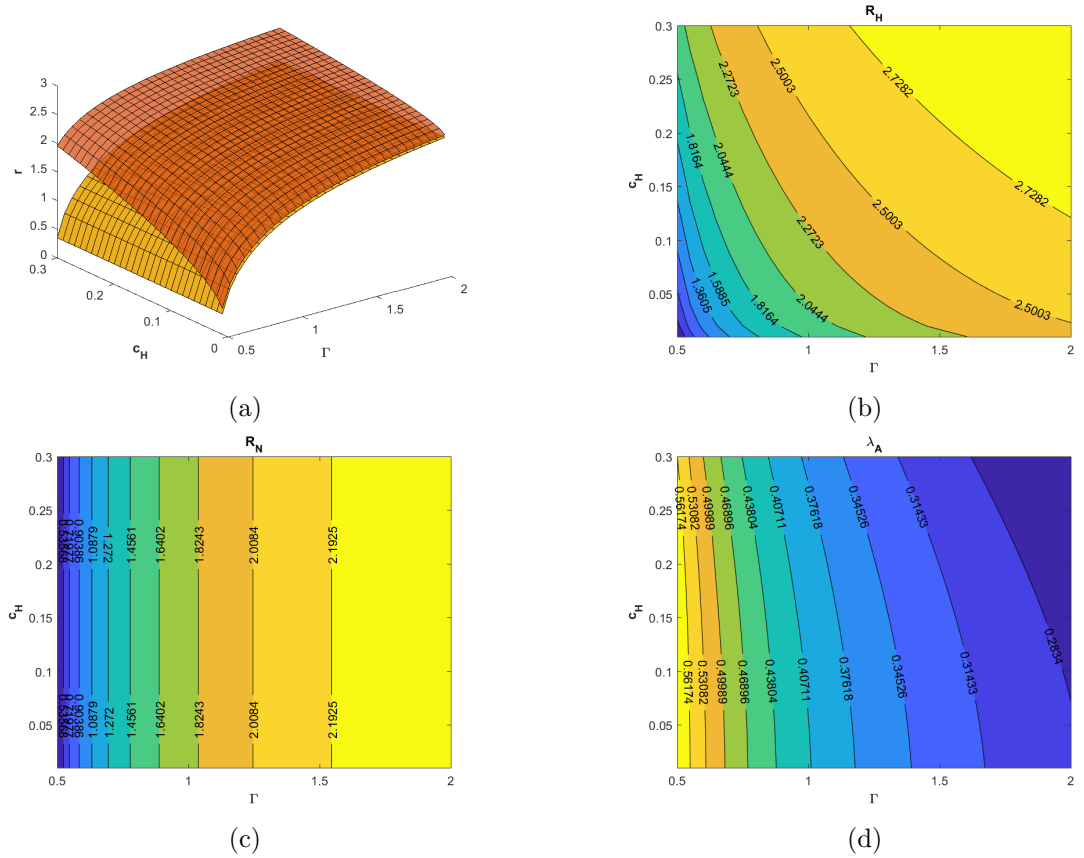

Figure 3.12: (a) Surfaces of steady state radii R_H (red) and R_N (yellow) varying the oxygen consumption rate, Γ, and hypoxia threshold, c_H, for fixed steady state outer radius $R = 3.5$ as given by Equations (3.47) and (3.48). (b) Contour plot in (Γ, c_H) parameter space for the steady state radius R_H as determined by Equation (3.48). (c) Contour plot in (Γ, c_H) parameter space for the steady state radius R_N as determined by Equation (3.47). (d) Contour plot in (Γ, c_H) parameter space for the apoptosis rate parameter, λ_A, as determined by Equation (3.49). The remaining model parameters are as listed in Table 3.1.

ues of R_N corresponding to a smaller decrease in tumour volume by the end of treatment. This result is intuitive from the model equations since we assume the necrotic core to be unaffected by radiation. We emphasise that the radiosensitivity parameters are held constant between the simulations and that the differences in response to radiotherapy are a result of the variations in tumour composition.

3.7 Discussion

In vivo tumours are highly heterogeneous cellular entities characterised by high inter-patient variability. Allied to this, the local efficacy of radiotherapy delivered to the tumour site is affected by a number of variables associated with the tumour's heterogeneous composition and micro-environment. In particular, the local oxygen concentration can significantly influence radiation-induced cell death, with well-oxygenated regions being shown to exhibit up to threefold greater radiosensitivity than hypoxic tumour populations. With this in mind, in this chapter we have presented a simple, spatially-resolved model in order to investigate the effects of tumour composition on radiotherapy response. The discussed model builds on the tumour growth model first proposed by Greenspan [63]. We extend this to incorporate the effects of radiotherapy taking into account spatially-varying radiosensitivities.

Numerical simulations and mathematical analysis of the model reveal how the tumour's growth dynamics and spatial composition change throughout treatment. Heterogeneity within the tumour not only affects the initial response to radiotherapy, but also how this response changes throughout the duration of the treatment protocol (see Figure 3.5b). For parameter regimes in which hypoxia re-emerges during treatment, a rapid transient increase in the width of the hypoxic annulus is observed. This behaviour arises naturally from the model and the underlying process driving this phenomenon remains to be elucidated. We also identify scenarios for which the radiotherapy induces a significant change in tumour composition with the necrotic core forming a large proportion of the irradiated tumour and influencing the subsequent dynamics.

The model more generally also classifies protocols that may result in tumour progression, a non-zero periodic tumour volume, or tumour decay. We identify a surface in

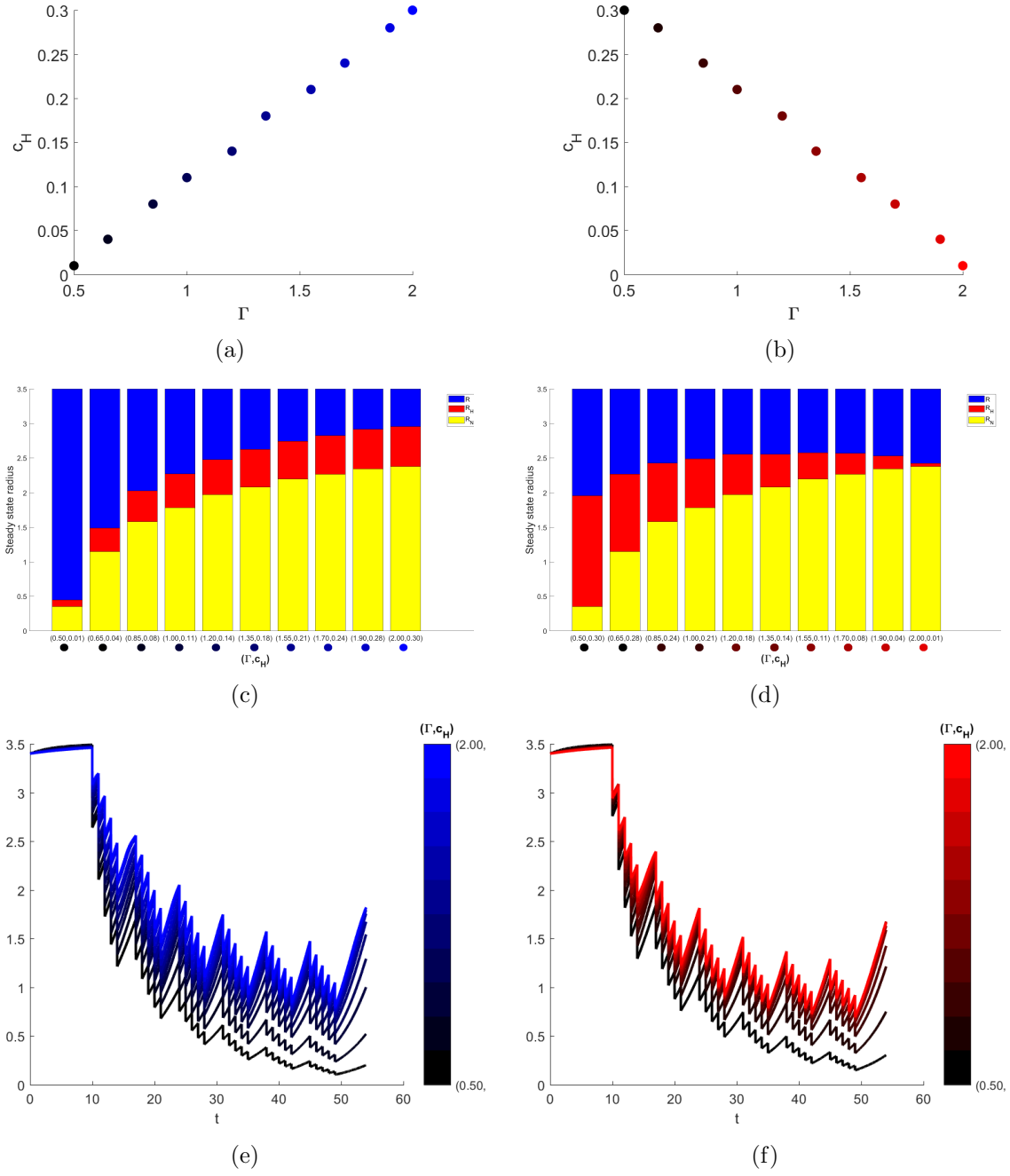

Figure 3.13: (a)-(b) Visualisation of the parameter sets chosen along each of the main diagonals in (Γ, c_H) parameter space for simulating radiotherapy response in tumours of the same overall size but with different tumour compositions. (c)-(d) Different steady state tumour compositions for fixed steady state radius $R = 3.5$ for a selection of parameter combinations traversing the diagonals between the corners of the region of (Γ, c_H) parameter space shown in Figure 3.12. (e)-(f) Tumour radius trajectories from simulating Equations (3.13)-(3.22) with the standard fractionation protocol using the parameter combinations shown in panels (c)-(d), respectively, with line colour corresponding to the parameter combination. The initial tumour radius for each simulation is taken to be $R_0 = 3.4$, just below the steady state value, with radiotherapy starting at $t_1 = 10$. The corresponding value of λ_A is specified by Equation (3.49). The remaining model parameters are as listed in Tables 3.1 and 3.2.

'treatment space' dependent on tumour-specific growth and radiosensitivity parameters and determine that successful protocols correspond to those that remain below this surface throughout treatment. We also identify parameter regimes which give rise to steady state tumours of the same size but of varying underlying composition. Simulations of these tumours show that tumours of the same volume prior to treatment may respond differently to radiotherapy. The wide variety of dynamics exhibited by the model suggests that spatial heterogeneity may be important for simulating tumour response to radiotherapy and, in particular, for making clinical predictions.

The model presented in this chapter makes numerous assumptions and simplifications about the underlying biology. For radiation-induced cell death we take the common approach of modelling this process as an instantaneous effect. However, the linear-quadratic model was established to determine long-term clonogenic survival after radiotherapy. Biologically, cell death after radiation may occur via a number of different mechanisms, with many irradiated cells dying only after attempting mitosis one or more times [144]. Consequently, radiation-induced cell death may not elicit the instantaneous volume reduction modelled here. In the more complex models presented in Chapters 4 and 5 we model this process in more detail in order to describe the short term response to radiotherapy and the corresponding spatial changes in tumour composition more accurately. Additionally, a more detailed model will allow us to relax the restrictions of the spherically symmetric geometry associated with the current model, making it more applicable to modelling vascular tumour growth and *in vivo* responses to radiotherapy.

Radiation biology has a rich history of integrating theoretical and quantitative approaches to advance biological studies and clinical concepts. From the simple and widely used LQ model emerged the concepts of *biologically equivalent dose* (BED) and *tumour control probability* (TCP) to guide the development of clinical fractionation protocols. Different TCP models with increasing complexity, from simple Poissonian TCP to stochastic birth-death processes, have recently been scrutinized, and mathematical analysis suggests that simple models may be best positioned for clinical utility [102]. Clinical data are often insufficient to inform mathematical models [113]. Both simple and more complex mathematical models are facing numerous hurdles in the attempt to integrate them into radiation oncology, and more work is needed to fully harness the potential of mathematical

modeling for precision radiation oncology [94].

However, for a model to be useful in making patient-specific predictions in the clinic, parameters must be identifiable with respect to the limited clinical data typically available. As such, current research in this area often focusses on phenomenological ODE models, such as those considered in Chapter 2, with few parameters to be estimated. Typically these models contain no information about the spatial heterogeneity in tumour composition and radiotherapy response. With this in mind, we also propose a comparison of the developed spatially-resolved model with these phenomenological approaches as future work. We aim to identify situations in which the spatially-resolved and spatially-averaged models agree well, and those in which there is a significant difference. The tumour composition changes observed in model simulations suggests that averaged parameter values in simple, phenomenological models may not sufficiently capture the tumour dynamics during treatment for some tumour compositions and parameter combinations.

Chapter 4

A multiphase model for tumour growth

4.1 Introduction

Tumours growing *in vivo* typically exhibit a greater degree of spatial heterogeneity than tumours growing *in vitro*. In Chapter 3 we exploited the simplicity (and reproducible structure) of avascular tumour spheroids to simplify the model geometry. However, the simplified geometry considered, restricted the distribution of material within the tumour. Cells forming biological tissues proliferate and move in an active manner, signalling and interacting with their local microenvironment. In particular, we may expect the different regions of the growing tumour, such as the normoxic, proliferative cells and the hypoxic necrotic core, for example, to interact in a manner which may affect the resulting growth dynamics.

There are multiple conditions under which tumour cells may die, including severe hypoxia and nutrient starvation. This cell death may occur via a number of different mechanisms over different durations of time, such as apoptosis, necrosis and mitotic catastrophe, for example. Apoptosis is a regulated, programmed form of cell death occurring over a timescale of hours, while necrosis is typically a mode of cell death induced by the surrounding microenvironmental conditions. Cells that are fated to die may instead attempt mitosis one or more times before dying, potentially via another cell death pathway. This

process is known as mitotic catastrophe and may occur over a couple of days/cell cycles [11, 29, 30, 144]. Furthermore, radiotherapy causes cell death throughout the tumour and results in non-viable tumour cells and cellular debris that is not solely localised to the necrotic core. We hypothesise that the spatial distribution of the dead material in the tumour may play a key role in the tumour's growth dynamics, and consequently, the observed response to radiotherapy. In this chapter we develop a more detailed model of tumour growth than the model presented in Chapter 3 with a view to extending the model to account for radiotherapy effects in the Chapter 5.

Multiphase models describe the spatiotemporal evolution of mixtures comprising two or more continuum phases. The simplest multiphase model formulations consider the conservation of mass and momentum for each phase, along with appropriate interaction terms for mass and momentum exchange between the phases. More complex models may include additional equations to account for other physical principles, such as thermodynamic or energy considerations, as appropriate to the system under investigation [73–75, 89]. This modelling framework has been applied to a wide range of scenarios, including biological tissue growth and, in particular, tumour growth [78, 81–83, 88, 149–151]. The simplest two phase models view tumours as a two-phase mixture of tumour cells and extracellular material. Under appropriate limits, these models have been shown to reduce to the Greenspan model of tumour growth [81], which we extended to incorporate the effects of radiotherapy in Chapter 3.

In this chapter we develop a novel, three phase model of tumour growth and use numerical simulation to investigate the different qualitative growth behaviours exhibited. The work presented in this chapter forms a basis for the work contained in Chapter 5 where we incorporate the effects of radiotherapy into the model. In Section 4.2 we derive the model equations governing our multiphase system and show how to eliminate some of the variables to obtain a final, reduced system of equations. In Section 4.3 we provide an overview of the numerical method we use to solve this system of equations. Full details of the numerical scheme are provided in Appendix C along with a demonstration of the convergence of our numerical solution. In Section 4.4 we simulate the model dynamics for a range of parameter combinations and reproduce tumour growth behaviours similar to those observed both *in vitro* and *in vivo*. We characterise further, non-monotonic

dynamics exhibited by the model in Section 4.5, and in Section 4.6 we demonstrate the influence of modelling the dead material on the resulting growth dynamics.

4.2 Multiphase model derivation

In this section we derive our multiphase, mixture model of tumour growth. There are a range of models of this type in the literature applied to tumour growth, most decomposing the tumour into two phases [80–82]. Our new model proposes that a non-viable cell population including necrotic material and cellular debris may form a significant portion of a growing tumour and may affect the growth dynamics. In particular, we view this material as a viscous fluid whose mechanical properties may differ from those of the tumour cells (also viewed as a viscous fluid) and extracellular fluid (viewed as inviscid). As such, we consider the tumour to be a mixture comprising these three distinct phases.

The spatial distribution of each phase is described by the volume fractions $\phi_i(\mathbf{x}, t)$ $(i = 1, 2, 3)$ for the tumour cell, dead material and extracellular fluid phases, respectively. The movement of each phase is given by the phase velocities, $v_i(\mathbf{x}, t)$, with the phase pressures and stress tensors represented by $p_i(\mathbf{x}, t)$ and $\sigma_i(\mathbf{x}, t)$, respectively. We use mass and momentum balances in each phase to determine how the dependent variables evolve over time. We assume that the tumour growth is nutrient-limited, and so the system is coupled to a reaction-diffusion equation for the oxygen field with concentration $c(\mathbf{x}, t)$.

The volume fraction ϕ_1 describes the spatial distribution of the tumour cells. The tumour cells are assumed to proliferate in well-oxygenated regions and to die in severely hypoxic conditions. On the macroscale, we model the tumour cells as a slow-moving, viscous fluid. The active motion of the tumour cells due to inter-cellular sensing is modelled via an additional pressure term.

We treat the phase with volume fraction ϕ_2 as comprising of all of the non-viable cellular material and cellular debris within the tumour, irrespective of cell death mechanism or stage of decay. As such, this phase gives in some sense an 'averaged' description of this component of the tumour environment across all of these modes of cell death and is a transitional phase between the viable tumour population and the extracellular fluid. We

hereafter refer to this phase simply as being comprised of 'dead material'.

The final constituent in our mixture is the extracellular fluid phase, with volume fraction ϕ_3. The extracellular fluid is assumed to provide the nutrients by which the viable tumour cell population is able to survive and proliferate. We model this phase as an inviscid fluid.

The tumour growth is assumed to depend on the availability of nutrients, in particular, oxygen. As such, we couple the equations governing the dynamics of the three phases to an oxygen field, c. The full system of equations is given by Equations (4.1)-(4.12), as detailed below.

4.2.1 Growth model equations

We apply the conservation of mass and momentum (Equations (4.1) and (4.2), respectively) for each phase ($i = 1, 2, 3$). We assume equal phase densities and justify this assumption by noting that the material comprising biological cells is broadly similar to the interstitial fluid. As such, mass fractions and volume fractions become equivalent and we may ignore densities in the resulting system of equations.

$$\frac{\partial \phi_i}{\partial t} + \nabla \cdot (\mathbf{v_i} \phi_i) = S_i \tag{4.1}$$

$$0 = \nabla \cdot (\phi_i \underline{\boldsymbol{\sigma}_{\boldsymbol{i}}}) + \mathbf{F_i} \tag{4.2}$$

We note that for biological tissues we consider slow-flow regimes and so the inertia terms drop out of the momentum equations to leading order [88]. Scaling arguments may be used to that these terms are of $\mathcal{O}(\epsilon^2)$, where $\epsilon \ll 1$ is the ratio between the micro- and macro- lengthscales [77]. The model equations are specialised to the problem at hand by specification of appropriate constitutive equations for the stress tensors, $\underline{\boldsymbol{\sigma}_{\boldsymbol{i}}}$, mass sources/sinks, S_i, and momentum sources/sinks, $\mathbf{F_i}$, which are described in detail in Section 4.2.2.

This system is coupled to a reaction-diffusion equation for the oxygen field, c, given by

$$0 = D\nabla^2 c - \Gamma \phi_1 H_\epsilon (c - c_N), \tag{4.3}$$

where the tumour cells, with volume fraction ϕ_1, consume oxygen at a rate Γ, and D is the diffusion coefficent. We define

$$H_\epsilon(c) = \frac{1}{2}\left(1 + \tanh\left(\frac{c}{\epsilon}\right)\right) \tag{4.4}$$

as a smooth approximation to the Heaviside function for oxygen consumption considered in previous work (c.f. Chapter 3) for small ϵ. The oxygen field is assumed to be in a quasi-steady state since oxygen diffuses on a much shorter timescale than tumour growth, taking ~ 10 seconds to diffuse 100 μm by comparison with a tumour growth period measured in days [63]. We note that this separation of timescales also removes the need for the dilution term that is typically required for reaction-diffusion equations on a growing domain to account for domain growth [152].

4.2.2 Constitutive relations

We close Equations (4.1)-(4.3) by prescribing appropriate constitutive equations, along with initial and boundary conditions. Firstly, we assume that the mixture is saturated. That is, the phases that we consider constitute the entirety of the tumour volume and so we impose the 'no voids' condition:

$$\sum_i \phi_i = 1. \tag{4.5}$$

The mass sources and sinks terms, S_i, in Equation (4.1) correspond to mass transfer between phases and may be associated with proliferation and cell death processes. The source term for the tumour cell phase, S_1, is given by

$$S_1 = \underbrace{\eta\phi_1\phi_3 H_\epsilon(c - c_H)}_{\text{proliferation}} - \underbrace{\chi\phi_1 H_\epsilon(c_N - c)}_{\text{necrosis}} - \underbrace{\kappa\phi_1}_{\text{apoptosis}}. \tag{4.6}$$

The first term in Equation (4.6) describes proliferation of the viable tumour cell population, with the rate of mitosis in normoxic conditions given by the parameter η. Proliferation is assumed to occur at rate proportional to the local volume fraction of the tumour cell phase, ϕ_1, and also of the extracellular fluid, ϕ_3, since the material and nutrients required for proliferation are derived from this phase. Proliferation is also assumed to be

oxygen-dependent with the tumour cells entering quiescence below the hypoxic oxygen threshold, c_H. The second term in S_1 relates to necrosis induced by nutrient starvation when the oxygen concentration drops below the threshold $c_N < c_H$ and occurs at rate χ. This happens alongside a baseline level of apoptotic cell death which occurs throughout the tumour at a constant rate, κ.

The material lost from the tumour phase due to cell death corresponds to a mass source in the dead material phase, S_2 (Equation (4.7)). This phase then undergoes exponential decay at a constant rate, λ.

$$S_2 = \chi\phi_1 H_\epsilon(c_N - c) + \kappa\phi_1 - \underbrace{\lambda\phi_2}_{\text{cellular decay}} \tag{4.7}$$

The entire system is assumed to conserve mass locally, with proliferation and cell death occurring as a transfer of mass between phases, and so we impose

$$S_3 = -(S_1 + S_2) = \lambda\phi_2 - \eta\phi_1\phi_3 H_\epsilon(c - c_H). \tag{4.8}$$

As such, the fluid phase is required for local proliferation in the cell phase, while the dead material decays to become part of the extracellular fluid.

In prescribing the momentum source/sink terms, $\mathbf{F_i}$, in Equation (4.2) we follow the form typically used in the literature and impose

$$\mathbf{F_i} = p_i \nabla\phi_i + \sum_{j \neq i} d_{ij}\phi_j\phi_i(\mathbf{v_j} - \mathbf{v_i}). \tag{4.9}$$

The first term in Equation (4.9) arises from the homogenisation process and describes the influence of the phase pressure p_i in transport down gradients in the volume fraction of phase i. We note that it is unclear how to specify the volume averaged pressure in this term. There is no clear consensus in the relevant literature, with some authors preferring to use the global pressure p [81, 82], while others us the phase pressures p_i [88]. We note that the Lagrange multiplier required due to the saturation constraint in Equation (4.5) is still satisfied in both cases due to the presence of the global pressure, p, in the specification of each of the phase pressures, p_i. We note that in this case momentum is not conserved across the phases modelled within the mixture ($i = 1, 2, 3$), although

we may assume the existence of another phase of constant volume fraction not modelled which ensures global conservation of momentum. Simulations instead specifying $p\nabla\phi_i$ in this term revealed a similar range of qualitative behaviours (results not shown), and as such the results in this chapter are not significantly affected by this choice.

The second term in Equation (4.9) describes the momentum exchange, or drag, due to the differential movement of the constituent phases. The drag terms are assumed to be equal and opposite and sum to 0 over all phases, so the interphase drag coefficients satisfy $d_{ij} = d_{ji}$.

The stress tensors, $\underline{\boldsymbol{\sigma_i}}$, account for the mechanical properties of each phase. There are many possible ways to model the material properties of each phase and thus different forms for specifying $\underline{\boldsymbol{\sigma_i}}$. Some models consider the tumour as a mixture of fluid phases [81, 82], while others consider multiple phase types within the mixture including rigid, non-deformable solid phases [92, 150], linear-elastic phases [89, 90] and those with viscoelastic/viscoplastic properties [91].

We treat each component as a fluid phase with potentially different viscosities and so the stress tensors take the form given in Equation (4.10) (where $\underline{\mathbf{I}}$ denotes the unit tensor). In particular we specify an ordering of the phases in which the dead material phase has intermediate viscosity, $\mu_2 = \theta_\mu \mu_1$, between the viscous tumour phase, with viscosity μ_1, and the inviscid extracellular fluid, where $0 \leq \theta_\mu \leq 1$. We note that each constituent phase is not incompressible and so we retain the bulk viscosity term, λ_i. However we follow Hubbard *et al.* [88], and assume local thermodynamic equilibrium which specifies $\lambda_i = -\frac{2}{3}\mu_i$.

$$\underline{\boldsymbol{\sigma_i}} = \underbrace{-p_i\underline{\mathbf{I}}}_{\text{isotropic phase pressure}} + \underbrace{\mu_i(\nabla\mathbf{v_i} + \nabla\mathbf{v_i}^T)}_{\text{shear viscosity}} + \underbrace{\lambda_i\left(\nabla\cdot\mathbf{v_i}\right)\underline{\mathbf{I}}}_{\text{bulk viscosity}} \tag{4.10}$$

$$\underbrace{\lambda_i = -\frac{2}{3}\mu_i,}_{\text{thermodynamic equilibrium}} \qquad \underbrace{\mu_1 \geq \mu_2 = \theta_\mu\mu_1 \geq \mu_3 = 0}_{\text{relative ordering of viscosities}}$$

The momentum interaction terms, $\mathbf{F_i}$, in Equation (4.9) and the stress tensors, $\underline{\boldsymbol{\sigma_i}}$, in Equation (4.10) include phase-specific pressure terms, p_i, which need to be specified to close the system. We assume a global isotropic fluid pressure, p, with an additional term,

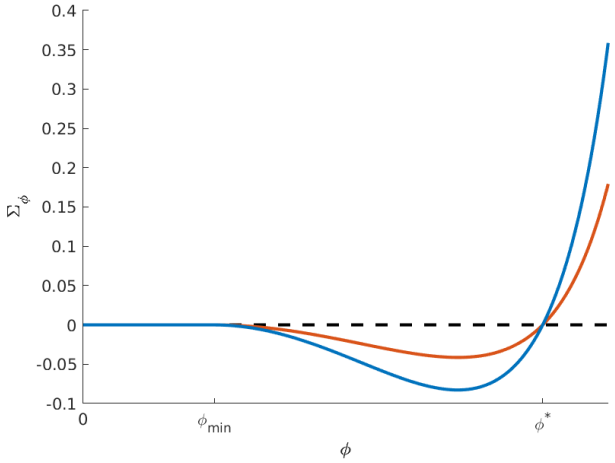

Figure 4.1: The cell sensing function $\Sigma_\phi(\phi)$ (defined by Equation (4.12)); no interaction between cells if they are too sparsely populated ($\Sigma_\phi = 0$ for $\phi \in [0, \phi_{min}]$), whereas $\Sigma_\phi < 0$ for $\phi \in (\phi_{min}, \phi^*)$ represents regions of cellular adhesion, while $\Sigma_\phi > 0$ for $\phi \in (\phi^*, 1)$ represents a repulsive cellular pressure. The red curve represents the cell-sensing function of the dead material given by $\theta_p \Sigma_\phi$ for $0 \leq \theta_p \leq 1$.

Σ_ϕ, describing the local pressure which may be ascribed to cell-sensing in the cell and dead material phases. The cell-sensing capacity of the dead material is assumed to be intermediate between that of the tumour cells and the extracellular fluid, which we model via the parameters $0 \leq \theta_p, \theta_\Sigma \leq 1$. A positive value of Σ_ϕ corresponds to a repulsive cell pressure, whilst negative values correspond to regions of cellular adhesion (see Figure 4.1). This term is similar to those used previously in the literature [81]. The phase pressures, p_i, are specified in Equation (4.11), while the cell-sensing term, Σ_ϕ, is defined in Equation (4.12) where $H(\cdot)$ is the Heaviside function.

$$p_1 = p + \Sigma_\phi(\phi_1 + \theta_\Sigma \phi_2), \quad p_2 = p + \theta_p \Sigma_\phi(\phi_1 + \theta_\Sigma \phi_2), \quad p_3 = p \tag{4.11}$$

$$\Sigma_\phi(\phi) = \frac{\zeta(\phi - \phi_{min})^2(\phi - \phi^*)}{(1 - \phi)} H(\phi - \phi_{min}) \tag{4.12}$$

Characterising the dead material phase

Of particular note, is the manner in which we model the dead material phase, which has volume fraction ϕ_2. As stated previously, we view the dead material as a viscous fluid whose properties are intermediate between those of the tumour cells and the extracellular fluid phases. One aim of this work is to investigate how the way in which the dead material is modelled affects the system dynamics. The parameter vector $\boldsymbol{\theta} = (\theta_\mu, \theta_p, \theta_\Sigma)$

summarises the mechanical properties of this phase relative to the other two phases in the mixture, with $\boldsymbol{\theta}$ taking values in $[0,1]^3$. In particular, $\boldsymbol{\theta} = (1,1,1)$, corresponds to a two-phase sub-case of the full model in which the dead material is essentially a compartment of the cellular phase and retains the same mechanical properties as the viable tumour cells. Conversely, the limit $(0,0,0)$ pertains to a two-phase model in which the dead phase has the same properties as the extracellular fluid.

The parameter θ_μ specifies the viscosity of the dead phase relative to the cell phase and is defined in Equation (4.10). The parameters θ_p and θ_Σ pertain to relative cell-sensing function of this phase. Biologically, this cell-sensing may arise through inter-cellular interactions between cells and their filopodia in the case of cellular adhesion, or stress imposed on the cell membrane and cytoskeleton in regions of high cellular density, for example. Depending on the cell death pathway and stage of decay, we propose that cells in this phase may retain some of this function. In particular, θ_p characterises the relative capacity of the non-viable cell population to perform this type of activity, while the parameter θ_Σ corresponds to the relative contribution of this phase to the cell-sensing pressures experienced by the surrounding cells, as defined in Equation (4.11).

A summary of all the model parameters defined in the system of Equations (4.1)-(4.12) is given in Table 4.1.

4.2.3 Initial and boundary conditions

The system of Equations (4.1)-(4.12) govern the dynamics of our full multiphase model. When closed with appropriate initial and boundary conditions, this model describes the spatial and temporal evolution of an asymmetric growing tumour in 3D. For simplicity and ease of comparison with the models considered in previous chapters, hereafter we restrict our attention to a 1D Cartesian geometry and investigate the dynamics exhibited by the model in this setting. We assume symmetry in our growing tumour and define coordinates such that $x = 0$ is at the centre of the tumour. At the centre of the tumour we impose symmetry conditions for the phase velocities, v_i, and oxygen concentration, c:

Symbol	Parameter
Γ	O_2 consumption rate
D	O_2 diffusion coefficient
c_∞	Normoxic O_2 concentration at exterior boundary
c_H	Tumour hypoxia threshold
c_N	Tumour necrosis threshold
ϵ	Heaviside smoothing parameter
η	Proliferation rate
κ	Apoptosis rate
χ	Necrosis rate
λ	Dead material decay rate
d_{ij}	Drag coefficient of phase j on phase i
μ_i	Viscosity of phase i
θ_μ	Relative viscosity of dead and tumour phases
θ_p	Relative 'cell-sensing' ability of dead phase
θ_Σ	Relative influence of dead phase on cell-sensing
ζ	Cell-sensing strength
ϕ^*	'Natural' cell volume fraction
ϕ_{min}	Minimum cell-sensing volume fraction

Table 4.1: Table of multiphase model parameters appearing in Equations (4.1)-(4.12).

$$v_i = 0, \quad \frac{\partial c}{\partial x} = 0 \quad \text{at} \quad x = 0. \tag{4.13}$$

The tumour boundary at $x = R(t)$ is defined to be at the exterior of the cell phase where the volume fraction ϕ_1 drops to 0 such that are no tumour cells for $x > R(t)$. The boundary then moves with the tumour cell phase velocity here such that

$$\frac{dR}{dt} = v_1|_{x=R(t)}. \tag{4.14}$$

We impose Dirichlet boundary conditions for the isotropic pressure, p, and the oxygen concentration, c, at the exterior boundary:

$$p = 0, \quad c = c_\infty \quad \text{at} \quad x = R(t). \tag{4.15}$$

The tumour is assumed to be growing into an extracellular fluid which offers little (or no) resistance to movement. In this scenario we assume that the boundary of the tumour is stress-free. Additionally, we follow the suggestion of Tao and Rajagopal [153, 154], and assume proportional splitting of traction on this boundary for our other boundary condition [1] which gives

$$\frac{4}{3}\mu_1 \frac{\partial v_1}{\partial x} - \Sigma_\phi(\phi_1 + \theta_\Sigma \phi_2) = \frac{4}{3}\theta_\mu \mu_1 \frac{\partial v_2}{\partial x} - \theta_p \Sigma_\phi(\phi_1 + \theta_\Sigma \phi_2) = 0 \quad \text{at} \quad x = R(t). \tag{4.16}$$

Equations (4.13) and (4.16) thus specify two boundary conditions for each of the phase velocities v_1 and v_2 whose evolution is described by two coupled second order elliptic equations (Equation (4.2)).

Equation (4.1) is a hyperbolic equation for the evolution of the volume fraction ϕ_1. Since the exterior boundary moves with the phase velocity v_1, we have that both $x = R(t)$ and $x = 0$ are characteristics and so we require no additional boundary conditions for the volume fraction ϕ_1. By contrast, this is not the case for the volume fraction ϕ_2. Where the exterior boundary of the tumour is an outflow boundary for this phase ($v_2 > v_1$ at

[1] We note that these boundary conditions do not require a factor of ϕ_1 and ϕ_2, respectively, since in our simulations we use non-zero initial conditions and thus the source terms, S_1 and S_2, in Equations (4.6) and (4.7) ensure that ϕ_1 and ϕ_2 remain non-zero.

$x = R(t)$) then the solution for ϕ_2 may still be specified along characteristics and we do not need to specify any additional boundary condition on $x = R(t)$. However, when we have an inflow boundary we must impose an additional boundary condition for this phase. We assume that any cellular debris that flows across the tumour boundary is cleared or decays away such that we have an exterior boundary layer for this phase in which the volume fraction ϕ_2 drops to 0, allowing for no inflow of non-viable material into the tumour. As such, we impose

$$\phi_2^+ = 0 \quad \text{at} \quad x = R(t), \tag{4.17}$$

where ϕ_2^+ represents the volume fraction of this phase immediately exterior to the tumour boundary $R(t)$.

It then only remains to specify the initial conditions

$$\phi_1 = \tilde{\phi_1}(x), \quad \phi_2 = \tilde{\phi_2}(x), \quad R = R_0 \quad \text{at} \quad t = 0. \tag{4.18}$$

4.2.4 Reducing the full multiphase system

Equations (4.1)-(4.18) describe the dynamics of our multiphase mixture. We may simplify this system by eliminating the volume fraction and velocity pertaining to the extracellular fluid, ϕ_3 and v_3, and the isotropic global pressure, p.

The no voids condition given by Equation (4.5) gives

$$\phi_3 = 1 - \phi_1 - \phi_2. \tag{4.19}$$

By summing the equations for conservation of mass of each phase (Equation (4.1)), integrating with respect to x and applying the boundary conditions at $x = 0$, we obtain an identity for the mixture velocity, $\sum_i \phi_i v_i = 0$. As such, the velocity of the fluid phase is given by

$$v_3 = \frac{1}{\phi_3}(-\phi_1 v_1 - \phi_2 v_2). \tag{4.20}$$

Similarly, by summing the equations for conservation of momentum (Equation (4.2)),

we may obtain an expression for $\frac{\partial p}{\partial x}$ in terms of the volume fractions ϕ_1 and ϕ_2, and the velocities v_1 and v_2:

$$\frac{\partial p}{\partial x} = -\phi_1 \frac{\partial \Sigma_\phi}{\partial x} - \theta_p \phi_2 \frac{\partial \Sigma_\phi}{\partial x} + \frac{4}{3}\mu_1 \frac{\partial}{\partial x}\left(\phi_1 \frac{\partial v_1}{\partial x}\right) + \frac{4}{3}\theta_\mu \mu_1 \frac{\partial}{\partial x}\left(\phi_2 \frac{\partial v_2}{\partial x}\right). \tag{4.21}$$

In this way, we obtain a reduced system of equations describing the evolution of the volume fractions ϕ_1 and ϕ_2, the phase velocities v_1 and v_2, and the oxygen tension c. The eliminated variables ϕ_3, v_3 and p may be recovered from Equations (4.19)-(4.21).

4.2.5 Summary of reduced model equations

We state below the reduced system of equations that define our multiphase model of tumour growth.

Mass conservation equations:

$$\frac{\partial \phi_1}{\partial t} + \frac{\partial}{\partial x}(\phi_1 v_1) = \eta \phi_1 (1 - \phi_1 - \phi_2) H_\epsilon(c - c_H) - \chi \phi_1 H_\epsilon(c_N - c) - \kappa \phi_1 \tag{4.22}$$

$$\frac{\partial \phi_2}{\partial t} + \frac{\partial}{\partial x}(\phi_2 v_2) = \chi \phi_1 H_\epsilon(c_N - c) + \kappa \phi_1 - \lambda \phi_2 \tag{4.23}$$

Oxygen profile:

$$0 = D\frac{\partial^2 c}{\partial x^2} - \Gamma \phi_1 H_\epsilon(c - c_H) \tag{4.24}$$

Momentum balances:

$$\begin{aligned} 0 = \frac{4}{3}\mu_1(1-\phi_1)\frac{\partial}{\partial x}\left(\phi_1 \frac{\partial v_1}{\partial x}\right) - \frac{4}{3}\theta_\mu \mu_1 \phi_1 \frac{\partial}{\partial x}\left(\phi_2 \frac{\partial v_2}{\partial x}\right) + d_{12}\phi_1\phi_2(v_2 - v_1) \\ - d_{13}\phi_1(\phi_2 v_2 + (1-\phi_2)v_1) - \phi_1(1-\phi_1)\frac{\partial \Sigma_\phi}{\partial x} + \theta_p \phi_1 \phi_2 \frac{\partial \Sigma_\phi}{\partial x} \end{aligned} \tag{4.25}$$

$$0 = -\frac{4}{3}\mu_1\phi_2\frac{\partial}{\partial x}\left(\phi_1\frac{\partial v_1}{\partial x}\right) + \frac{4}{3}\theta_\mu\mu_1(1-\phi_2)\frac{\partial}{\partial x}\left(\phi_2\frac{\partial v_2}{\partial x}\right) + d_{12}\phi_1\phi_2(v_1 - v_2) - d_{23}\phi_2(\phi_1 v_1 + (1-\phi_1)v_2) - \theta_p\phi_2(1-\phi_2)\frac{\partial \Sigma_\phi}{\partial x} + \phi_1\phi_2\frac{\partial \Sigma_\phi}{\partial x} \quad (4.26)$$

$$\Sigma_\phi(\phi) = \frac{\zeta(\phi - \phi_{min})^2(\phi - \phi^*)}{(1-\phi)}H(\phi - \phi_{min}) \quad (4.27)$$

Initial and boundary conditions:

$$\frac{dR}{dt} = v_1|_{x=R(t)} \quad (4.28)$$

$$\frac{\partial c}{\partial x} = 0, \quad v_1 = v_2 = 0 \quad \text{at} \quad x = 0 \quad (4.29)$$

$$\phi_2^+ = 0, \quad c = c_\infty \quad \text{at} \quad x = R(t) \quad (4.30)$$

$$\frac{4}{3}\mu_1\frac{\partial v_1}{\partial x} - \Sigma_\phi(\phi_1 + \theta_\Sigma\phi_2) = \frac{4}{3}\theta_\mu\mu_1\frac{\partial v_2}{\partial x} - \theta_p\Sigma_\phi(\phi_1 + \theta_\Sigma\phi_2) = 0 \quad \text{at} \quad x = R(t) \quad (4.31)$$

$$\phi_1 = \tilde{\phi_1}(x), \quad \phi_2 = \tilde{\phi_2}(x), \quad R = R_0 \quad \text{at} \quad t = 0 \quad (4.32)$$

4.3 Overview of numerical scheme

We solve Equations (4.22)-(4.32) numerically in order to simulate tumour growth for a variety of different parameter regimes. There are many ways in which we may solve this system of equations numerically, including finite difference [155], finite volume [156] and finite element [86, 88] methods. We develop a simple, stable finite difference scheme, however we note that a more sophisticated regime may be required for more rigorous

investigation of edge cases (see Appendix C.3 for further discussion).

Since Equations (4.22)-(4.32) are defined on a growing domain, we first map the governing equations onto a fixed domain, $x \mapsto \xi \in [0,1]$ in order to preserve the mesh spacing. The finite difference scheme is implemented on the fixed domain equations (presented in Appendix C.1.1) with N equally spaced nodes, with $\Delta\xi = \frac{1}{N-1}$. For simplicity, we use an explicit scheme with fixed timestep Δt. We use an upwind scheme to solve the hyperbolic mass conservation equations for the tumour and dead material phases, with the direction of upwinding dependent on the local phase velocities. The discretisation of the coupled elliptic equations for the phase velocities, v_1 and v_2, leads to a 'block tridiagonal' matrix system which we solve at each timestep. The quasi-steady oxygen concentration profile is solved using a fixed-point iteration scheme and pseudo-timestepping in order to deal with the non-linearities in the equation. An overview of the numerical method is given in pseudo-code in Algorithm 4, while a more detailed description is given in Appendix C.1.

Algorithm 4: Pseudo-code for numerical scheme.

Set mesh size $\Delta\xi$ and timestep Δt

/**Initialisation at $t = 0$*/*
Set initial conditions: $\phi_1(\xi, 0) = \tilde{\phi}_1(\xi)$, $\phi_2(\xi, 0) = \tilde{\phi}_2(\xi)$, $R(0) = R_0$
Solve coupled momentum equations for initial phase velocities $v_1(\xi, 0)$ and $v_2(\xi, 0)$ (Equations (C.21) and (C.22))
Solve for initial O_2 field, $c(\xi, 0)$ (Equations (C.34)-(C.36))

for *each timestep* **until** $t = T$ **do**
  /**Update variables with explicit time dependence*/*
  Update hyperbolic equations for volume fractions $\phi_1(\xi, t)$ and $\phi_2(\xi, t)$ using upwind method (Equations (C.12)-(C.17))
  Check CFL condition for stability of upwind method satisfied
  Update tumour radius $R(t)$ with forward Euler timestepping (Equation (C.19))
  /**Update variables without explicit time dependence*/*
  Solve coupled elliptic equations for phase velocities $v_1(\xi, t)$ and $v_2(\xi, t)$ (Equations (C.21) and (C.22))
  Update oxygen field, $c(\xi, t)$, using fixed-point iteration scheme with pseudo-timestepping (Equations (C.34)-(C.36))
end

4.4 Achieving a steady state

Having implemented the numerical scheme outlined in Section 4.3 (and detailed in Appendix C.1) and satisfied ourselves that the method is convergent as described in Appendix C.2, we proceed to investigate the dynamics of growing tumours in a variety of parameter regimes under these model equations. In Section 4.4.3 we perform a parameter sweep over a range of parameter values and characterise the qualitative growth behaviours observed. Unless specified otherwise the parameters given in Table 4.2 remain fixed for all simulations shown.

Parameter	**Value**
Γ	2
c_∞	1
c_H	0.3
D	1
d_{12}	1

Table 4.2: Table of fixed model parameter values for all simulations.

For all simulations, we start with an initial radius $R_0 = 0.3$. The initial volume fraction of tumour cells is uniform on $x = [0, R_0]$ with volume fraction $\tilde{\phi_1} = \phi^*$. Since the governing equations are singular when $\phi_2 \equiv 0$, we prescribe the uniform initial condition $\tilde{\phi_2} = 0.005$ for $x = [0, R_0]$.

The choice of uniform initial composition does not significantly affect the resulting evolution of the tumour over time (results not shown). Varying the uniform initial volume fraction of the tumour cell phase, $\tilde{\phi_1}$, simply introduces a small time delay in which the material within the tumour is initially redistributed before starting on the same growth trajectory. More specifically, if $\tilde{\phi_1} + \theta_\Sigma \tilde{\phi_2} < \phi^*$ on $x = [0, R_0]$ then the adhesion in the tumour phase, as given by Σ_ϕ in Equation (4.12), results in an initial contraction of the tumour radius while the volume fraction of the tumour phase within the tumour increases. When $\Sigma_\phi(\phi_1 + \theta_\Sigma \phi_2)|_{x=R(t)} > 0$, then the tumour radius starts to increase and the tumour follows the same qualitative growth trajectory as for other choices of initial condition.

In a similar manner, we may vary the initial tumour radius, R_0. For all values of R_0 chosen, our simulations resulted in the same steady state configuration (results not

shown). However for simulations in which the internal composition is important in driving the qualitative growth behaviour (c.f. Sections 4.5.1 and 4.5.2), starting the simulation at too large an initial radius may result in a different qualitative trajectory towards the steady state. In these cases, the uniform initial tumour composition, $\tilde{\phi_1}$, does not have enough time to be redistributed in order to influence the dynamics in the manners described in Sections 4.5.1 and 4.5.2. However for all reasonable, small values of R_0 relative to the steady state tumour radius, the resulting trajectories simulated were the same.

	Parameter value												
Case	c_N	η	χ	κ	λ	$d_{13} = d_{23}$	ζ	ϕ^*	ϕ_{min}	μ_1	θ_μ	θ_p	θ_Σ
i	0.1	1	1	0.05	0.1	0.1	3	0.8	0	1	0.5	1	1
ii	0.1	2	1	0.05	0.2	1	2	0.6	0.12	3	0.25	1	0.5
iii	0.2	1	1	0.05	0.05	0	2	0.8	0.16	0.5	0.1	0.5	1
iv	0.3	0.5	0.75	0.02	0.5	0	2	0.7	0	2	0.75	0.25	0.1
A	0.1	0.5	0.1	0.02	0.5	0	3	0.8	0	5	0.75	0.25	1
B	0.1	0.5	2	0.05	0.5	0.1	0.5	0.8	0.16	0.5	0.25	0.1	0.5
C	0.1	1	0.75	0.1	0.05	0.5	3	0.6	0.45	2	0.1	0.25	0.25
D	0.1	0.5	0.3	0.05	0.1	0.1	2	0.8	0.16	2	1	0.1	1

Table 4.3: Table of parameter values for each simulation discussed; cases i-iv pertain to the examples of different qualitative behaviours exhibited by the model presented in Sections 4.4 and 4.5, and cases A-D refer to the simulations discussed in Section 4.6.

4.4.1 Steady state solutions

The typical evolution of a tumour spheroid follows monotonic, sigmoidal growth-saturation [15]. The model is able to reproduce these dynamics which result in a steady state tumour radius, with one such example shown in Figure 4.2. The parameter values used for this simulation are listed in Table 4.3, case i.

Figure 4.2 visualises a snapshot of the tumour at the end of the simulation at $t = 100$. The top plot represents a cross-section of the tumour at this time point, showing the underlying composition with regards to the volume fractions of each phase. The volume fractions ϕ_1, ϕ_2 and ϕ_3 are represented by the dark blue, light blue and yellow regions, respectively. Note that we work in a 1D Cartesian geometry with symmetry such that

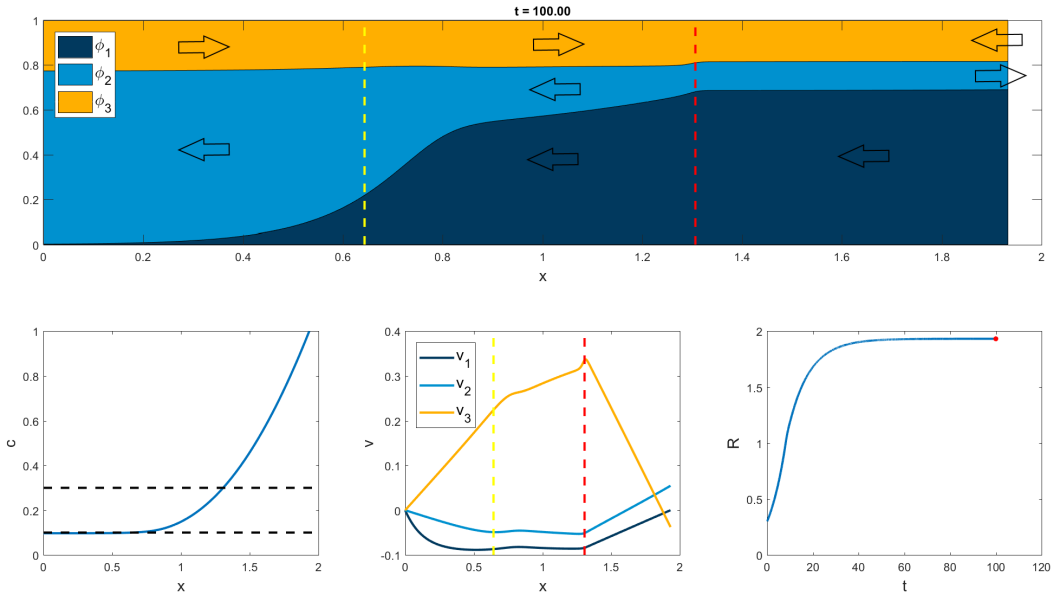

Figure 4.2: Example of a simulation in which the tumour grows monotonically and approaches a steady state, solving Equations (4.22)-(4.32) and using the parameter values in Tables 4.2 and 4.3, case i. **Top plot:** A cross-section of tumour profile at time $t = 100$ showing the internal distribution of each phase. The volume fraction of the tumour cells, ϕ_1, is shown in dark blue, the dead material volume fraction, ϕ_2, is shown in light blue, and the volume fraction for the extracellular fluid, ϕ_3, is represented in yellow. The dashed red and yellow vertical lines mark the positions of the internal radii R_H and R_N, respectively. The arrows represent the internal flow of material at steady state. **Bottom left plot:** The oxygen concentration, c, throughout the tumour at time $t = 100$ (blue line). The black horizontal dashed lines mark the thresholds for hypoxia and necrosis ($c_H > c_N$). **Bottom central plot:** The phase velocities v_i for $i = 1, 2, 3$ at time $t = 100$ coloured corresponding to the respective volume fractions, ϕ_i. **Bottom right plot:** The tumour radius trajectory $R(t)$ (blue line) with the red point marking the time point $t = 100$ corresponding the other plots.

$x = 0$ represents the centre of the tumour. The dashed red and yellow lines mark the positions of the internal contours R_H and R_N, respectively. These contours are defined by the oxygen thresholds for the onset of hypoxia and necrosis such that $c(R_H(t), t) = c_H$ and $c(R_N(t), t) = c_N$.

The bottom left subplot shows the corresponding oxygen tension at each point in space. The top horizontal dashed line marks the hypoxic threshold, c_H, while the bottom horizontal dashed line marks the threshold for necrosis, c_N. The central subplot shows the phase velocities v_1, v_2 and v_3 with line colours corresponding to the respective volume fractions in the composition plot. We note that the fluid phase velocity may be recovered using the mixture velocity as described in Section 4.2.4 even though we do not solve for it explicitly. Finally, the bottom right plot tracks the trajectory of the outer tumour radius over time.

The tumour composition at steady state is as we might expect from *in vitro* tumour spheroid experiments [15]. We observe an outer proliferative rim, $R_H < x < R$, in which the tumour phase volume fraction is approximately constant. At $x = R_H = 1.31$, the tumour becomes hypoxic and the cell phase is in a state of quiescence. This corresponds to the gradual decrease observed in the tumour phase volume fraction towards the centre of the tumour. At $x = R_N = 0.65$, the oxygen concentration reaches the threshold for necrosis, c_N, and we observe the formation of a central necrotic core, characterised by large a volume fraction in the dead material phase, ϕ_2, and very little volume fraction in the tumour cell phase, ϕ_1.

We also note that the steady state is achieved without the entirety of the tumour being in a dormant state. At steady state, the tumour reaches an equilibrium in which the mass gained in the tumour phase by proliferation balances that lost due to cell death. The tumour phase velocity, v_1, is zero at the tumour boundary, but is negative inside the tumour, $x \in (0, R)$. As such, an internal circulation is set up whereby the proliferation occurring in the outer rim acts to replace cell death occurring in the central necrotic core. This inward movement has also been observed experimentally in *in vitro* tumour spheroids [20]. We note that in this case, mass is lost from the tumour due to the flow of cellular debris out of the tumour boundary. The dead material in the necrotic core is undergoing exponential decay and acts as a mass source for the extracellular fluid phase

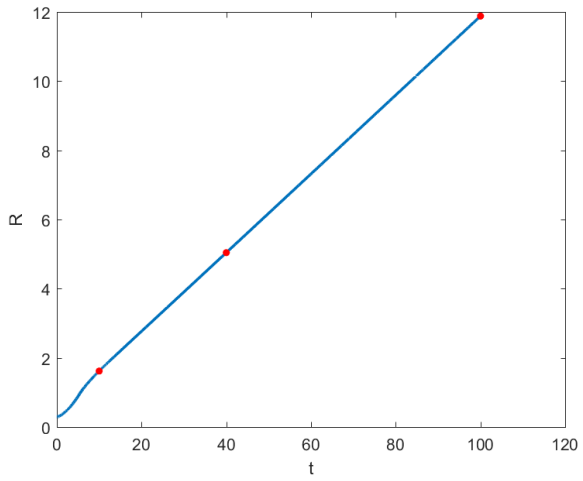

Figure 4.3: Tumour radius trajectory (blue line) exhibiting travelling wave behaviour from simulation of Equations (4.22)-(4.32) using the parameter values in Tables 4.2 and 4.3, case ii. The red dots mark the time points $t = 10, 40, 100$ for which we visualise the formation of the travelling wave profile in Figure 4.4.

(see Equations (4.7) and (4.8)). The flow of extracellular fluid is positive in the centre of the tumour, $x \in (0, R_H]$, but also flows into the tumour at the exterior boundary, providing the material required for proliferation at the outer rim of the tumour. The full circulation pattern at steady state for all phases is shown by the arrows in Figure 4.2.

4.4.2 Travelling wave solutions

For large regions of parameter space, the model generates travelling wave solutions. That is, after an initial transient period during which the tumour composition is dynamic, the tumour profile settles to a steady composition which moves with a constant velocity as a travelling wave. This is evident from the trajectory of the tumour radius shown in Figure 4.3 for one such simulation exhibiting this behaviour, with the parameter values for this simulation listed in Table 4.3, case ii.

Figure 4.4 visualises a snapshot of the tumour compositions at 3 different time points throughout the simulation, as marked by the red points in Figure 4.3. We see that at early times ($t = 10$) the evolution of the tumour composition is similar to in the previous case. As the tumour grows sufficiently large such that $c(0, t) \leq c_N \leq c_H$ we observe a region of high necrosis at the centre of the tumour. As with the previous example (c.f. Figure 4.2), this corresponds with a change of composition towards the centre of the tumour whereby, broadly speaking, $\frac{\partial \phi_1}{\partial x} > 0$ and $\frac{\partial \phi_2}{\partial x} < 0$ for $x < R_H$. However, in this case,

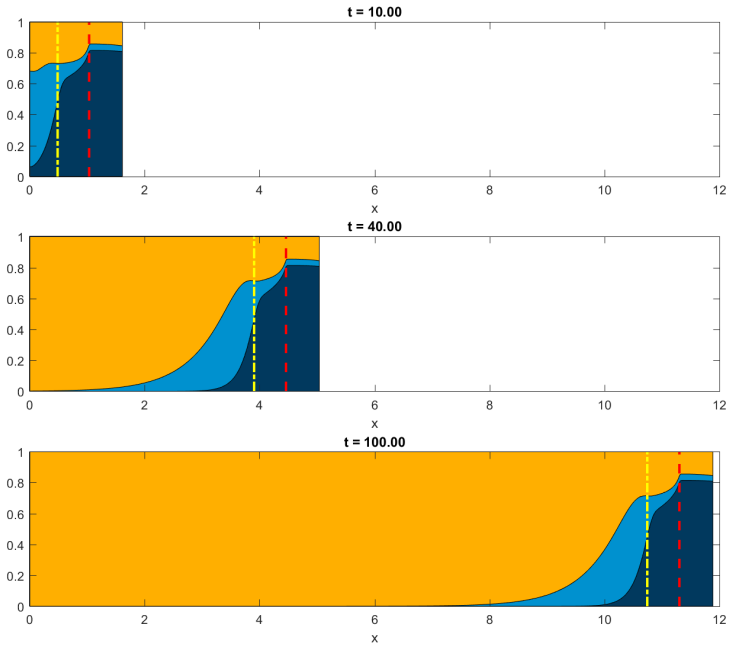

Figure 4.4: Visualisation of the internal composition of the tumour for the time series $t = 10, 40, 100$ showing the formation of a travelling wave profile, with corresponding tumour radius, $R(t)$, shown in Figure 4.3. The composition of the tumour is represented as in Figure 4.2.

as the tumour grows larger we see a decay of the dead material phase at the centre of the tumour resulting in $\phi_1, \phi_2 \ll 1$ at $x = 0$ and the composition shown in Figure 4.4 at $t = 40$. This profile remains the same at all later times, processing as a travelling wave with constant wave speed.

Equations (4.22)-(4.32) contain 19 parameters and a preliminary attempt to determine the ranges in parameter space in which we observe different behaviours was unable to come up with any meaningful results, due to the enormous complexity of the system. It is thus unclear which parameters/mechanisms determine the formation of a travelling wave as opposed to reaching a steady state tumour radius. A full study of parameter space remains an open question and is beyond the scope of this thesis. The formation of travelling waves has been reported in other similar multiphase models [82, 157].

While it may be possible for spheroids to grow as travelling waves *in vitro*, we typically observe tumours both *in vitro* and *in vivo* that evolve to a steady state. As such, we choose to focus on regions of parameter space that demonstrate eventual steady state behaviour. We note here that travelling wave solutions should not be interpreted as indicative of an

Parameter	Values for parameter sweep
c_N	$\{0.1, 0.2, 0.3\}$
η	$\{0.5, 1, 1.5, 3\}$
χ	$\{0.1, 0.3, 0.5, 0.75, 1, 2\}$
κ	$\{0.02, 0.05, 0.1, 0.5\}$
λ	$\{0.05, 0.1, 0.15, 0.25, 0.5, 0.75\}$
$d_{13} = d_{23}$	$\{0, 0.1, 0.5, 1\}$
ζ	$\{0.5, 1, 2, 3\}$
ϕ^*	$\{0.5, 0.6, 0.7, 0.8\}$
ϕ_{min}	$\{0, 0.2, 0.5, 0.75, 1\} \times \phi^*$
μ_1	$\{0.5, 1, 2, 3, 5\}$
θ_μ	$\{0.1, 0.25, 0.5, 0.75, 1\}$
θ_p	$\{0.1, 0.25, 0.5, 0.75, 1\}$
θ_Σ	$\{0.1, 0.25, 0.5, 0.75, 1\}$

Table 4.4: The parameter ranges included in the parameter sweep for the multiphase tumour growth model as defined by Equations (4.22)-(4.32).

invasive tumour. For such an interpretation, the model would need adapting to consider a tumour growing into surrounding tissue, in contrast to the stress-free boundary conditions imposed here.

4.4.3 Parameter sweep of tumour growth model

In Sections 4.4.2 and 4.4.1 we showed that the model exhibits two different qualitative growth dynamics. In order to characterise a wider range of behaviours captured by the model, we perform a wide-ranging parameter sweep. We vary 13 different model parameters, randomly selecting parameter values from the sets given in Table 4.4. The remaining model parameters are fixed to the values in Table 4.2. We simulate the model for each parameter combination up to time $t = 100$. The total number of parameter sets that may be generated is too large to feasibly simulate all possible combinations. As such we randomise the order in which we search this large parameter space and, in so doing, capture a range of qualitative growth dynamics exhibited by the model.

We catalogue all parameter combinations which generated steady state solutions and summarise the resulting equilibrium compositions in Figure 4.5. In the left-hand plot of

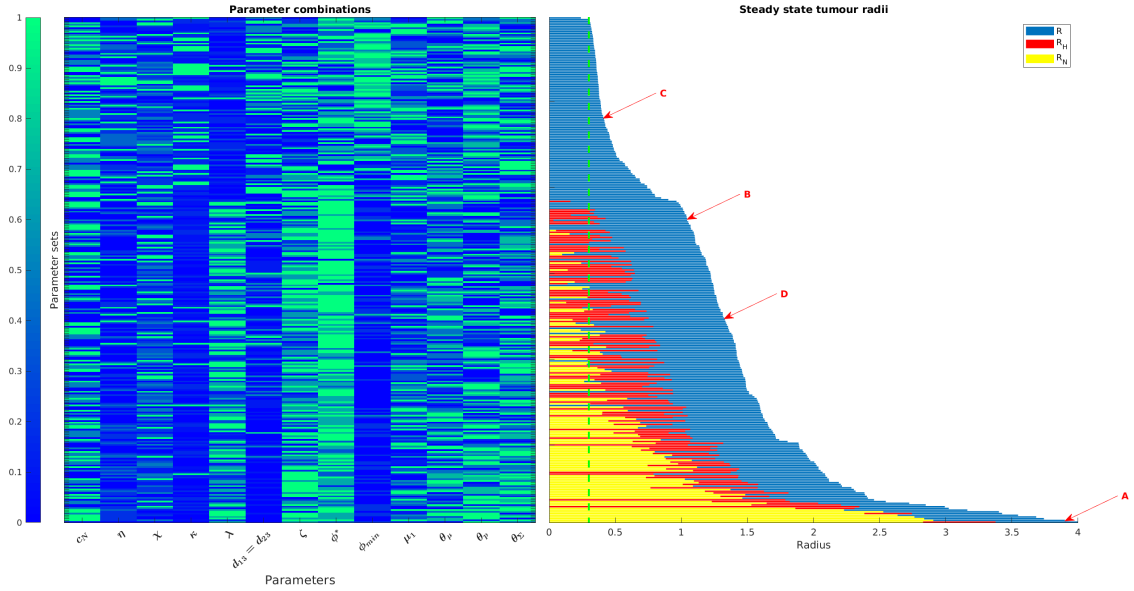

Figure 4.5: Catalogue of parameter combinations from the parameter sweep which generated steady state solutions. **Left plot:** Heat map of parameter values with each row pertaining to a particular parameter set. The colour scale corresponds to the range of values included in the parameter sweep for each parameter (see Table 4.4), with green representing the maximum of the range and blue the minimum. **Right plot:** Histogram of steady state tumour radii for the simulations corresponding to each row of the parameter heatmap. The blue bars show the steady state outer tumour radii, R, while the red and yellow bars show the positions of the internal radii R_H and R_N, respectively. The dashed green line represents the initial condition R_0 for each simulation.

Figure 4.5 we visualise the parameter combinations which resulted in a steady state by the end of the simulation at $t = 100$. Each row relates to a parameter set with each column pertaining to a single parameter. The colours correspond to the parameter values taken relative to the range of values included in the parameter sweep (i.e. green represents the maximum value for that parameter, whilst blue is the smallest).

The right hand plot in Figure 4.5 shows the corresponding tumour radii at steady state for the aforementioned parameter sets. The blue bars give the position of the outer tumour radius at steady state, with the dashed green line representing R_0 for reference. Where applicable, we also display the positions of internal radii R_H (red bars) and R_N (yellow bars) as a summary of the steady state tumour composition. The radii R_H, and R_N mark the spatial positions at which the oxygen concentration drops below the thresholds c_H and c_N, respectively. We also mark the positions of key parameter sets which we investigate further in Section 4.6 with the labels corresponding to those in Figure 4.10.

The parameter combinations are sorted by the resulting steady state tumour radius. At a glance, it is difficult to determine any particular correlations between the parameters and the tumour radius at steady state, however we may make some general observations. The central columns of parameters, namely ζ, ϕ^* and ϕ_{min}, relate to the cell-sensing activity in the tumour. It appears that stronger cellular interactions, ζ, combined with a larger values of $\phi^* - \phi_{min}$, the range of densities for which the cells experience adhesion, give rise to larger steady state solutions which do not become travelling wave solutions. Additionally, the more 'cell-like' the dead material phase is deemed to be, corresponding to large values of $(\theta_\mu, \theta_p, \theta_\Sigma)$, then the more active material within the tumour drives the evolution to a larger steady state radius. We observe this in the greater prominence of 'green' values in the bottom right of the heat map. We also notice that low necrotic decay rates, λ, tend to give rise to smaller steady state tumours, whilst low rates of apoptosis, κ, and low drag coefficients with the fluid phase, d_{i3}, tend to correspond to larger tumours.

More generally, it is difficult to identify meaningful parameter correlations and their effect on the tumour dynamics without further analysis. For any of the parameter combinations catalogued here, another, very different, parameter set may give rise to a similar steady state radius.

The results presented in Figure 4.5 also show that the model may give rise to steady state solutions with similar radii but different spatial structures. In particular, the locations of the internal radii at which the oxygen concentration drops below the thresholds for hypoxia and necrosis may vary with the system parameters while the outer radius remains unchanged. We note that this occurs even when the oxygen consumption rate, Γ, is held fixed. This heterogeneity in spatial composition may be significant when we extend our model to incorporate the effects of radiotherapy; we anticipate that the underlying spatial structure will affect treatment response, even for tumours of similar size.

4.5 Non-monotonic dynamics exhibited by multiphase model

As a result of our parameter sweep, we can catalogue many parameter sets which give rise to steady state solutions of varying compositions and and overall size. However, the dynamics by which the steady state is attained are also of interest. The qualitative

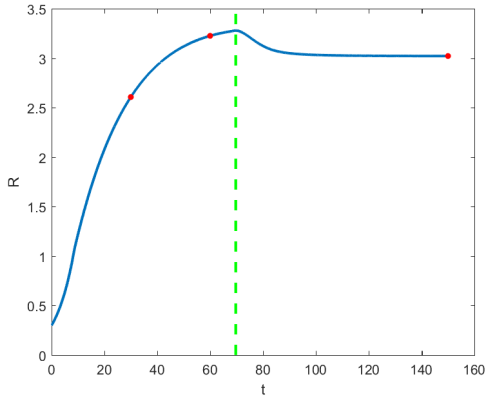

Figure 4.6: Tumour radius trajectory (blue line) for a simulation in which the steady state reached after an initial 'overshoot', solving Equations (4.22)-(4.32) and using the parameter values in Tables 4.2 and 4.3, case iii. The red dots mark the time points $t = 30, 60, 150$ for which we visualise snapshots of the internal tumour composition and phase velocities in Figure 4.7. The vertical dashed green line marks the time, t_{max}, at which the tumour attains its maximum radius, R_{max}.

behaviours described in Sections 4.4.1 and 4.4.2 match what is observed experimentally, with spatial structures that mimic those of avascular spheroids. Such results have been reported previously from similar (and also simpler) models [81, 82]. In this section we characterise two distinct types of non-monotonic dynamics exhibited by our multiphase model that, to the best of our knowledge, have not been generated by existing models of avascular tumour growth.

4.5.1 'Overshooting' the steady state

The first behaviour that we characterise is shown by the trajectory in Figure 4.6. In this case, the outer tumour radius initially increases monotonically, overshooting its steady state size. The tumour then shrinks and approaches the steady state radius monotonically from above. The dashed green line in Figure 4.6 marks the point at which the tumour attains its maximum radius, R_{max}, occurring at time t_{max}. The red points mark the time points for which we visualise the corresponding tumour compositions in Figure 4.7a and phase velocities in Figure 4.7b.

This 'overshoot' behaviour arises due to a change in the nature of the solution at the tumour boundary. During the initial growth phase, the tumour appears to approach steady state in a standard, monotonic manner with the phase velocity for the dead cells at the boundary, v_2, less than the cell velocity there, v_1 (see Figure 4.7). So for $0 <$

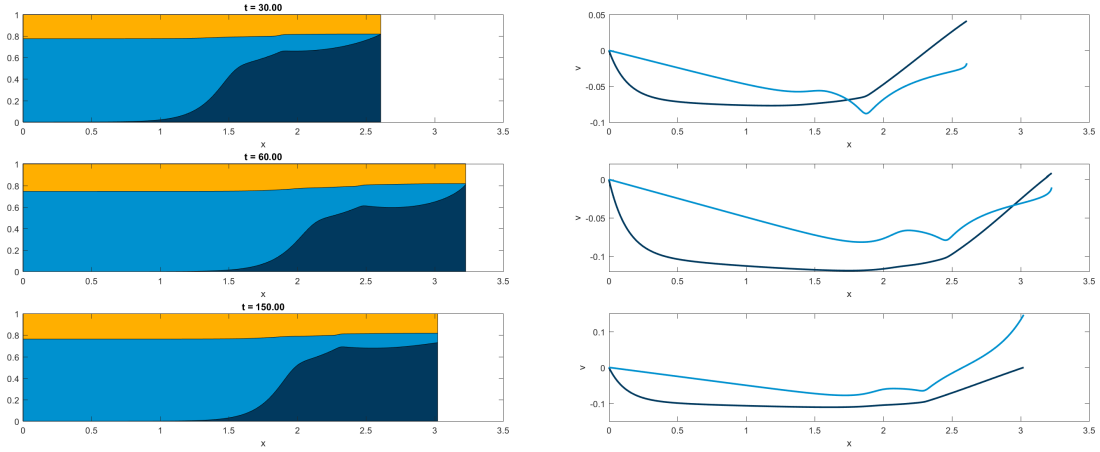

(a) (b)

Figure 4.7: Time series showing the (a) internal tumour composition and (b) phase velocities v_1 and v_2 throughout the simulation resulting in 'overshoot' dynamics shown in Figure 4.6. We observe a switch in the ordering of v_1 and v_2 at $x = R(t)$ between $t = 60$ and $t = 150$ which results in the non-monotonic trajectory. The volume fractions, ϕ_i, and phase velocities, v_i, are represented as in Figure 4.2 (v_3 not shown).

$t < t_{max}$, $v_1(R(t), t) > v_2(R(t), t)$. However, as the velocity of the boundary decreases ($\frac{dR}{dt} = v_1(R(t), t)$), it approaches the velocity of the dead material phase there. The turnaround point at $t = t_{max}$, marked by the vertical dashed green line on Figure 4.6, occurs when $v_1(R(t), t) = v_2(R(t), t)$. For $t > t_{max}$, $v_1(R(t), t) < v_2(R(t), t)$ and we observe a switch to an outflow boundary for the dead material. Thereafter dead material is lost from the interior of the tumour and the tumour decreases in volume. This continues until the tumour settles to a steady state radius which is smaller than the maximum radius, R_{max}, achieved at an earlier stage of growth. The steady state tumour composition is shown in Figure 4.7a and the tumour boundary is an outflow boundary for dead material at steady state. We note that the steady state tumour composition is similar to that presented in Section 4.4.1 (c.f. Figure 4.2) although the tumour's growth dynamics are very different.

The parameter values for this particular example are given in Table 4.3, case iii. Additional analysis of the numerics for this behaviour regarding identifying (t_{max}, R_{max}) is presented in Appendix C.3.1, although more in-depth analysis, both analytical and numerical, is required to more fully investigate this qualitative behaviour.

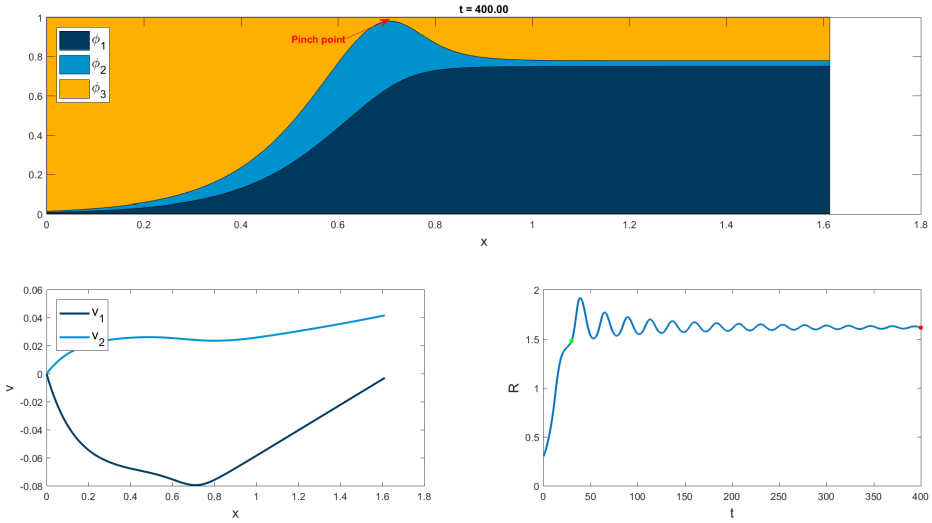

Figure 4.8: Example of a simulation of Equations (4.22)-(4.32) for which the tumour undergoes damped oscillations about a steady state. A snapshot of the internal tumour composition at $t = 400$ is shown in the top plot. The build up of the dead material phase at the edge of the necrotic core drives oscillatory dynamics and we annotate the 'pinch point' at which the fluid phase volume fraction v_3 is at its minimum. We visualise the velocities v_1 and v_2 at $t = 400$ in the bottom left plot while the oscillatory tumour radius trajectory is shown in the bottom right plot. The green and red dots mark the start and end points of the oscillations, respectively. The volume fractions, ϕ_i, and phase velocities, v_i, are visualised as in Figure 4.2. The parameter values for this simulation are listed in Tables 4.2 and 4.3, case iv.

4.5.2 Damped oscillations about the steady state

In Sections 4.4.1 and 4.5.1 we characterise tumour growth trajectories that eventually approach a steady state radius monotonically, either from below or above. However, our model also admits solutions for which the tumour undergoes damped oscillations about the steady state radius. The long-term dynamics for one such simulation are shown in Figure 4.8, with the model parameters for this simulation listed in Table 4.3, case iv.

In this case, the outer tumour boundary is an outflow boundary for the dead phase. In particular, $v_2(x,t) > 0 \quad \forall x \in (0, R(t)]$, which leads to the gradual loss of this cellular debris from the interior of the tumour across the boundary. However this outward flow of non-viable cells results in a build up of dead material at the edge of the necrotic core, where there is also a significant volume fraction of viable tumour cells, ϕ_1. It is this internal build-up of dead material which drives the oscillations in tumour radius observed.

In our model, the material required for proliferation of the viable tumour cells is provided by the extracellular fluid phase and therefore the rate of proliferation is proportional to the volume fraction of this phase, $\phi_3 = 1 - \phi_1 - \phi_2$. In the previous simulations shown,

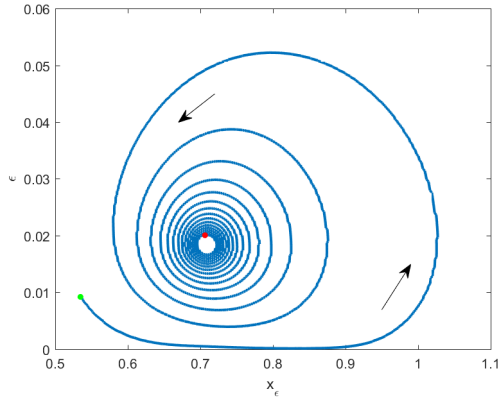

Figure 4.9: Phase plot in the (x_ϵ, ϵ)-plane of the oscillatory tumour dynamics, where $\epsilon(t) = \min_x \phi_3(x,t)$ and $x_\epsilon(t)$ is the location of $\epsilon(t)$. The arrows show the direction of increasing t, and the green and red points mark the start and end of the trajectory, respectively.

at steady state a balance is reached within the tumour between the total new tumour mass from proliferation and the mass lost due to cell death. When the dead material builds up at the edge of the necrotic core, it creates a 'pinch point' at which $\phi_3 \ll 1$, as annotated in Figure 4.8. We introduce the notation $\epsilon(t) = \min_x \phi_3(x,t)$ and denote by $x_\epsilon(t)$ the position within the tumour at which this pinch point occurs. In Figure 4.9 we visualise the damped oscillations as a spiral in the (x_ϵ, ϵ) phase plane. The start and end point of the oscillations are marked by the green and red points respectively in both Figure 4.8 and 4.9.

The build up of dead material locally restricts the ability of the tumour cells to proliferate even in the presence of sufficient oxygen. This results in a decrease in tumour volume while this build-up of necrotic material clears. This corresponds to an increase in $\epsilon(t)$ and a decrease in x_ϵ. Once sufficient necrotic material has been cleared the tumour cells then resume proliferation. The increased proliferation again results in the build up of dead material and the pinching off of the fluid phase, so that $\dot{\epsilon} < 0$. Once the total proliferation within the tumour surpasses cell death, the tumour radius begins to increase again and correspondingly $\dot{x_\epsilon} > 0$. This continued process results in the oscillations observed in the trajectory in Figure 4.8 and corresponding spiral in the (x_ϵ, ϵ) phase plane shown in Figure 4.9.

Further investigation of the dynamics of this 'pinch point' is presented in Appendix C.3.2. As for the overshoot dynamics, further analysis of this class of growth behaviour

may be tractable but is left as further work.

4.6 The influence of the dead material on tumour growth dynamics

Whilst the dynamics detailed in Sections 4.4 and 4.5 are of interest, in the face of often limited data (both temporally and spatially) it is natural to question the value of the additional complexity required to model an avascular tumour as a three phase mixture rather than a two phase mixture, for example.

As described in Section 4.2.2, the parameter vector $\boldsymbol{\theta} = (\theta_\mu, \theta_p, \theta_\Sigma)$ summarises the mechanical properties of the dead material phase relative to the tumour cell phase and the extracellular fluid phase. The parameter θ_μ specifies the relative viscosity of the dead phase (Equation (4.10)), while the parameters θ_p and θ_Σ pertain to the cell-sensing properties of this phase (see Equation (4.11)). In this section we perform a parameter sensitivity analysis in which the parameters θ_μ, θ_p and θ_Σ range across the unit cube. In this way we aim to determine how the manner in which we model the dead material phase affects the system dynamics. We note that the two corners of the cube, $(1, 1, 1)$ and $(0, 0, 0)$, correspond to two-phase limits of the full multiphase model.

We take a selection of parameter sets from the catalogue of values used to generate the steady state solutions described in Section 4.4.3. For each parameter combination, we perform a new parameter sweep over the sub-space $\boldsymbol{\theta} \in [0, 1]^3$, holding all other parameters fixed. As such, we isolate, in each case, the dependence on the material properties of the dead phase of the growth dynamics given an original parameter combination for which the tumour evolves to a steady state. We visualise the resulting trajectories for tumour radius over time for a selection of 4 such parameter sweeps in Figure 4.10. The original parameter sets for each case are annotated in Figure 4.5 with the values listed in Table 4.3, cases A-D.

The results presented in Figure 4.10 reveal a large variation in qualitative growth dynamics for certain parameter choices as we sweep over the sub-space $\boldsymbol{\theta} \in [0, 1]^3$. In the rest of this section we analyse further the range of different effects observed.

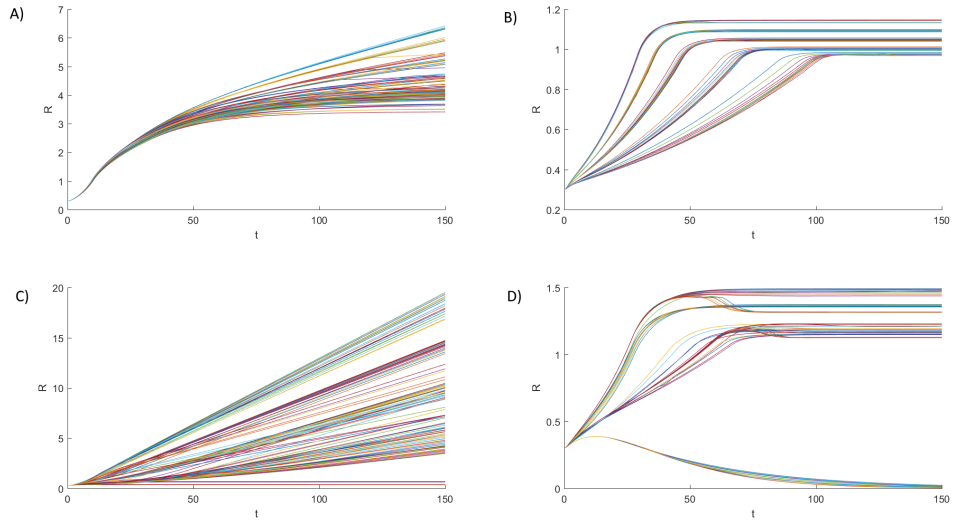

Figure 4.10: Tumour trajectories from a parameter sweep of the mechanical properties of the dead material phase, $\boldsymbol{\theta} \in [0,1]^3$ for 4 different cases, obtained by solving Equations (4.22)-(4.32). The parameter values for each case are listed in Table 4.3, cases A-D, and have been correspondingly annotated on in Figure 4.5.

4.6.1 Qualitative dynamics insensitive to the properties of the dead material

We observe some parameter regimes for which the properties of the dead material phase have little influence on the tumour radius trajectory. In case A in Figure 4.10 the growth dynamics are almost identical at early times. In this case, the parameter vector $\boldsymbol{\theta}$ appears to modulate the rate at which the tumour approaches its steady state, with a few cases evolving to travelling wave solutions rather than reaching equilibria.

We may summarise the proportion of the tumour volume at time t that is comprised of each phase by defining the averaged quantities

$$\bar{\phi}_i(t) = \frac{1}{R(t)} \int_0^{R(t)} \phi_i(x,t) dx. \tag{4.33}$$

In Figure 4.11 we visualise the composition of the tumour at the end of the simulation for each parameter set. We sort the parameter combinations by final tumour radius and plot a heatmap of parameter sets as previously, with each row corresponding to a particular value of $\boldsymbol{\theta}$. In the central plot of Figure 4.11 we visualise the final tumour composition, while the right-hand plot shows the final outer tumour radius, R, and the

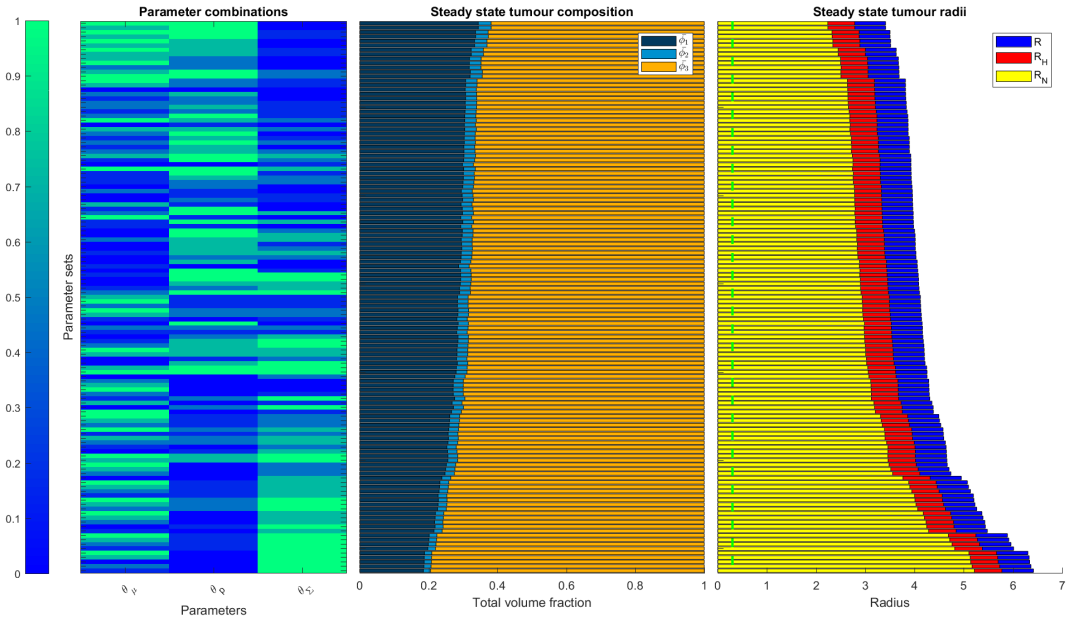

Figure 4.11: Summary of the steady state tumour compositions arising from case A of the $\boldsymbol{\theta}$-sweep (see Figure 4.10). **Left plot:** Heatmap of $\boldsymbol{\theta}$ parameter values corresponding to each simulation (visualisation as for Figure 4.5). **Central plot:** Proportion of the tumour volume at steady state comprised by each phase where $\bar{\phi}_i$ is defined by Equation (4.33). The tumour cell, dead material and extracellular fluid phases are represented by the dark blue, light blue and yellow regions, respectively. **Right plot:** Histogram showing the positions of the outer tumour radius, R (blue), and the internal radii, R_H (red) and R_N (yellow), at steady state for each simulation. The vertical dashed green line marks the initial radius, R_0, for each simulation.

positions of the internal radii, R_H and R_N.

We notice that in this case, in addition to very similar tumour radius trajectories, varying $\boldsymbol{\theta}$ does not significantly affect the resulting tumour composition. An increase in the steady state outer tumour radius corresponds with a similar decrease in the average tumour cell volume fraction, $\bar{\phi}_1$. As such, the resulting steady state tumours all have a similar total mass of tumour cells, with the parameter vector $\boldsymbol{\theta}$ acting to modulate the distribution of this material.

In case B in Figure 4.10, all trajectories exhibit the same qualitative behaviour. Furthermore, the trajectories appear to group into 5 bands. This grouping suggests dominance of a single parameter or parameter combination. In Figure 4.12 we visualise the parameter combinations along with summary statistics for the steady state tumour composition, as previously. For this case the steady state tumour radii are not sufficiently large to create a necrotic core and so $R_N = 0$ for all parameter combinations. The grouping of the tumours is also evident from the compositions at steady state. From the $\boldsymbol{\theta}$ parameter heatmap it is clear that the contribution of the dead phase to cell-sensing, θ_Σ, is the dominant parameter, with a larger value of θ_Σ resulting in a faster growing tumour which reaches a larger steady state radius.

In both of these cases discussed, the material properties of the dead phase, as summarised by the parameter vector $\boldsymbol{\theta}$, did not significantly alter the qualitative growth dynamics or the internal composition of the tumour. As such, we might expect that for cases such as these, the additional complexity of modelling the tumour as a three phase mixture is not necessary and that a simpler, two phase approach may be sufficient to capture the tumour dynamics.

4.6.2 Dead material has a quantitative effect on growth dynamics

However there are cases for which variation in the $\boldsymbol{\theta}$ parameters has a more significant impact on the tumour growth dynamics. While the original parameter sets all gave rise to tumours which evolved to a steady state, we see in case C in Figure 4.10 that most regions in the cube $\boldsymbol{\theta} \in [0, 1]^3$ result in travelling wave solutions.

For this case, we may quantify the affect of the parameter vector $\boldsymbol{\theta}$ by considering the resulting wave speed. In Figure 4.13 we plot the velocity of the tumour boundary at the

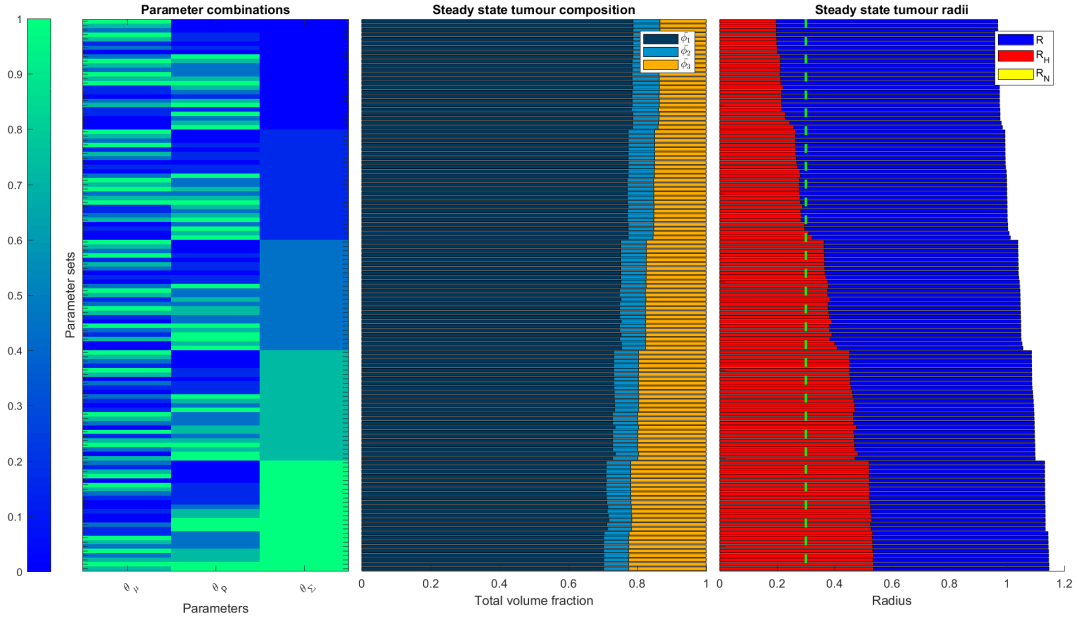

Figure 4.12: Summary of the steady state tumour compositions arising from case B of the $\boldsymbol{\theta}$-sweep (see Figure 4.10). Visualisation for each plot as in Figure 4.11. NB: $R_N = 0$ at steady state for all simulations in this case.

end of each simulation. We again notice that, for large values at least, θ_Σ is the dominant parameter in determining wave speed. Large values of θ_Σ creates larger pressures in the tumour cell phase which thus drives faster tumour growth. When θ_Σ takes smaller values this effect is not so clear with the other two parameters, θ_μ and θ_p, having more of an influence on the dynamics. It is not clear why a small number of simulations reach a steady state rather than evolving to a travelling wave profile, with further investigation of this difference a possible direction for future work.

4.6.3 Dead material has a qualitative effect on growth dynamics

In case D in Figure 4.10, we see that the mechanical properties of the dead material phase has an even greater influence on the resulting tumour growth trajectories. In this case, we see both monotonic and non-monotonic approaches to the steady state for different values of $(\theta_\mu, \theta_p, \theta_\Sigma)$, while for some regions of parameter space the system is unable to sustain a viable tumour.

We illustrate the influence of the $\boldsymbol{\theta}$ parameters more clearly in Figure 4.14 by considering a sub-space of the unit cube. We traverse a line between two corners of the cube,

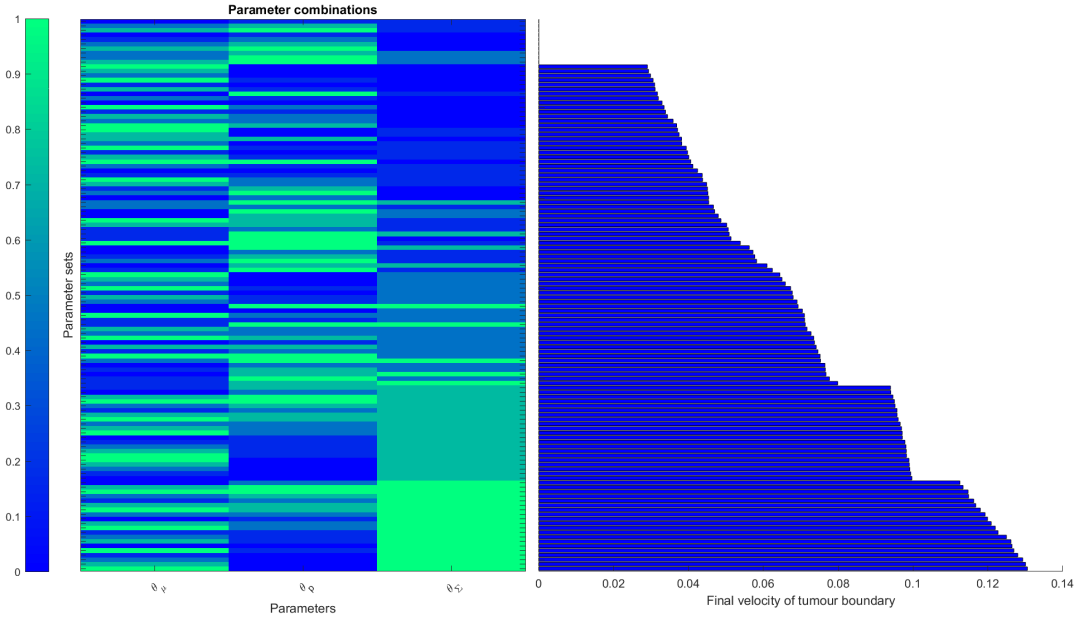

Figure 4.13: Visualisation of the travelling wave speeds arising for each simulation in case C of the $\boldsymbol{\theta}$ parameter sweep (see Figure 4.10). **Left plot:** Heatmap of $\boldsymbol{\theta}$ parameter values, visualised as in Figure 4.5. **Right plot:** Histogram of the velocity of the tumour boundary at the end of each simulation.

taking $\theta_\mu = \theta_p = \theta_\Sigma \in [0, 1]$. We note again that the corners $\boldsymbol{\theta} = (0, 0, 0)$ and $\boldsymbol{\theta} = (1, 1, 1)$ may be considered as two-phase limits of our three phase model.

In Figure 4.14 the colour of each trajectory corresponds to the value taken by the $\boldsymbol{\theta}$ parameters. We observe large variation in the qualitative tumour dynamics, with larger values of $\boldsymbol{\theta}$ corresponding to faster growing tumours that reach a larger steady state size. Conversely, smaller values result in smaller tumours with the smallest parameter regimes unable to sustain a viable tumour [2].

As such, we see that the dead material phase and its mechanical properties can have a large influence on the qualitative growth dynamics in some cases. In particular, the two different two phase limits may give rise to very different growth trajectories, with intermediate values of $\boldsymbol{\theta}$ resulting in a range of behaviours in between.

[2]Simulations for small values of $\boldsymbol{\theta}$ resulted in numerical instability due to the volume fraction for the fluid phase, ϕ_3, becoming very small upon contraction of the tumour radius. Accurately simulating this computationally would require a more sophisticated numerical scheme. Equally, the validity of the multiphase assumptions when one or more phases becomes extinct is also an open question to be addressed, but beyond the scope of this thesis.

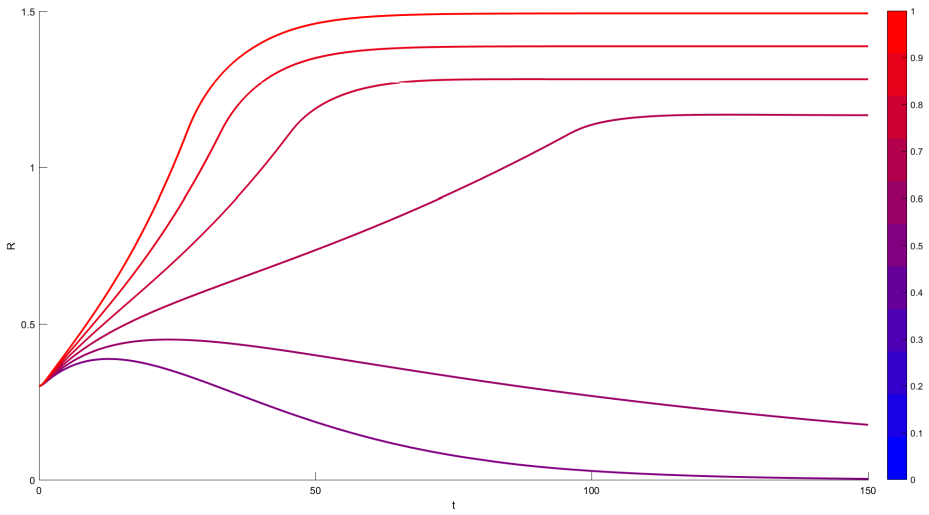

Figure 4.14: Tumour radius trajectories obtained by imposing $\theta_\mu = \theta_p = \theta_\Sigma \in [0, 1]$ for case D in Figure 4.10. The colour scale corresponds to the value taken by each of the $\boldsymbol{\theta}$ parameters.

4.7 Discussion

Tumour cells may die via a number of different mechanisms occurring over different timescales [11, 29, 30, 144]. As such, the non-viable cells may occupy a significant proportion of the tumour and interact with other constituents of the tumour microenvironment. This may also vary between different tumours. The simplest multiphase models consider two constituent phases; tumour cells and extracellular fluid. It is unclear both how to model the non-viable cells, and the resulting effect this may have on the tumour dynamics. In this chapter we have presented a novel three phase, mixture model of nutrient-limited tumour growth. We model the tumour as being comprised of tumour cells, non-viable cells and necrotic material, and extracellular fluid. In our model, the dead material phase differs from both the tumour cell and extracellular fluid phases in its physical properties, which we hypothesise to have a significant effect on both tumour growth and response to radiotherapy.

In Section 4.2 we derived the model equations for our multiphase system and, in particular, introduce three key model parameters, $\boldsymbol{\theta} = (\theta_\mu, \theta_p, \theta_\Sigma)$, which summarise the physical properties of the dead material. We explained how to reduce this set of equations to the model system given by Equations (5.15)-(5.25). This system of equations comprises two hyperbolic equations for mass conservation in the tumour cell and dead material

phases, along with two elliptic equations for the corresponding phase velocities. The system is coupled to a reaction-diffusion equation for the intratumoural oxygen tension upon which the tumour growth is assumed to depend. We developed a finite difference scheme in Section 4.3 and Appendix C.1 to solve this system numerically.

We used numerical simulation to investigate the range of growth dynamics exhibited by the model. We demonstrated that the model can reproduce biologically realistic tumour dynamics and spatial structures which we may expect to observe in *in vitro* avascular spheroids [15].

We also characterised some non-monotonic growth behaviours exhibited by the model which are driven by the dynamics of the dead material phase. To the best of our knowledge these dynamics have not been captured by existing models of avascular tumour growth. It is unclear whether some of these features may be artefacts of the 1D geometry used here. In particular, we may expect that the 'pinch-off' of the fluid phase resulting in oscillatory tumour dynamics may not be stable to symmetry-breaking perturbations in 2D and 3D. Directions for future work on this model could include asymptotic analysis of these dynamics and extension of the numerics into 2D and/or 3D.

In Section 4.6 we investigated the influence of the dead phase on the tumour growth dynamics. For some cases considered, we observe large variations in tumour radius over time as we move around the parameter sub-space $\boldsymbol{\theta} \in [0,1]^3$. We conclude that the material properties of the non-viable cells, and the way in which we model them, may have a significant influence on the dynamics observed.

The work in this chapter is presented in anticipation of the inclusion of radiotherapy effects into the model in Chapter 5. In applying radiation to the tumour, we introduce a significant alteration to the tumour composition which will result in redistribution of material between the tumour and non-viable cell phases. Given the results presented in this chapter, we may expect the volume fraction of the dead phase to significantly impact the qualitative response of the tumour to radiotherapy.

However, we also illustrated cases for which the tumour dynamics were not significantly affected by variations in the properties of the dead material phase. In these cases, we may anticipate that a simpler model may adequately describe the tumour dynamics. This is of particular significance when we consider the limited data, in both temporal and

spatial resolution, which is typically available for parametrising models in the clinic.

Chapter 5

A multiphase model for radiotherapy response

5.1 Introduction

When radiotherapy is delivered to a tumour, the radiation causes lesions in the DNA within the cells upon absorption [24]. The damage caused may be fatal to the cells, with cell death potentially occurring via a number of different mechanisms over potentially different timescales [29, 30]. As such, cells that are fated to die may occupy volume within the tumour for some time after irradiation and may subsequently affect the response dynamics.

The Linear-Quadratic (LQ) model, and its extensions, is typically used to describe the dose-dependent radiation-induced cell death [40]. This model was initially proposed as an empirical formula derived from *in vitro* clonogenic survival assays [40]. As such, the LQ model is most suited to describing the long-term dose-dependent survival fraction post-irradiation but may not adequately model the dynamics of the radiation-induced cell death. More specifically, the LQ model may be used to determine the proportion of tumour cells fated to die post-irradiation, although this may not correspond to an instantaneous loss of material from the tumour volume as is often modelled.

In this chapter we extend the multiphase model for tumour growth developed in Chapter 4 to incorporate the effects of radiotherapy. The multiphase framework allows for spa-

tial variation in each of the constituent phases in the mixture, generalising the restrictive geometry considered in the model developed in Chapter 3. This framework provides a natural setting to investigate the influence of the non-viable, dying cells and cellular debris on the tumour dynamics in the context of radiotherapy response. Radiation-induced cell death may be incorporated as a mass transfer between the phases in the mixture, thus altering the internal tumour composition without the, perhaps unrealistic, instantaneous volume loss. The effect of the radiotherapy on the tumour volume may then be realised as a redistribution of material within the tumour post-irradiation.

In light of the rich dynamics observed for the multiphase tumour growth model presented in the previous chapter, we expect this model to capture a wider range of the qualitative responses to radiotherapy observed in clinical data. In particular, given the demonstrated importance of the dead material within the tumour on the resulting growth dynamics for many parameter regimes (see Section 4.6), we hypothesise that the properties of the dead material may have a strong influence on radiotherapy response. However, in Section 4.6 we also identified cases for which the mechanical properties of the dead material did not have a significant effect on the resulting growth dynamics. This is of interest since, if radiotherapy response is similarly unaffected by the dead material, then such cases may be adequately described by simpler models which may be more easily calibrated from limited clinical data.

In Section 5.2 we recap the multiphase model for tumour growth developed in Chapter 4 and explain how we incorporate the effects of radiotherapy into the model. In Section 5.3 we use numerical simulation to demonstrate the effects of radiation on the internal tumour composition and the resulting dynamics. In Section 5.4 we demonstrate the ability of the multiphase model to reproduce the range qualitative response dynamics observed in clinical data, while in Section 5.5 we focus on the regrowth dynamics exhibited by the model post-radiotherapy. Finally, in Section 5.6 we investigate the influence of the dead material within the tumour on the dynamics of radiotherapy response.

5.2 Incorporating radiotherapy into the multiphase model

In this section we extend the multiphase model developed in the previous chapter to include the effects of radiotherapy. We restate the full growth model equations in Section 5.2.1 before explaining how we adapt these to include radiotherapy response in Section 5.2.2. We eliminate some of the variables to obtain a reduced set of equations, as in Chapter 4, which is stated in Section 5.2.3. The final system of equations are solved numerically in order to simulate the dynamics of tumour growth and radiotherapy exhibited by our multiphase model. In Section 5.2.4, we describe how we incorporate the simulation of radiotherapy protocols into the numerical scheme developed in the previous chapter.

5.2.1 Growth model equations

Here we restate the multiphase model for tumour growth developed in Chapter 4. We model the growing tumour as a multiphase mixture comprising three different phases, namely, the tumour cell phase, the non-viable cells and cellular debris, and the extracellular fluid. Each phase is associated with a volume fraction at each point in space and time, ϕ_i, and a phase velocity, $\mathbf{v_i}$, for $i = 1, 2, 3$. We apply the principles of conservation of mass and momentum to each phase (Equations (5.1) and (5.2)). We model nutrient-limited tumour growth whereby the local oxygen tension affects the proliferative status of the tumour cells. As such the system is coupled to a reaction-diffusion equation for the oxygen concentration, c, given by Equation (5.3).

$$\text{(Conservation of mass)} \qquad \frac{\partial \phi_i}{\partial t} + \nabla \cdot (\mathbf{v_i}\phi_i) = S_i \tag{5.1}$$

$$\text{(Conservation of momentum)} \qquad 0 = \nabla \cdot (\phi_i \underline{\boldsymbol{\sigma}_i}) + \mathbf{F_i} \tag{5.2}$$

$$(O_2 \text{ reaction-diffusion}) \qquad 0 = D\nabla^2 c - \Gamma \phi_1 H_\epsilon(c - c_N) \tag{5.3}$$

The function H_ϵ is a smooth approximation to the Heaviside step function and is defined by

$$H_\epsilon(c) = \frac{1}{2}\left(1 + \tanh\left(\frac{c}{\epsilon}\right)\right). \tag{5.4}$$

This system of equations governing the dynamics of each phase within the tumour must be closed by specification of appropriate constitutive relations describing the physical properties of each phase and the interactions between them. The full set of constitutive relations are given by Equations (5.5)-(5.9).

(No voids)
$$\sum_i \phi_i = 1 \tag{5.5}$$

(Mass sources)
$$S_1 = \eta\phi_1\phi_3 H_\epsilon(c - c_H) - \chi\phi_1 H_\epsilon(c_N - c) - \kappa\phi_1 \tag{5.6}$$
$$S_2 = \chi\phi_1 H_\epsilon(c_N - c) + \kappa\phi_1 - \lambda\phi_2, \quad S_3 = -(S_1 + S_2)$$

(Momentum sources)
$$\mathbf{F_i} = p_i\nabla\phi_i + \sum_{j\neq i} d_{ij}\phi_j\phi_i(\mathbf{v_j} - \mathbf{v_i}) \tag{5.7}$$

(Stress tensors)
$$\underline{\boldsymbol{\sigma_i}} = -p_i\underline{\mathbf{I}} + \mu_i(\nabla\mathbf{v_i} + \nabla\mathbf{v_i}^T) + \lambda_i(\nabla\cdot\mathbf{v_i})\,\underline{\mathbf{I}} \tag{5.8}$$
$$\lambda_i = -\frac{2}{3}\mu_i, \quad \mu_1 \geq \mu_2 = \theta_\mu\mu_1 \geq \mu_3 = 0$$

(Pressures)
$$p_1 = p + \Sigma_\phi(\phi_1 + \theta_\Sigma\phi_2), \quad p_2 = p + \theta_p\Sigma_\phi(\phi_1 + \theta_\Sigma\phi_2), \quad p_3 = p \tag{5.9}$$
$$\text{where} \quad \Sigma_\phi(\phi) = \frac{\zeta(\phi - \phi_{min})^2(\phi - \phi^*)}{(1-\phi)}H(\phi - \phi_{min})$$

We model the tumour and necrotic phases as viscous fluids, while the extracellular fluid is modelled as inviscid. Of particular note is the parameter vector $\boldsymbol{\theta} = (\theta_\mu, \theta_p, \theta_\Sigma)$ which describes the material properties of the necrotic phase relative to the tumour cell phase. A full explanation of each term is provided in Chapter 4.

5.2.2 Modelling radiotherapy response

We include the effects of radiotherapy as an instantaneous mass transfer between the tumour cell and dead material phases at the time of delivery of each fraction, t_j. As such we modify the mass source terms, S_i, to include an additional term for radiotherapy effects as follows:

$$S_1 = \eta\phi_1\phi_3 H_\epsilon(c - c_H) - \chi\phi_1 H_\epsilon(c_N - c) - \kappa\phi_1 - \sum_j \nu(c)\phi_1\delta(t - t_j), \tag{5.10}$$

$$S_2 = \chi\phi_1 H_\epsilon(c_N - c) + \kappa\phi_1 - \lambda\phi_2 + \sum_j \nu(c)\phi_1\delta(t - t_j), \tag{5.11}$$

$$S_3 = -S_1 - S_2. \tag{5.12}$$

Here, $\nu(c)$ encompasses the radiation-induced cell death as dependent on the local oxygen concentration, c, and may be related to the cell survival fraction, sf, by $\nu = 1 - sf$.

We note that, while still modelled as an instantaneous effect, our treatment of radiotherapy in this model is markedly different from that presented in previous chapters and as is common in the literature. In particular, the radiation results in an immediate change in tumour composition without changing the tumour radius, in contrast with the jump in tumour volume observed in other models. The effect of the radiotherapy on the total tumour volume is then given by the resulting dynamics between fractions as influenced by the new internal distribution of the tumour constituents. As such, we might expect that this model may reproduce some of the qualitative behaviours not captured by the simpler models and result in more realistic, continuous trajectories for tumour radius over time, $R(t)$.

As described in Chapter 1, the Linear-Quadratic (LQ) model is typically used to describe the dose-dependent survival fraction, sf, of tumour cells after irradiation. The standard LQ model is given by

$$sf = e^{-\alpha d - \beta d^2}, \tag{5.13}$$

where α and β are intrinsic radiosensitivity parameters for the tissue. The response characteristics of the tumour are typically characterised by the ratio α/β [40].

The local oxygen status within the tumour is well-known to affect radiosensitivity, with hypoxic regions responding poorly to radiation. The LQ model is often extended to account for this effect by way of the oxygen enhancement ratio (OER). Here we modify the LQ model to incorporate oxygen dependence in the same way as described in Chapter

3.

The simplest implementation of the this effect is to create a step function for the LQ model at the threshold for hypoxia, c_H (Equation (5.14)). In this case, the OER is a constant factor in hypoxic areas of the tumour, taken to be equal to 3 in our simulations.

$$sf(c) = \begin{cases} \exp(-\alpha d - \beta d^2) & c > c_H \\ \exp\left(-\frac{\alpha}{OER} d - \frac{\beta}{OER^2} d^2\right) & c < c_H \end{cases} \tag{5.14}$$

In practice, $sf(c)$ is likely to depend continuously on the local oxygen concentration, c. Within this model, we might expect the two forms for the OER to produce markedly different behaviour in both the model solution and the numerical simulation since the discontinuous form of the OER (Equation (5.14)) induces a corresponding discontinuity in the volume fractions ϕ_1 and ϕ_2. We provide a comparison of the two different OER formulations within the model in Appendix B.2.

5.2.3 Reduced model equations

As in the previous chapter we solve a reduced system of equations by eliminating the variables pertaining to the extracellular fluid phase, ϕ_3 and v_3, and the global pressure variable, p.

The final system of equations is stated below.

Mass conservation equations:

$$\frac{\partial \phi_1}{\partial t} + \frac{\partial}{\partial x}(\phi_1 v_1) = \eta \phi_1 (1 - \phi_1 - \phi_2) H_\epsilon(c - c_H) - \chi \phi_1 H_\epsilon(c_N - c) - \kappa \phi_1 - \sum_j \nu(c) \phi_1 \delta(t - t_j) \tag{5.15}$$

$$\frac{\partial \phi_2}{\partial t} + \frac{\partial}{\partial x}(\phi_2 v_2) = \chi \phi_1 H_\epsilon(c_N - c) + \kappa \phi_1 - \lambda \phi_2 + \sum_j \nu(c) \phi_1 \delta(t - t_j) \tag{5.16}$$

Oxygen profile:

$$0 = D \frac{\partial^2 c}{\partial x^2} - \Gamma \phi_1 H_\epsilon(c - c_H) \tag{5.17}$$

Momentum balances:

$$0 = \frac{4}{3}\mu_1(1-\phi_1)\frac{\partial}{\partial x}\left(\phi_1\frac{\partial v_1}{\partial x}\right) - \frac{4}{3}\theta_\mu\mu_1\phi_1\frac{\partial}{\partial x}\left(\phi_2\frac{\partial v_2}{\partial x}\right) + d_{12}\phi_1\phi_2(v_2-v_1) \\ - d_{13}\phi_1(\phi_2 v_2 + (1-\phi_2)v_1) - \phi_1(1-\phi_1)\frac{\partial \Sigma_\phi}{\partial x} + \theta_p\phi_1\phi_2\frac{\partial \Sigma_\phi}{\partial x} \quad (5.18)$$

$$0 = -\frac{4}{3}\mu_1\phi_2\frac{\partial}{\partial x}\left(\phi_1\frac{\partial v_1}{\partial x}\right) + \frac{4}{3}\theta_\mu\mu_1(1-\phi_2)\frac{\partial}{\partial x}\left(\phi_2\frac{\partial v_2}{\partial x}\right) + d_{12}\phi_1\phi_2(v_1-v_2) \\ - d_{23}\phi_2(\phi_1 v_1 + (1-\phi_1)v_2) - \theta_p\phi_2(1-\phi_2)\frac{\partial \Sigma_\phi}{\partial x} + \phi_1\phi_2\frac{\partial \Sigma_\phi}{\partial x} \quad (5.19)$$

$$\Sigma_\phi(\phi) = \frac{\zeta(\phi-\phi_{min})^2(\phi-\phi^*)}{(1-\phi)}H(\phi-\phi_{min}) \quad (5.20)$$

Initial and boundary conditions:

$$\frac{dR}{dt} = v_1|_{x=R(t)} \quad (5.21)$$

$$\frac{\partial c}{\partial x} = 0, \quad v_1 = v_2 = 0 \quad \text{at} \quad x = 0 \quad (5.22)$$

$$\phi_2^+ = 0, \quad c = c_\infty \quad \text{at} \quad x = R(t) \quad (5.23)$$

$$\frac{4}{3}\mu_1\frac{\partial v_1}{\partial x} - \Sigma_\phi(\phi_1 + \theta_\Sigma\phi_2) = \frac{4}{3}\theta_\mu\mu_1\frac{\partial v_2}{\partial x} - \theta_p\Sigma_\phi(\phi_1+\theta_\Sigma\phi_2) = 0 \quad \text{at} \quad x = R(t) \quad (5.24)$$

$$\phi_1 = \tilde{\phi_1}(x), \quad \phi_2 = \tilde{\phi_2}(x), \quad R = R_0 \quad \text{at} \quad t = 0 \quad (5.25)$$

Radiotherapy is delivered in fractions of dose d_j Gy at times t_j. The radiation-induced cell death is modelled by the term $\nu = 1 - sf$, where sf takes the form of the modified

LQ formulation stated in Equation (5.14).

5.2.4 Numerical scheme for simulating radiotherapy response

In order to simulate the model dynamics for radiotherapy response we solve the system of equations (5.15)-(5.25) numerically. We adapt the scheme detailed in Chapter 4 and Appendix C.1 to include radiotherapy effects as outlined in the pseudo-code presented in Algorithm 5.

Algorithm 5: Pseudo-code for numerical scheme.

Set mesh size $\Delta\xi$ and timestep Δt

/**Initialisation at* $t = 0$*/*
Set initial conditions: $\phi_1(\xi, 0) = \tilde{\phi_1}(\xi)$, $\phi_2(\xi, 0) = \tilde{\phi_2}(\xi)$, $R(0) = R_0$
Solve coupled momentum equations for initial phase velocities $v_1(\xi, 0)$ and $v_2(\xi, 0)$ (Equations (C.21) and (C.22))
Solve for initial O_2 field, $c(\xi, 0)$ (Equations (C.34)-(C.36))

/**Solve model equations for initial pre-treatment growth period**/*
Apply Algorithm 4 until $t = t_1$

for *each fraction of radiotherapy* **do**
  /**Apply radiotherapy effects**/*
  Update tumour radius $R(t)$ with forward Euler timestepping (Equation (C.19))
  Update volume fractions $\phi_1(\xi, t)$ and $\phi_2(\xi, t)$ with radiotherapy effects only, applying LQ model for survival fractions at each point in space
  Solve coupled elliptic equations for phase velocities $v_1(\xi, t)$ and $v_2(\xi, t)$ with new tumour composition (Equations (C.21) and (C.22))
  Update oxygen field, $c(\xi, t)$, using fixed-point iteration scheme with pseudo-timestepping for new composition (Equations (C.34)-(C.36))
  /**Solve equations for inter-fraction tumour growth**/*
  Apply Algorithm 4 for inter-fraction growth until $t = t_{j+1}$
end

5.3 Tumour dynamics for radiotherapy response

Having adapted our model equations and numerical scheme to incorporate the effects of radiotherapy we simulate the response to treatment for a variety of *in silico* tumours and fractionation protocols in order to investigate the dynamics exhibited by the model. In this section we illustrate the effects of irradiation in our model, simulating the response to a single fraction. This section serves as a preliminary investigation of the model before

simulating full radiotherapy protocols. The results in the following sections are obtained from a parameter sweep which is described in more detail in Appendix D.

In this section we illustrate the effects of radiotherapy within the model by considering the response to a single fraction of radiation. For these purposes we consider a parameter regime for which the tumour exhibits regular, monotonic growth and eventually approaches a steady state with an outer proliferative rim and central necrotic core (see Section 4.4.1 for details and Tables 4.2 and 4.3, case i for growth parameter values). We simulate a single fraction of radiotherapy of dose 2 Gy delivered at time $t = 20$. For these simulations we use radiosensitivity parameters of $\alpha = 0.35$ Gy^{-1} and $\alpha/\beta = 10$ Gy, and use the step function form of the OER given by Equation 5.14.

The tumour radius trajectory for this simulation is shown in Figure 5.1. A time series of the internal tumour composition and phase velocities at selected times pre- and post-irradiation corresponding to the red dots on the tumour trajectory is presented in Figure 5.2. The first two time points visualised correspond to immediately before (-) and after (+) the delivery of the first fraction of radiotherapy at $t_1 = 20$.

We see in Figure 5.2a that the step function formulation of the OER results in a jump in the tumour cell volume fraction ϕ_1 either side of the pre-radiotherapy contour $x = R_H(t_1^-)$ due to the effects of hypoxia on the survival fraction of the tumour population. The loss of mass from the tumour cell phase results in re-oxygenation within the tumour and correspondingly we see that post-radiotherapy hypoxia threshold moves towards the centre of the tumour such that $R_H(t_1^+) < R_H(t_1^-)$. However, we also note a key feature of this model that the outer tumour radius, R, does not experience an instantaneous jump due to radiotherapy and so $R(t_1^+) = R(t_1^-)$. Instead we see from Figure 5.2b that the composition change within the tumour induces a change in the phase velocities, v_i. In particular, we note that $v_1(R(t_1^+), t_1^+) < 0$ and thus the tumour radius decreases in response to irradiation in this case.

The radiotherapy effects a big change in the tumour composition. The regrowth dynamics post-irradiation are thus affected by the redistribution of material within the tumour. In Figure 5.2a we visualise the composition at 3 further times during the regrowth of the tumour. We see that the volume fractions smooth out over time as the material is gradually redistributed towards a composition similar to the control, growth composition

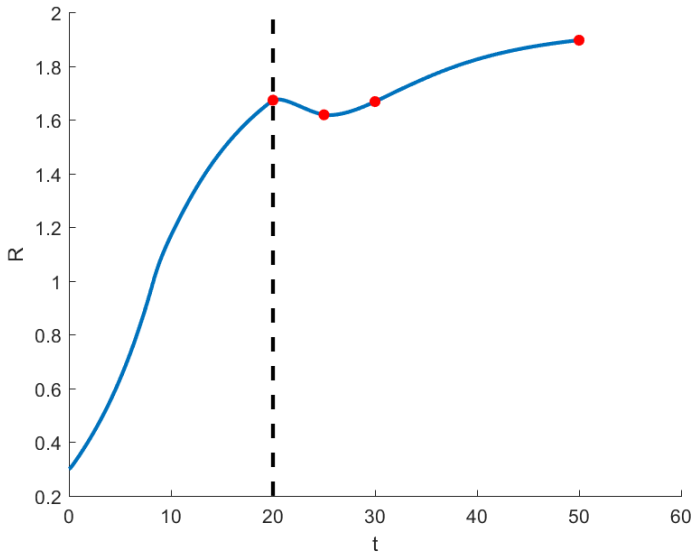

Figure 5.1: Tumour radius trajectory, $R(t)$, (blue line) from simulating Equations (5.15)-(5.25) with a single fraction of radiation (2 Gy) delivered at $t_1 = 20$ (marked by the dashed black line). The growth parameter values for this simulation are listed in Tables 4.2 and 4.3, case i, while the radiosentivity parameters are taken to be $\alpha = 0.35$ Gy^{-1} and $\alpha/\beta = 10$ Gy. The red dots mark the time points for which we visualise the tumour composition in Figure 5.2.

pre-radiotherapy. This redistribution of material internally affects the growth trajectory and we note the difference between the velocity of the tumour boundary, $v_1(R(t), t)$, at similar radii pre- and post-irradiation (c.f. $t = 20$ and $t = 30$).

Our discussion thus far has focussed on the impact of irradiation on the tumour cell phase. We note however that, since we model the effects of radiotherapy as an instantaneous mass transfer between the tumour cell and dead material phases, radiation has a similarly large influence on the distribution of the dead material phase within the tumour. In light of the results presented in the previous chapter, we anticipate that these effects may result in a wide range of response dynamics exhibited by our model.

5.4 Reproducing qualitative responses to treatment observed in clinical data

Having implemented the numerical scheme for simulating radiotherapy response in our multiphase tumour model, we first and foremost hope to capture the range of qualitative response dynamics observed in clinical data. As described in Chapter 2, patient-specific data in the clinic is often limited. After the start of the treatment protocol, CT scans

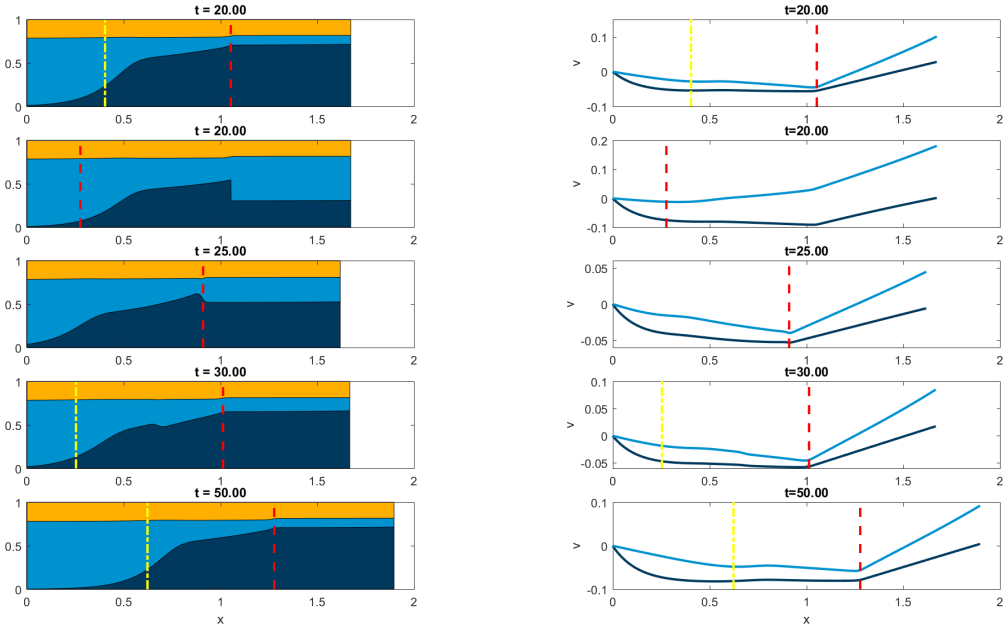

(a) (b)

Figure 5.2: Time series of a) tumour compositions and b) phase velocities for the simulation shown in Figure 5.1. The second time point in each series corresponds to the timestep immediately after irradiation at $t_1 = 20$. a) Snapshots showing the composition of the tumour at each time point. The tumour cell volume fraction, ϕ_1, is represented in dark blue, the dead material phase, ϕ_2, in light blue, and the extracellular fluid volume fraction, ϕ_3, is shown in yellow. The dashed red and yellow line mark the positions of the contours $x = R_H$ and $x = R_N$, respectively. b) Plots of the phase velocities v_1 (dark blue) and v_2 (light blue) for the tumour and dead phases, respectively, at each time point.

are typically used for the sole purpose of checking alignment and the images may be of low resolution. As such, we are left to identify the *in vivo* tumour response dynamics by measurements of tumour volume obtained via these CT scans. As described in Chapter 2, we may broadly characterise 4 different types of qualitative response to radiotherapy with respect to the evolution of tumour volume over time: fast responding tumours, poor response to radiotherapy, tumours which exhibit an initial response to treatment followed by a plateau in response, and those which initially appear to progress through treatment before showing a positive treatment response in the latter stages. In the following sub-sections we present cases for which the multiphase model is able to qualitatively reproduce each class of response in turn [1]. The data used as examples for each type of response in this section are taken from the head and neck cancer data set described in Chapter 2. The parameter values for each simulation are listed in Table 5.1.

	Growth parameters													**Radiotherapy parameters**		
Case	c_N	η	χ	κ	λ	$d_{13} = d_{23}$	ζ	ϕ^*	ϕ_{min}	μ_1	θ_μ	θ_p	θ_Σ	t_1	α	α/β
FR	0.3	1	0.5	0.02	0.75	0	1	0.8	0	1	0.1	0.5	0.5	50	0.35	10
PR	0.3	1	1	0.1	0.75	0.1	2	0.7	0	5	0.5	1	0.25	50	0.5	15
P	0.2	1.5	0.3	0.1	0.5	0	2	0.7	0	3	0.25	1	1	50	0.1	5
PP	0.2	0.5	2	0.02	0.1	0	2	0.6	0	2	0.5	1	0.75	10	0.1	10

Table 5.1: Table of parameter values used for the simulations in Section 5.4 reproducing the qualitative dynamics observed *in vivo*.

5.4.1 Fast responder

The first behaviour that we characterise are the 'fast responders' to radiotherapy. These patients exhibit the most desired response to treatment, typified by a fast, continued decline in tumour volume throughout the radiotherapy and a final tumour volume that is substantially smaller than prior to treatment. A typical example of this response is shown in the data plotted in Figure 5.3a. In Figure 5.3b we present the tumour radius trajectory for a simulation which follows similar response dynamics. The parameter values used for this simulation are listed in Table 5.1, case FR.

[1] NB. The examples in the following sub-sections have been selected due to the qualitative dynamics observed and are not the result of any parameter estimation techniques, for which the computational complexity of the model would be prohibitively slow.

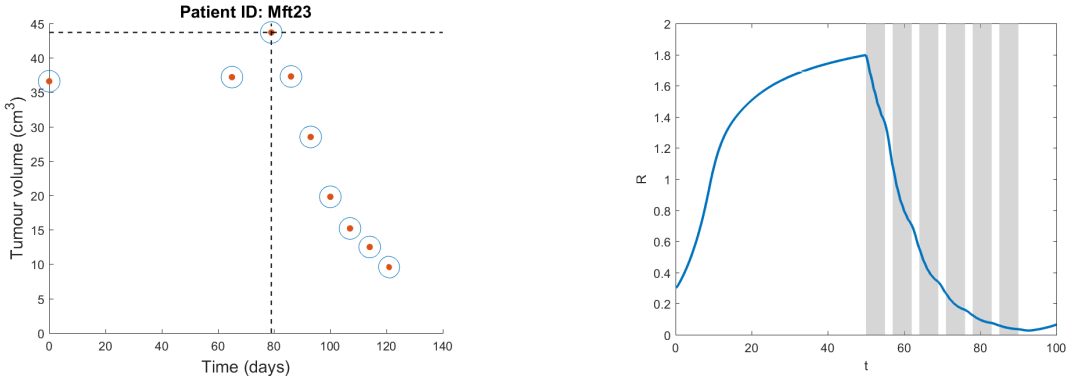

(a) (b)

Figure 5.3: a) Example of a 'fast responder' to radiotherapy treatment. Clinical data taken from the data set of 51 head and neck cancer patients (described in Chapter 2). b) Simulation of Equations (5.15)-(5.25) for which the model exhibits a fast response to treatment. The parameter values for this simulation are listed in Table 5.1, case (FR).

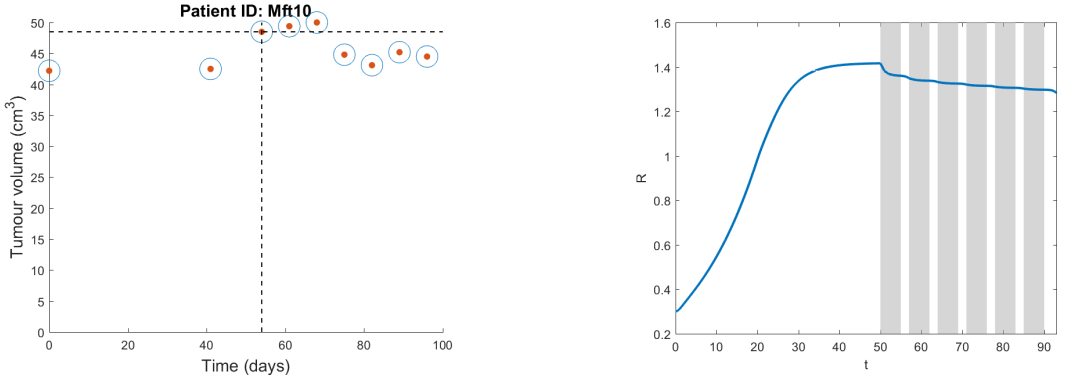

(a) (b)

Figure 5.4: a) Example of a 'poor responder' to radiotherapy treatment. Clinical data taken from the data set of 51 head and neck cancer patients (described in Chapter 2). b) Simulation of Equations (5.15)-(5.25) for which the model exhibits a poor response to treatment. The parameter values for this simulation are listed in Table 5.1, case (PR).

5.4.2 Poor responder

By contrast, there are often cases for which the radiotherapy is not effective in reducing the measured tumour volume. For these patients, the tumour volume remains at a similar size throughout the treatment (see Figure 5.4a). In Figure 5.4b we present simulation results which exhibit a similar qualitative response trajectory. The parameter values for this simulation are given in Table 5.1, case PR.

We note that there a two mechanisms by which our model may exhibit this qualitative behaviour. Both are sub-cases of the 'plateau' type of response characterised in the next section. The response shown in Figure 5.4b is of the category described in Section 5.5.1.

5.4.3 Plateau in treatment effect

For some patients, we observe dynamics which are intermediate between the 'fast' and 'poor' responders. In these cases, the tumour initially responds well to treatment, exhibiting a decrease in tumour volume, before levelling-off to a plateau after which the radiation has minimal effect on the measured volume. This type of response is observed in the data presented in Figure 5.5a.

In Figure 5.5b we visualise the tumour radius trajectory for a simulation which also exhibits a plateau in treatment effect in the latter stages of the radiotherapy protocol. We see that the regrowth of the tumour over the weekend break between fractions is sufficient to compensate for the volume loss due to radiation-induced cell death in the last few weeks of treatment. In this case even though the tumour radius $R(t)$ undergoes oscillations as driven by the weekly fraction schedule, single tumour volume measurements at the same time each week would reveal no net treatment effect. This mode of response plateau by which the tumour regrows fast enough between fractions to overcome the effects of radiotherapy was also analysed in our previous model in Chapter 3. The parameter values used for this simulation are listed in Table 5.1, case P.

In this case, the fast regrowth between tumours would indicate an aggressive tumour for which the prognosis is likely to be poor, even after a full radiotherapy protocol. By contrast, in Section 5.5.1 we characterise alternative dynamics for which the tumour volume appears to plateau but the prognosis post-treatment is likely to be significantly better.

In Figure 5.6 we visualise the composition of the simulated tumour at times $t \in \{79, 79 + \Delta t, 83, 86\}$ during the 'plateau' phase of the radiotherapy response. The time point $t = 79 + \Delta t$ shows the composition of the tumour immediately after irradiation. The step function form of the OER results in a local maximum in the tumour cell phase volume fraction, ϕ_1. At this location within the tumour $v_1 < 0$ and the volume fraction profile moves inwards as the material is redistributed and the composition smooths out. At future time points (e.g. $t = 83$) we see a legacy of previous fractions of radiotherapy in the smooth undulations in the tumour composition for $x < R_H$. At $t = 86$, a week after the first time point in our time series, we see that the tumour composition is almost

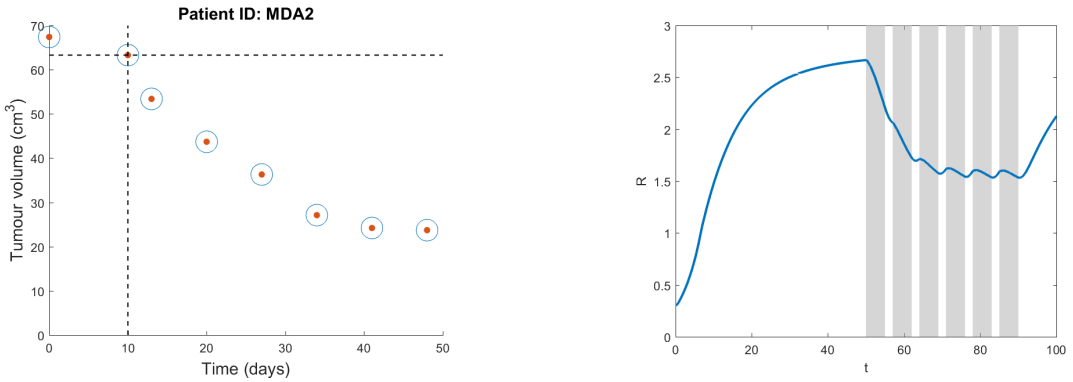

(a) (b)

Figure 5.5: a) Example of a response to radiotherapy exhibiting a plateau in treatment effect. Clinical data taken from the data set of 51 head and neck cancer patients (described in Chapter 2). b) Simulation of Equations (5.15)-(5.25) for which the model exhibits a response plateau during radiotherapy. The parameter values for this simulation are listed in Table 5.1, case (P).

identical to that at $t = 79$, indicative of the plateau in response.

5.4.4 Pseudo-progression

The final class of response which we identify are those tumours which undergo 'pseudo-progression' during the initial stages of treatment. This behaviour is characterised by continued growth of the tumour despite the application of radiotherapy, before exhibiting a delayed decrease in tumour volume during the latter stages of the treatment protocol. An example of this type of response is shown in Figure 5.7a. The simulation in Figure 5.7b using the parameter values given in Table 5.1, case PP, exhibits similar dynamics. We note that, since the tumour volume continues to increase after the delivery of the first fraction of radiation, such a qualitative response may not be captured by any model in which the effects of radiotherapy are to induce an instantaneous tumour volume change.

In this case, we have $\theta_\Sigma = 0.75$ and so the dead material still contributes significantly to the cell-sensing activity. At the start of radiotherapy in this simulation, the internal tumour composition is still approximately uniform and so we may use the averaged quantities

$$\bar{\phi}_i(t) = \frac{1}{R(t)} \int_0^{R(t)} \phi_i(x,t)dx \tag{5.26}$$

to gain some insight on the tumour dynamics. In Figure 5.8 we plot $\bar{\phi_1} + \theta_\Sigma \bar{\phi_2}$ over time to

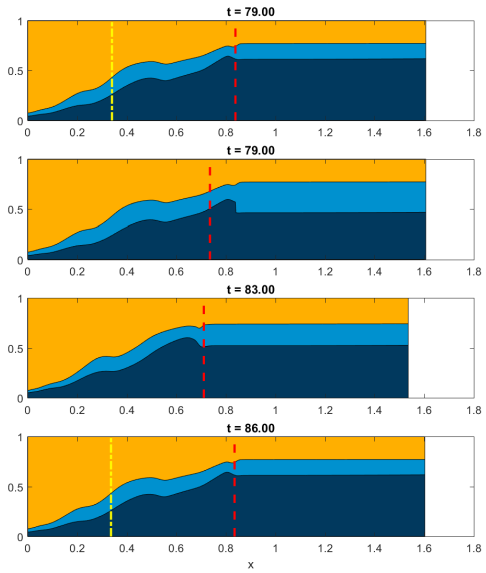

Figure 5.6: Time series of tumour compositions spanning a week of the fractionation protocol for the simulation presented in Figure 5.5b. The second time point corresponds immediately after irradiation at time $t = 79$. The volume fractions ϕ_1, ϕ_2 and ϕ_3 are represented by the dark blue, light blue and yellow regions, respectively.

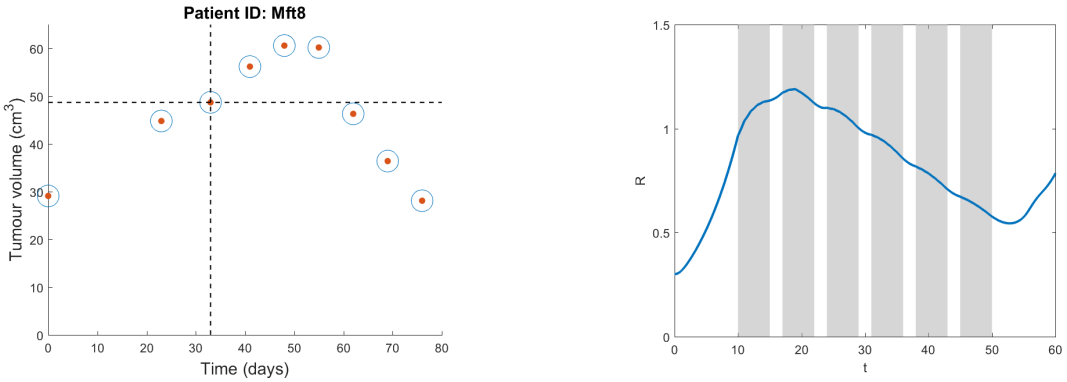

(a) (b)

Figure 5.7: a) Example of response to radiotherapy exhibiting 'pseudo-progression' of the tumour. Clinical data taken from the data set of 51 head and neck cancer patients (described in Chapter 2). b) Simulation of Equations (5.15)-(5.25) for which the model exhibits pseudo-progression. The parameter values for this simulation are listed in Table 5.1, case (PP).

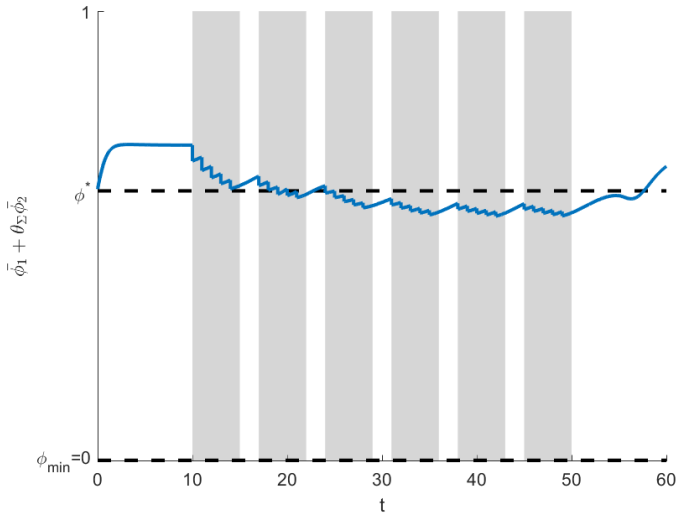

Figure 5.8: Plot showing $\bar{\phi_1} + \theta_\Sigma \bar{\phi_2}$ over time for the simulation shown in Figure 5.7b. The quantities $\bar{\phi_i}$ represent the volume fraction of phase i averaged over the whole tumour at time t, as defined by Equation (5.26).

get a gauge on the cell pressures occurring within the tumour throughout the course of the treatment protocol, remembering that quantities greater than ϕ^* correspond to positive, repulsive pressures, while those less than ϕ^* gives rise to adhesive forces. We see that, since θ_Σ is large, the value of $\bar{\phi_1} + \theta_\Sigma \bar{\phi_2}$ does not observe a large drop upon the delivery of radiotherapy fractions, despite the instantaneous mass transfer between the tumour cell and non-viable phases. As such $\bar{\phi_1} + \theta_\Sigma \bar{\phi_2} > \phi^*$ for the first couple of weeks of the protocol and we see continued progression of the tumour during this period. However, the accumulated effects of the radiotherapy by week 3 of the protocol are sufficient to result in $\bar{\phi_1} + \theta_\Sigma \bar{\phi_2} < \phi^*$ and induce a decrease in tumour volume which persists for the remainder of the treatment period. We therefore see that in our simulation, this pseudo-progression of the tumour is driven by a build-up of non-viable cells and dead material within the tumour, rather than an increase in the tumour cell population despite irradiation of the tumour.

5.5 Characterising regrowth dynamics post-radiotherapy

In this section we characterise some of the regrowth dynamics observed post-radiotherapy. In particular, we see many cases for which the dynamics of the tumour after the end of treatment differ from those prior to irradiation. In each case, the distribution of material

differs from the configuration under standard growth conditions for the same tumour radius and thus alters the growth trajectory of the tumour. In the following sub-sections we present two different types of regrowth behaviour exhibited by the model. The parameters for simulations shown are listed in Table 5.2.

	Growth parameters													**Radiotherapy parameters**		
Case	c_N	η	χ	κ	λ	$d_{13} = d_{23}$	ζ	ϕ^*	ϕ_{min}	μ_1	θ_μ	θ_p	θ_Σ	t_1	α	α/β
i	0.3	0.5	0.1	0.1	0.5	0	3	0.6	0	0.5	1	0.5	1	50	0.35	15
ii	0.1	1	0.3	0.1	0.25	0.1	3	0.6	0	5	0.5	0.75	0.25	50	0.35	15

Table 5.2: Table of parameter values used for the simulations presented in Section 5.5 showing different regrowth dynamics post-radiotherapy.

5.5.1 Post-radiotherapy decrease in tumour volume

In Section 5.4 we characterised 4 different qualitative responses to radiotherapy observed in tumour volume measurements taken in the clinic. Amongst these is a class of dynamics for which the tumour volume initially responds well to irradiation before experiencing a diminished treatment effect towards the end of the protocol. In Section 5.4.3 we demonstrated that our multiphase model may reproduce this behaviour. In this case, the regrowth of the tumour over the weekend break in the latter stages of the treatment protocol is sufficient to compensate for the volume lost due to irradiation. The tumour thus reaches a plateau in response, with no net treatment effect observed. However, in our simulations we also identify another mode of response for which the tumour volume plateaus towards the end of treatment. This response is qualitatively different to the case shown in Figure 5.5b. In Figure 5.9a we see that the plateau in the tumour radius trajectory is such that $\frac{dR}{dt} = 0$, in contrast with the oscillations between death and regrowth driven by the on-off nature of the treatment protocol presented in Section 5.4.3. These dynamics are also characterised by a dip in tumour volume some time after the end of the last fraction of radiotherapy, before an increase in the tumour radius $R(t)$ and regrowth of the tumour. The parameters for the simulation shown in Figure 5.9 are listed in Table 5.2, case i.

These two modes of response plateau are very different with regards to the underlying

tumour composition and thus the actual efficacy of the radiotherapy, despite both simulations resulting in a diminished treatment effect while the tumour is still of significant radius. In Figure 5.9c we visualise the tumour composition at 5 different time points throughout the regrowth period of the tumour after radiotherapy. We notice that at the end of treatment the tumour cell population is actually very small, contrary to what might be expected from measuring the outer tumour radius (see composition at $t = 100$). In this case, the plateau in tumour radius is not due to a lack of effect of the radiotherapy on the tumour cell population. The radiation actually kills the tumour population faster than the effects of adhesion such that $\phi_1 + \theta_\Sigma \phi_2 \leq \phi_{min}$. The tumour cells therefore become too sparsely populated to interact with each other, and so the tumour radius is unable to contract further. Subsequent fractions of radiation thus kill tumour cells and reduce the volume fraction ϕ_1 locally without inducing a change in the tumour volume as measured by the outer tumour radius. The value of $\Sigma_\phi(\bar{\phi_1} + \theta_\Sigma \bar{\phi_2})$ at $t = 100$ is represented by the green dot in Figure 5.9b.

In a similar manner, the regrowth of the tumour cell phase after the end of the treatment protocol initially occurs locally. Once the tumour composition is such that $\Sigma_\phi(\phi_1 + \theta_\Sigma \phi_2) < 0$ the tumour cells are able to interact and cellular adhesion results in a contraction of the tumour (see time $t = 107.5$ in Figure 5.9). While $\phi_{min} < \phi_1 + \theta_\Sigma \phi_2 < \phi^*$, the tumour radius continues to decrease and $\bar{\phi_1}$ increases due to both proliferation of the tumour cells and contraction of the tumour volume. The point at which $\bar{\phi_1} + \theta_\Sigma \bar{\phi_2} = \phi^*$ corresponds to the minimum radius in this post-radiotherapy dip such that $\frac{d^2R}{dt^2} > 0$ (see time $t = 109.5$). Thereafter, $\bar{\phi_1} + \theta_\Sigma \bar{\phi_2} > \phi^*$ and the tumour assumes a regrowth trajectory similar to that prior to treatment.

Analysis of the waiting time before the dip in tumour radius would proceed in a similar manner to that presented in Breward *et al.* [82]. Further analysis of the tumour tumour radius trajectory throughout the subsequent dip is likely to be tractable but is left as further work.

5.5.2 Altered regrowth dynamics

As described in the previous sections, as well as affecting the overall tumour volume, radiotherapy induces a large change in the underlying tumour composition in our multi-

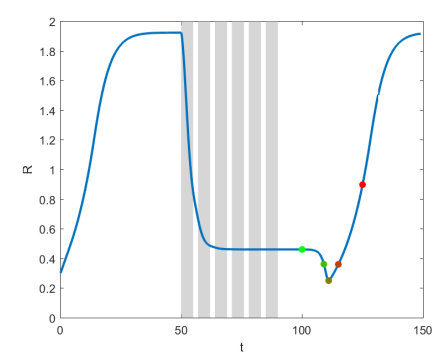

(a)

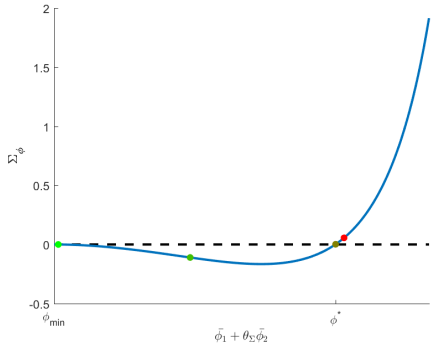

(b)

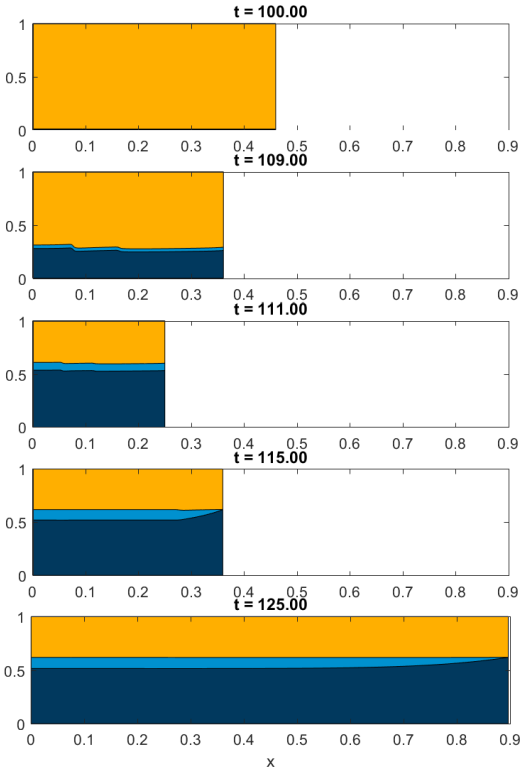

(c)

Figure 5.9: Simulation of Equations (5.15)-(5.25) exhibiting a dip in tumour radius after the end of the radiotherapy fractionation schedule, using the parameter values in Table 5.2, case i. a) Tumour radius trajectory (blue line) for the simulation. The dots plotted along the trajectory mark the key time points in the dynamics. b) The cell sensing function Σ_ϕ (blue line) defined by Equation (5.20). The points plotted mark the approximate cellular pressures within the tumour, $\Sigma_\phi(\bar{\phi}_1 + \theta_\Sigma \bar{\phi}_2)$, for the time points plotted in panel a). c) The corresponding tumour compositions for the time points marked on the trajectory in panel a).

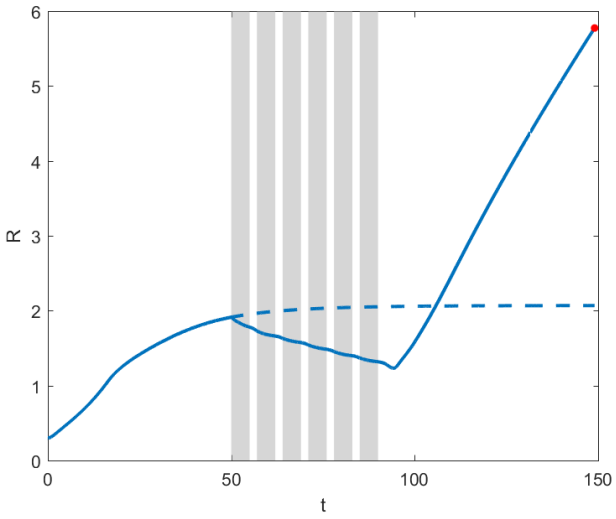

Figure 5.10: Tumour radius trajectory (solid blue line) for a simulation of Equations (5.15)-(5.25) for which the radiotherapy alters the regrowth trajectory of the tumour. The growth trajectory in the absence of radiotherapy is shown by the dashed blue line. the parameter values for this simulation are listed in Table 5.2, case ii.

phase mixture. In some cases, this perturbation is significant enough to completely alter the qualitative growth dynamics post-treatment when compared with the control growth trajectory in the absence of radiotherapy. The tumour radius trajectory for one such simulation is shown in Figure 5.10 (solid blue line) along with the corresponding control growth trajectory (dashed blue line). The parameter values pertaining to this simulation are given in Table 5.2, case ii.

In this case, the original tumour growth would have given a monotonic, sigmoidal trajectory approaching a steady state solution. However, the regrowth post-radiotherapy clearly results in a travelling wave solution. The parameter regime here clearly gives rise to growth dynamics which exhibit bistability, with both steady state and travelling wave solutions possible. By significantly altering the underlying tumour composition, it is possible to change the qualitative growth dynamics of the tumour. Further analysis of this bistability is a possible direction for future work.

	Growth parameters										Radiotherapy parameters		
Case	c_N	η	χ	κ	λ	$d_{13} = d_{23}$	ζ	ϕ^*	ϕ_{min}	μ_1	t_1	α	α/β
A	0.1	0.5	2	0.02	0.75	0	3	0.7	0	0.5	100	0.1	5
B	0.2	0.5	1	0.02	0.75	0.1	3	0.8	0.4	5	50	0.5	15
C	0.1	1	0.5	0.05	0.1	0.5	3	0.8	0	1	50	0.5	10
D	0.2	1	1	0.02	0.1	0	1	0.8	0.16	1	10	0.5	15
E	0.2	0.5	2	0.02	0.1	0	2	0.6	0	2	10	0.1	10

Table 5.3: Table of growth parameter values for each case presented in Figure 5.11 of the parameter sweep of dead material properties defined by $\boldsymbol{\theta} = (\theta_\mu, \theta_p, \theta_\Sigma) \in [0,1]^3$.

5.6 The influence of the dead material on tumour response dynamics

As in Chapter 4 for the growth dynamics, we are interested in the influence of the properties and spatial distribution of the dead material within the tumour on the response dynamics. In particular, since pre-treatment data in the clinic is often limited and provides little information on the composition of the tumour, simpler models that do not incorporate such detail would be desirable if shown to be of sufficient predictive power. In Chapter 4 we highlighted some examples for which the properties of the dead material phase did not significantly affect the tumour growth dynamics. For these cases we might expect that the subsequent radiotherapy response may also not significantly differ between simulations and that a simpler model may suffice. In this section we address some of these questions and illustrate the varying degrees of influence of the dead material phase on the radiotherapy response.

We perform a focussed parameter sweep on the parameter subspace $(\theta_\mu, \theta_p, \theta_\Sigma) = \boldsymbol{\theta} \in [0,1]^3$ in order to investigate the influence of the material properties of the dead phase on the response dynamics. In each case all other model parameters are held fixed, including the radiosensitivity parameters. The resulting trajectories for a selection of these parameter sweeps are shown in Figure 5.11 with the parameter values for each case listed in Table 5.3. We also present histograms showing the variation in simulated tumour radii, R, at the end of the radiotherapy protocol in each case.

In case A in Figure 5.11 we observe tumour radius trajectories which all follow similar growth dynamics while also exhibiting a similar response to radiotherapy. Each trajectory

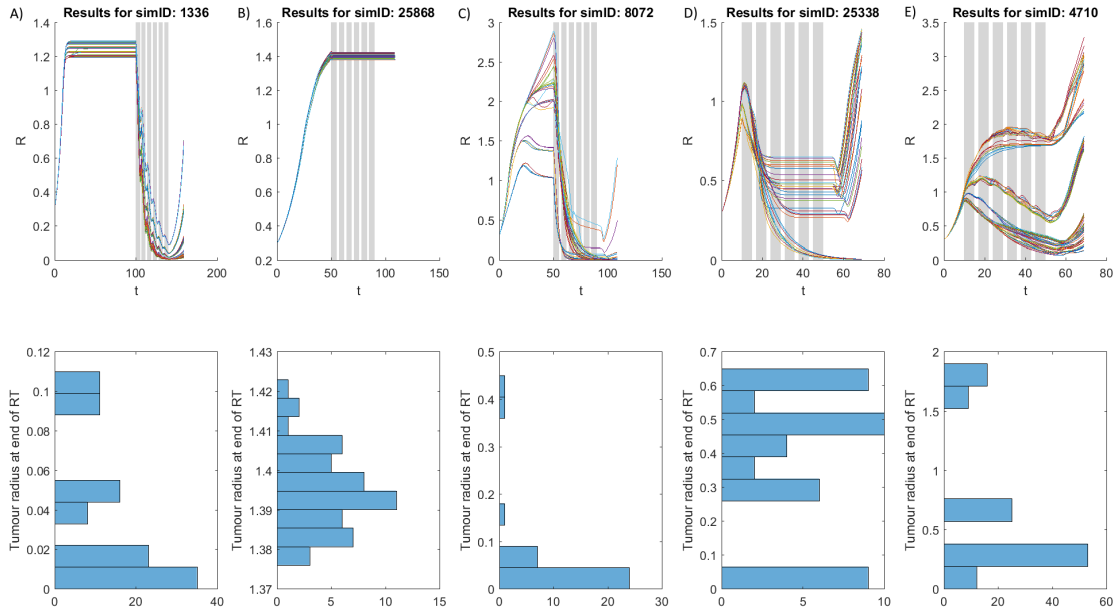

Figure 5.11: Selection of cases A-E showing the tumour radius trajectories obtained by sweeping over the parameter sub-space $\boldsymbol{\theta} = (\theta_\mu, \theta_p, \theta_\Sigma) \in [0,1]^3$ summarising the material properties of the dead phase. The histograms for each case show the distribution of tumour radii at the end of the radiotherapy protocol across each of the parameter sweeps. The parameter values for each case are given in Table 5.3.

may be classified as a 'fast responder' to treatment and we note that the predicted final tumour radii are all clustered together around small values, $R < 0.12$. In particular the properties of the dead material phase do not appear to significantly affect the tumour dynamics either before, during or after radiotherapy. As such we would anticipate that a less complex model could adequately describe the observed response in this case, without necessarily taking into account the spatial distribution of the tumour composition.

In case B we similarly observe trajectories for which the growth and response dynamics differ only very slightly with variation in the $\boldsymbol{\theta}$ parameters. In this case the simulations all fall into the category of 'poor responders' to treatment, showing only a very slight change in tumour radius between the start and end of the protocol. However, we note that the plateau in response is such that $\frac{dR}{dt} = 0$ which may be indicative of the behaviour characterised in Section 5.5.1 and a greater radiotherapy effect on the tumour population than may be observed by measuring the outer tumour radius alone. We note that while a simpler model may be able to reproduce the observed dynamics with respect to tumour radius over time, in this case it is still the underlying composition that drives the

qualitative behaviour and this may not be captured by some simpler models.

As described in the previous chapter, changes in the properties of the dead material are able to significantly change the qualitative tumour growth dynamics. In case C we see the results of a $\boldsymbol{\theta}$ parameter sweep which exhibits a large degree of heterogeneity in the pre-treatment growth trajectories. However, this heterogeneity is not mirrored in the corresponding response dynamics, with most trajectories responding well to radiotherapy and final simulated tumour radii significantly smaller than prior to treatment.

However we do observe cases for which the properties of the dead material invoke a greater heterogeneity in tumour response. In case D, the simulations all follow similar growth trajectories although we observe a range of different values for the outer tumour radius at the end of the radiotherapy protocol between the simulations. We also observe a qualitative difference in trajectories, with some simulations in the 'fast responder' category while many simulations exhibit a plateau in response. We again note that these simulations show a dip in tumour radius post-treatment and so the response exhibited with regards to tumour volume fraction is actually more similar than may be suggested by measuring tumour volume alone. However, we also see that those simulations that plateau regrow quickly, whilst those that respond well to treatment do not regrow within the timeframe of the simulation.

In case E in Figure 5.11 we observe an even greater degree of heterogeneity in the tumour response dynamics, ranging from pseudo-progression to fast responders. In Figure 5.12 we illustrate these results using two extremal cases corresponding to the two corners of the unit cube, $\boldsymbol{\theta} = (0.01, 0.01, 0.01)$ [2] and $\boldsymbol{\theta} = (1, 1, 1)$. In Figure 5.12a we show the two different tumour trajectories and in Figures 5.12b and c we visualise the tumour compositions for each case at multiple time points.

We again observe that there is very little difference in the growth trajectories prior to treatment. Furthermore, the composition of the tumours before the start of treatment are also very similar. In particular, it would therefore not be possible to distinguish between these two cases from pre-treatment scans, even if we had imaging data of the underlying tumour composition.

[2] The model equations are singular for $\theta_\mu = 0$ so we instead choose positive values of $(\theta_\mu, \theta_p, \theta_\Sigma)$ close to 0.

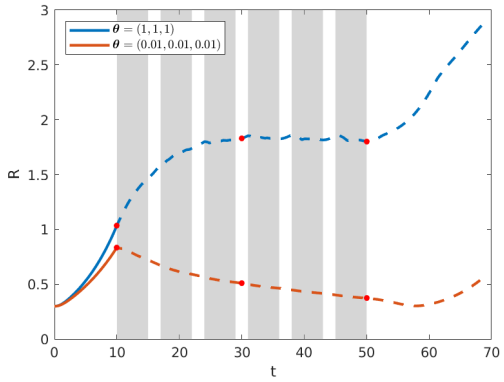

(a)

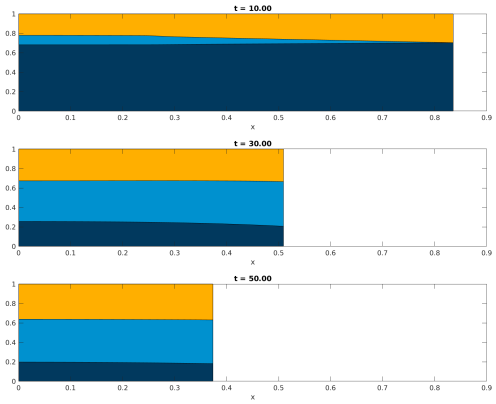

(b)

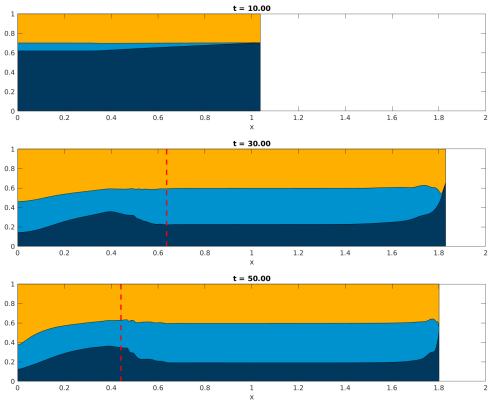

(c)

Figure 5.12: Two simulations of Equations (5.15)-(5.25) exhibiting a large variation in response to radiotherapy, taken from case E in Figure 5.11. a) Two tumour radius trajectories corresponding to $\boldsymbol{\theta} = (0.01, 0.01, 0.01)$ (red) and $\boldsymbol{\theta} = (1, 1, 1)$ (blue). The red points mark the time points for which we visualise the compositions in b). b),c) Tumour compositions for each simulation prior to radiotherapy at $t = 10$, during the radiotherapy protocol at $t = 30$, and at the end of treatment at $t = 50$. The simulations in b) correspond to $\boldsymbol{\theta} = (0.01, 0.01, 0.01)$ while c) corresponds to $\boldsymbol{\theta} = (1, 1, 1)$.

Given the similarity between the pre-treatment growth trajectories and underlying compositions, we might expect that this would be another case for which the $\boldsymbol{\theta}$ parameters have little effect on the resulting dynamics. Instead, this example highlights the fact that radiotherapy induces a large change to the tumour composition. The properties of the non-viable phase may subsequently affect the redistribution of material within the tumour and therefore response dynamics, despite not significantly influencing the pre-treatment growth trajectories.

5.7 Discussion

In Chapter 4 we developed a three phase, mixture model of tumour growth in which the tumour was modelled to be comprised of tumour cells, dead material and extracellular fluid. The dead material phase was assumed to account for all non-viable cells and cellular debris within the tumour regardless of cell death mechanism or stage of decay. Irradiation of *in vivo* tumours induces widespread cell death throughout the tumour. In particular, we anticipate that the dead material within the tumour post-radiotherapy may not be confined to areas of necrosis induced by nutrient-starvation, such as the necrotic core of *in vitro* tumour spheroids. In light of the results presented in Chapter 4 we would expect that the mechanical properties of the dead material combined with the composition changes induced by radiotherapy, may have a significant impact on the observed response dynamics. As such, in this chapter we have extended our multiphase tumour growth model to account for the effects of radiotherapy.

The linear-quadratic (LQ) model is typically used to describe the survival fraction of a tumour cell population post-irradiation [40]. The 'standard' LQ model is often modified to incorporate the effects of factors other than intrinsic radiosensitivity which may influence radiation-induced cell death, including the oxygen enhancement effect. Clonogenic survival assays are often used to investigate radiation dose-dependent cell death *in vitro*, with the LQ model initially arising as an empirical formula from these results. As such the LQ model is most suited to describing the long-term tumour cell survival fraction post-irradiation. In this model we incorporate the effects of radiotherapy as an instantaneous mass transfer between the tumour cell phase and the non-viable phase using the LQ model to determine the survival fraction of the tumour cell population. This corresponds to a redistribution of material internally within the tumour whilst avoiding the instantaneous volume loss often observed in radiotherapy response models (c.f. Chapters 2 and 3).

We adapt the numerical scheme developed in Chapter 4 to simulate radiotherapy fractionation protocols and the resulting tumour response dynamics. In Section 5.4 we show that the model can capture the different qualitative behaviours observed in tumour volume measurements taken from clinical data. For the class of response for which the

tumour plateaus in tumour radius after an initial positive response to treatment, we observe dynamics that are very similar in nature to the results presented in Chapter 3 whereby the weekend break allows for sufficient regrowth to overcome the effects of radiotherapy. With this model we are also able to capture a 'pseudo-progression' response to radiotherapy. In these cases the tumour appears to continue tumour growth through the initial stages of treatment before a reduction in tumour volume is observed during the latter stages of the protocol. In our model, this behaviour is attributed to a build-up of dead material within the tumour as opposed to an aggressive tumour population which continues to increase despite irradiation. We note that this type of response is not possible to achieve with the instantaneous volume loss models presented in Chapters 2 and 3.

In addition to investigating the radiotherapy response dynamics, in Section 5.5 we characterised two different types of regrowth behaviour post-radiotherapy that differ from the growth dynamics described in Chapter 4. These dynamics were driven by aspects of the underlying tumour composition, highlighting the potential importance of the spatial distribution of constituents of the tumour microenvironment on the resulting dynamics.

We further investigated the influence of the dead phase on the radiotherapy response dynamics in Section 5.6 by performing a parameter sweep on the sub-space describing the material properties of this phase, $(\theta_\mu, \theta_p, \theta_\Sigma) = \boldsymbol{\theta} \in [0,1]^3$, in a manner analogous to that presented in Chapter 4. We find that there are examples for which the observed response, as measured by tumour radius/volume, is not significantly affected by changes in the $\boldsymbol{\theta}$ parameter values. In these cases, we anticipate that a simpler model that may be more easily calibrated using clinical data could be adequate for predicting radiotherapy response. However, such a scenario would rely on *a priori* identification of these patients. Further analysis of the growth dynamics would be required in order to identify metrics which may distinguish these cases.

Conversely, we also find examples which display a large degree of heterogeneity in response by solely varying the $\boldsymbol{\theta}$ parameters. In particular we highlight case E in Figure 5.11 for which the qualitative growth trajectories are very similar but the response trajectories vary greatly. Moreover, the spatial compositions prior to the start of treatment are also indistinguishable. These cases highlight the fact that radiotherapy is not just a small perturbation to the tumour but may induce large changes to the tumour com-

position. As such the material properties of the dead phase become significant to the response dynamics even though they were not influential in determining pre-treatment growth. The similarity of the compositions during the growth phase suggest that these cases would not be distinguishable from pre-treatment imaging, even if the aspects of tumour composition considered in this model were measured. For these cases, further work would be to identify how early during the fractionation protocol we may reasonably determine the future response and what tumour metrics would be required.

In Section 5.6 we demonstrated that the $\boldsymbol{\theta}$ parameters may have a significant influence on the radiotherapy response dynamics. However, as in Chapter 4, the large parameter space makes it difficult to determine which parameters most influence the qualitative response to treatment. Further investigation of this parameter space remains as future work.

Chapter 6

Discussion

6.1 Introduction

In Chapter 2 we considered a range of scalar ODE models used to predict *in vivo* radiotherapy responses. The models considered employ a non-spatial, phenomenological description for the evolution of the tumour volume throughout treatment. While these models provide good fits for some patients, they were unable to adequately describe the full range of behaviours observed in clinical datasets.

We hypothesised that heterogeneity in tumour composition may affect the tumour growth dynamics and, consequently, radiotherapy response. We further anticipated that such heterogeneity is likely to be dynamic throughout the course of the radiotherapy protocol as a result of the widespread cell death induced by irradiation. In order to test this hypothesis we developed a series of more complex models in Chapters 3-5 that incorporate spatial heterogeneity. Investigation of the resulting dynamics exhibited by each model revealed that, in particular, the necrotic or dead material within the tumour mass may have a significant impact on the observed qualitative response to radiotherapy. Whilst providing mechanistic insight, the models developed in Chapters 3-5 are likely to be too complicated for clinical applications due to the lack of data typically available.

Compartmental ODE models decompose the tumour volume into two or more constituent parts. These models extend the phenomenological models considered in Chapter 2 by incorporating more biological detail, viewing the tumour as a well-mixed system which comprises more than one component.

In this chapter we revisit phenomenological modelling of tumour responses to radiotherapy targeted towards clinical application. In light of the results presented in Chapters 3-5, we present a two compartment model, decomposing the tumour into a viable tumour cell population and a necrotic or dead material compartment. The model equations represent a natural extension of the logistic model considered in Chapter 2. We note that other compartmental models for radiotherapy response exist in the literature, with some taking a similar form to the model presented here [108–110].

In Section 6.2 we introduce our two compartment model and analyse the response dynamics. In Section 6.3 we fit the model to both synthetic and *in vivo* datasets, focussing on the qualitative responses not captured by the models considered in Chapter 2. In Section 6.4 we present the results of synthetic data studies comparing the single ODE models with the new two compartment extension.

The work in this chapter is presented to facilitate an extended discussion about the influence of the spatial models developed in this thesis and the manner in which they may be used to guide the development of simpler, predictive models. The preliminary results illustrate the benefits of considering such compartmental models, whilst also highlighting some of the difficulties associated with incorporating more biological detail. Many open questions remain regarding the comparison of models of varying complexity. Some of these issues are discussed in Section 6.5 and Chapter 7.

6.2 A two compartment model for radiotherapy response

In Chapter 2 we considered a range of non-spatial ODE models of tumour growth and radiotherapy response targeted towards clinical applications. These models provide a phenomenological description of tumour growth and treatment response while not explicitly accounting for the complexity and heterogeneity of the underlying biology. Such models are not limited to single ODEs: we may instead treat the tumour as comprising two (or more) well-mixed compartments. When proposing such ODE descriptions for the dynamics of these compartments we aim to better describe the heterogeneity observed within both *in vitro* spheroids and *in vivo* tumours, whilst maintaining the relative simplicity afforded by such a framework. In Chapter 2 we showed that the scalar ODE models

were unable to fully capture the array of response dynamics observed *in vivo*. In extending these single ODE models to consider tumours as being comprised of more than one compartment, we aim to incorporate more heterogeneity in tumour composition and thus replicate a wider array of dynamics.

In Section 6.2.1 we introduce a new two compartment model that describes tumour response to radiotherapy and extends the logistic model presented in Chapter 2. We investigate the qualitative dynamics exhibited by the model in Section 6.2.2 and analyse its long-term dynamics for general fractionation protocols in Section 6.2.4.

6.2.1 Model equations

In Chapter 2 we investigated the performance of a scalar ODE model for radiotherapy response that is based on the familiar logistic growth model. The effects of radiotherapy are incorporated as an instantaneous volume loss proportional to the logistic term, the logistic term assumed to be proportional to the volume of viable, proliferating tumour cells that are sensitive to irradiation [105].

In this section we propose a new model in which the tumour comprises two compartments, viable tumour cells, V, and dead or necrotic material, N. The overall tumour volume at any time is given by $V(t) + N(t)$. Viable tumour cells are assumed to undergo logistic growth with growth rate λ and carrying capacity K. Additionally, viable tumour cells become necrotic at a constant rate η. The necrotic or dead material is assumed to undergo exponential decay at constant rate ζ. The effects of radiotherapy are included as an instantaneous transfer of mass between the viable tumour volume, V, and the necrotic compartment, N, for fractions delivered at times t_i. We note that the radiation-induced death term differs from the logistic model considered in Chapter 2. We assume that the dead material is unaffected by radiotherapy, consistent with the models developed in Chapters (3)-(5), and so model radiation-induced cell death as proportional to the viable tumour cell compartment, V, with death rate γ.

The ODEs governing the dynamics of each of these compartments are given by

$$\frac{dV}{dt} = \lambda V\left(1 - \frac{V}{K}\right) - \eta V - \gamma \sum_{i=1}^{n} V\delta(t - t_i), \tag{6.1}$$

$$\frac{dN}{dt} = \eta V - \zeta N + \gamma \sum_{i=1}^{n} V\delta(t - t_i). \tag{6.2}$$

Coupled with appropriate initial conditions for the viable and necrotic volumes, $V(0)$ and $N(0)$, Equations (6.1) and (6.2) define our two compartment model for tumour growth and radiotherapy response. This model is similar in form to those proposed in [108–110].

We note that the dynamics of the tumour cell compartment, V decouples from the necrotic dynamics, N. In practice, we might expect there to be some feedback between the two compartments, with necrotic material perhaps releasing toxic factors that inhibit the growth of viable cells. We may further anticipate that the necrotic material competes for space with the viable tumour cells and should be considered within the logistic growth term. A comprehensive comparison of these possible models is beyond the scope of the work presented here. For simplicity, we ignore such effects here and examine the model given by Equations (6.1) and (6.2).

In Equations (6.1) and (6.2) we distinguish necrotic cell death from other mechanisms that may contribute to decelerating tumour growth rates and lead to growth saturation. We note that, in the absence of radiotherapy, the viable cell population exhibits logistic growth with an effective carrying capacity $\xi = K\left(1 - \frac{\eta}{\lambda}\right)$ and net growth rate $\lambda - \eta$. As such we may solve Equation (6.1) to give

$$V(t) = \frac{\xi}{1 + \left(\frac{\xi - V(0)}{V(0)}\right) e^{-(\lambda - \eta)t}}. \tag{6.3}$$

Equation (6.2) then becomes

$$\frac{dN}{dt} + \zeta N = \frac{\eta \xi}{1 + \frac{\xi - V(0)}{V(0)} e^{-(\lambda - \eta)t}}. \tag{6.4}$$

We may use an integrating factor to write the solution for $N(t)$ in terms of a hypergeometric function, although doing so provides no additional insight.

By considering steady state solutions as $t \to \infty$, we find that the overall tumour

carrying capacity, $\tilde{K}$, and thus the steady state total tumour volume $Y \coloneqq V + N$, is given by

$$\tilde{K} = \xi\left(1 + \frac{\eta}{\zeta}\right) = K\left(1 - \frac{\eta}{\lambda}\right)\left(1 + \frac{\eta}{\zeta}\right). \tag{6.5}$$

The necrotic fraction, defined to be $\Phi \coloneqq \frac{N}{Y}$, at equilibrium is thus $\frac{\eta}{\eta+\zeta}$. In Figure 6.1 we visualise the results of a simple parameter sweep for these growth dynamics. We vary the necrosis rate, η, and necrotic decay rate, ζ, in order to modulate the properties of the dead material within the tumour. From the results of our multiphase model in particular we anticipate that such model parameters may have a significant impact on growth and treatment response dynamics (c.f. Chapters 4 and 5).

The numerical results of the parameter sweep support the results of the previous analysis. Increasing the rate of necrosis, η, results in a larger necrotic fraction at equilibrium, while increasing the rate of decay of necrotic material, ζ, corresponds to decreasing necrotic fractions, as expected. Increasing the necrotic decay rate, ζ, also corresponds to decreasing steady state tumour volumes, whilst the effect of varying the necrosis rate, η, is non-linear. We observe simulations for which the initial condition for the total tumour volume, $Y(0) \coloneqq V(0) + N(0)$, is above the steady state and thus the tumour exhibits non-monotonic dynamics and approaches the steady state from above.

6.2.2 Investigation of model dynamics

We further perform a parameter sweep varying the necrosis rate, η, and the decay rate of necrotic material, ζ, in order to determine the qualitative responses to radiotherapy that the model exhibits. In all cases we simulating the standard fractionation protocol for 6 weeks, starting at $t = 14$.

In Figure 6.2 we display the results of the parameter sweep. We show how the dynamics of the necrotic volume, N, and total tumour volume, Y, change as η and ζ vary. As expected, increasing the necrosis rate, η, results in smaller tumour volumes post-radiotherapy since the steady state growth behaviour supports a tumour composition containing a larger necrotic fraction and smaller proliferative tumour population. As the rate of necrotic decay, ζ, increases, the trajectories for the overall tumour volume resem-

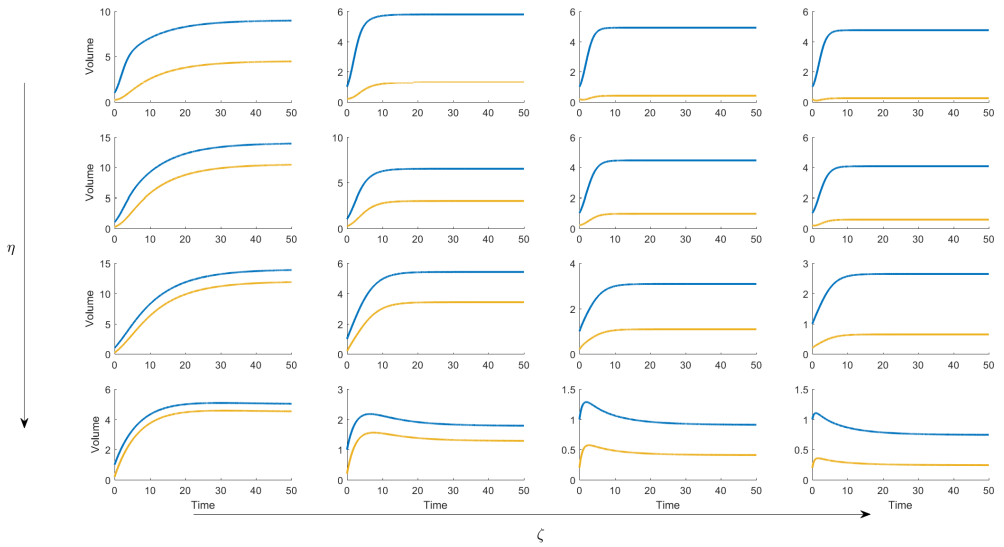

Figure 6.1: Results of a parameter sweep for the two compartment model, simulating Equations (6.1) and (6.2) for tumour growth without radiotherapy. Parameters increase in the direction of the arrows with necrosis rate, $\eta \in [0.1, 0.99]$, varying by row, and the decay rate of necrotic material, $\zeta \in [0.1, 2]$, by column. Trajectories for the total tumour volume, Y, and the underlying volume of necrotic material, N, are shown in blue and yellow, respectively. For each simulation the remaining parameter values are held fixed: $\lambda = 1$, $\gamma = 0.3$, $K = 5$, $Y(0) = 1$ and $\Phi(0) = 0.2$.

ble those obtained from models which simulate instantaneous cell death upon irradiation. Conversely, smaller values of ζ result in less pronounced changes in total tumour volume following irradiation and allow necrotic material to accumulate within the tumour. We note the wider array of qualitative response observed compared to the one compartment models considered in Chapter 2 and, in particular, note that different parameter regimes may give rise to curves which resemble each of the response shapes characterised in Chapter 2. In particular, varying the value of ζ may give rise to both pseudo-progression behaviour and response plateau dynamics. We investigate these qualitative behaviours further in Section 6.3.

6.2.3 Achieving a post-irradiation decrease in tumour volume

In this section we identify the conditions needed to achieve a decrease in the total tumour volume within the two compartment model immediately following irradiation. We may recast the two compartment model equations in terms of the total tumour volume, $Y := V + N$, and the necrotic volume fraction, $\Phi := \frac{N}{Y}$. The resulting equations governing inter-fraction tumour growth are thus given by

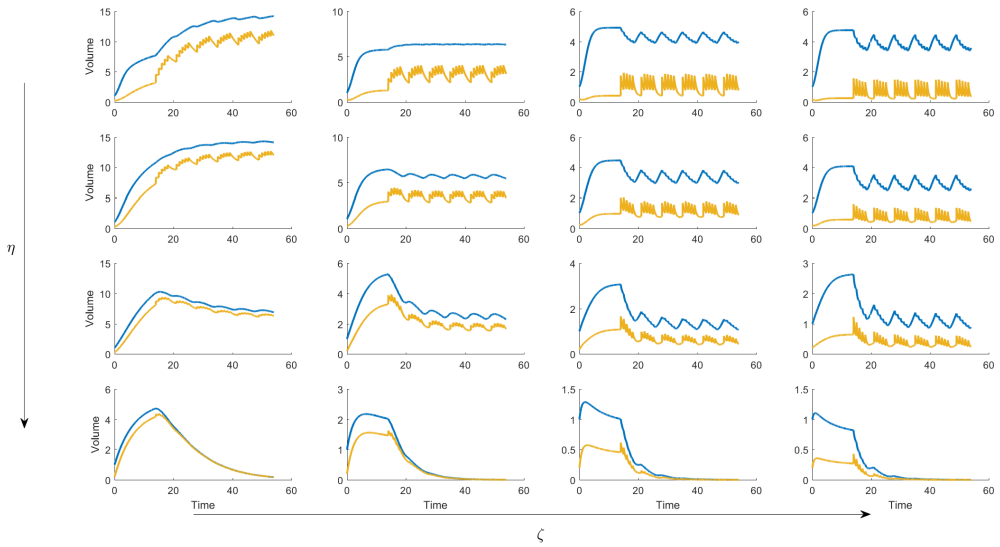

Figure 6.2: Results of a parameter sweep for the two compartment model, simulating Equations (6.1) and (6.2). Parameters increase in the direction of the arrows with necrosis rate, $\eta \in [0.1, 0.99]$, varying by row, and the decay rate of necrotic material, $\zeta \in [0.1, 2]$, by column. Trajectories for the total tumour volume, Y, and the underlying volume of necrotic material, N, are shown in blue and yellow, respectively. For each simulation the remaining parameter values are held fixed: $\lambda = 1$, $\gamma = 0.3$, $K = 5$, $Y(0) = 1$ and $\Phi(0) = 0.2$. Radiotherapy is simulated for the standard fractionation protocol starting after a 2 week pre-treatment growth period.

$$\frac{dY}{dt} = \lambda(1-\Phi)Y\left(1-(1-\Phi)\frac{Y}{K}\right) - \zeta\Phi Y, \tag{6.6}$$

$$\frac{d\Phi}{dt} = (1-\Phi)\left[\eta - \lambda\Phi\left(1-(1-\Phi)\frac{Y}{K}\right) - \zeta\Phi\right]. \tag{6.7}$$

Let $*^{-/+}$ denote the value of $*$ immediately before/after a fraction of radiation. Then for an initial decrease in Y in response to a fraction of radiation we require $\frac{dY}{dt}^{+} < 0$. Since the radiotherapy induces an instantaneous mass transfer between the tumour and necrotic compartments, $Y^{+} = Y^{-}$. However, radiotherapy induces a change in tumour composition such that

$$\Phi^{+} = \frac{N^{+}}{Y^{+}} = \Phi^{-} + \gamma(1-\Phi^{-}). \tag{6.8}$$

Therefore, for an immediate decrease in total tumour volume to be observed after irradiation of the tumour we require

$$\overbrace{\lambda(1-\Phi^-)(1-\gamma)Y^-\left(1-(1-\Phi^-)(1-\gamma)\frac{Y^-}{K}\right)}^{\text{growth of remaining viable tumour population}}-\underbrace{\zeta\Phi^-Y^-}_{\text{decay of previous necrotic material}}-\overbrace{\zeta\gamma(1-\Phi^-)Y^-}^{\text{decay of RT-induced necrotic material}}<0. \quad (6.9)$$

We group the terms in this inequality such that the expression may be viewed as balance of the regrowth of the remaining viable tumour population and the decay of the necrotic compartment. Denoting the left-hand side of the inequality in Equation (6.9) by $f(\Phi,\gamma)$, we may view this criteria as a function of the necrotic fraction of the tumour volume and the radiation-induced death rate. In Figure 6.3a we visualise contours of f in (Φ,γ) parameter space, holding the values of Y, K and ζ constant. The contour $f(\Phi,\gamma)=0$ therefore delineates the boundary between scenarios resulting in a post-irradiation decrease in tumour volume and those for which the tumour continues to grow following irradiation. By varying the necrosis rate, η, we simulate tumours with different necrotic fractions for the same total tumour volume. We subsequently simulate the 5 daily fractions of radiotherapy for 3 tumours of differing pre-radiotherapy compositions and observe the resulting treatment response. The 3 tumours each have the same total tumour volume, Y, but have contain different volumes of necrotic material. For the tumour corresponding to P1, $f(\Phi,\gamma)>0$ and Figure 6.3b shows that the simulated tumour continues to grow during treatment. Conversely, in Figure 6.3d for point P3, the tumour volume decreases monotonically during radiotherapy since $f(\Phi,\gamma)<0$ at the start of treatment. However, the intermediate point P2 yields dynamics that are not monotonic (Figure 6.3c). In this case, $f(\Phi,\gamma)>0$ prior to treatment and thus the tumour continues to grow at the start of treatment. However, the value of f is sufficiently close to 0 that the build-up of necrotic material due to radiation-induced cell death eventually results in a change of sign of f and a subsequent decrease in tumour volume. As such, the qualitative behaviour resembles the 'pseudo-progression' dynamics characterised in previous chapters.

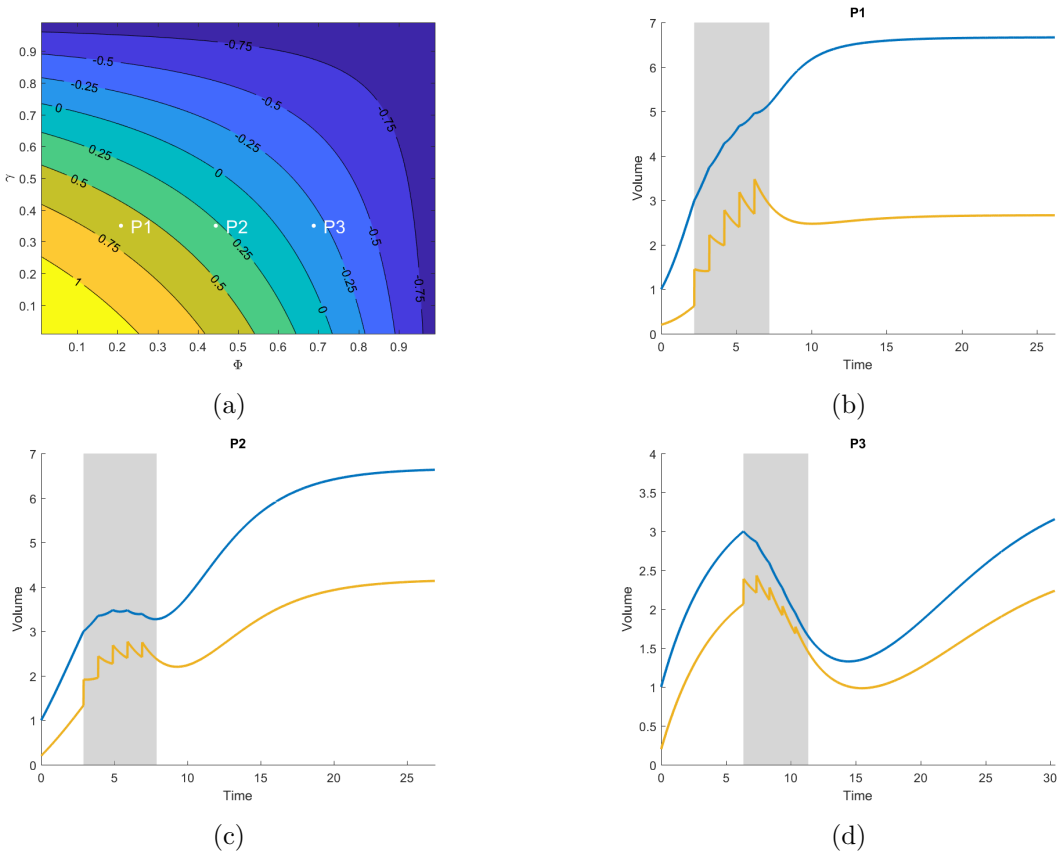

Figure 6.3: a) Contour plot evaluating the left-hand side of the inequality in Equation (6.9) as a function of the pre-radiotherapy necrotic fraction, Φ, and the radiation-induced death rate, γ. Positive values correspond to a sustained increase in tumour volume following irradiation, whilst negative values correspond to a decrease in tumour volume. The remaining parameter values are fixed as: $\lambda = 1$, $\zeta = 0.3$, $K = 5$ and $Y = 3$. b)-d) Total tumour volume, Y, (blue) and necrotic volume, N, (yellow) trajectories simulating 5 fractions of radiotherapy (highlighted in grey) with interfraction time $\Delta t = 1$, starting when the tumour is of volume $Y = 3$. The radiation-induced death rate is fixed as $\gamma = 0.35$. The necrosis rate for each simulation is $\eta = 0.2, 0.5, 0.8$. The pre-treatment compositions thus differ in their necrotic fractions, Φ, corresponding to the points P1, P2, and P3 in panel a), respectively.

6.2.4 Small tumour dynamics

In order to determine whether a treatment protocol may eradicate a tumour, it is informative to consider the model in the limit $V = \mathcal{O}(\epsilon)$ for $0 < \epsilon \ll 1$, and a small viable tumour population. With $0 < V = (1 - \Phi)Y \ll 1$, we deduce from Equation (6.6) that the inter-fraction dynamics for the whole tumour volume are governed by

$$\frac{dY}{dt} \sim \lambda V - \zeta N. \tag{6.10}$$

If $N \gg V$ then the dynamics in the necrotic compartment dominate and the whole tumour volume undergoes exponential decay to leading order. If, however, the volume of the necrotic compartment is also small so that $N = \mathcal{O}(\epsilon)$, and therefore $Y = \mathcal{O}(\epsilon)$, then Equation (6.1) gives

$$V \sim V(0)e^{(\lambda-\eta)t}. \tag{6.11}$$

and Equation (6.2) becomes

$$\frac{dN}{dt} = \eta V(0)e^{(\lambda-\eta)t} - \zeta N. \tag{6.12}$$

Solving Equation (6.12) we find that

$$Y \coloneqq V + N \sim N(0)e^{-\zeta t} + \frac{\lambda + \zeta}{\lambda - \eta + \zeta}V(0)e^{(\lambda-\eta)t} - \frac{\eta V(0)}{\lambda - \eta + \zeta}e^{-\zeta t} \tag{6.13}$$

at leading order. We note that if the tumour is assumed to have been growing originally, then $\lambda - \eta > 0$.

Without loss of generality, assuming that a fraction of radiotherapy is delivered to the small tumour volume at $t = 0^-$, then Equation (6.13) describes the tumour response dynamics with $V(0) = (1-\gamma)(1-\Phi^-)Y^-$ and $N(0) = \Phi^- Y^- + \gamma(1-\Phi^-)Y^-$. Linearising the inequality in Equation (6.9) provides a condition for observing an initial decrease in tumour volume.

6.2.5 Calculating regrowth times

In Chapter 3, analysis of the model equations allowed for calculation of the time after irradiation for which a small tumour would regrow to its original size. Such calculations were shown to be important for determining response to radiotherapy and identifying protocols for which the observed tumour response plateaued.

Assuming the radiation is sufficient to induce a decrease in tumour volume, we may use Equation (6.13) to find that the regrowth time Δt for the two compartment model presented here is given implicitly as a solution of

$$(\lambda+\zeta)(1-\gamma)(1-\Phi^-)\tau^{\frac{\lambda-\eta+\zeta}{\zeta}} - (\lambda-\eta+\zeta)\tau + (\lambda-\eta+\zeta)(\Phi^- + \gamma(1-\Phi^-)) - \eta(1-\gamma)(1-\Phi^-) = 0, \quad (6.14)$$

at leading order, where $\tau = e^{\zeta\Delta t}$. By applying the generalised Descartes' rule of signs [158] it is possible to show that Equation (6.14) has a unique positive root for Δt, and thus the time to regrowth may be determined.

6.2.6 Analysis of long-term radiotherapy response

We now consider the response of small tumour volumes to arbitrary radiotherapy protocols. The dynamics are therefore described to leading order by linearising Equations (6.1) and (6.2). For small tumour volumes, we find that

$$V+N \sim N(0)e^{-\zeta t} + \frac{1}{\lambda-\eta+\zeta}\left[(\lambda+\zeta)V(0)e^{(\lambda-\eta)t} - \eta V(0)e^{-\zeta t} + \sum_i \gamma(1-\gamma)^{i-1}V(0)(\lambda+\zeta)e^{(\lambda-\eta)t_i}e^{-\zeta(t-t_i)}H(t-t_i)\{1-e^{(\lambda-\eta+\zeta)(t-t_i)}\}\right], \quad (6.15)$$

for a general fractionation protocol in which we administer doses of radiation at times t_i (proof omitted).

For simplicity, consider a dosing strategy whereby the dose and inter-fraction time are constant such that $t_{i+1} - t_i = \Delta t$ and, without loss of generality, let $t_1 = 0$. Then it may

be shown that $\lim_{t\to\infty} V + N = 0$ if

$$\Delta t < \frac{1}{\lambda - \eta} \log \frac{1}{1-\gamma}. \tag{6.16}$$

We note that $\lambda - \eta$ corresponds to the exponential growth rate for small tumour volumes, while $1 - \gamma$ corresponds to the survival fraction of the viable tumour population to radiotherapy. We compare this result to the results found in Chapter 3, where the same relationship between the exponential growth rate at small tumour volumes, the radiotherapy survival fraction and the interfraction time is found (c.f. Equation 3.45). We note that this analysis is similar to that performed by McAneney *et al.* for a variety of one compartment ODE models [107]. The relationship in 6.16 is also similar to that found by Wheldon *et al.* for optimised fractionation within an exponential tumour model for a finite number of fractions [104].

We verify the validity of this relationship in Figure 6.4, where we plot contours of the long-term tumour volume for constant daily fractionation protocols ($\Delta t = 1$) in $(\lambda - \eta, \gamma)$ parameter space. We observe that contours of decreasing final tumour volume converge to the condition given by Equation (6.16). Clearly, the large number of fractions simulated in Figure 6.4 is unrealistic as a treatment protocol, however it approximates the limiting case analysed here. The relationship in Equation (6.16) thus represents the minimum required in order to overcome the exponential regrowth dynamics at small tumour volumes.

From the condition in Equation (6.16), we find that the necrotic compartment is unimportant in terms of long-term outcome; for continued radiotherapy response, it is sufficient to ensure that the cell kill induced by the fractionation protocol outweighs the exponential regrowth rate. However, as shown in previously, the necrotic compartment is an important factor in determining the qualitative response observed throughout treatment.

6.3 Fitting the model to data

Given the analysis in the previous section, we anticipate that it may be possible to fit the two compartment model to a wider range of qualitative behaviours observed in *in vivo* datasets than was possible for the logistic growth model considered in Chapter 2. In this section we use a combination of synthetic data and clinical data to investigate the range

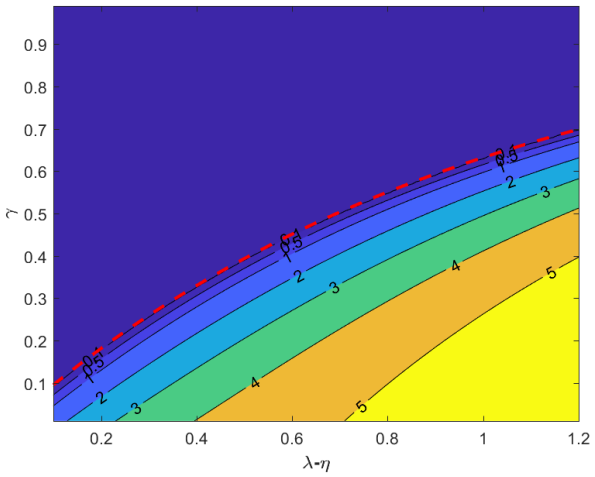

Figure 6.4: Contour plot showing the the final tumour volumes after simulating 500 fractions of radiotherapy with interfraction time $\Delta t = 1$ as the effective growth rate, $\lambda - \eta$, and radiation-induced death rate, γ, vary. The red dashed line marks the theoretical position of the contour for achieving zero tumour volume in the limit as $t \to \infty$, as given by equality in Equation (6.9).

of responses that the two compartment model can capture.

6.3.1 Synthetic data studies

We first use synthetic data generated from the multiphase model presented in Chapters 4 and 5 as a ground truth. We aim to fit our two compartment model to synthetic datasets exhibiting responses not well-captured by the ODE models considered in Chapter 2. We generate synthetic datasets from the simulations exhibiting a plateau in treatment response and pseudo-progression dynamics (see Figures 5.5 and 5.7). We replicate similar temporal resolution typical to clinical datasets.

- For the **plateau** case, we simulate a 'diagnosis' tumour volume measurement 35 days before that start of the radiotherapy schedule, followed by a 'treatment planning' measurement 1 week prior to the first fraction of radiotherapy. Thereafter, we take data points weekly throughout treatment for a total dataset of 8 tumour volume measurements.

- For the **pseudo-progression** case, the multiphase simulation starts the fractionation protocol after just 10 days of pre-treatment growth. In this case, we simply take two pre-treatment data points at $t = 0$ and $t = 10$ and so obtain a dataset containing 7 tumour volume measurements in total, comprising 1 'diagnosis' data

point and 6 further scans at the start of each week of the treatment protocol.

We fit the two compartment model parameters to each dataset using the ABC SMC algorithm (described in Chapter 1), choosing an error tolerance threshold, ϵ_T, corresponding to 1% noise per data point. We note that we use perfect data (i.e. no noise has been added to the values obtained from the multiphase simulations). We perform parameter inference for the 5 model parameters and an initial condition, $\Phi(0)$. We consider parameter regimes for which the tumour is initially growing and choose priors for each parameter to reflect this. More specifically, we require $\lambda - \eta > 0$ for growth and thus specify a $U(0, \lambda)$ prior for η given a growth rate λ. Similarly, we assume that the initial tumour volume is not greater than the effective total carrying capacity, $\tilde{K}$, and thus assume a uniform prior for the ratio $\frac{Y(0)}{\tilde{K}}$, which may be used to ascertain a value for K from Equation (6.5). We finally constrain a uniform prior for the initial necrotic fraction such that neither $\Phi(0)$ or $1 - \Phi(0)$ are greater than the volume fractions at equilibrium for the necrotic and tumour cell compartments, respectively. The full list of options for setting up the ABC SMC algorithm are listed in Table 6.1.

Algorithm option	**Setup used**
Threshold schedule method, ϵ_t	Adaptive - 10% quantile
Number of particles	4000
Parameter perturbation kernel type	Multivariate normal optimal local covariance matrix
Growth rate prior, λ	$U(0, 1)$
Death rate prior, γ	$U(0, 1)$
Necrosis rate prior, η	$U(0, \lambda)$
Necrotic decay rate prior, ζ	$U(0, 1)$
Initial tumour volume:carrying capacity prior, $\frac{Y(0)}{\tilde{K}}$	$U(0, 1)$
Initial necrotic fraction prior, $\Phi(0)$	$U(\max(0, 1 - \xi), \frac{\eta}{\eta+\zeta})$

Table 6.1: Options used for setting up the ABC SMC algorithm. Further explanation of these options can be found in Chapter 1.

The results from fitting the model for the two cases mentioned above are presented in Figures 6.5a and 6.5b. We sample parameter combinations from the posterior distribution and simulate the resulting model trajectories. We plot 95% credible intervals at each time point for both the total tumour volume and the necrotic volume. In both cases, the two compartment model provides a good fit to the synthetic data. This represents an improvement in fit, particularly for the pseudo-progression case, in comparison to the

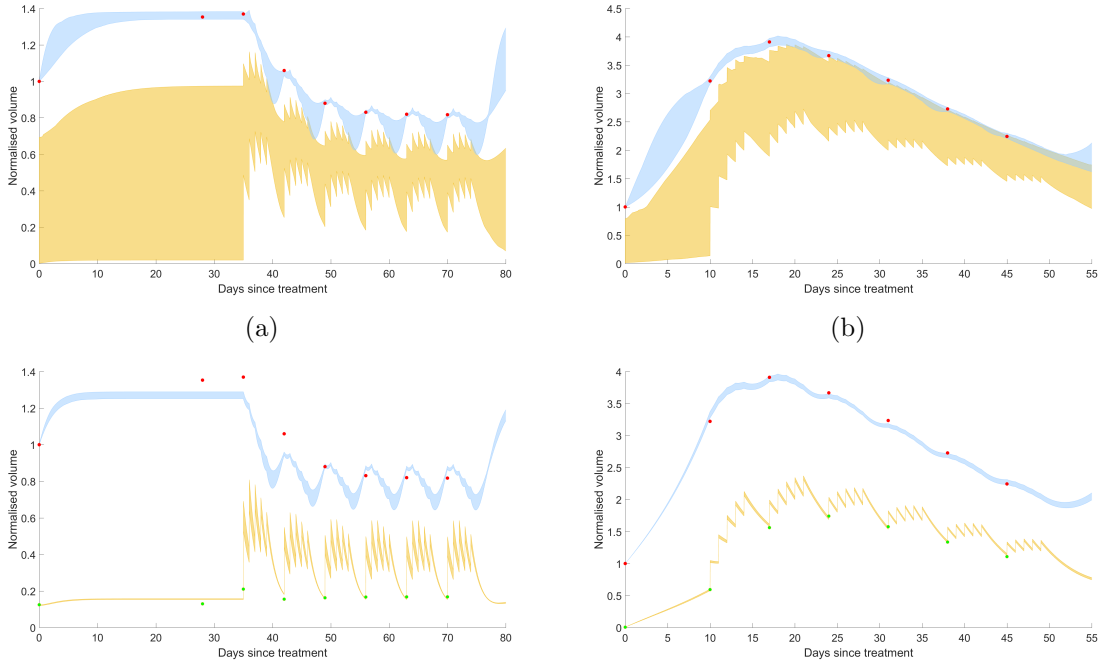

Figure 6.5: Results from fitting the two compartment model, Equations (6.1)-(6.2), to synthetic datasets generated from the multiphase model from Chapter 5 using the ABC SMC algorithm, with options as listed in Table 6.1. Panels a) and c) correspond to data from the response plateau case (P), while panels b) and d) use data from the pseudo-progression case (PP) - see Chapter 5 for more details. 95% credible intervals for the total tumour volume (blue regions) and underlying necrotic volume (yellow regions) at each time point are obtained by sampling 120 parameter combinations from the posterior distributions and simulating Equations (6.1) and (6.2). The synthetic data points for total tumour volume are marked by the red dots. In panels c) and d) green dots correspond to additional data points for the necrotic volume which are used for model calibration.

single compartment models in Chapter 2, which were unable to capture such dynamics. We note however, that the data consisting of tumour volume measurements alone are insufficient to constrain the underlying tumour composition dynamics; in both cases the credible intervals for the necrotic fraction of the tumour are wide.

We now repeat the parameter fitting, extending our synthetic dataset to include measurements of the necrotic volume within the tumour at each time point. We quantify the necrotic fraction from the multiphase simulation by evaluating

$$\bar{\phi_2}(t) = \frac{1}{R(t)} \int_0^{R(t)} \phi_2(x,t) dx, \tag{6.17}$$

with the necrotic volume thus given by $\bar{\phi_2}(t)R(t)$. The results of including this additional data in the parameter fitting process for both the plateau and pseudo-progression cases are shown in Figures 6.5c and 6.5d. We see that the inclusion of data relating to necrotic volumes improves the accuracy of the tumour composition dynamics while preserving a good fit to the data for the total tumour volume. We note however that, for the plateau case, the two compartment is not able to fit the data points for overall tumour volume as well when constrained by additional composition data.

6.3.2 Clinical dataset studies

Having shown the good fit of the two compartment model to synthetically generated data, we proceed to consider *in vivo* clinical data. We again use the ABC SMC algorithm to fit the model to a representative subset of 9 patients from a clinical dataset of oropharyngeal cancer volumes throughout treatment (DS3 from Table 2.1 in Chapter 2). We estimate the model parameters individually for each patient, and take a target error threshold, ϵ_T, equivalent to 10% noise per data measurement. The resulting credible intervals are shown in Figure 6.6.

As with the *in silico* patient data generated from the multiphase model, the two compartment model can reproduce the qualitative dynamics. However, we again observe a large uncertainty in the dynamics of the underlying tumour composition due to the lack of spatial data. Furthermore, since we allow for a greater potential error in the data measurements than for our synthetic data studies, we may observe different qualitative

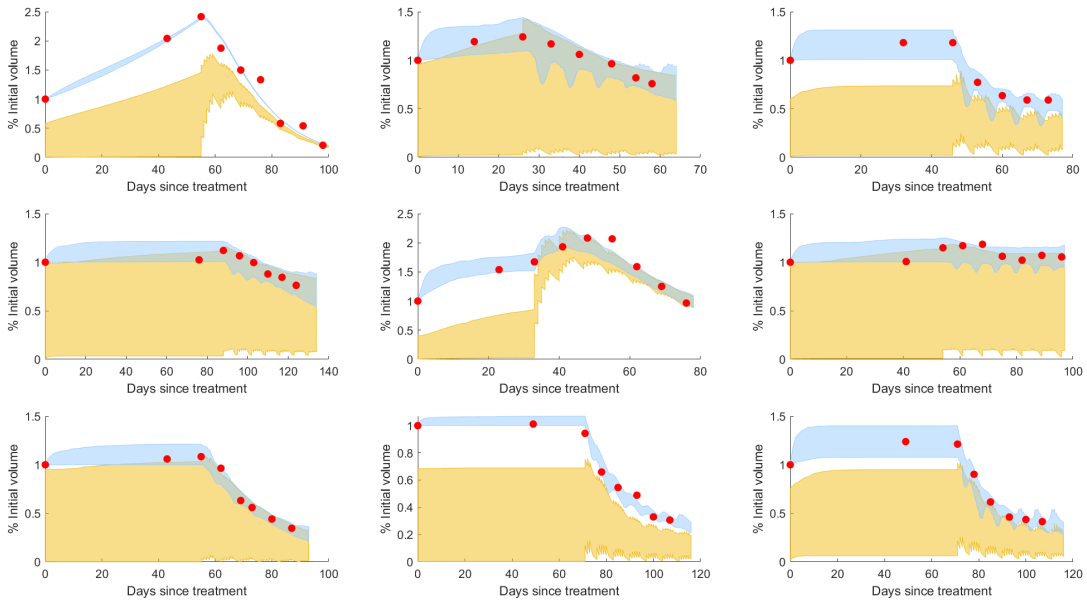

Figure 6.6: Results from fitting the two compartment model to 9 patients individually from the dataset DS3 (see Table 2.1) using the ABC SMC algorithm with setup options as listed in Table 6.1. 95% credible intervals for the total tumour volume (blue regions) and underlying necrotic volume (yellow regions) at each time point are obtained by sampling 120 parameter combinations from the posterior distributions and simulating Equations (6.1) and (6.2). The true data points are marked by the red dots.

response trajectories that fit within our threshold tolerance, ϵ_T. For example, the posterior trajectories for the second patient in the dataset (top middle plot in Figure 6.6) exhibit two types of qualitative behaviour, with trajectories exhibiting a monotonically decreasing tumour volume response in some cases and others plateauing during treatment. As such we may decompose the parameter sets in the posterior distribution into two different groups based on the qualitative behaviour of the simulation dynamics. We visualise the clustering of these two behaviours in the posterior parameter space for $(\eta, \zeta, \Phi(0))$ in Figure 6.7b, where $\Phi(0) = \frac{N(0)}{V(0)+N(0)}$ is the necrotic fraction at the start of treatment. We see that the model parameters are correlated, with the samples in the posterior forming a surface in parameter space.

This example provides another illustration whereby the data are insufficient to fully determine the dynamics for this model. In light of the results in previous chapters, we expect that the tumour composition may significantly affect response dynamics. As such, distinguishing the appropriate underlying dynamics is important when using such models accurately to simulate alternative fractionation protocols and predicting treatment

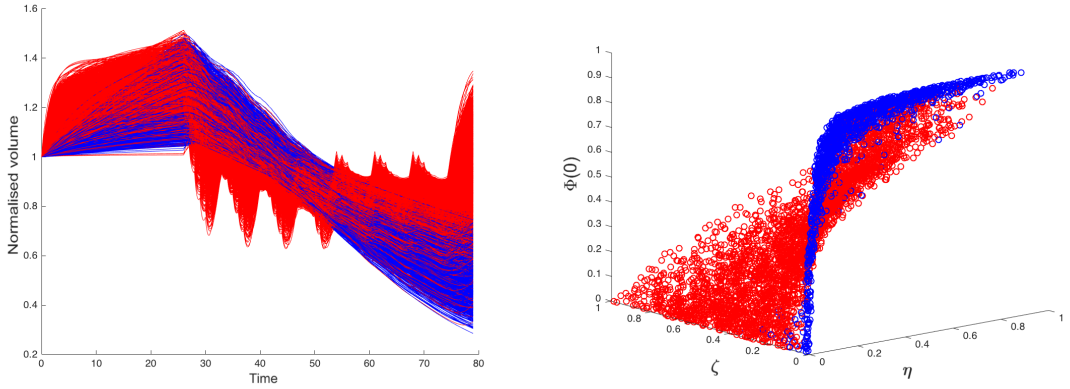

(a) (b)

Figure 6.7: a) The bimodal distribution in qualitative radiotherapy response exhibited by simulating Equations (6.1) and (6.2) using parameter combinations sampled from the posterior distribution for patient 2 in Figure 6.6. Tumour volume trajectories are coloured by qualitative response: monotonic trajectories are shown in blue and those exhibiting a plateau in treatment response coloured in red. b) Visualisation of the corresponding parameter combinations in the posterior parameter space for $(\eta, \zeta, \Phi(0))$. Each circle is coloured according to the qualitative behaviour of the corresponding simulation trajectory.

outcome. We anticipate that further time points or spatial data, as in our synthetic data study, may constrain the posterior in such cases to unimodal qualitative dynamics.

6.4 Comparison of phenomenological ODE models

Having ascertained that the two compartment model exhibits a wider range of dynamics than the single compartment models considered in Chapter 2, we proceed now to compare them directly. While the two compartment model may capture non-monotonic response dynamics that are not well-described by the one compartment models, we anticipate that the simplicity of the one compartment models, in terms of number of model parameters, may be more favourable for certain qualitative behaviours. More precisely, if both the one compartment and two compartment models both fit equally well to the data, the simpler model is preferred when compared using the Aikaike information criterion (AIC), for example.

In this section we compare the two compartment model with the logistic and Gompertz models presented in Chapter 2. We generate synthetic datasets that exemplify the range of qualitative dynamics exhibited by the multiphase model and then assess the performance of the models by fitting them to the data. We choose two simulations from Chapter 5 exhibiting monotonic treatment responses; an example of a 'fast responder' (FR), and an

example taken from our case A of our parameter sweep in $\boldsymbol{\theta}$-space for which the dead material phase has little effect on the response trajectory. In both cases we anticipate that the simpler models will adequately capture the dynamics in the data. We consider two further examples corresponding to pseudo-progression (case PP) and a treatment response plateau (case P); we expect that the two compartment model will better describe these data than the one compartment models. For each case, we generate perfect data in the manner described in Section 6.3.

For each case, parameter inference using the ABC SMC model selection algorithm strongly favoured the two compartment model, with a posterior model marginal probability ≈ 1 (results not shown). The two compartment model more closely fits the data than the logistic and Gompertz models, with most parameter combinations resulting in simulations outside of the error threshold, ϵ_T. As such, we instead use the EBO algorithm, described in Chapter 1, to separately identify the best-fitting parameter set for each model in order to further compare their performances. The resulting best fit model trajectories for each dataset are shown in Figure 6.8. The corresponding sums of residual squares errors, $\Sigma(\boldsymbol{p})$, weighted by the magnitude of each data point are listed in Table 6.2.

	logistic		**Gompertz**		**two compartment**	
Case	$\Sigma(\boldsymbol{p})$	$AICc$	$\Sigma(\boldsymbol{p})$	$AICc$	$\Sigma(\boldsymbol{p})$	$AICc$
FR	0.0015	-56.42	0.0069	-44.47	5.5×10^{-5}	0.93
A	9.8×10^{-4}	-60.06	0.015	-38.46	2.7×10^{-6}	-23.12
P	0.065	-26.52	0.067	-26.28	1.9×10^{-4}	10.66
PP	0.032	-23.68	0.030	-24.28	1.3×10^{-4}	Undefined

Table 6.2: Summary statistics for the quality of fit of the logistic, Gompertz and two compartment models to each of the synthetic datasets corresponding to Figure 6.8. $\Sigma(\boldsymbol{p})$ gives the sum of residual squares error between the model solution and the data points, with each residual error weighted by the magnitude of the data point. $AICc$ refers to the Akaike information criterion value corrected for small sample sizes.

As anticipated, the three candidate models perform comparably for the monotonic response dynamics, cases FR and A, in Figures 6.8a-b. Similarly, while the two compartment model provides a good fit to non-monotonic dynamics, cases P and PP, shown in Figures 6.8c-d, the logistic and Gompertz models fail to capture the qualitative behaviour exhibited by the data. We use the Akaike information criterion, adjusted for the limited

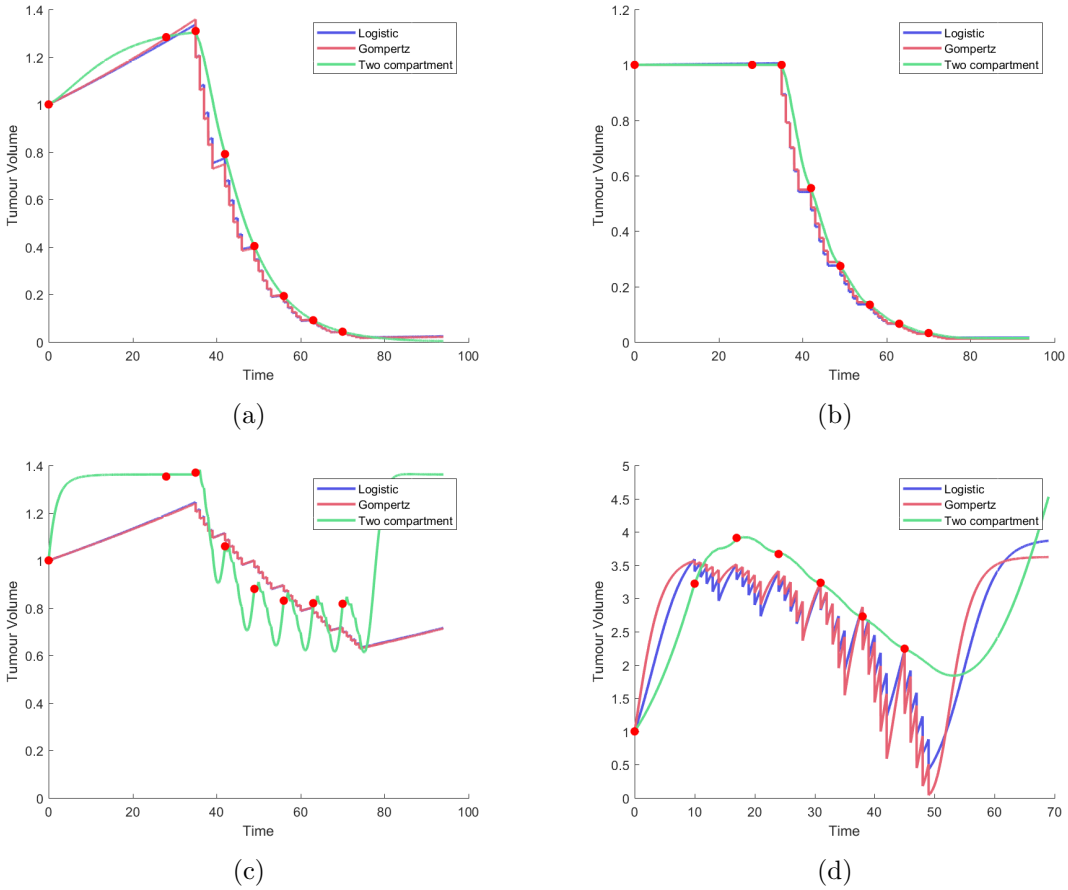

Figure 6.8: The best-fitting solutions for the logistic, Gompertz and two compartment models obtained using the EBO algorithm to fit to synthetic datasets generated from the multiphase model. The synthetic datasets (red points) in panels a)-d) are taken from cases FR, A, P and PP, respectively (refer to Chapter 5 for more details).

size of the dataset in order to quantify the quality of each model with respect to the data in each case (see Chapter 1, Section 1.7). The $AICc$ values for each case are listed in Table 6.2, with lower values corresponding to a better performance of the model [1]. We see that, even in the response plateau (P) and pseudo-progression (PP) cases, the two compartment model is not favoured. Having used synthetic datasets of similar temporal resolution to *in vivo* clinical data, the two compartment model is penalised for having the number of model parameters too similar in size to the number of data points, despite the superior fit. In the pseudo-progression case (PP), the dataset used is too small and the model is deemed to be saturated with respect to the data, corresponding to $n-k-1=0$ in the formula for calculating the $AICc$ value.

From the best-fit trajectories shown in Figure 6.8 it is clear that, for cases P and PP, the two compartment model clearly describes the dynamics better than the logistic and Gompertz models. However, the limited nature of the calibration data is insufficient to adequately make inference about this model given the increased number of parameters. Let us assume that for any hypothetical additional data points, the models fit equally well per data point as for the values listed in Table 6.2. Then we may fix $\Sigma(\boldsymbol{p})/n$ in the definition of $AICc$ and thus estimate the number of data points required before the two compartment model is deemed to out-perform the logistic and Gompertz models. For both the plateau and pseudo-progression cases we find that a dataset of $n=9$ data points would suffice for the two compartment model to attain the lowest $AICc$ value of the three models.

6.5 Perspectives on future work

When designing predictive models for clinical application, it is necessary to identify the key factors driving the system dynamics and to ensure that these processes are captured in sufficient detail to replicate the range of qualitative responses observed *in vivo*. Our modelling work in previous chapters revealed that tumour composition may significantly affect the observed response to radiotherapy as measured by tumour volume. In particular, the underlying composition is dynamic, changing over time, particularly in response to

[1] Note that the magnitude of the $AICc$ value is not meaningful, we are solely interested in the relative ordering of the values for the different models.

irradiation. As such, we have proposed a two compartment model in this chapter as an extension to the one compartment models considered in Chapter 2; the new model decomposes the tumour into a viable tumour cell population, $V(t)$, and a compartment containing necrotic or dead material, $N(t)$.

Analysis of the model, defined by Equations (6.1) and (6.2), in Section 6.2 revealed conditions required for observing favourable treatment responses. These results were consistent with those obtained for more complex models presented previously in this thesis (c.f. Chapter 3).

In Chapter 5 we demonstrated that our multiphase model can reproduce the different qualitative responses to radiotherapy identified in *in vivo* clinical datasets. Conversely, the one compartment models presented in Chapter 2 fail to capture the full range of dynamic behaviours. Synthetic studies using data generated from simulations of our multiphase model showed that the two compartment model may reproduce non-monotonic radiotherapy responses, such as 'pseudo-progression' of the tumour, that are not captured by the simpler models. Indeed, further considering *in vivo* clinical data we observed that the two compartment model provides a good fit to the *in vivo* clinical data across the range of observed responses. However, the extra detail incorporated within compartmental ODE models comes at the cost of extra model parameters. Given the lack of clinical data typically available for model calibration, parameter values for models of this complexity are likely to be 'practically unidentifiable' with respect to typical datasets. Despite the good fit to measurements of overall tumour volume, analysis of simulated trajectories obtained from sampling parameter sets from the posterior distribution showed a large variation in estimates of the underlying tumour composition dynamics. In light of this, model predictions from compartmental models calibrated in the absence of spatial data should be treated with caution. The results presented in previous chapters demonstrated that heterogeneity in tumour composition may affect the qualitative response to radiotherapy. Furthermore, we anticipate that uncertainty due of inadequate calibration data may lead to spurious predictions.

The results of our synthetic data studies in Section 6.3.1 emphasise the caution that should be taken when interpreting the fit of such models to datasets which do not incorporate spatial data. This is evident in other results in the literature. Tariq *et al.* [110]

present results of fitting a similar model to *in vivo* data from 25 NSCLC patients. They use a Bayesian framework for parameter inference but consider only the best-fitting simulations for each patient. As such, they present results which fit the overall tumour volume data well but result in unrealistic underlying tumour compositions dynamics, whereby the entire tumour population is killed shortly after the start of irradiation, for example. Given the results presented here, it is likely that their inference would also demonstrate a large amount of uncertainty in the predicted dynamics of the underlying tumour composition.

In Section 6.4 we presented preliminary studies comparing the phenomenological models considered in Chapter 2 and the two compartment model introduced here. We used the Akaike information criterion to evaluate the goodness of fit of each model with respect to the data, taking into account the number of model parameters that need to be estimated for each model. For the monotonic treatment response cases, the logistic and Gompertz models both adequately captured the dynamics and were preferred over the two compartment model for their simplicity. However, for the response plateau and pseudo-progression cases, where the two compartment model should be preferred to models which cannot describe such behaviour, lack of data points results in an unfavourable $AICc$ compared to the simpler models with fewer parameters. We note that the problem of limited data is further exaggerated if we consider calibrating the models from pre-treatment data only. However, for the studies presented in Section 6.4, simple calculations estimated that only 1 or 2 more data points would be required for the two compartment model to be favoured in these cases.

For compartmental ODE models, additional data for sufficiently inferring parameter values does not necessarily need to be restricted to increased temporal resolution. The decomposition of the tumour implicit in the two compartment model presented in this chapter would lend itself to calibration using 'spatial' data estimating the necrotic fraction at each time point. Models such as this, when combined with *in silico* data, may be used for experimental design studies to identify sufficient data collection paradigms. Thus, more sophisticated imaging techniques may improve the calibration of such models without requiring improved temporal resolution. However, such considerations also raise further questions about model comparison as it is not obvious how to compare models that operate on different levels of resolution and may therefore take advantage of different

calibration datasets. As a result, whilst compartmental models have the potential to more accurately describe *in vivo* radiotherapy response dynamics, there are many avenues for further work in this area.

The need for additional data may be further reduced by considering sub-cases of such models whereby some parameters are assumed to show less inter-patient variability in others and may thus be assumed to be global. This approach follows that taken by Prokopiou *et al.* [105] and may reduce the number of parameters that require patient-specific calibration.

The potential of these studies is further enhanced through the use of a more sophisticated model, such as our multiphase model, to generate 'ground truth' *in silico* data. The illustrative studies presented here represent a small sample of the possible areas for future work. In particular, it is not clear how the parameter values in the calibrated two compartment models are related to those used in the multiphase model to generate the synthetic data. Uncertainty in the parameter estimates may be further studied by investigating the effects of varying the multiphase model parameters on the variation in two compartment model parameters estimated upon calibration.

In the studies presented here, while the two compartment model captured the qualitative dynamics and fit to the data points well, the predictive power of the model was not assessed. Interesting possibilities for further model comparison studies, beyond the AIC, may consider the accuracy of predicted data points. The power of using synthetically generated data may further be harnessed by first calibrating these models to data, and subsequently simulating the response to a alternative fractionation protocol to investigate the predictive potential of these models.

Chapter 7

Conclusions

There have been many recent technological advances in the application of radiotherapy with the development of more precise techniques for delivering a higher dose of radiation to the tumour whilst sparing the surrounding normal tissue, including intensity-modulated radiotherapy (IMRT), image-guided radiotherapy, stereotactic body radiotherapy, charged particle therapies and more [5]. Advanced imaging and radiomic techniques also allow for improved *in vivo* tumour imaging of different intratumoural microenvironments [39, 141, 159].

With the range of treatment options available and the potential for routine use of more sophisticated imaging techniques in clinical practice, it is natural to anticipate that the next major development in radiotherapy is the prescription of more personalised treatment protocols [5]. Indeed, the simple observation that two tumours presenting with the same TNM stage at treatment-planning may respond substantially differently to the same radiotherapy protocol suggests that current practice is not sufficient to stratify patients and determine response to treatment.

Effective personalisation of treatment requires accurate prediction of response in order to determine the optimal treatment option. Predictive mathematical models should thus be sufficiently calibrated and validated against appropriate datasets [115]. Pre-treatment patient-specific data in the clinic is typically limited, which consequently motivates the use of simple, phenomenological models for clinical application. In Chapter 2 we investigated the use of a range of such models for fitting to and predicting clinical radiotherapy

data from head and neck cancer patients. We used synthetic data studies to illustrate some of the key issues regarding uncertainty quantification, predictive power and model selection in the face of limited and potentially noisy data obtained from clinical CT scans. However, such issues are secondary to developing models which are sufficiently detailed to adequately describe the range of dynamics observed *in vivo*. We hypothesised that heterogeneity in tumour composition may account for some of the dynamics not captured by these simple, non-spatial models. As a result, we were led to develop a range of models of increasing spatial heterogeneity and complexity.

In vitro tumour spheroids exhibit an approximately symmetrical geometry and reproducible structure that is enticing for mathematical modelling [15]. In Chapter 3 we extended a well-studied model of nutrient-limited tumour spheroid growth [63] to incorporate the effects of radiotherapy. The heterogeneity in tumour composition exhibited at various growth stages was observed to affect the efficacy of radiotherapy fractions delivered to the tumour. We identified a relationship between the tumour growth rates, radiotherapy survival fraction and inter-fraction time between doses for which the tumour response to treatment may plateau without eradicating the tumour. Such dynamics are observed qualitatively in datasets of tumour volume measurements in the clinic in some patients. Further simulation results showed that tumour composition may affect treatment response without altering intrinsic radiosensitivity parameters.

However, the instantaneous volume loss upon irradiation incorporated in our tumour spheroid model, and many other models in the literature, renders it incapable of capturing the complete range of radiotherapy response dynamics observed *in vivo*. This is perhaps unsurprising since it is well-established that tumour cells that are fatally damaged by radiation may die via a number of mechanisms on different timescales and may thus occupy space within the tumour for some time after irradiation. As such, the spatial distribution of material within the tumour is likely to be dynamic. In Chapter 4 we developed a novel three phase model of tumour growth with the tumour volume being comprised of a viable tumour cell phase, a dead material phase and extracellular fluid. The model was shown to reproduce growth dynamics and spatial structures consistent with the *in vitro* spheroids discussed previously. However, the physical interactions between the phases and the spatiotemporal changes in distribution was shown to result in additional

non-monotonic growth dynamics not observed in previous models for some parameter regimes. The stability of these dynamics upon extension to 3D growth and symmetry breaking is not obvious and warrants further analysis and investigation.

In Chapter 5 we extend our multiphase tumour growth model to account for radiotherapy effects. The model is able to qualitatively reproduce all of the behaviours identified within our *in vivo* datasets. Investigation of the effects of varying the physical properties of the dead material within the tumour on radiotherapy response demonstrated that pre-treatment measurements of tumour volume alone are likely to be insufficient to determine response dynamics. Furthermore, simulations reveal that tumours with similar pre-treatment growth dynamics and tumour compositions may markedly differ in their response. Using the model to investigate the identification of potential metrics that may be used to stratify patients by qualitative response prior to treatment may provide an interesting avenue for further work. Furthermore, if accurate pre-treatment predictions are not possible, how early during treatment is it possible to differentiate between different response dynamics?

Of course, *in vivo* tumours grow surrounded by normal tissue which may exert stress on the tumour boundary. From the analysis presented in Chapters 4 and 5 it is unclear what effect modifying the boundary conditions may have on the resulting dynamics. This may provide an interesting extension to the model, particularly in the radiotherapy case, whereby the surrounding normal tissue may exhibit a different response to irradiation and toxicity effects may be investigated. The spatial detail incorporated within this model would also lend itself to simulation and investigation of more sophisticated radiotherapy paradigms such as dose-painting, for example.

However, perhaps the most important benefit of developing more complex mathematical models such as this is for aiding the development of better models for clinical application with greater predictive power. Some of the many possibilities and open questions in this area regarding model selection and experimental design were illustrated in our previous discussion. More complex models may be used to generate synthetic data with the advantage of knowing the 'ground truth'. This data is thus more useful for studies assessing the quality of fits of candidate models to data and subsequent predictive power. In particular, while a candidate model may provide a good fit to one dataset,

the true test of predictive power and whether the model captures sufficient mechanistic detail would be to assess the quality of predictions subsequently simulating alternative fractionation protocols using the calibrated model. Such *in silico* studies are likely to provide fertile ground for future work.

Bibliography

[1] L. A. Torre, F. Bray, R. L. Siegel, J. Ferlay, J. Lortet-Tieulent, and A. Jemal. Global cancer statistics, 2012. *CA: A Cancer Journal for Clinicians*, 65(2):87–108, mar 2015. doi: 10.3322/caac.21262.

[2] J. F. Fowler. Development of radiobiology for oncology—a personal view. *Physics in Medicine and Biology*, 51(13):R263–R286, jul 2006. ISSN 0031-9155. doi: 10.1088/0031-9155/51/13/R16.

[3] K. A. Ahmed, C. R. Correa, T. J. Dilling, N. G. Rao, R. Shridhar, A. M. Trotti, R. B. Wilder, and J. J. Caudell. Altered Fractionation Schedules in Radiation Treatment: A Review. *Seminars in Oncology*, 41(6):730–750, dec 2014. doi: 10.1053/j.seminoncol.2014.09.012.

[4] L. G. Marcu. Altered fractionation in radiotherapy: From radiobiological rationale to therapeutic gain. *Cancer Treatment Reviews*, 36(8):606–614, dec 2010. doi: 10.1016/j.ctrv.2010.04.004.

[5] J. J. Caudell, J. F. Torres-Roca, R. J. Gillies, H. Enderling, S. Kim, A. Rishi, E. G. Moros, and L. B. Harrison. The future of personalised radiotherapy for head and neck cancer. *The Lancet Oncology*, 18(5):e266–e273, may 2017. doi: 10.1016/S1470-2045(17)30252-8.

[6] D. Hanahan and R. A. Weinberg. The Hallmarks of Cancer. *Cell*, 100(1):57–70, jan 2000. doi: 10.1016/S0092-8674(00)81683-9.

[7] D. Hanahan and R. A. Weinberg. Hallmarks of Cancer: The Next Generation. *Cell*, 144(5):646–674, mar 2011. doi: 10.1016/j.cell.2011.02.013.

[8] P. Carmeliet and R. K. Jain. Angiogenesis in cancer and other diseases. *Nature*, 407(6801):249–257, sep 2000. doi: 10.1038/35025220.

[9] J. M. Brown and A. J. Giaccia. The Unique Physiology of Solid Tumors : Opportunities (and Problems) for Cancer Therapy. *Cancer Research*, 58(7):1408–16, 1998.

[10] S. Proskuryakov and V. Gabai. Mechanisms of Tumor Cell Necrosis. *Current Pharmaceutical Design*, 16(1):56–68, jan 2010. doi: 10.2174/138161210789941793.

[11] H. Okada and T. W. Mak. Pathways of apoptotic and non-apoptotic death in tumour cells. *Nature Reviews Cancer*, 4(8):592–603, aug 2004. doi: 10.1038/nrc1412.

[12] R. M. Sutherland. Cell and Environment Interactions in Tumor Microregions: The Multicell Spheroid Model. *Science*, 240:177–240, 1988.

[13] F. Hirschhaeuser, H. Menne, C. Dittfeld, J. West, W. Mueller-Klieser, and L. A. Kunz-Schughart. Multicellular tumor spheroids: An underestimated tool is catching up again. *Journal of Biotechnology*, 148(1):3–15, jul 2010. doi: 10.1016/j.jbiotec.2010.01.012.

[14] L.-B. Weiswald, D. Bellet, and V. Dangles-Marie. Spherical Cancer Models in Tumor Biology. *Neoplasia*, 17(1):1–15, jan 2015. doi: 10.1016/j.neo.2014.12.004.

[15] J. Folkman. Self-regulation of growth in three dimensions. *Journal of Experimental Medicine*, 138(4):745–753, oct 1973. doi: 10.1084/jem.138.4.745.

[16] W. Mueller-Klieser. Multicellular spheroids: A review on cellular aggregates in cancer research. *Journal of Cancer Research and Clinical Oncology*, 113(2):101–122, apr 1987. doi: 10.1007/BF00391431.

[17] W. Mueller-Klieser. Method for the determination of oxygen consumption rates and diffusion coefficients in multicellular spheroids. *Biophysical Journal*, 46(3):343–348, sep 1984. ISSN 00063495. doi: 10.1016/S0006-3495(84)84030-8.

[18] J. P. Freyer, E. Tustanoff, A. J. Franko, and R. M. Sutherland. In situ oxygen consumption rates of cells in V-79 multicellular spheroids during growth.

Journal of Cellular Physiology, 118(1):53–61, jan 1984. ISSN 0021-9541. doi: 10.1002/jcp.1041180111.

[19] J. J. Casciari, S. V. Sotirchos, and R. M. Sutherland. Glucose diffusivity in multicellular tumor spheroids. *Cancer Research*, 48(14):3905–3909, 1988.

[20] M. J. Dorie, R. F. Kallman, D. F. Rapacchietta, D. Van Antwerp, and Y. R. Huang. Migration and internalization of cells and polystyrene microspheres in tumor cell spheroids. *Experimental Cell Research*, 141(1):201–209, 1982. doi: 10.1016/0014-4827(82)90082-9.

[21] C. Dubessy, J. L. Merlin, C. Marchal, and F. Guillemin. Spheroids in radiobiology and photodynamic therapy. *Critical Reviews in Oncology/Hematology*, 36(2-3):179–192, 2000. doi: 10.1016/S1040-8428(00)00085-8.

[22] M. C. Joiner, J. W. Burmeister, and W. Dörr. Linear energy transfer and relative biological effectiveness. In M. C. Joiner and A. J. van der Kogel, editors, *Basic Clinical Radiobiology*. CRC Press, 2009.

[23] W. Tinganelli, M. Durante, R. Hirayama, M. Krämer, A. Maier, W. Kraft-Weyrather, Y. Furusawa, T. Friedrich, and E. Scifoni. Kill-painting of hypoxic tumours in charged particle therapy. *Scientific Reports*, 5(1):17016, dec 2015. ISSN 2045-2322. doi: 10.1038/srep17016.

[24] M. C. Joiner, A. J. van der Kogel, and G. G. Steel. Introduction: The significance of radiobiology and radiotherapy for cancer treatment. In M. C. Joiner and A. J. van der Kogel, editors, *Basic Clinical Radiobiology*. CRC Press, 2009.

[25] E. J. Hall. *Radiobiology for the Radiologist*. aug . doi: 10.1148/radiol.2242022530.

[26] W. H. McBride and H. R. Withers. Biologic Basis of Radiation therapy. In C. A. Perez and L. W. Brady, editors, *Principles and Practice of Radiation Oncology*. 1997.

[27] V. P. Muriel. The impact on oncology of the interaction of radiation therapy and radiobiology. *Clinical and Translational Oncol-*

ogy, 8(2):83–93, feb 2006. doi: 10.1007/s12094-006-0163-0. URL `http://link.springer.com/10.1007/s12094-006-0163-0`.

[28] C. Vens, M. Koritzinsky, and B. G. Wouters. Irradiation-induced damage and the DNA damage response. In M. C. Joiner and A. J. van der Kogel, editors, *Basic Clinical Radiobiology*. CRC Press, 2009.

[29] D. Eriksson and T. Stigbrand. Radiation-induced cell death mechanisms. *Tumor Biology*, 31(4):363–372, aug 2010. doi: 10.1007/s13277-010-0042-8.

[30] B. Endlich, I. R. Radford, H. B. Forrester, and W. C. Dewey. Computerized video time-lapse microscopy studies of ionizing radiation-induced rapid-interphase and mitosis-related apoptosis in lymphoid cells. *Radiation research*, 153(1):36–48, jan 2000. ISSN 0033-7587.

[31] H. Withers. Four R's of radiotherapy. *Advances in Radiation Biology*, 5 p. 241-2, 1975.

[32] G. G. Steel, T. McMillan, and J. Peacock. The 5Rs of Radiobiology. *International Journal of Radiation Biology*, 56(6):1045–1048, jan 1989. ISSN 0955-3002. doi: 10.1080/09553008914552491.

[33] D. Zips. Tumour growth and response to radiation. In M. C. Joiner and A. J. van der Kogel, editors, *Basic Clinical Radiobiology*. CRC Press, 2009.

[34] B. G. Wouters and M. Koritzinsky. The tumour microenvironment and cellular hypoxia responses. In M. C. Joiner and A. J. van der Kogel, editors, *Basic Clinical Radiobiology*. CRC Press, 2009.

[35] M. Nordsmark, M. Overgaard, and J. Overgaard. Pretreatment oxygenation predicts radiation response in advanced squamous cell carcinoma of the head and neck. *Radiother Oncol*, 41(96):31–39, 1996. doi: 10.1016/S0167-8140(96)91811-3.

[36] M. Nordsmark, S. M. Bentzen, V. Rudat, D. Brizel, E. Lartigau, P. Stadler, A. Becker, M. Adam, M. Molls, J. Dunst, D. J. Terris, and J. Overgaard. Prognostic value of tumor oxygenation in 397 head and neck tumors after primary radiation

therapy. An international multi-center study. *Radiotherapy and Oncology*, 77(1): 18–24, 2005. doi: 10.1016/j.radonc.2005.06.038.

[37] T. Alper and P. Howard-Flanders. Role of Oxygen in Modifying the Radiosensitivity of E. Coli B. *Nature*, 178:978–979, 1956.

[38] M. R. Horsman, B. G. Wouters, M. C. Joiner, and J. Overgaard. The oxygen effect and fractionated radiotherapy. In M. C. Joiner and A. J. van der Kogel, editors, *Basic Clinical Radiobiology*. CRC Press, 2009.

[39] J. A. Bertout, S. A. Patel, and M. C. Simon. The impact of O2 availability on human cancer. *Nature Reviews Cancer*, 8(12):967–975, 2008. doi: 10.1038/nrc2540.

[40] M. C. Joiner. Quantifying cell kill and cell survival. In M. C. Joiner and A. J. van der Kogel, editors, *Basic Clinical Radiobiology*. CRC Press, 2009.

[41] A. M. Kellerer and H. H. Rossi. A Generalized Formulation of Dual Radiation Action. *Radiation Research*, 75(3):471–488, sep 1978. doi: 10.2307/3574835.

[42] P. Nilsson, H. D. Thames, and M. C. Joiner. A generalized formulation of the 'incomplete-repair' model for cell survival and tissue response to fractionated low dose-rate irradiation. *International journal of radiation biology*, 57(1):127–142, 1990. doi: 10.1080/09553009014550401.

[43] R. K. Sachs, P. Hahnfeld, and D. J. Brenner. The link between low-LET dose-response relations and the underlying kinetics of damage production/repair/misrepair. *International journal of radiation biology*, 72(4):351–374, 1997. doi: 10.1080/095530097143149.

[44] H. R. Withers. Radiation biology and treatment options in radiation oncology. *Cancer research*, 59(7 Suppl):1676s–1684s, 1999.

[45] C. Stevens, S. J. Bondy, and D. A. Loblaw. Wait times in prostate cancer diagnosis and radiation treatment. *Canadian Urological Association journal = Journal de l'Association des urologues du Canada*, 4(4):243–8, 2010.

[46] S. Sharma, J. Bekelman, A. Lin, J. N. Lukens, B. R. Roman, N. Mitra, and S. Swisher-McClure. Clinical impact of prolonged diagnosis to treatment interval (DTI) among patients with oropharyngeal squamous cell carcinoma. *Oral Oncol*, 56:17–24, 2016. doi: 10.1016/j.oraloncology.2016.02.010.

[47] L. Wang, C. R. Correa, J. A. Hayman, L. Zhao, K. Cease, D. Brenner, D. Arenberg, J. Curtis, G. P. Kalemkerian, and F.-M. Kong. Time to Treatment in Patients With Stage III Non–Small Cell Lung Cancer. *International Journal of Radiation Oncology*Biology*Physics*, 74(3):790–795, jul 2009. doi: 10.1016/j.ijrobp.2008.08.039.

[48] W. Lydiatt, S. Patel, B. O'Sullivan, M. Brandwein-Gensler, J. Ridge, J. Migliacci, A. Loomis, and J. Shah. Head and Neck Cancers-Major changes in the American Joint Committe on Cancer Eighth Edition Cancer Staging Manual. *CA Cancer J Clin*, 67(2):122–137, 2017. doi: 10.3322/caac.21389.

[49] M. C. Joiner and S. M. Bentzen. Fractionation: the linear-quadratic approach. In M. C. Joiner and A. J. van der Kogel, editors, *Basic Clinical Radiobiology*, page 375. CRC Press, 2009. ISBN 978 0 340 929 667.

[50] S. M. Bentzen. Radiation therapy: Intensity modulated, image guided, biologically optimized and evidence based. *Radiotherapy and Oncology*, 77(3):227–230, 2005. doi: 10.1016/j.radonc.2005.11.001.

[51] H. Mirghani and P. Blanchard. Treatment de-escalation for HPV-driven oropharyngeal cancer: Where do we stand? *Clinical and Translational Radiation Oncology*, 8:4–11, 2018. doi: 10.1016/j.ctro.2017.10.005.

[52] L. Masterson, D. Moualed, Z. W. Liu, J. E. Howard, R. C. Dwivedi, J. R. Tysome, R. Benson, J. C. Sterling, H. Sudhoff, P. Jani, and P. K. Goon. De-escalation treatment protocols for human papillomavirus-associated oropharyngeal squamous cell carcinoma: A systematic review and meta-analysis of current clinical trials. *European Journal of Cancer*, 50(15):2636–2648, 2014. doi: 10.1016/j.ejca.2014.07.001.

[53] Z. Wang, J. D. Butner, R. Kerketta, V. Cristini, and T. S. Deisboeck. Simulating

cancer growth with multiscale agent-based modeling. *Seminars in Cancer Biology*, 30:70–78, 2015. doi: 10.1016/j.semcancer.2014.04.001.

[54] K. Rejniak and A. Anderson. Hybrid Models of Tumor Growth. *Wiley Interdisciplinary Reviews: ...*, 3:115–125, 2011. doi: 10.1002/wsbm.102.Hybrid.

[55] P. Gerlee. The model muddle: In search of tumor growth laws. *Cancer Research*, 73(8):2407–2411, 2013. ISSN 00085472. doi: 10.1158/0008-5472.CAN-12-4355.

[56] R. K. Sachs, L. R. Hlatky, and P. Hahnfeldt. Simple ODE models of tumor growth and anti-angiogenic or radiation treatment. *Mathematical and Computer Modelling*, 33(12-13):1297–1305, 2001. doi: 10.1016/S0895-7177(00)00316-2.

[57] A. K. Laird. Dynamics of tumor growth. *British Journal of Cancer*, 18(3):490–502, 1964. doi: 10.1038/bjc.1964.55.

[58] H. Murphy, H. Jaafari, and H. M. Dobrovolny. Differences in predictions of ODE models of tumor growth: a cautionary example. *BMC Cancer*, 16(1):163, 2016. doi: 10.1186/s12885-016-2164-x.

[59] M. Marusic and Z. Bajzer. Generalized two-parameter equation of growth. *Journal of mathematical analysis and applications*, 179:446–462, 1993. doi: 10.1006/jmaa.1993.1361.

[60] A. Achilleos, C. Loizides, M. Hadjiandreou, T. Stylianopoulos, and G. D. Mitsis. Multiprocess Dynamic Modeling of Tumor Evolution with Bayesian Tumor-Specific Predictions. *Annals of Biomedical Engineering*, 42(5):1095–1111, 2014. doi: 10.1007/s10439-014-0975-y.

[61] D. Csercsik, J. Sápi, and L. Kovács. A bicompartmental dynamic tumor growth model. *IFAC-PapersOnLine*, 50(1):12216–12221, 2017. doi: 10.1016/j.ifacol.2017.08.2119.

[62] E. O. Alzahrani, A. Asiri, M. M. El-Dessoky, and Y. Kuang. Quiescence as an explanation of Gompertzian tumor growth revisited. *Mathematical Biosciences*, 254(1):76–82, 2014. doi: 10.1016/j.mbs.2014.06.009.

[63] H. Greenspan. Models for the Growth of a Solid Tumor by Diffusion. *Studies in Applied Mathematics*, L1(4):317–340, 1972.

[64] H. P. Greenspan. On the growth and stability of cell cultures and solid tumors. *Journal of Theoretical Biology*, 56(1):229–242, 1976. doi: 10.1016/S0022-5193(76)80054-9.

[65] D. R. Grimes and F. J. Currell. Oxygen diffusion in ellipsoidal tumour spheroids. *Journal of The Royal Society Interface*, 15(145):20180256, aug 2018. doi: 10.1098/rsif.2018.0256.

[66] D. McElwain and L. Morris. Apoptosis as a volume loss mechanism in mathematical models of solid tumor growth. *Mathematical Biosciences*, 39(1-2):147–157, may 1978. doi: 10.1016/0025-5564(78)90033-0.

[67] H. Byrne and M. Chaplain. Necrosis and apoptosis: distinct cell loss mechanisms in a mathematical model of avascular tumour growth. *Journal of Theoretical Medicine*, 1:223–235, 1998. doi: 10.1080/10273669808833021.

[68] J. Landry, J. Freyer, and R. Sutherland. A model for the growth of multicellular spheroids. *Cell Proliferation*, pages 585–594, 1982.

[69] A. S. Deakin. Model for the growth of a solid in vitro tumor. *Growth*, 39(1):159–65, mar 1975. doi: 10.1017/S001221730004628X.

[70] D. R. Grimes, C. Kelly, K. Bloch, and M. Partridge. A method for estimating the oxygen consumption rate in multicellular tumour spheroids. *Journal of the Royal Society, Interface*, 11(92):20131124, 2014. doi: 10.1098/rsif.2013.1124.

[71] G. Pettet, C. P. Please, M. J. Tindall, and D. L. S. McElwain. The Migration of Cells in Multicell Tumor Spheroids. *Bulletin of Mathematical Biology*, 63(2): 231–257, mar 2001. ISSN 00928240. doi: 10.1006/bulm.2000.0217.

[72] Y. Davit, C. G. Bell, H. M. Byrne, L. A. Chapman, L. S. Kimpton, G. E. Lang, K. H. Leonard, J. M. Oliver, N. C. Pearson, R. J. Shipley, S. L. Waters, J. P. Whiteley, B. D. Wood, and M. Quintard. Homogenization via formal multiscale

asymptotics and volume averaging: How do the two techniques compare? *Advances in Water Resources*, 62:178–206, dec 2013. doi: 10.1016/j.advwatres.2013.09.006.

[73] S. Whitaker. The transport equations for multi-phase systems. *Chemical Engineering Science*, 28(1):139–147, jan 1973. ISSN 00092509. doi: 10.1016/0009-2509(73)85094-8.

[74] D. A. Drew and L. A. Segel. Averaged Equations for Two-Phase Flows. *Studies in Applied Mathematics*, 50(3):205–231, sep 1971. ISSN 00222526. doi: 10.1002/sapm1971503205.

[75] D. A. Drew. Mathematical Modeling of Two-Phase Flow. *Annual Review of Fluid Mechanics*, 15(1):261–291, jan 1983. ISSN 0066-4189. doi: 10.1146/annurev.fl.15.010183.001401.

[76] F. A. Howes and S. Whitaker. The spatial averaging theorem revisited. *Chemical Engineering Science*, 40(8):1387–1392, 1985. doi: 10.1016/0009-2509(85)80078-6.

[77] R. D. O'Dea, M. R. Nelson, A. J. El Haj, S. L. Waters, and H. M. Byrne. A multiscale analysis of nutrient transport and biological tissue growth in vitro. *Mathematical Medicine and Biology*, 32(3):345–366, 2015. doi: 10.1093/imammb/dqu015.

[78] J. P. Ward and J. R. King. Mathematical modelling of avascular-tumour growth. *IMA journal of mathematics applied in medicine and biology*, 14(1):39–69, 1997. doi: 10.1.1.586.1417.

[79] J. P. Ward and J. R. King. Mathematical modelling of avascular-tumour growth. II: Modelling growth saturation. *IMA journal of mathematics applied in medicine and biology*, 16(2):171–211, 1999. doi: 10.1093/imammb/16.2.171.

[80] K. A. Landman and C. P. Please. Tumour dynamics and necrosis : surface tension and stability. *IMA journal of mathematics applied in medicine and biology*, 18: 131–158, 2001.

[81] H. Byrne and L. Preziosi. Modelling solid tumour growth using the theory of mixtures. *Mathematical medicine and biology : a journal of the IMA*, 20(4):341–366, 2003. ISSN 1477-8599. doi: 10.1093/imammb/20.4.341.

[82] C. J. Breward, H. M. Byrne, and C. E. Lewis. The role of cell-cell interactions in a two-phase model for avascular tumour growth. *Journal of Mathematical Biology*, 45(2):125–152, 2002. doi: 10.1007/s002850200149.

[83] C. Breward, H. Byrne, and C. E. Lewis. A Multiphase Model Describing Vascular Tumour Growth. *Bulletin of Mathematical Biology*, 65(4):609–640, 2003. doi: 10.1016/S0092-8240(03)00027-2.

[84] J. M. Osborne and J. P. Whiteley. A numerical method for the multiphase viscous flow equations. *Computer Methods in Applied Mechanics and Engineering*, 199(49-52):3402–3417, 2010. doi: 10.1016/j.cma.2010.07.011.

[85] J. P. Whiteley. A Discontinuous Galerkin Finite Element Method for Multiphase Viscous Flow. *SIAM Journal on Scientific Computing*, 37(4):B591–B612, jan 2015. doi: 10.1137/14098497X.

[86] J. Collis, M. E. Hubbard, and R. D. O'Dea. Computational modelling of multiscale, multiphase fluid mixtures with application to tumour growth. *Computer Methods in Applied Mechanics and Engineering*, 309:554–578, 2016. doi: 10.1016/j.cma.2016.06.015.

[87] G. Sciumè, S. Shelton, W. G. Gray, C. T. Miller, F. Hussain, M. Ferrari, P. Decuzzi, and B. A. Schrefler. A multiphase model for three-dimensional tumor growth. *New Journal of Physics*, 15, 2013. doi: 10.1088/1367-2630/15/1/015005.

[88] M. E. Hubbard and H. M. Byrne. Multiphase modelling of vascular tumour growth in two spatial dimensions. *Journal of Theoretical Biology*, 316:70–89, 2013. doi: 10.1016/j.jtbi.2012.09.031.

[89] R. P. Araujo and D. L. S. McElwain. A Mixture Theory for the Genesis of Residual Stresses in Growing Tissues I: A General Formulation. *SIAM Journal on Applied Mathematics*, 65(4):1261–1284, 2005. doi: 10.1137/040607113.

[90] R. P. Araujo and D. L. S. McElwain. A Mixture Theory for the Genesis of Residual Stresses in Growing Tissues II: Solutions to the Biphasic Equations for a Multi-

cell Spheroid. *SIAM Journal on Applied Mathematics*, 66(2):447–467, 2005. doi: 10.1137/040607125.

[91] D. Ambrosi and L. Preziosi. Cell adhesion mechanisms and stress relaxation in the mechanics of tumours. *Biomechanics and Modeling in Mechanobiology*, 8(5): 397–413, 2009. doi: 10.1007/s10237-008-0145-y.

[92] L. Preziosi and A. Tosin. Multiphase modelling of tumour growth and extracellular matrix interaction: mathematical tools and applications. *Journal of Mathematical Biology*, 58(4-5):625–656, 2009. doi: 10.1007/s00285-008-0218-7.

[93] T. Hillen, G. de Vries, J. Gong, and C. Finlay. From cell population models to tumor control probability: including cell cycle effects. *Acta oncologica (Stockholm, Sweden)*, 49(8):1315–1323, 2010. doi: 10.3109/02841861003631487.

[94] R. C. Rockne and P. Frankel. Mathematical Modeling in Radiation Oncology. In J. Y. C. Wong, T. E. Schultheiss, and E. H. Radany, editors, *Advances in Radiation Oncology*, chapter 12, pages 255–271. Springer International Publishing, 2017. ISBN 978-3-319-53235-6.

[95] H. Enderling, M. A. J. Chaplain, and P. Hahnfeldt. Quantitative Modeling of Tumor Dynamics and Radiotherapy. *Acta Biotheoretica*, 58(4):341–353, 2010. doi: 10.1007/s10441-010-9111-z.

[96] D. J. Brenner, L. R. Hlatky, P. J. Hahnfeldt, E. J. Hall, and R. K. Sachs. A convenient extension of the linear-quadratic model to include redistribution and reoxygenation. *International journal of radiation oncology, biology, physics*, 32(2): 379–390, 1995. doi: 10.1016/0360-3016(95)00544-9.

[97] D. J. Carlson, R. D. Stewart, and V. A. Semenenko. Effects of oxygen on intrinsic radiation sensitivity: A test of the relationship between aerobic and hypoxic linear-quadratic (LQ) model parameters. *Medical physics*, 33(9):3105–3115, 2006. doi: 10.1118/1.2229427.

[98] D. J. Brenner, L. R. Hlatky, P. J. Hahnfeldt, Y. Huang, and R. K. Sachs. The linear-quadratic model and most other common radiobiological models result in similar

predictions of time-dose relationships. *Radiation research*, 150(1):83–91, 1998. doi: 10.2307/3579648.

[99] M. Zaider and G. N. Minerbo. Tumour control probability : a formulation applicable to any temporal protocol of dose delivery. *Physics in medicine and biology*, 45:279–293, 2000.

[100] M. Zaider and L. Hanin. Tumor control probability in radiation treatment. *Medical Physics*, 38(2):574–583, 2011. doi: 10.1118/1.3521406.

[101] S. F. C. O'Rourke, H. McAneney, and T. Hillen. Linear quadratic and tumour control probability modelling in external beam radiotherapy. *Journal of Mathematical Biology*, 58(4-5):799–817, 2009. doi: 10.1007/s00285-008-0222-y.

[102] J. Gong, M. M. Dos Santos, C. Finlay, and T. Hillen. Are more complicated tumour control probability models better? *Mathematical Medicine and Biology*, 30:1–19, 2013. doi: 10.1093/imammb/dqr023.

[103] L. G. Hanin. A stochastic model of tumor response to fractionated radiation: Limit theorems and rate of convergence. *Mathematical Biosciences*, 191(1):1–17, 2004. doi: 10.1016/j.mbs.2004.04.003.

[104] T. E. Wheldon, J. Kirk, and J. S. Orr. Optimal radiotherapy of tumour cells following exponential-quadratic survival curves and exponential repopulation kinetics. *The British Journal of Radiology*, 50(597):681–682, sep 1977. doi: 10.1259/0007-1285-50-597-681.

[105] S. Prokopiou, E. G. Moros, J. Poleszczuk, J. Caudell, J. F. Torres-Roca, K. Latifi, J. K. Lee, R. Myerson, L. B. Harrison, and H. Enderling. A proliferation saturation index to predict radiation response and personalize radiotherapy fractionation. *Radiation Oncology*, 10(1):159, 2015. doi: 10.1186/s13014-015-0465-x.

[106] J. Poleszczuk, R. Walker, E. G. Moros, K. Latifi, J. J. Caudell, and H. Enderling. Predicting Patient-Specific Radiotherapy Protocols Based on Mathematical Model Choice for Proliferation Saturation Index. *Bulletin of Mathematical Biology*, 80(5): 1195–1206, may 2018. doi: 10.1007/s11538-017-0279-0.

[107] H. McAneney and S. F. C. O'Rourke. Investigation of various growth mechanisms of solid tumour growth within the linear-quadratic model for radiotherapy. *Physics in medicine and biology*, 52(4):1039–1054, 2007. doi: 10.1088/0031-9155/52/4/012.

[108] A. V. Chvetsov. Tumor response parameters for head and neck cancer derived from tumor-volume variation during radiation therapy. *Medical Physics*, 40(3):034101, feb 2013. ISSN 00942405. doi: 10.1118/1.4789632.

[109] A. V. Chvetsov, S. Yartsev, J. L. Schwartz, and N. Mayr. Assessment of interpatient heterogeneity in tumor radiosensitivity for nonsmall cell lung cancer using tumor-volume variation data. *Medical Physics*, 41(6Part1):064101, may 2014. doi: 10.1118/1.4875686.

[110] I. Tariq, T. Chen, N. F. Kirkby, and R. Jena. Modelling and Bayesian adaptive prediction of individual patients' tumour volume change during radiotherapy. *Physics in medicine and biology*, 61(5):2145–2161, 2016. doi: 10.1088/0031-9155/61/5/2145.

[111] A. V. Chvetsov, L. Dong, J. R. Palta, and R. J. Amdur. Tumor-Volume Simulation During Radiotherapy for Head-and-Neck Cancer Using a Four-Level Cell Population Model. *International Journal of Radiation Oncology Biology Physics*, 75(2):595–602, 2009. doi: 10.1016/j.ijrobp.2009.04.007.

[112] P. Wang and Y. Feng. A mathematical model of tumor volume changes during radiotherapy. *TheScientificWorldJournal*, 2013:181070, 2013. doi: 10.1155/2013/181070.

[113] A. V. Chvetsov, G. A. Sandison, J. L. Schwartz, and R. Rengan. Ill-posed problem and regularization in reconstruction of radiobiological parameters from serial tumor imaging data. *Physics in Medicine and Biology*, 60(21):8491–8503, 2015. doi: 10.1088/0031-9155/60/21/8491.

[114] K. Leder, K. Pitter, Q. Laplant, D. Hambardzumyan, B. D. Ross, T. a. Chan, E. C. Holland, and F. Michor. Mathematical modeling of pdgf-driven glioblastoma reveals optimized radiation dosing schedules. *Cell*, 156(3):603–616, 2014. doi: 10.1016/j.cell.2013.12.029.

[115] T. E. Yankeelov, N. Atuegwu, D. Hormuth, J. A. Weis, S. L. Barnes, M. I. Miga, E. C. Rericha, and V. Quaranta. Clinically Relevant Modeling of Tumor Growth and Treatment Response. *Science Translational Medicine*, 5(187):187ps9–187ps9, may 2013. doi: 10.1126/scitranslmed.3005686.

[116] R. Rockne, E. C. Alvord, J. K. Rockhill, and K. R. Swanson. A mathematical model for brain tumor response to radiation therapy. *Journal of Mathematical Biology*, 58 (4-5):561–578, 2009. doi: 10.1007/s00285-008-0219-6.

[117] R. Rockne, J. K. Rockhill, M. Mrugala, a. M. Spence, I. Kalet, K. Hendrickson, A. Lai, T. Cloughesy, E. C. Alvord, and K. R. Swanson. Predicting the efficacy of radiotherapy in individual glioblastoma patients in vivo: a mathematical modeling approach. *Physics in medicine and biology*, 55(12):3271–3285, 2010. doi: 10.1088/0031-9155/55/12/001.

[118] R. C. Rockne, A. D. Trister, J. Jacobs, A. J. Hawkins-Daarud, M. L. Neal, K. Hendrickson, M. M. Mrugala, J. K. Rockhill, P. Kinahan, K. A. Krohn, and K. R. Swanson. A patient-specific computational model of hypoxia-modulated radiation resistance in glioblastoma using (18)F-FMISO-PET. *Journal of the Royal Society Interface*, 12(103):20141174, 2015. doi: 10.1098/rsif.2014.1174.

[119] G. G. Powathil, A. J. Munro, M. A. Chaplain, and M. Swat. Bystander effects and their implications for clinical radiation therapy: Insights from multiscale in silico experiments. *Journal of Theoretical Biology*, 401:1–14, jul 2016. ISSN 00225193. doi: 10.1016/j.jtbi.2016.04.010.

[120] J. C. L. Alfonso, N. Jagiella, L. Nunez, M. A. Herrero, and D. Drasdo. Estimating dose painting effects in radiotherapy: a mathematical model. *PloS one*, 9(2):e89380, 2014. doi: 10.1371/journal.pone.0089380.

[121] J. T. Poleszczuk, K. A. Luddy, S. Prokopiou, M. Robertson-Tessi, E. G. Moros, M. Fishman, J. Y. Djeu, S. E. Finkelstein, and H. Enderling. Abscopal benefits of localized radiotherapy depend on activated T-cell trafficking and distribution between metastatic lesions. *Cancer Research*, 76(5):1009–1018, 2016. doi: 10.1158/0008-5472.CAN-15-1423.

[122] U. Ledzewicz and H. Schättler. Multi-input Optimal Control Problems for Combined Tumor Anti-angiogenic and Radiotherapy Treatments. *Journal of Optimization Theory and Applications*, 153(1):195–224, 2012. doi: 10.1007/s10957-011-9954-8.

[123] F. Saberian, A. Ghate, and M. Kim. Optimal fractionation in radiotherapy with multiple normal tissues. *Mathematical Medicine and Biology*, 33(2):211–252, jun 2016. ISSN 1477-8599. doi: 10.1093/imammb/dqv015.

[124] A. Gelman, J. B. Carlin, H. S. Stern, and D. B. Rubin. *Bayesian Data Analysis*. 2014. ISBN 978-1-4398-9820-8.

[125] J. Collis, A. J. Connor, M. Paczkowski, P. Kannan, J. Pitt-Francis, H. M. Byrne, and M. E. Hubbard. Bayesian Calibration, Validation and Uncertainty Quantification for Predictive Modelling of Tumour Growth: A Tutorial. *Bulletin of Mathematical Biology*, 79(4):939–974, apr 2017. ISSN 0092-8240. doi: 10.1007/s11538-017-0258-5.

[126] H. Miao, X. Xia, A. S. Perelson, and H. Wu. On Identifiability of Nonlinear ODE Models and Applications in Viral Dynamics. *SIAM Review*, 53(1):3–39, jan 2011. doi: 10.1137/090757009.

[127] N. D. Evans, H. A. J. Moyse, D. Lowe, D. Briggs, R. Higgins, D. Mitchell, D. Zehnder, and M. J. Chappell. Structural identifiability of surface binding reactions involving heterogeneous analyte: Application to surface plasmon resonance experiments. *Automatica*, 49(1):48–57, 2013. doi: 10.1016/j.automatica.2012.09.015.

[128] T. R. B. Grandjean, M. J. Chappell, J. W. T. Yates, and N. D. Evans. Structural identifiability analyses of candidate models for in vitro Pitavastatin hepatic uptake. *Computer Methods and Programs in Biomedicine*, 114(3):0–10, 2014. doi: 10.1016/j.cmpb.2013.06.013.

[129] S. Andradottir. A review of simulation optimization techniques. *1998 Winter Simulation Conference. Proceedings (Cat. No.98CH36274)*, 1(0):151–158, 1998. doi: 10.1109/WSC.1998.744910.

[130] L. J. Park, C. H. Park, C. Park, and T. Lee. Application of genetic algorithms to parameter estimation of bioprocesses. *Medical & Biological Engineering & Computing*, 35(1):47–49, 1997. doi: 10.1007/BF02510391.

[131] J. E. Cavanaugh. Unifying the derivations for the Akaike and corrected Akaike information criteria. *Statistics & Probability Letters*, 33(2):201–208, 1997. doi: 10.1016/S0167-7152(96)00128-9.

[132] C. Andrieu and J. Thoms. A tutorial on adaptive MCMC. *Statistics and Computing*, 18(4):343–373, 2008. doi: 10.1007/s11222-008-9110-y.

[133] P. Del Moral, A. Doucet, and A. Jasra. Sequential Monte Carlo samplers. *Journal of the Royal Statistical Society: Series B (Statistical Methodology)*, 68(3):411–436, jun 2006. doi: 10.1111/j.1467-9868.2006.00553.x.

[134] P. Del Moral, A. Doucet, and A. Jasra. An adaptive sequential Monte Carlo method for approximate Bayesian computation. *Statistics and Computing*, 22(5):1009–1020, 2012. doi: 10.1007/s11222-011-9271-y.

[135] T. Toni and M. P. H. Stumpf. Simulation-based model selection for dynamical systems in systems and population biology. *Bioinformatics*, 26(1):104–110, 2009. doi: 10.1093/bioinformatics/btp619.

[136] T. Toni, D. Welch, N. Strelkowa, A. Ipsen, and M. P. H. Stumpf. Approximate Bayesian computation scheme for parameter inference and model selection in dynamical systems. *Journal of the Royal Society, Interface / the Royal Society*, 6(31): 187–202, 2009. doi: 10.1098/rsif.2008.0172.

[137] R. E. Kass and A. E. Raftery. Bayes Factors. *Journal of the American Statistical Association*, 90(430):773, jun 1995. ISSN 01621459. doi: 10.2307/2291091.

[138] S. Filippi, C. P. Barnes, J. Cornebise, and M. P. H. Stumpf. On optimality of kernels for approximate Bayesian computation using sequential Monte Carlo. *Statistical Applications in Genetics and Molecular Biology*, 12(1):87–107, 2013. doi: 10.1515/sagmb-2012-0069.

[139] D. Silk, S. Filippi, and M. P. H. Stumpf. Optimizing threshold-schedules for sequential approximate Bayesian computation: applications to molecular systems. *Statistical Applications in Genetics and Molecular Biology*, 12(5):1–18, jan 2013. ISSN 1544-6115. doi: 10.1515/sagmb-2012-0043.

[140] E. Lima, J. Oden, B. Wohlmuth, A. Shahmoradi, D. Hormuth, T. Yankeelov, L. Scarabosio, and T. Horger. Selection and validation of predictive models of radiation effects on tumor growth based on noninvasive imaging data. *Computer Methods in Applied Mechanics and Engineering*, 327(June):277–305, dec 2017. ISSN 00457825. doi: 10.1016/j.cma.2017.08.009.

[141] R. A. Gatenby, O. Grove, and R. J. Gillies. Quantitative imaging in cancer evolution and ecology. *Radiology*, 269(1):8–15, 2013. doi: 10.1148/radiol.13122697.

[142] A. V. Chvetsov, J. J. Palta, and Y. Nagata. Time-dependent cell disintegration kinetics in lung tumors after irradiation. *Physics in medicine and biology*, 53(9): 2413–23, 2008. doi: 10.1088/0031-9155/53/9/013.

[143] O. J. Britton, A. Bueno-Orovio, K. Van Ammel, H. R. Lu, R. Towart, D. J. Gallacher, and B. Rodriguez. Experimentally calibrated population of models predicts and explains intersubject variability in cardiac cellular electrophysiology. *Proceedings of the National Academy of Sciences*, 110(23):E2098–E2105, 2013. doi: 10.1073/pnas.1304382110.

[144] M. Joiner and A. van der Kogel. *Basic Clinical Radiobiology Fourth Edition*. CRC Press, mar 2009. ISBN 1444166689. doi: 10.1201/b13224.

[145] R. Sutherland, J. Carlsson, R. Durand, and J. Yuhas. Spheroids in Cancer Research. *Cancer Research*, 41(July):2980–2984, 1981.

[146] H. M. Byrne. Continuum models of avascular tumour growth. In A. V. Antoniouk and R. V. N. Melnik, editors, *Mathematics and Life Sciences*, chapter 12, pages 279–312. 2012. ISBN 978-3-11-028853-7.

[147] H. B. Frieboes, J. S. Lowengrub, S. Wise, X. Zheng, P. Macklin, E. L. Bearer, and

V. Cristini. Computer simulation of glioma growth and morphology. *NeuroImage*, 37:S59–S70, 2007. doi: 10.1016/j.neuroimage.2007.03.008.

[148] G. Schaller and M. Meyer-Hermann. Continuum versus discrete model: a comparison for multicellular tumour spheroids. *Philosophical Transactions of the Royal Society A: Mathematical, Physical and Engineering Sciences*, 364(1843):1443–1464, 2006. doi: 10.1098/rsta.2006.1780.

[149] J. Collis, M. E. Hubbard, and R. D. O'Dea. A multi-scale analysis of drug transport and response for a multi-phase tumour model. *European Journal of Applied Mathematics*, 28(3):499–534, 2017. doi: 10.1017/S0956792516000413.

[150] G. Lemon, J. R. King, H. M. Byrne, O. E. Jensen, and K. M. Shakesheff. Mathematical modelling of engineered tissue growth using a multiphase porous flow mixture theory. *Journal of Mathematical Biology*, 52(5):571–594, 2006. doi: 10.1007/s00285-005-0363-1.

[151] L. Preziosi and A. Tosin. Multiphase and Multiscale Trends in Cancer Modelling. *Math. Model. Nat. Phenom*, 4(3):1–11, 2009. doi: 10.1051/mmnp/20094301.

[152] E. J. Crampin, E. A. Gaffney, and P. K. Maini. Reaction and diffusion on growing domains: Scenarios for robust pattern formation. *Bulletin of Mathematical Biology*, 61(6):1093–1120, 1999. doi: 10.1006/bulm.1999.0131.

[153] L. Tao and K. R. Rajagopal. On Boundary Conditions In Mixture Theory. pages 130–149. feb 1995. doi: 10.1142/97898128312860009.

[154] M. Massoudi. Boundary conditions in mixture theory and in CFD applications of higher order models. *Computers and Mathematics with Applications*, 53(2):156–167, 2007. doi: 10.1016/j.camwa.2006.02.016.

[155] S. Wise, J. Lowengrub, and V. Cristini. An adaptive multigrid algorithm for simulating solid tumor growth using mixture models. *Mathematical and computer modelling*, 53:1–20, 2011. doi: 10.1016/j.mcm.2010.07.007.An.

[156] P. Jenny, S. H. Lee, and H. A. Tchelepi. Adaptive Multiscale Finite-Volume Method for Multiphase Flow and Transport in Porous Media. *Multiscale Modeling & Simulation*, 3(1):50–64, jan 2005. doi: 10.1137/030600795.

[157] G. Lemon and J. R. King. Travelling-wave behaviour in a multiphase model of a population of cells in an artificial scaffold. *Journal of Mathematical Biology*, 55(4): 449–480, 2007. doi: 10.1007/s00285-007-0091-9.

[158] G. J. O. Jameson. Counting Zeros of Generalised Polynomials: Descartes' Rule of Signs and Laguerre's Extensions. *The Mathematical Gazette*, 518(518):223–234, 2006.

[159] R. T. Leijenaar, M. Bogowicz, A. Jochems, F. J. Hoebers, F. W. Wesseling, S. H. Huang, B. Chan, J. N. Waldron, B. O'Sullivan, D. Rietveld, C. R. Leemans, R. H. Brakenhoff, O. Riesterer, S. Tanadini-Lang, M. Guckenberger, K. Ikenberg, and P. Lambin. Development and validation of a radiomic signature to predict HPV (p16) status from standard CT imaging: a multicenter study. *The British Journal of Radiology*, (July 2017):20170498, 2018. doi: 10.1259/bjr.20170498.

[160] R. J. LeVeque. *Finite Difference Methods for Ordinary and Partial Differential Equations*. Society for Industrial and Applied Mathematics, jan 2007. ISBN 978-0-89871-629-0. doi: 10.1137/1.9780898717839.

Appendix A

Original Greenspan tumour growth model

A.1 Explanation of Greenspan's original growth model

Here we provide further explanation of Greenspan's original model for the nutrient-limited growth of tumour spheroids [63]. We restate the equations for the evolution of the nutrient concentration profile, c, and the tumour radii, R, R_H and R_N.

$$0 = \underbrace{\frac{1}{r^2}\frac{\partial}{\partial r}\left(r^2\frac{\partial c}{\partial r}\right)}_{\text{diffusion term}} - \underbrace{\Gamma H(c - c_N)}_{\text{oxygen consumption}} \quad , \tag{A.1}$$

$$\underbrace{\frac{1}{4\pi}\frac{d}{dt}\left(\frac{4\pi R^3}{3}\right)}_{\text{rate of change of tumour volume}} = \int_0^R [\underbrace{cH(c - c_H)}_{\text{cell proliferation term}} - \underbrace{\lambda_A - \lambda_N H(c_N - c)}_{\text{cell death term}}]r^2 dr, \tag{A.2}$$

$$R_H = 0 \quad \text{if} \quad c > c_H \,\forall r \quad \text{and otherwise} \quad c(R_H, t) = c_H, \tag{A.3}$$

$$R_N = 0 \quad \text{if} \quad c > c_N \,\forall r \quad \text{and otherwise} \quad c(R_N, t) = c_N, \tag{A.4}$$

$$\frac{\partial c}{\partial r} = 0 \quad \text{at } r = 0, \tag{A.5}$$

$$c = c_\infty \quad \text{at } r = R, \tag{A.6}$$

$$R(0) = R_0. \tag{A.7}$$

In (A.1), we assume that the oxygen concentration within the tumour is regulated by its diffusion across the tumour (with diffusion constant D) and consumption by the tumour cells. We make the further assumption that both normoxic and hypoxic cells consume oxygen at the same constant rate, Γ, and that cells in the necrotic core do not consume oxygen. Since oxygen diffuses on a much shorter timescale than tumour growth we assume that the oxygen concentration is in a quasi-steady state. Hence, $c(r,t)$ satisfies (A.1), where $H(\cdot)$ is the Heaviside function, with associated boundary conditions (A.5) and (A.6) imposing symmetry at $r = 0$ and a Dirichlet boundary condition at $r = R(t)$.

We assume that rates of cell proliferation and death within the tumour are determined by the local oxygen concentration. Proliferation occurs at a rate proportional to c where there is sufficient oxygen supply ($c > c_H$). Both apoptosis and necrosis contribute to cell death within the tumour, with apoptosis occurring at a constant rate throughout the tumour and necrosis localised to the necrotic core (where $c < c_N$). Degradation of the necrotic core is assumed to result in material that is freely permeable throughout the tumour spheroid. We assume that adhesion and surface tension forces acting on the tumour cells maintain the shape of the tumour spheroid, and that these same forces push cells inwards to compensate for the outward flux of necrotic material from the necrotic core. The evolution of $R(t)$ is then given by the mass balance in Equation (A.2), with λ_A, $\lambda_N > 0$, accompanied by the initial condition (A.7).

The radii at which the tumour becomes hypoxic and necrotic, R_H and R_N, respectively, are determined as contours of the oxygen concentration profile (Equations (A.3) and (A.4)). For situations in which the tumour spheroid is small enough that one or both of these contours do not exist, we define the corresponding radius to be 0.

An analytic solution can be found for $c(r,t)$ that depends on R, R_H and R_N, and so this system can be reduced to an ODE for R and algebraic equations for R_H and R_N. The resulting equations in the case of a fully developed, 3-layer tumour spheroid are given in Equations (A.8)-(A.12). The system of equations for the earlier growth phases are similar and can be obtained in the same manner.

$$c = \begin{cases} c_N & 0 < r < R_N \\ c_N + \frac{\Gamma}{6r}(r - R_N)^2(r + 2R_N) & R_N < r < R, \end{cases} \tag{A.8}$$

$$\frac{dR}{dt} = \frac{R}{3}\left[c_N\left(1 - \frac{R_H^3}{R^3}\right) - \left(\lambda_A + \lambda_N \frac{R_N^3}{R^3}\right)\right] + \frac{\Gamma R^3}{6}\left[\frac{1}{5}\left(1 - \frac{R_H^5}{R^5}\right) - \frac{R_N^2}{R^2}\left(1 - \frac{R_H^3}{R^3}\right) + \frac{R_N^3}{R^3}\left(1 - \frac{R_H^2}{R^2}\right)\right], \tag{A.9}$$

$$\left(1 - \frac{R_N}{R}\right)^2\left(1 + \frac{2R_N}{R}\right) = \frac{6}{\Gamma R^2}(c_\infty - c_N), \tag{A.10}$$

$$\left(1 - \frac{R_N}{R_H}\right)^2\left(1 + \frac{2R_N}{R_H}\right) = \frac{6}{\Gamma R_H^2}(c_H - c_N), \tag{A.11}$$

$$R(0) = R_0. \tag{A.12}$$

Figure 3.2 (main text) demonstrates the growth and various stages (labelled C1, C2 & C3) of tumour spheroid composition under the Greenspan model using the parameter values in Table A.1. In using partial pressures of oxygen rather than concentration, we follow Grimes *et al.* [70] and use Henry's law to convert between the two, so that $p = \Omega c$, with $\Omega = 3.0318\text{x}10^7$ mmHgkgm^{-3}. The oxygen concentration profile at each time point is a monotonic function increasing outwards from the tumour centre. Initially, for very small, avascular tumour spheroids, the entire tumour is made up of viable, proliferating cells (case A). We notice that as the tumour grows and so the oxygen concentration at the centre of the tumour decreases, a hypoxic region within the tumour begins to develop (case B) followed by a central necrotic core when the oxygen concentration falls so low as to be unable to support viable cells (case C). These different regions, and their varying responses to radiation, require careful consideration when extending Greenspan's model to account for radiotherapy. Further discussion of the different phases of growth is given in [146].

Parameter	**Symbol**	**Value**	**Source**
Oxygen consumption rate, $m^3kg^{-1}s^{-1}$	Γ	$7.29\text{x}10^{-7}$	[70]
Partial pressure at tumour boundary, $mmHg$	p_∞	100	[70]
Hypoxic partial pressure, $mmHg$	p_H	10	[70]
Anoxic partial pressure, $mmHg$	p_N	0.8	[70]
Oxygen diffusion constant, m^2s^{-1}	D	$2\text{x}10^{-9}$	[70]
Apoptosis constant, m^3kg^{-1}	λ_A	$1.0555\text{x}10^{-6}$	[147]
Necrosis constant, m^3kg^{-1}	λ_N	$2\text{x}10^{-8}$	[148]
Cell birth/death constant, $kgm^{-3}s^{-1}$	s	3.509	[147]

Table A.1: Parameter values for Greenspan's model of tumour spheroid growth. (Note: dimensional apoptosis and necrosis rates, s^{-1}, are given by $s\lambda_A$ and $s\lambda_N$, respectively. p_∞, p_H and p_N are partial pressures which, for consistency, are then converted into concentrations c_∞, c_H and c_N, respectively. For further details see Appendix A.1.)

A.2 Parameter sweep of Greenspan growth dynamics

We initially investigate the sensitivity of the standard Greenspan growth dynamics to some of its key parameters. In particular, as we sweep over a region of parameter space, we observe the resulting long-time, steady-state properties of the tumour spheroids. Specifically, we investigate how the availability of oxygen, c_∞, the oxygen consumption rate of the cells, Γ, and the rates of apoptosis and necrosis, λ_A and λ_N, respectively, affect the growth of the tumour under this model. We choose appropriate intervals for each parameter, in each case encompassing the corresponding value shown in Table A.1, and systematically explore the resulting region of parameter space, solving the model numerically. We plot heatmaps in parameter space in order to observe the behaviour of a variety of quantities of interest of the tumours at steady state (Figures A.1 & A.2). We have omitted here the results of varying both c_∞ and λ_N since, in the case of c_∞, increasing the parameter value simply has the effect of an increase in overall tumour size and the width of the corresponding proliferating rim as might be expected, while, for the range of values swept over, λ_N had little effect on the observed tumour characteristics.

Broadly speaking, we see in Figure A.1 that relatively increasing the amount of oxygen available to the tumour cells (by decreasing the consumption rate Γ), or decreasing the death rate, λ_A, results in larger steady state tumours, as we might expect. Point A

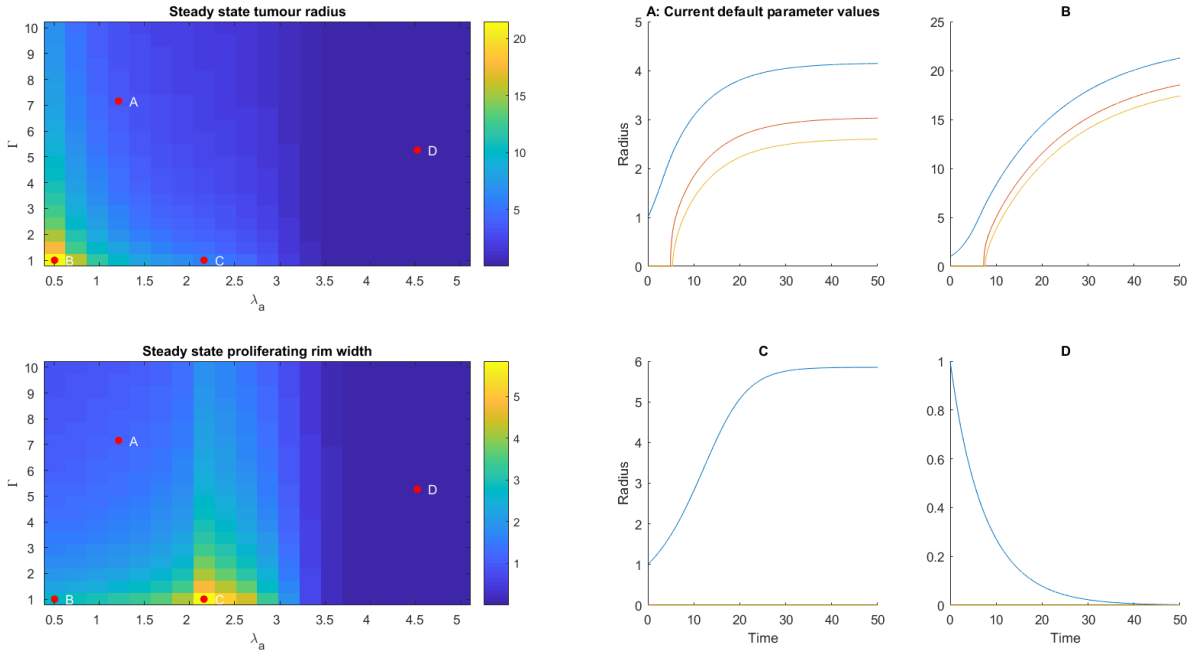

Figure A.1: Results of a parameter sweep for the steady state tumour radius and width of proliferating rim with corresponding tumour growth profiles at points of interest in parameter space, A, B, C and D.

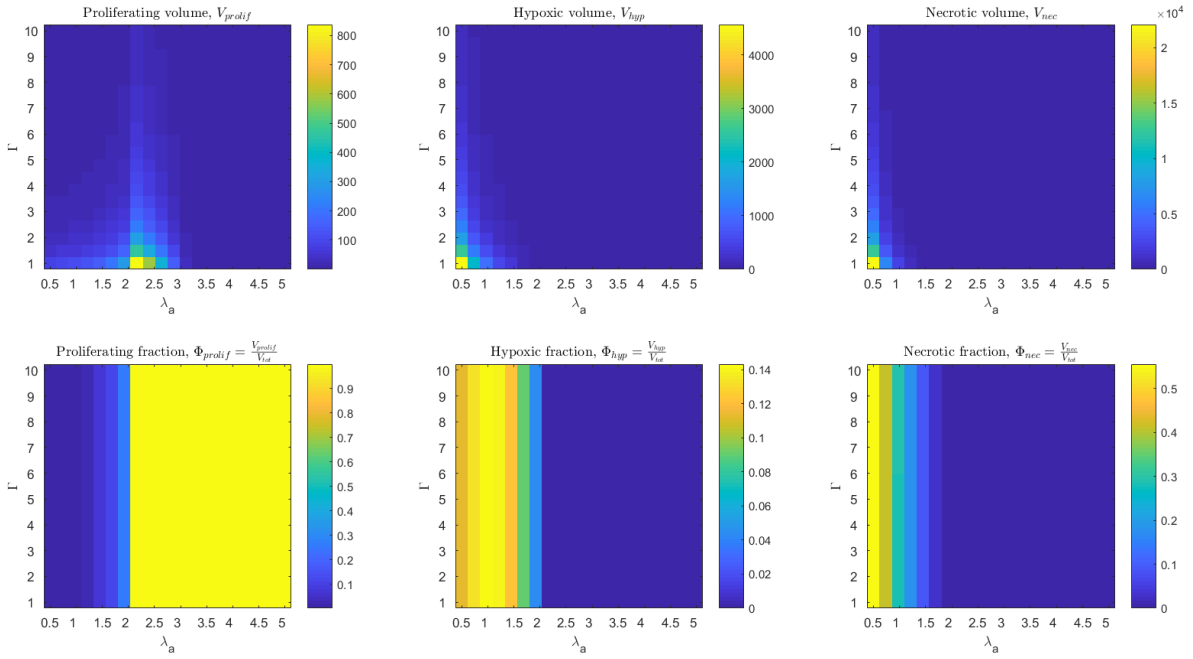

Figure A.2: Heatmaps for the steady state volumes of proliferating, hypoxic and necrotic cells, and the corresponding volume fractions.

marks the location of the parameter values from Table A.1. Extreme points in the region of concern in parameter space are labelled B, C and D and the corresponding tumour evolution profiles shown. We see that the greater relative availability of oxygen and the low death rate at point B results in a large, fully-developed tumour spheroid, whereas the high rate of apoptosis at D is such that a viable, tumour cell population cannot be sustained.

For a given Γ, we can determine the onset of necrosis as the radius $\bar{R} = \sqrt{\frac{6}{\Gamma}(c_\infty - c_N)}$. At the point C, and any other point on a vertical line through C, the rate of apoptosis is such that the tumour reaches a steady state of radius $\bar{R}$, and is given by $\lambda_A = \frac{1}{5}(3c_\infty + 2c_N)$. Beyond C, at lower death rates (eg B), we enter a new phase of growth that includes hypoxia and necrosis. The rapid, transient increase in R_H/R_N at onset of hypoxia/necrosis (c.f. asymptotics in Chapter 3) means that for each tumour the width of the proliferating rim decreases until it reaches a steady state and as such C represents a 'local maximum'. Figure A.2 shows the corresponding heatmaps for both the steady state volumes and volume fractions for each constituent of the tumour spheroid.

Appendix B

Comparison of OER models

In this appendix we compare the influence of different models for the oxygen enhancement ratio (OER) on the radiotherapy response dynamics exhibited by both the tumour spheroid model developed in Chapter 3 and the multiphase model in Chapter 5.

As described previously, the oxygen tension within the tumour has a significant effect on the cell death induced by irradiating a tumour. When hit by ionising radiation, potent oxygen free radicals are formed in well-oxygenated regions that result in increased DNA damage. This mechanism has been shown to enhance tumour radiosensitivity by up to a factor of 3 when compared with hypoxic tumour regions [37]. We incorporate this effect in our models via the oxygen enhancement ratio (OER), which decreases the radiosensitivity parameters of the tumour tissue (α, β) in hypoxic regions. In practice, the survival fraction, sf, is likely to depend continuously on the oxygen concentration, c. In this section we compare the simple step function approximation with an alternative form, $OER(c)$, which has continuous dependence on the oxygen tension [37].

$$OER(c) = \frac{OER_m c + k}{c + k} \tag{B.1}$$

In Equation (B.1), c is the oxygen concentration within the tissue, OER_m is the maximal oxygen enhancement ratio (taken to be 3 in our discrete formulation), and k is the oxygen concentration at which we observe half-maximal effect (this varies markedly between tissue types).

Given that the radiosensitivity parameters, α and β, are typically determined for

well-oxygenated tissues, we determine the survival fraction, sf, following radiotherapy by modifying the linear-quadratic model as follows:

$$sf(c) = exp(-\alpha d\frac{OER(c)}{OER_m} - \beta d^2 \left(\frac{OER(c)}{OER_m}\right)^2). \tag{B.2}$$

We compare this model with the step function formulation used in both models. In Section B.1 we compare the two models within the spheroid model, while in Section B.2 we do the same for the multiphase model. In Section B.3 we provide a brief discussion of the results.

B.1 Comparison of OER models within the tumour spheroid model

In our tumour spheroid model presented in Chapter 3, we incorporate the effects of radiotherapy as an instantaneous effect. The standard LQ model was applied in the normoxic proliferative rim, while a modified LQ formulation using a constant $OER = 3$ was used in the hypoxic regions of the tumour. The necrotic core was assumed to be unaffected by irradiation.

As before, we model cell death as an instantaneous event upon irradiation and dead material is immediately removed from the tumour volume. Therefore, the tumour volume post-radiotherapy, V^+, for the continuous OER model is now given by

$$V^+ = 4\pi \int_{R_N}^{R} sf(c(r))r^2 dr, \tag{B.3}$$

where we note that c itself is a function of the distance r from the tumour centre.

We approximate the integral in Equation (B.3) numerically. We can then simulate a full radiotherapy treatment using this continuous formulation of the OER and compare the model predicted tumour volumes post-treatment with our discrete OER predictions. We note that the value of k may vary significantly across tissue types and, as such, simulate radiotherapy across a range of values for k (Figure B.1). Since k represents the partial pressure at which we observe half-maximal effect of oxygen enhancement, and we expect that cells are hypoxic below 10mmHg [70], we only need to consider values of k up

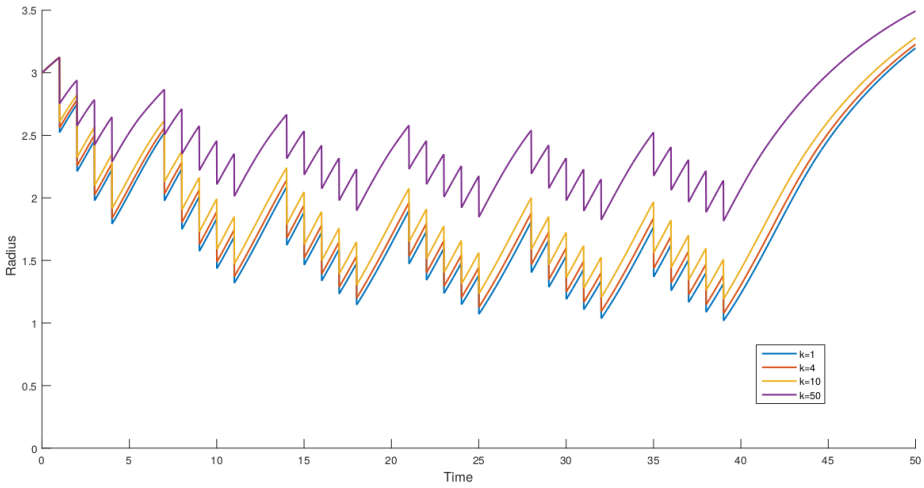

Figure B.1: The effect of varying k in our continuous formulation of the OER on the radius of the tumour spheroid throughout simulated radiotherapy, solving model equations (3.13)-(3.19) with the effects of radiotherapy determined by Equations (B.1)-(B.3).

to 10mmHg. As we can see from Figure B.1, varying k across this range of values does not significantly affect the simulated tumour volumes.

We also compare the predictions of our model using the continuous OER formulation to the discrete model, shown in Figure B.2. Again our simulations did not significantly vary depending on the version of the OER used. As such, we favour the simpler model and retain the step function formulation of the OER in the model for tumour spheroid growth presented in Chapter 3.

B.2 Comparison of OER models within the multiphase model

For the multiphase model, we might expect that the two forms of the OER could result in noticeably different behaviour in both the model solution and the numerical simulation since the discontinuous form of the OER induces a corresponding discontinuity in the volume fractions ϕ_1 and ϕ_2. As such, we again consider both within our model. In Figure B.3a we plot the two forms of the OER as a function of oxygen concentration, c. We note that since we fix a boundary condition of $c(R(t), t) = 1$, we have scaled OER_m in Figure B.3a such that $OER(c(R(t), t)) = 1$.

While the continuous form of the OER may appear to be a reasonable smooth approximation to the step function, we see from Figure B.3a that OER values near to 1

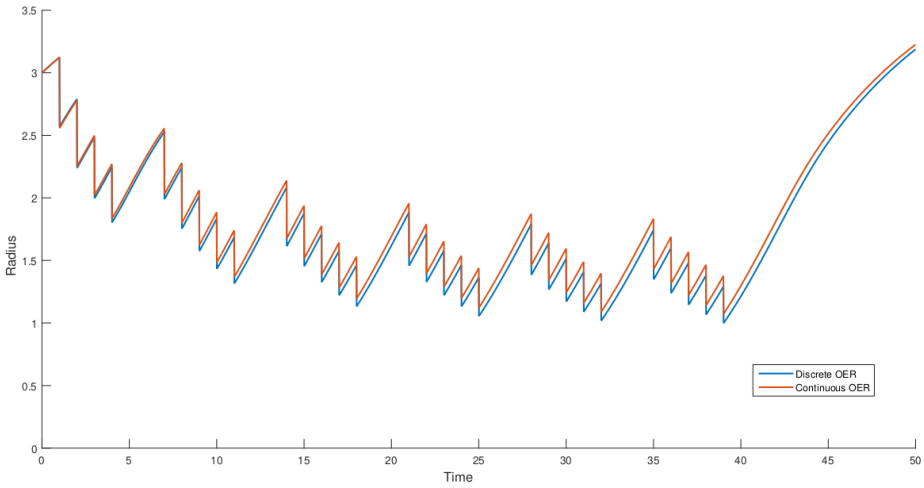

Figure B.2: Comparison between the model solutions using the continuous version of the OER postulated in [37] and the discrete version described in Section 3.2.2.

are only achieved for small values of c. In Figure B.3b we plot the oxygen profile within the tumour immediately prior to irradiation for the simulation presented in Section 5.3. All viable cells within the tumour are assumed to consume oxygen, however tumour cells in the necrotic core, $x < R_N$ are assumed to be anoxic and undergo necrotic cell death. As such, these cells are assumed to no longer consume oxygen. This is reflected in the reaction-diffusion equation for the oxygen concentration (Equation (5.17)) as a Heaviside function for oxygen consumption and results in an oxygen profile which never reaches zero, regardless of tumour size or composition. As such, the OERs realised for any given oxygen profile within our simulations do not get close to 1 for the continuous formulation, resulting in a potentially significant discrepancy in the survival fractions predicted by each model. In Figure B.3c we plot the survival fractions at each point within the tumour given by each model using the oxygen profile in Figure B.3b.

It is evident that the two proposed models for the OER may result in significantly different tumour compositions post-irradiation which may subsequently affect the resulting tumour dynamics. We note that the comparison presented here is a result of the form for the oxygen consumption term chosen in our model (see Equation (5.17)), and that a different choice here may lend itself to the continuous form of the OER being the more appropriate model. However, for our purposes we restrict our attention to the step function form of the cell survival fraction, given by Equation (5.14), in order to more

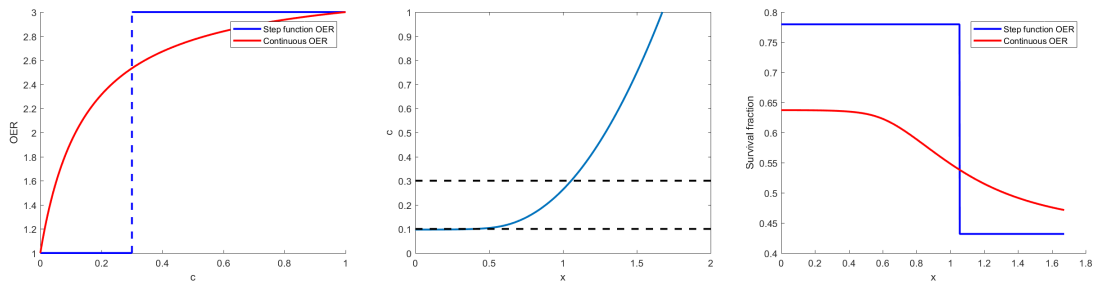

(a) (b) (c)

Figure B.3: Comparison of the two different models for the oxygen enhancement ratio (OER) as defined by Equations (5.14) and (B.1). a) Plot showing OER as a function of oxygen concentration, c, for both the step function (blue) and continuous (red) formulations. b) Typical oxygen profile from simulation of Equations (5.15)-(5.25). The profile shown here is taken from the simulation in Figure 5.1 at $t = 20$, immediately prior to irradiation. c) Comparison of the actual survival fractions realised by each model when applied to the oxygen profile in b).

fully include the effects of hypoxia within our multiphase model. We also note that in Appendix D we perform a parameter sweep in which we include both OER formulations and find that both models may realise the same range of qualitative response dynamics.

B.3 Discussion

Since the necrotic core of the tumour spheroid model was assumed to be unaffected by radiotherapy, the survival fraction post-irradiation for both the discrete and the continuous formulation of the OER models is actually a step function in both cases when viewed as a function of radial position, with a discontinuity at the edge of the necrotic core, $r = R_N$. As a result, model predictions for both formulations did not significantly differ. However for the multiphase model, radiation is assumed to affect the tumour cell phase, ϕ_1, throughout the entirety of the tumour. As a result there is a more significant discrepancy in the survival fraction viewed as a function of position within the tumour in both models. One of the aims of this thesis is to investigate the effect of variations in spatial composition on the qualitative tumour response to radiotherapy. To reconcile the discrepancies between these two models of the OER is beyond the scope of this thesis, and as such we restrict our attention to the form most appropriate to the models we develop.

Appendix C

Multiphase numerics

C.1 Numerical method in detail

In this section we detail the numerical method that we develop in order to solve Equations (4.22)-(4.32). In Section C.1.1 we first map the system of equations to a fixed domain. In Sections C.1.2-C.1.5 we take each equation in turn and derive the finite difference scheme used to solve it numerically. In each case there are many methods which could be employed to solve the given equations. For our purposes, we choose to develop a simple, convergent finite difference scheme since we are mostly interested in the qualitative behaviour of the model dynamics. Further discussion of the numerical scheme with regards to particular cases is given in Appendix C.3. The numerical methods for each equation are combined to solve the entire system of equations as described in the pseudo-code presented in Section 4.3, Algorithm 4.

The numerical method is implemented on a fixed mesh in the fixed domain coordinates with N equally-spaced nodes such that $\Delta\xi = \frac{1}{N-1}$. We index the nodes in space by $j = 1, ..., N$ and denote $\xi_j = (j-1)\Delta\xi$. We solve the system of equations using explicit time-stepping with fixed timestep Δt and denote the simulation timestep by $t_n = n\Delta t$. We then introduce the following subscript-superscript notation for variables evaluated at each mesh node and timestep, here using the volume fraction ϕ_1 as an example:

$$\phi_{1,j}^n = \phi_1(\xi_j, t_n).$$

C.1.1 Fixed domain equations

The final system of reduced model equations, Equations (4.22)-(4.32), are defined on the growing tumour domain from $x = 0$ to $x = R(t)$. From a numerical standpoint, the growing domain makes it difficult to keep a mesh with equally-spaced nodes on which to solve the model equations. As such it is convenient to first map the equations onto a fixed domain, $x \mapsto \xi \in [0, 1]$, such that $\xi = \frac{x}{R(t)}$. We then solve the resulting system of equations in these coordinates and map the solution back onto the growing domain afterwards. The fixed domain equations to be solved numerically are given by Equations (C.1)-(C.11).

$$\frac{\partial \phi_1}{\partial t} - \frac{\xi}{R}\frac{dR}{dt}\frac{\partial \phi_1}{\partial \xi} + \frac{1}{R}\frac{\partial}{\partial \xi}(\phi_1 v_1) = \eta\phi_1(1-\phi_1-\phi_2)H_\epsilon(c-c_H) - \chi\phi_1 H_\epsilon(c_N - c) - \kappa\phi_1 \tag{C.1}$$

$$\frac{\partial \phi_2}{\partial t} - \frac{\xi}{R}\frac{dR}{dt}\frac{\partial \phi_2}{\partial \xi} + \frac{1}{R}\frac{\partial}{\partial \xi}(\phi_2 v_2) = \chi\phi_1 H_\epsilon(c_N - c) + \kappa\phi_1 - \lambda\phi_2 \tag{C.2}$$

$$0 = \frac{D}{R^2}\frac{\partial^2 c}{\partial \xi^2} - \Gamma\phi_1 H_\epsilon(c - c_H) \tag{C.3}$$

$$\begin{aligned} 0 = \frac{4}{3}\frac{\mu_1}{R^2}(1-\phi_1)\frac{\partial}{\partial \xi}\left(\phi_1\frac{\partial v_1}{\partial \xi}\right) - \frac{4}{3}\frac{\theta_\mu \mu_1}{R^2}\phi_1\frac{\partial}{\partial \xi}\left(\phi_2\frac{\partial v_2}{\partial \xi}\right) + d_{12}\phi_1\phi_2(v_2 - v_1) \\ - d_{13}\phi_1(\phi_2 v_2 + (1-\phi_2)v_1) + \frac{\theta_p\phi_1\phi_2}{R}\frac{\partial \Sigma_\phi}{\partial \xi} - \frac{\phi_1(1-\phi_1)}{R}\frac{\partial \Sigma_\phi}{\partial \xi} \end{aligned} \tag{C.4}$$

$$\begin{aligned} 0 = \frac{4}{3}\frac{\theta_\mu \mu_1}{R^2}(1-\phi_2)\frac{\partial}{\partial \xi}\left(\phi_2\frac{\partial v_2}{\partial \xi}\right) - \frac{4}{3}\frac{\mu_1}{R^2}\phi_2\frac{\partial}{\partial \xi}\left(\phi_1\frac{\partial v_1}{\partial \xi}\right) + d_{12}\phi_1\phi_2(v_1 - v_2) \\ - d_{23}\phi_2(\phi_1 v_1 + (1-\phi_1)v_2) + \frac{\phi_1\phi_2}{R}\frac{\partial \Sigma_\phi}{\partial \xi} - \theta_p\frac{\phi_2(1-\phi_2)}{R}\frac{\partial \Sigma_\phi}{\partial \xi} \end{aligned} \tag{C.5}$$

$$\Sigma_\phi(\phi) = \frac{\zeta(\phi - \phi_{min})^2(\phi - \phi^*)}{(1-\phi)}H(\phi - \phi_{min}) \tag{C.6}$$

$$\frac{dR}{dt} = v_1|_{\xi=1} \tag{C.7}$$

$$\frac{\partial c}{\partial \xi} = 0, \quad v_1 = v_2 = 0 \quad \text{at} \quad \xi = 0 \tag{C.8}$$

$$\phi_2^+ = 0, \quad c = c_\infty \quad \text{at} \quad \xi = 1 \tag{C.9}$$

$$\frac{4}{3}\frac{\mu_1}{R}\frac{\partial v_1}{\partial \xi} - \Sigma_\phi(\phi_1 + \theta_\Sigma \phi_2) = \frac{4}{3}\frac{\theta_\mu \mu_1}{R}\frac{\partial v_2}{\partial \xi} - \theta_p \Sigma_\phi(\phi_1 + \theta_\Sigma \phi_2) = 0 \quad \text{at} \quad \xi = 1 \tag{C.10}$$

$$\phi_1 = \tilde{\phi_1}(\xi), \quad \phi_2 = \tilde{\phi_2}(\xi), \quad R = R_0 \quad \text{at} \quad t = 0 \tag{C.11}$$

C.1.2 Upwinding for conservation of mass equations

The first set of equations that we must solve are the pair of hyperbolic equations for the conservation of mass for the tumour cell and dead material phases (Equations (C.1) and (C.2)).

Interior nodes

We choose to solve these hyperbolic equations using upwinding for the advection terms and standard, central differences for the non-advection terms. Since the phase velocities, v_i, are not constant in ξ, the direction of advection is given by the sign of $v_i - \xi\frac{dR}{dt}$ at each node. As such we take care to choose the correct upwinding formulation in each case. Note that since the tumour boundary moves with the tumour phase velocity, $\frac{dR^n}{dt} = v_{1,N}^n$. The finite difference scheme for the interior nodes, $j = 2, ..., N-1$, is given below.

Case: $\frac{1}{R^n}\left(v_{i,j}^n - \xi_j^n v_{1,N}^n\right) > 0$

$$\phi_{i,j}^{n+1} = \phi_{i,j}^{n} - \frac{1}{R^n}\left(v_{i,j}^{n} - \xi_j^n v_{1,N}^{n}\right)\frac{\Delta t}{\Delta \xi}(\phi_{i,j}^{n} - \phi_{i,j-1}^{n}) - \frac{\Delta t}{R^n}\phi_{i,j}^{n}\frac{1}{2\Delta\xi}(v_{i,j+1}^{n} - v_{i,j-1}^{n}) + \Delta t S_{i,j}^{n} \tag{C.12}$$

Case: $\frac{1}{R^n}\left(v_{i,j}^{n} - \xi_j^n v_{1,N}^{n}\right) < 0$

$$\phi_{i,j}^{n+1} = \phi_{i,j}^{n} - \frac{1}{R^n}\left(v_{i,j}^{n} - \xi_j^n v_{1,N}^{n}\right)\frac{\Delta t}{\Delta \xi}(\phi_{i,j+1}^{n} - \phi_{i,j}^{n}) - \frac{\Delta t}{R^n}\phi_{i,j}^{n}\frac{1}{2\Delta\xi}(v_{i,j+1}^{n} - v_{i,j-1}^{n}) + \Delta t S_{i,j}^{n} \tag{C.13}$$

Since we are using an upwinding scheme, we must check at each timestep that Equations (C.12) and (C.13) satisfy the CFL stability condition. In this case we require that $\left|\frac{1}{R}\left(v_i - \xi\frac{dR}{dt}\right)\right|\frac{\Delta t}{\Delta\xi} \leq 1$ for all nodes.

Boundary Nodes

We exploit the fact that $\xi = 0$ is a characteristic and use forward differences to solve the characteristic equation for $\phi_{i,1}$. Note that the boundary condition for symmetry at the origin gives $v_{i,1} = 0$. Thus our finite difference scheme at $\xi_1 = 0$ is

$$\phi_{i,1}^{n+1} = \phi_{i,1}^{n} + \Delta t\left(-\frac{\phi_{i,1}^{n}}{R^n}\frac{v_{i,2}^{n}}{\Delta\xi} + S_{i,1}^{n}\right). \tag{C.14}$$

At the exterior boundary, $\xi = 1$, for ϕ_1 we use the fact that it is also characteristic (since the boundary moves with the phase velocity) and use a backward difference for $v_{1,N}$. The corresponding difference equation is given by

$$\phi_{1,N}^{n+1} = \phi_{1,N}^{n} + \Delta t\left(-\frac{\phi_{1,N}^{n}}{R^n}\frac{(v_{1,N}^{n} - v_{1,N-1}^{n})}{\Delta\xi} + S_{1,N}^{n}\right). \tag{C.15}$$

For the exterior boundary for ϕ_2 we have two cases, since the boundary is no longer a characteristic. In the case of an outflow boundary, where $v_{2,N}^{n} > v_{1,N}^{n}$, it is simple and we have the usual upwind equation with a one-sided backward difference for ϕ_2:

$$\phi_{2,N}^{n+1} = \phi_{2,N}^{n} - \frac{1}{R}\frac{\Delta t}{\Delta\xi}(v_{2,N}^{n} - v_{1,N}^{n})(\phi_{2,N}^{n} - \phi_{2,N-1}^{n}) + \Delta t\left(-\frac{\phi_{2,N}^{n}}{R^n}\frac{(v_{2,N}^{n} - v_{2,N-1}^{n})}{\Delta\xi} + S_{2,N}^{n}\right). \tag{C.16}$$

When we have an inflow boundary, whereby $v_{2,N}^{n} < v_{1,N}^{n}$, we again use upwinding but

impose the additional boundary condition $\phi_2^+ = 0$ as described in the main text. Thus, our 'ghost node' at "$j = N + 1$" is 0 and we get

$$\phi_{2,N}^{n+1} = \phi_{2,N}^n - \frac{1}{R}\frac{\Delta t}{\Delta \xi}(v_{2,N}^n - v_{1,N}^n)(-\phi_{2,N}^n) + \Delta t\left(-\frac{\phi_{2,N}^n}{R^n}\frac{(v_{2,N}^n - v_{2,N-1}^n)}{\Delta \xi} + S_{2,N}^n\right). \quad \text{(C.17)}$$

C.1.3 Forward difference for R(t)

The tumour boundary, $R(t)$, moves with the tumour phase velocity there and is governed by

$$\frac{dR}{dt} = v_1|_{\xi=1}. \quad \text{(C.18)}$$

We use an explicit scheme to solve our model equations and so we simply step forward in time with

$$R^{n+1} = R^n + \Delta t v_{1,N}^n. \quad \text{(C.19)}$$

C.1.4 Coupled equations for conservation of momentum

Having updated the equations with explicit time dependence, we next solve the coupled system of elliptic equations for the phase velocities v_1 and v_2, given by Equations (C.4) and (C.5).

Interior nodes

We again choose a finite difference discretisation for this system. We choose to follow ([160], p36) and discretise $\frac{\partial}{\partial \xi}\left(\phi_i \frac{\partial v_i}{\partial \xi}\right)$ using a central difference at half grid points in order to obtain a symmetric approximation that retains some of the properties of the original operator. We use a Taylor expansion and one-sided differences to obtain an approximation for $\phi_{i,j\pm\frac{1}{2}}$. Thus we obtain the discretisation in Equation (C.20) which we denote by $\Delta_{i,j}$ for convenience, where i indexes the phase and j the central node of the approximation. For the derivatives of Σ_ϕ we use a standard central difference.

$$\frac{\partial}{\partial\xi}\left(\phi_i\frac{\partial v_i}{\partial\xi}\right) \approx \frac{1}{\Delta\xi^2}[\frac{1}{2}(\phi_{i,j}^{n+1}+\phi_{i,j-1}^{n+1})v_{i,j-1}^{n+1} - (\frac{1}{2}\phi_{i,j-1}^{n+1}+\phi_{i,j}^{n+1}+\frac{1}{2}\phi_{i,j+1}^{n+1})v_{i,j}^{n+1} \quad \text{(C.20)}$$
$$+\frac{1}{2}(\phi_{i,j}^{n+1}+\phi_{i,j+1}^{n+1})v_{i,j+1}^{n+1}]$$
$$:= \Delta_{i,j}$$

Applying these approximations results in the finite difference equations:

$$\begin{aligned}0 = &-\phi_{1,j}^{n+1}\frac{(1-\phi_{1,j}^{n+1})}{R^{n+1}}\frac{1}{2\Delta\xi}(\Sigma_{\phi,j+1}^{n+1}-\Sigma_{\phi,j-1}^{n+1}) + \frac{4}{3}(1-\phi_{1,j}^{n+1})\frac{\mu_1}{(R^{n+1})^2}\Delta_{1,j}\\ &+\frac{\theta_p\phi_{1,j}^{n+1}\phi_{2,j}^{n+1}}{(R^{n+1})^2}\frac{1}{2\Delta\xi}(\Sigma_{\phi,j+1}^{n+1}-\Sigma_{\phi,j-1}^{n+1}) - \frac{4}{3}\frac{\theta_\mu\mu_1}{(R^{n+1})^2}\phi_{1,j}^{n+1}\Delta_{2,j}\\ &+d_{12}\phi_{1,j}^{n+1}\phi_{2,j}^{n+1}(v_{2,j}^{n+1}-v_{1,j}^{n+1}) - d_{13}\phi_{1,j}^{n+1}(\phi_{2,j}^{n+1}v_{2,j}^{n+1}+(1-\phi_{2,j}^{n+1})v_{1,j}^{n+1})\end{aligned} \quad \text{(C.21)}$$

$$\begin{aligned}0 = &-\theta_p\phi_{2,j}^{n+1}\frac{(1-\phi_{2,j}^{n+1})}{R^{n+1}}\frac{1}{2\Delta\xi}(\Sigma_{\phi,j+1}^{n+1}-\Sigma_{\phi,j-1}^{n+1}) + \frac{4}{3}(1-\phi_{2,j}^{n+1})\frac{\theta_\mu\mu_1}{(R^{n+1})^2}\Delta_{2,j}\\ &+\frac{\phi_{1,j}^{n+1}\phi_{2,j}^{n+1}}{(R^{n+1})^2}\frac{1}{2\Delta\xi}(\Sigma_{\phi,j+1}^{n+1}-\Sigma_{\phi,j-1}^{n+1}) - \frac{4}{3}\frac{\mu_1}{(R^{n+1})^2}\phi_{2,j}^{n+1}\Delta_{1,j}\\ &+d_{12}\phi_{1,j}^{n+1}\phi_{2,j}^{n+1}(v_{1,j}^{n+1}-v_{2,j}^{n+1}) - d_{23}\phi_{2,j}^{n+1}(\phi_{1,j}^{n+1}v_{1,j}^{n+1}+(1-\phi_{1,j}^{n+1})v_{2,j}^{n+1})\end{aligned} \quad \text{(C.22)}$$

NB: $\Sigma_{\phi,j}$ is evaluated at $(\phi_{1,j}+\theta_\Sigma\phi_{2,j})$.

The discretisation in Equations (C.21) and (C.22) gives a coupled linear system and may alternatively be written in the form $M\boldsymbol{v}=\boldsymbol{d}$ for the velocity vector $\boldsymbol{v}=[\boldsymbol{v_1},\boldsymbol{v_2}]^T$. The matrix, M, is of 'block tridiagonal' form such that

$$M = \left(\begin{array}{c|c} A & B \\ \hline C & D \end{array}\right)$$

where A, B, C, D are tridiagonal matrices defined by:

$$A_{j,j} = -\frac{4}{3}(1-\phi_{1,j}^{n+1})\frac{\mu_1}{(R^{n+1})^2}\frac{1}{\Delta\xi^2}(\frac{1}{2}\phi_{1,j-1}^{n+1}+\phi_{1,j}^{n+1}+\frac{1}{2}\phi_{1,j+1}^{n+1})-\phi_{1,j}^{n+1}(d_{12}\phi_{2,j}^{n+1}+d_{13}(1-\phi_{2,j}^{n+1})), \tag{C.23}$$

$$A_{j,j\pm1} = \frac{4}{3}(1-\phi_{1,j}^{n+1})\frac{\mu_1}{(R^{n+1})^2}\frac{1}{2\Delta\xi^2}(\phi_{1,j}^{n+1}+\phi_{1,j\pm1}^{n+1}), \tag{C.24}$$

$$B_{j,j} = \frac{4}{3}\frac{\theta_\mu\mu_1}{(R^{n+1})^2}\phi_{1,j}^{n+1}\frac{1}{\Delta\xi^2}(\frac{1}{2}\phi_{2,j-1}^{n+1}+\phi_{2,j}^{n+1}+\frac{1}{2}\phi_{2,j+1}^{n+1})+(d_{12}-d_{13})\phi_{1,j}^{n+1}\phi_{2,j}^{n+1}, \tag{C.25}$$

$$B_{j,j\pm1} = \frac{4}{3}\frac{\theta_\mu\mu_1}{(R^{n+1})^2}\phi_{1,j}^{n+1}\frac{1}{2\Delta\xi^2}(\phi_{2,j}^{n+1}+\phi_{2,j\pm1}^{n+1}), \tag{C.26}$$

$$C_{j,j} = \frac{4}{3}\frac{\mu_1}{(R^{n+1})^2}\phi_{2,j}^{n+1}\frac{1}{\Delta\xi^2}(\frac{1}{2}\phi_{1,j-1}^{n+1}+\phi_{1,j}^{n+1}+\frac{1}{2}\phi_{1,j+1}^{n+1})+(d_{12}-d_{23})\phi_{1,j}^{n+1}\phi_{2,j}^{n+1}, \tag{C.27}$$

$$C_{j,j\pm1} = \frac{4}{3}\frac{\mu_1}{(R^{n+1})^2}\phi_{2,j}^{n+1}\frac{1}{2\Delta\xi^2}(\phi_{1,j}^{n+1}+\phi_{1,j\pm1}^{n+1}), \tag{C.28}$$

$$D_{j,j} = -\frac{4}{3}(1-\phi_{2,j}^{n+1})\frac{\theta_\mu\mu_1}{(R^{n+1})^2}\frac{1}{\Delta\xi^2}(\frac{1}{2}\phi_{2,j-1}^{n+1}+\phi_{2,j}^{n+1}+\frac{1}{2}\phi_{2,j+1}^{n+1})-\phi_{2,j}^{n+1}(d_{12}\phi_{1,j}^{n+1}+d_{23}(1-\phi_{1,j}^{n+1})), \tag{C.29}$$

$$D_{j,j\pm1} = \frac{4}{3}(1-\phi_{2,j}^{n+1})\frac{\theta_\Sigma\mu\mu_1}{(R^{n+1})^2}\frac{1}{2\Delta\xi^2}(\phi_{2,j}^{n+1}+\phi_{2,j\pm1}^{n+1}). \tag{C.30}$$

Boundary Nodes

We combine the discretisation for the interior nodes with the boundary conditions at the boundaries $\xi = 0$ and $\xi = 1$. The symmetry conditions at $\xi = 0$ give:

$$v_{\alpha,1}^{n+1} = v_{\beta,1}^{n+1} = 0. \tag{C.31}$$

We apply backward differences for the no-stress conditions at the exterior boundary $\xi = 1$:

$$v_{1,N}^{n+1} = v_{1,N-1}^{n+1} + \frac{3}{4}\frac{R^{n+1}}{\mu_1}\Delta\xi\Sigma_{\phi,N}^{n+1}, \tag{C.32}$$

$$v_{2,N}^{n+1} = v_{2,N-1}^{n+1} + \frac{3}{4}\frac{\theta_p R^{n+1}}{\theta_\mu\mu_1}\Delta\xi\Sigma_{\phi,N}^{n+1}. \tag{C.33}$$

C.1.5 Fixed-point iteration scheme for c with pseudo-timestepping

The final equation that we are required to solve is the reaction-diffusion equation for the oxygen concentration, c, given by Equation (C.3). We note that Equation (C.3) has no explicit time dependence since the oxygen field is in an assumed quasi-steady state.

Interior nodes

We use a fixed-point iteration scheme in order to deal with the non-linearity in Equation (C.3) arising from the tanh term. That is, for a non-linear system $A(\boldsymbol{u})\boldsymbol{u} = b(\boldsymbol{u})$ we perform iterations, indexed by k, solving the linear system $A(\boldsymbol{u}^k)\boldsymbol{u}^{k+1} = b(\boldsymbol{u}^k)$ until convergence is reached. We combine this fixed-point iteration scheme with a 'pseudo-timestep', ρ, in order to iterate towards the quasi-steady state solution. We use an implicit scheme for this pseudo-timestepping and so we solve the following finite difference scheme for c^{k+1}:

$$\frac{1}{\rho}(c_j^{k+1} - c_j^k) = \frac{D}{(R^{n+1})^2}\frac{1}{(\Delta\xi)^2}(c_{j+1}^{k+1} - 2c_j^{k+1} + c_{j-1}^{k+1}) - \frac{\Gamma}{2}\phi_{1,j}^{n+1}\left(1 + \tanh\left(\frac{c_j^k - c_N}{\epsilon}\right)\right). \tag{C.34}$$

We determine convergence when in the iterations k when $\max_j|c_j^k - c_j^{k-1}|$ falls below a pre-determined threshold, at which point we define $c^{n+1} = c^k$.

Boundary nodes

The linearised system in Equation (C.34) is solved with the boundary conditions at $\xi = 0$ and $\xi = 1$ at each iteration. The symmetry boundary condition at $\xi = 0$ gives:

$$c_1^{k+1} = c_2^{k+1}, \tag{C.35}$$

while the Dirichlet condition at the exterior boundary, $\xi = 1$, gives:

$$c_N^{k+1} = c_\infty. \tag{C.36}$$

C.2 Numerical checks for convergence

Having implemented the numerical system stated in Section C.1 it is necessary to perform numerical checks to determine the convergence and consistency of the numerical approximation.

We choose a few test parameter sets resulting in different steady states in order to

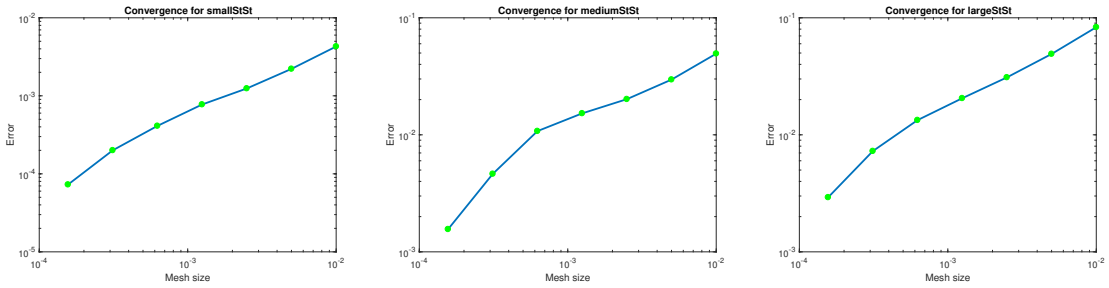

(a) Small size tumour example

(b) Medium size tumour example

(c) Large tumour example

Figure C.1: Log-log convergence plots for the numerical scheme

test a range of behaviours. We perform a sequence of mesh refinements for a total of 8 iterations of each case. Starting with a mesh such that $\Delta\xi = 0.01$ and $\Delta t = 0.01$, we take 7 successive finer meshes, halving the timestep and spacestep each time. In the absence of an exact, analytical solution to our system of equations, we test the consistency of our numerics using the finest mesh as a reference solution. As such we evaluate the difference between each of the coarser meshes and the reference solution using the discrete l_2 norm as defined by

$$||\mathbf{f}(\xi,t)||_{l_2} = \left(\sum_k \sum_n \Delta t \sum_j \Delta\xi f_k(\xi_j, t_n)^2 \right)^{\frac{1}{2}} \tag{C.37}$$

for a vector function $\mathbf{f}$ defined on mesh points ξ_j and t_n. For our multiphase system we define the solution by

$$\mathbf{u}(\xi,t) = (R(t), \alpha(\xi,t), \beta(\xi,t), c(\xi,t), v_\alpha(\xi,t), v_\beta(\xi,t))^T. \tag{C.38}$$

We determine the distance between our numerical solutions and the reference solution, $\mathbf{u_{ref}}(\xi,t)$, by evaluating $||\mathbf{u} - \mathbf{u_{ref}}||_{l_2}$ at all common mesh points.

The convergence plots for a range of steady state behaviours are shown in Figure C.1. In each case, we observe a decrease in the error to our reference solution with each successive mesh refinement. As such, we satisfy ourselves that our numerical method converges and is self-consistent. The results and analysis of additional numerical checks on some interesting edge cases are presented in Section C.3.

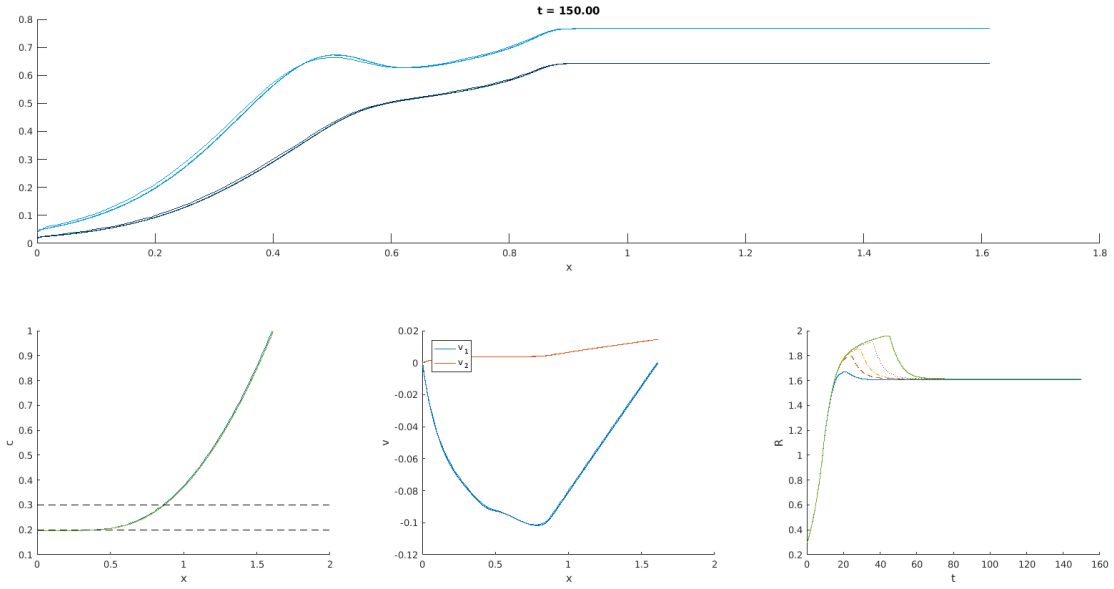

Figure C.2: Comparison of the numerical solutions for decreasing mesh sizes for dynamics in which the tumour growth exceeds the eventual steady state size.

C.3 Additional numerical tests

In Section C.2 we perform numerical tests in order to determine the convergence of our numerical scheme. We carry out these tests with a few parameter sets that result in a range of tumour steady states. In this section we detail further numerical tests performed on the qualitative dynamics described in Section 4.5.

C.3.1 Overshoot case

In this section we perform the mesh refinement checks for a case which exhibits dynamics whereby the tumour growth initially exceeds the steady state tumour size before decreasing again and reaching steady state from above, as described in Section 4.5.1. In Figure C.2 we overlay the solutions at the end of our simulations, $t = 150$, for each mesh size. We observe that the solutions converge to the same steady state tumour composition although the trajectories by which this steady state is reached noticeably differ. In particular, the time at which the tumour growth turns around and begins to recede increases for decreasing mesh size.

As described in Section 4.5.1, these dynamics arise due to the change in sign of v_1 –

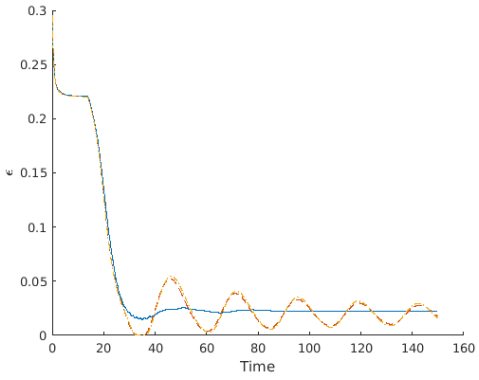

(a) Evolution of 'pinch point' in fluid phase over time

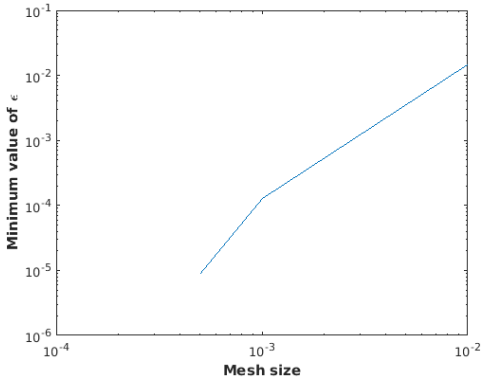

(b) Minimum value of pinch point for different mesh sizes

Figure C.3: Behaviour of 'pinch point' in fluid phase for mesh refinement checks.

$v_2|_{x=R(t)}$ and therefore the flow of the necrotic phase relative to the movement of the tumour boundary. When $v_1 - v_2|_{x=R(t)} > 0$, we have an inflow boundary and impose the additional boundary condition $\phi_2^+ = 0$ as explained in Section 4.2.3. This results in very small volume fractions in the necrotic phase, ϕ_2, at the tumour boundary. As mentioned previously, the moment at which $v_1 - v_2|_{x=R(t)}$ changes sign is important for driving the observed dynamics resulting in the turnaround of the tumour radius. As such, the accuracy with which we resolve the velocities v_1 and v_2 here is important, especially given the small volume fraction ϕ_2. This effect results in the discrepancies in the growth trajectories observed in Figure C.2.

C.3.2 Oscillatory case

Here we provide further discussion of the growth dynamics in which the tumour exhibits damped oscillations in tumour radius about a steady state. We again consider a mesh refinement check of the numerics in this case. Upon performing this mesh refinement, we notice that the numerical solution actually becomes unstable as the mesh size decreases.

If we denote by ϵ the minimum value in space at time t of the fluid phase volume fraction, then in Figure C.3a we plot $\epsilon(t)$ for the solution on each mesh size. We observe that once the 'pinch point' in this phase occurs, as described in Section 4.5.2, then the value of $\epsilon(t)$ also undergoes damped oscillations. In particular, the initial amplitude of the oscillations increases for decreasing mesh size with the minimum value of $\epsilon(t)$ occurring

on the first oscillation. We track the minimum value of $\epsilon(t)$ as we decrease the mesh size as shown in the log-log plot in Figure C.3b. We note that the fluid phase volume fraction elsewhere in the tumour is $\mathcal{O}(1)$ and, as such, our numerical scheme may be affected by floating point precision for small mesh sizes. Further investigation of this may require a more sophisticated numerical method.

Appendix D

Parameter sweep of multiphase radiotherapy response dynamics

In this section we describe the parameter sweep of our multiphase model, given by Equations (5.15)-(5.25), used to identify the range of qualitative responses to radiotherapy exhibited by the model and presented in Chapter 5. We use parameter combinations governing tumour growth taken from our catalogue of parameter sets for which the corresponding simulations reach a steady state tumour profile, as described in Section 4.4.3. Radiotherapy is simulated for the standard fractionation protocol of 2 Gy delivered daily 5 days a week with a weekend break. For the purposes of this parameter sweep in which we simply investigate the range of qualitative response dynamics exhibited by the model, we only simulate the first 3 or 4 weeks of treatment in order to reduce computation time. It is unfeasible to simulate all possible parameter combinations considered in this parameter sweep, and so selection of parameter combinations was performed at random to investigate the full range of dynamics.

All model simulations are started from the same initial conditions as for the simulations presented in Chapter 4. For any choice of growth parameter combination, we consider a range of radiotherapy parameters in our parameter sweep. We vary the time of delivery of the first radiotherapy fraction and the intrinsic radiosensitivity of the tumour cell phase, characterised by the parameters α and α/β. We also consider both the continuous and discrete OER formulations within the parameter sweep, although we note the limitations

Parameter	Values for parameter sweep
t_1	$\{10, 25, 50, 75, 100\}$
α	$\{0.1, 0.35, 0.5\}$
α/β	$\{5, 10, 15\}$
OER version	'discrete' or 'continuous'

Table D.1: The parameter ranges included in the parameter sweep for the multiphase tumour growth model with radiotherapy as defined by Equations (5.15)-(5.25).

presented in Appendix B. The ranges of each radiotherapy parameter included in the parameter sweep are listed in Table D.1.

A range of simulation results are shown in Figures D.1-D.3 with dynamics of particular interest highlighted. In Figure D.1 the simulation outlined in blue exhibits a plateau in treatment response followed by a dip in the tumour radius trajectory after the end of radiotherapy. The simulation highlighted in green also displays interesting post-treatment dynamics, with regrowth appearing to differ from the untreated growth behaviour. In contrast, the radiotherapy appears to have little effect on the tumour radius for the simulation outlined in red.

In Figure D.2, the simulation with the green border exhibits a plateau in response that qualitatively appears to occur via a different process than the plateau observed in the blue example of Figure D.1. The trajectory for the simulation outlined in orange exhibits dynamics which are qualitatively common to many radiotherapy models in the literature, characterised by a consistent decrease in tumour volume throughout the weekly fractionation and a slight increase due to regrowth over the weekend break.

In Figure D.3, we highlight in orange a simulation for which the tumour continues to grow throughout the early stages of treatment before exhibiting a delayed response in which the outer tumour radius subsequently decreases.

We use the qualitative dynamics observed from this parameter sweep, and the corresponding parameter sets, to identify cases for further study, the results of which are presented in Chapter 5.

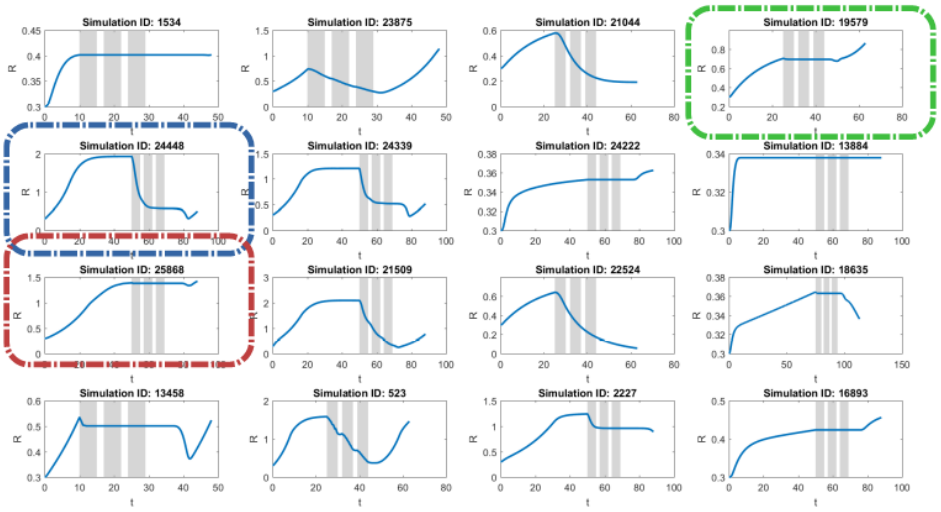

Figure D.1: A selection of radiotherapy responses from simulations of Equations (5.15)-(5.25) obtained from the parameter sweep of the multiphase model presented in Chapter 5. Dynamics of particular interest are outlined in colour. (1)

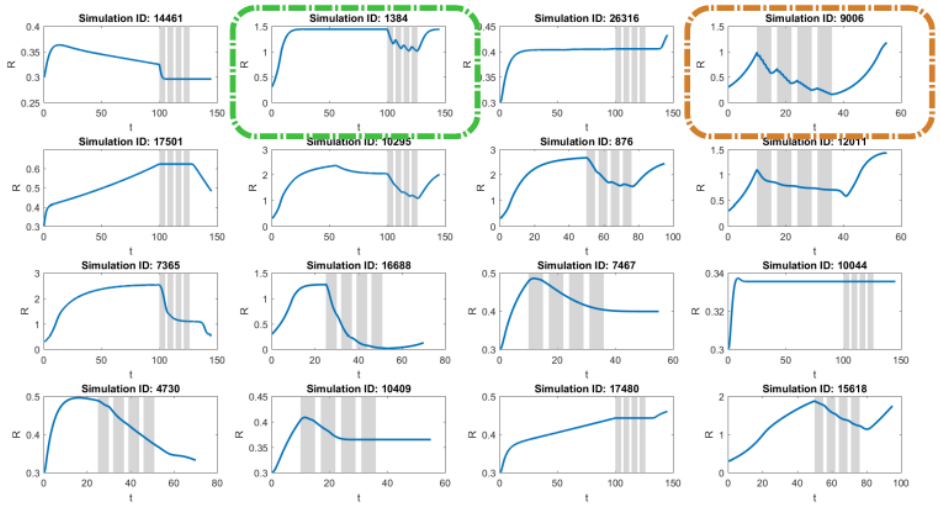

Figure D.2: A selection of radiotherapy responses from simulations of Equations (5.15)-(5.25) obtained from the parameter sweep of the multiphase model presented in Chapter 5. Dynamics of particular interest are outlined in colour. (2)

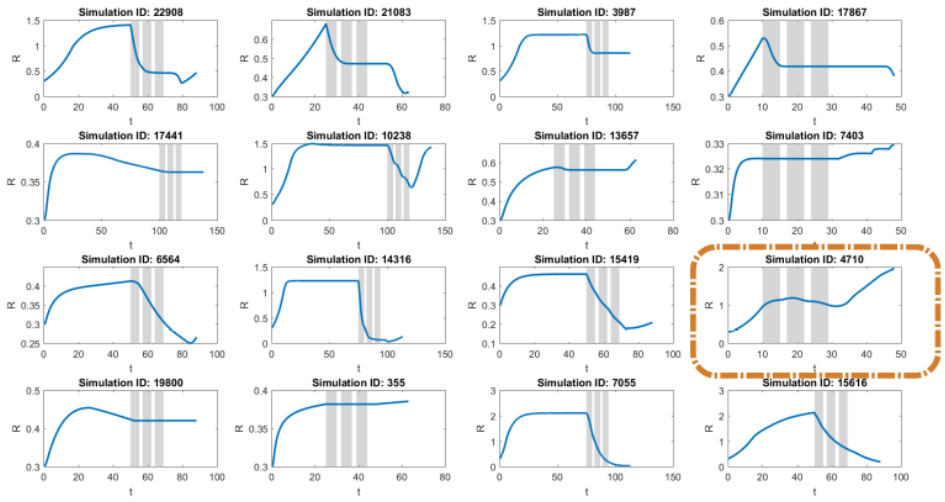

Figure D.3: A selection of radiotherapy responses from simulations of Equations (5.15)-(5.25) obtained from the parameter sweep of the multiphase model presented in Chapter 5. Dynamics of particular interest are outlined in colour. (3)